Optimization of SHJ Bottom Cells for 2T Perovskite/c-Si Tandem applications

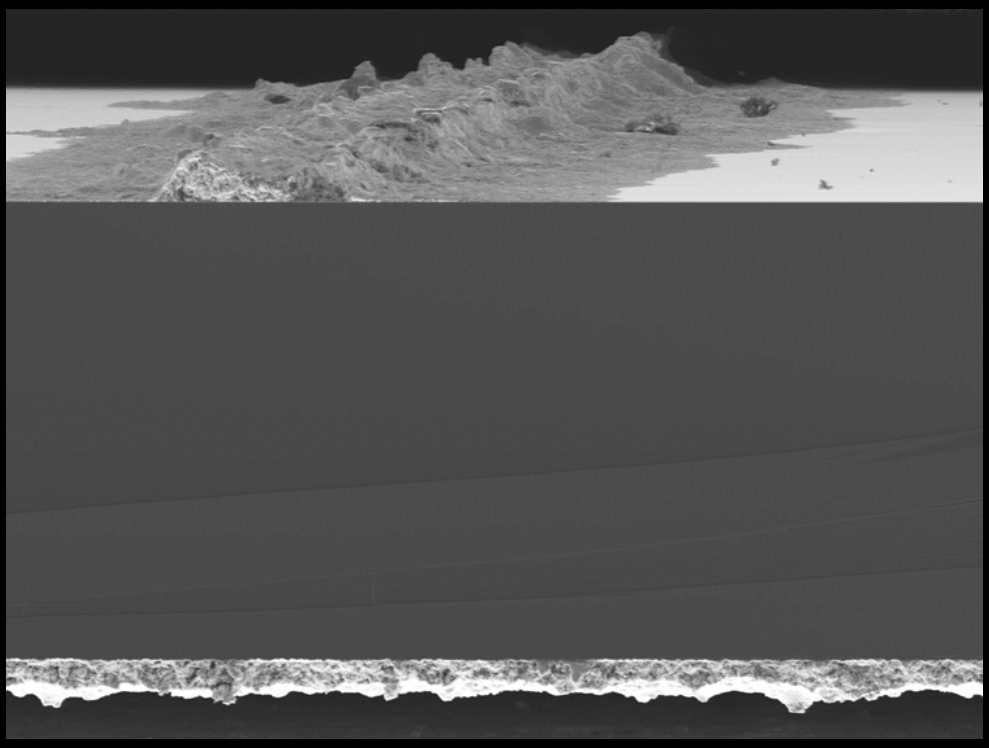

Delft University of Technology

Mohua Fardousi

TU Delft

Optimization of SHJ Bottom Cells for 2T Perovskite/c-Si Tandem applications

by

Mohua Fardousi

to obtain the degree of Master of Science
at the Delft University of Technology.

Student number:	4817230	
Defended on:	August 31st , 2023	
Supervisors:	Prof. dr. Olindo Isabella	Head of the PVMD group, EEMCS
	Dr. Luana Mazzarella	Assistant professor at PVMD group, EEMCS
	Ir. Yifeng Zhao	Researcher at PVMD group, EEMCS

This thesis is confidential and cannot be made public until August 31, 2024.

TU Delft Delft University of Technology

Else Kooi Laboratory

PVMD Delft University of Technology

Graduate

Mohua Fardousi

MSc Sustainable Energy Technology

Specialization in Solar Energy

Faculty of Electrical Engineering, Mathematics of Computer Science (EEMCS)

fardousi.mohua21@gmail.com

MSc Thesis Committee

Prof. dr. Olindo Isabella - PVMD, Department of Electrical Sustainable Energy, TU Delft

Dr. Milos Cvetkovic - IEPG, Department Electrical Engineering, Mathematics of Computer Science, TU Delft

Dr. Rudi Santbergen - PVMD, Department of Electrical Sustainable Energy, TU Delft

Ir. Yifeng Zhao - PVMD, Department of Electrical Sustainable Energy, TU Delft

Delft University of Technology

Department of Electrical Sustainable Energy - Photovoltaic Materials and Devices (PVMD)

TU Delft Delft University of Technology

EKL Else Kooi Laboratory

PVMD Delft University of Technology

Preface

‘Solar power is a safe form of nuclear energy. We are using fusion reactions that are 93 million miles away to make light that we then convert to electricity with photovoltaic modules.’

-Sean White

”Go Green” is the ideal catchphrase to support the 2015 Paris Agreement, which aims to protect the world from the worst effects of anticipated global warming by keeping the rise in average global temperature to well below 2°C. It is crucial to concentrate on large-scale renewable energy harvesting if you want it to succeed. It is feasible to achieve the intent of saving the planet by reducing the carbon footprint by taking into account the superiority of solar power in combination with the miracle of materials, semiconductors, quantum mechanics, physics, arithmetic, and the continued dedication of scientists to make it work. This very interesting hybrid project provided an excellent opportunity to get directly involved with this fastest-lifting research area by working with scientists and researchers, learning technical expertise, and contributing to their research to serve the world. Among the various types of solar cells (monocrystalline, polycrystalline, thin-film, etc.), silicon solar cells made from c-Si wafers (both monocrystalline and polycrystalline) currently account for 95% of the market. A thin layer of hydrogenated intrinsic amorphous silicon, sometimes known as ”buffer layers,” and doped selective contact layers passivate an active crystalline silicon absorber substrate, which is the basic building block of SHJ cells. With its so-called heterostructure nanomaterials, SHJ is a market pioneer in both research and commercial production thanks to its superior efficiency, high V_{oc}, high conductivity, raised cyclic stability, high energy and power densities, and low-temperature coefficients. Making single junction SHJ solar cells for the 2T tandem application based on optically optimized parameters was an unparalleled opportunity and accomplishment. With regard to competing with current conventional or fossil-fueled electricity sources, PV technology has emerged as the most promising. I firmly believe that this Master’s thesis, which focuses on the optoelectrical characteristics optimization of 2T tandem and single junction SHJ solar cells, can advance the state of knowledge in the field of photovoltaic technology for more effective green energy harvesting. I would like to convey my sincere gratitude to my superior and daily supervisor for their assistance, direction, and never-ending support. I also want to thank my loved ones, friends, and roommates for their unwavering support and affection throughout the writing of this master’s thesis.

Mohua Fardousi
Delft, August 2023

Abstract

Silicon heterojunction solar cells (SHJ) showed a record efficiency of 26.81%, approaching the theoretical limit of single-junction crystalline silicon (c-Si) solar cells. To further improve the efficiency, a wide bandgap perovskite top cell can be stacked on top of the SHJ bottom cell forming tandem solar cells, which utilize better the solar spectrum. Recently, a record efficiency of 33.70% was achieved for a monolithic two-terminal perovskite/SHJ tandem solar cell. Typically, a transparent conductive oxide (TCO) layer, functioning as the recombination junction, is used to connect the two sub-cells. However, tandem solar cells with this conventional TCO recombination junction often feature high reflection losses originating from the intermediate interfaces between the two sub-cells. Therefore, this master thesis focused on minimizing these intermediate reflection losses by substituting the TCO-based recombination junction with proposed TCO-free recombination junctions.

Firstly, comprehensive optical simulation studies that compared 2T tandem solar cells with various recombination junctions were performed. In the case of single-side-textured (front-side-flat) tandem configuration, as compared to the reference cell with tin-doped indium oxide (ITO) recombination junctions, the use of the more transparent tungsten-doped indium oxide (IWO) allowed an improved implied photocurrent density in the bottom cell ($J_{imp,bottom}$) from 18.30 mA/cm^2 to 18.70 mA/cm^2. Further, by using the TCO-free recombination junction composed of (*p*)nc-SiO_x:H/(*n*)nc-SiO_x:H or (*p*)nc-Si:H/(*n*)nc-Si:H, ranges of optimum thickness combinations were discovered, which allowed high $J_{imp,bottom}$ values of 20.30 mA/cm^2 or 19.80 mA/cm^2, respectively. Both TCO-free recombination junctions demonstrated enhanced light coupling to the bottom cell thanks to the optimized interference effect at the intermediate interfaces between two sub-cells, minimizing the associated reflection losses. Furthermore, the designs of tandem solar cells featuring various recombination junctions were optimized to reach maximum matched tandem current density. For the reference cell with ITO recombination junction, a matched tandem current density of 19.40 mA/cm^2 was obtained, while the use of TCO-free recombination junctions, for instance, 60 nm (*p*)nc-SiO_x:H/ 70 nm (*n*)nc-SiO_x:H or 30 nm (*p*)nc-Si:H/75 nm (*n*)nc-Si:H, demonstrated high $J_{imp,bottom}$ values of 19.80 mA/cm^2 and 19.80 mA/cm^2, respectively. These results highlight the optical advantageous implementations of proposed TCO-free recombination junctions for monolith tandem solar cells. Similar observations but less significant improvement by using the proposed TCO-free recombination junctions were found in double-side-textured tandem solar cells. This is due to the already minimized reflection losses of the (*p*)nc-SiO_x:H/(*n*)nc-SiO_x:H or (*p*)nc-Si:H/(*n*)nc-Si:H configurations (1.3 mA/cm^2 and 1.4 mA/cm^2 respectively) as a result of the textured front surface.

Based on optical simulation studies conducted on 2T tandem solar cells, the electrical effectiveness of proposed TCO-free recombination junctions was examined by fabricating proof-of-concept single junction single-side-textured SHJ solar cells. First, we focused on the passivation optimization of the flat (100) c-Si surface as it is prone to detrimental epitaxial growth. An impressive minority carrier lifetime of 16.87 ms was achieved by combing (*n*)nc-Si: H and (*i*)a-Si: H bi-layer in a symmetrical configuration. Moreover, we also observed, in general, better conductivity when increasing thicknesses of doped nc-SiO_x: H layers when they were deposited on glass or (*i*)a-Si: H coated glass substrates. Eventually, proof-of-concept single junction single-side-textured SHJ solar cells featuring the proposed TCO-free recombination junction were fabricated. According to the optical simulations, various optimum thickness combinations of (*p*)nc-SiO_x: H and (*n*)nc-SiO_x: H or (*p*)nc-Si: H and (*n*)nc-Si: H that composes the recombination junction were tested. Overall, the optically promising TCO-free recombination junctions in 2T tandem solar cells also delivered high FF values in proof-of-concept single-junction SHJ solar cells, demonstrating their potential to be implemented to fabricate high-efficiency monolithic 2T tandem solar cells.

Contents

1 Introduction **1**
1.1 Solar Energy: Bearer of Clean Energy . . . 1
1.2 Fundamentals of Solar Cells . . . 2
1.2.1 Semiconductor Materials: . . . 2
1.2.2 Generation: . . . 3
1.2.3 Recombination: . . . 3
1.3 Solar Cell's Working Principle : . . . 4
1.3.1 Perovskite Solar Cells: . . . 5
1.3.2 Silicon Heterojunction Solar Cells: . . . 6
1.3.3 PVK/c-Si Tandem Solar Cells: Paving the Way of High Efficiency . . . 7
1.3.4 Challenges With single-side-textured SHJ Bottom Cells . . . 9
1.4 Research Outline . . . 11
1.5 Research Proposal . . . 11

2 Fundamentals **13**
2.1 SHJ solar cells: Traditional and Proposed Architecture . . . 13
2.2 Hydrogenated Amorphous Silicon . . . 14
2.2.1 Atomic composition of (*i*)a-Si:H . . . 14
2.2.2 Growth mechanism of (*i*)a-Si:H . . . 15
2.3 Doper Layers:(*n*)/(*p*)nc-Si:H . . . 18
2.3.1 Atomic Structure . . . 19
2.3.2 Growth Mechanism . . . 20
2.4 Doped Layers: (*n*)/(*p*)nc-SiO_x:H . . . 20
2.4.1 Atomic Structure . . . 21
2.4.2 Growth Mechanism . . . 21
2.5 Transparent Conducting Oxides . . . 22
2.5.1 Optical and Electrical properties of TCOs . . . 22
2.5.2 Recombination Junction (RJ) . . . 22

3 Instrumentation of SHJ Solar Cells: Fabrication and Characterization **25**
3.1 Optimal Simulation Tool: GenPro4 . . . 25
3.1.1 Optical Properties . . . 25
3.2 Experimental Simulation Tools: Dark Conductivity of Doped Layers . . . 26
3.2.1 Ultrasonic Cleaner: Corning Eagle XG . . . 26
3.2.2 Electron Beam- Physical Vapor Deposition(EB-PVD) . . . 26
3.2.3 Dark Conductivity and Activation Energy . . . 27
3.3 Characterization of Doped Layer . . . 29
3.4 Experimental Simulation Tools: Fabrication of Single-Junction SHJ Solar Cells . . . 29
3.4.1 Wafer Texturing . . . 30
3.4.2 Wafer Cleaning . . . 30
3.4.3 Radio Frequency Plasma-Enhanced Chemical Vapor Deposition (RF-PECVD) . . . 31
3.4.4 Radio-frequency Magnetron Sputtering . . . 32
3.4.5 Screen printing . . . 34
3.5 Characterization of Single Junction SHJ Solar Cells . . . 34
3.5.1 Photoconductance Lifetime Tester . . . 35
3.5.2 Spectroscopic Ellipsometry . . . 36
3.5.3 J-V Measurements . . . 37
3.5.4 EQE . . . 38
3.5.5 UV-Vis-NIR Spectroscopy . . . 39
3.5.6 SunsVoc . . . 39

3.5.7 SEM . . . 40

4 Optical Simulation 43
4.1 Previously Optimized Tandem and Some Intro. . . . 43
4.1.1 Layers of 2T Tandem Device: Brief Intro. . . . 44
4.2 Single-side-textured 2T Tandem Solar Cells . . . 46
4.2.1 Optimizing Various Combinations RJ and Rear-TCO Layers . . . 46
4.3 Intro. of Various Combinations of TCO-free RJ in the 2T Tandem Devices . . . 48
4.3.1 Optimizing Doped nc-SiO_x:H Layers as RJ with Various Rear-TCO . . . 48
4.3.2 Optimizing Doped nc-Si:H Layers as RJ with Various Rear-TCO . . . 51
4.3.3 Optimization of Doped nc-Si:H/nc-SiO_x:H RJ Layers with Various Rear TCOs . . . 53
4.3.4 Comparison Among Different RJs and Rear TCOs: Single-side-textured Perovskite/c-Si 2T Tandem Solar Cells . . . 55
4.4 Double-side-textured 2T Tandem Solar Cells . . . 56
4.4.1 Optimization of Various Recombination Junction and Rear TCOs . . . 57
4.5 Intro. of Various Combinations of TCO-free RJ in the 2T Tan- dem Devices . . . 59
4.5.1 Optimizing Doped nc-SiO_x:H Layers as RJ with Various Rear-TCO . . . 60
4.5.2 Optimizing Doped nc-Si:H Layers as RJ with Various Rear-TCO . . . 60
4.5.3 Optimization of Doped nc-Si:H/nc-SiO_x:H RJ Layers with Various Rear TCOs . . . 62
4.5.4 Comparison Among Different RJs and Rear TCOs: Single-side-textured Perovskite/c-Si 2T Tandem Solar Cells . . . 64
4.6 Perovskite/c-Si 2T Tandem Device: Pre and Post Optimization . . . 66
4.6.1 (*p*)/(*n*)nc-SiO_x:H as RJ with Rear IWO : Single-side-textured . . . 66
4.6.2 (*p*)/(*n*)nc-SiO_x:H as RJ with Rear IWO : Double-side-textured . . . 67

5 Optimizing single-junction SHJ solar cells 71
5.1 Passivation Optimization . . . 72
5.1.1 Symmetrical Monolayer Passivation (*i*-1 Layer). . . . 72
5.1.2 Symmetrical Bilayer Passivation (*i*-1 and *i*-2) . . . 74
5.1.3 Symmetrical Bilayer Passivation with Intermediate HPT (*i*-1 + HPT + *i*-2). . . . 76
5.1.4 Symmetrical Passivation of *i*-layers with *p*-contact . . . 78
5.1.5 Summary of *i*-layer Passivation: . . . 80
5.2 Optimizing Doped nc-SiO_x:H Layers . . . 81
5.3 Optimizing Single-side-textured single-junction SHJ Solar Cells for TCO-free RJ Layers . 84
5.4 Single-junction SHJ Solar Cells with Oxidic RJ . . . 86
5.4.1 J-V measurement. . . . 87
5.4.2 EQE Measurement . . . 90
5.5 Single-junction SHJ Solar Cells with Non-oxidic RJ . . . 92
5.5.1 J-V measurement. . . . 92
5.5.2 EQE Measurement . . . 95
5.6 Single-junction SHJ Solar Cells with Bilayer *p*-contact/*n*-layer as RJ . . . 98
5.6.1 J-V measurement. . . . 98
5.6.2 EQE Measurement . . . 99
5.7 Investigating Crystalline Growth of Prepared Samples . . . 101

6 Conclusions and Outlooks 103
6.1 Conclusions . . . 103
6.1.1 Optical Optimization of Monolithic 2T Perovskite/c-Si Tandem Devices . . . 103
6.1.2 Optimization of Proof-of-concept Single-side-textured SHJ Solar Cells for Tandem Applications . . . 104
6.2 Outlooks . . . 105
6.2.1 Optical Optimization of Perovskite/c-Si Tandem Devices. . . . 105
6.2.2 Electrical Investigation as 'proof of concept' . . . 106

Acknowledgements 109

Appendix 111

List of Tables

1.1 List of recent studies of silicon solar cells with tandem current, open circuit voltage, fill factor, power conversion efficiency order by publication date 9

4.1 Optimizing MgF_2 Thickness from different cell configurations: 44
4.2 Optical outcomes of 2T Perovskite/c-Si tandem with TCO-RJ: Single-side-textured devices. 48
4.3 Optical outcomes of 2T Perovskite/c-Si tandem with TCO-free Oxidic layers as RJ : Single-side-textured devices. 50
4.4 Optical outcomes of 2T Perovskite/c-Si tandem with TCO-free non-oxidic layers as RJ: Single-side-textured devices. 52
4.5 Optical outcomes of 2T Perovskite/c-Si tandem with TCO-free Non-oxidic/Oxidic layers as RJ: Single-side-textured devices. 54
4.6 Summarizing optical outcomes of Single-side-textured 2T Perovskite/c-Si tandem (with initial RJ thickness) devices. 55
4.7 Optical outcomes of 2T Perovskite/c-Si tandem with TCO-RJ: Double-side-textured devices. 60
4.8 Optical outcomes of 2T Perovskite/c-Si tandem with TCO-free Oxidic layers as RJ : Double-side-textured devices. 61
4.9 Optical outcomes of 2T Perovskite/c-Si tandem with TCO-free Non-oxidic layers as RJ: Double-side-textured devices. 62
4.10 Optical outcomes of 2T Perovskite/c-Si tandem with TCO-free Non-oxidic/Oxidic layers as RJ: Double-side-textured devices. 64
4.11 Summarizing optical outcomes of Double-side-textured 2T Perovskite/c-Si tandem devices (with initial RJ thickness). 65
4.12 Summarizing optical outcomes of Single-side-textured 2T Perovskite/c-Si tandem devices (with current matching). 69
4.13 Summarizing optical outcomes of Double-side-textured 2T Perovskite/c-Si tandem devices (with current matching). 69

5.1 Deposition parameters of numerous intrinsic and doped layers. 71
5.2 Activation Energy (E_a) and Dark Conductivity (σ_d) of nc-SiO_x and *i*/nc-SiO_x layers 83
5.3 Deposition parameters of doped Si layers. 85
5.4 Deposition parameters of ITO layers 85
5.5 Deposition parameters of Single-side-textured Single-junction SHJ solar cells (front layers stacks) 85
5.6 Deposition parameters of Single-side-textured Single-junction SHJ solar cells (rear layers stacks) 86
5.7 Optimized J-V data of Single-side-textured SHJ solar cells fabricated by 60 nm (*n*)nc-SiO_x:H (60 nm) layers with distinct (*p*)nc-SiO_x:H layers. 89
5.8 Optimized J-V data of Single-side-textured SHJ solar cells fabricated by 10/20 nm (*p*)nc-Si:H layers with distinct (*n*)nc-Si:H layers. 93
5.9 Optimized J-V data of Single-side-textured SHJ solar cells fabricated by 60 nm (*n*)nc-Si:H layers with distinct (*p*)nc-Si:H layers. 95
5.10 Optimized J-V data of Single-side-textured SHJ solar cells fabricated by 30/5 nm (*p*)nc-Si:H /(*p*)nc-SiO_x:H layers with distinct (*n*)nc-Si:H layers. 99

List of Figures

1.1 Globally installed renewable energy capacity bar chart (2000-2020). Adapted from [2]. . 1
1.2 Worldwide employment in renewable energy technology sectors (2012-20). Adapted from [2]. . . . 2
1.3 Schemetic describes (a) different types of materials, (b) generation and (c) fermi level positions. . . . 3
1.4 The schematics (a),(b), and (c) demonstrate the types of recombination. . . . 4
1.5 Solar cell basic working principle. Adapted from [12]. . . . 5
1.6 Crystal structure of a 3D Perovskite. Adapted from [16]. . . . 6
1.7 Device architecture of single-junction (rear-junction) SHJ solar cell. . . . 6
1.8 Spectral irradiance absorbance of Perovskite (P) and Silicon (Si) are shown in (a) and (b) respectively. Adapted from [25]. . . . 7
1.9 Perovskite/Silicon tandem architectures : (a). Four-terminal (4T), (b). Two-terminal (2T); (c). Four-terminal optical spectral splitting; and (d). Four-terminal reflective tandem device . Adapted from [30]. . . . 8
1.10 Device architecture of 2T Perovskite/c-Si Tandem solar cells: (a) 'p-i-n' Perovskite/Rear junction SHJ and (b) 'n-i-p' Perovskite/Front emitter SHJ configurations. . . . 10

2.1 Device architecture of (a) front-side-flat and (b) double-side-textured single-junction SHJ solar cell with proposed doped oxidic layers as RJ. . . . 13
2.2 A schematic illustrating of the atomic composition (a) crystalline silicon (c-Si), (b) hydrogenated nanocrystalline silicon (μc-Si:H), and (c) hydrogenated amorphous silicon (a-Si:H). Adopted from [78]. . . . 14
2.3 The schematic illustrates the interaction between SiH_3 and the c-Si growing surface. Adopted from [88]. . . . 16
2.4 Atomic growth on various c-Si surface orientations: (a) <111>; (b) <100> (unreconstructed); and (c) <100> (- 2x1) (reconstructed). Adopted from [92]. . . . 17
2.5 The schematic of the surface passivation process on c-Si surfaces. Adopted from [95]. 18
2.6 Schematic of chemical passivation at c-Si/*(i)*a-Si:H interface. Adopted from [84] . . . 19
2.7 Atomic structure of nc-Si:H: crystalline phase on the left (yellow) and amorphous silicon on the right (orange). Adopted from [110]. . . . 19
2.8 Growth mechanism of nc-Si:H. Adopted from [119]. . . . 20
2.9 Schematic of an amorphous matrix with nano- and microcrystalline phases. Adapted from [123]. . . . 21
2.10 Band diagrams of the interface between perovskite/c-Si silicon tandem solar cell: (a) without and (b)with an ITO as RJ, whereas (c) represents a closer image of the tunneling region to observe different recombination mechanisms such as : (1) Local, (2) Trap-assisted and (3) Direct tunneling. Adopted from [64]. . . . 22

3.1 The optical simulation system of 2T tandem devices and single-junction SHJ solar cells are depicted in a flowchart. . . . 25
3.2 Flowchart of doped layers investigation. . . . 26
3.3 Metal evaporation system in PVDM group with electron beam evaporation (left) and resistive evaporation (right). Adapted from [139]. . . . 27
3.4 Flowchart of EM-PVD metal deposition process. . . . 27
3.5 Definition of activation energy of *n*-type (a) and *p*-type (b) materials. . . . 27
3.6 (a) Dark current at 10V and (b) conductivity, measured at various temperatures. Adapted from [140]. . . . 28
3.7 An illustration of a sample measuring setup for Activation Energy and Dark Conductivity. Adapted from [139]. . . . 29

3.8 Flowchart to fabricate single-side-textured single-junction SHJ solar cells. 29
3.9 Schematic of RF-PECVD deposition system. Adapted from [10]. 31
3.10 Top view of RF-PECVD tool (Amigo) in PVMD group depicting six deposition chambers connected with pumps for vacuum transfer and thin-films deposition. 31
3.11 Flowchart of RF-PECVD deposition process. 32
3.12 A traditional magnetron sputtering system. Adapted from [108]. 33
3.13 Top view of RF-PVD sputtering tool (Zorro) developed by PVMD group depicting two deposition chambers connected with pumps for vacuum transfer and TCO deposition. . 33
3.14 Flowchart of RF-PVD deposition process. 34
3.15 A traditional screen printing system (The top part represents the process and the bottom part denotes the end). Adapted from [147]. 34
3.16 Depiction of photoconductance lifetime tester. Adapted from [148]. 35
3.17 Minority carrier density (MCD) as a function of concentration for different recombination mechanisms. Adapted from [84]. 36
3.18 Spectroscopic Ellipsometry setup with the light source, polarizer, polarization analyzer, and detector. Adapted form [151]. 37
3.19 Steps for characterizing physical properties with SE measurements. 37
3.20 A typical J-V curve with the required equations regarding solar cell efficiency and fill factor. Adapted from [84]. 38
3.21 Optical design of a UV-Vis-NIR spectrometer with a 150 mm integrating sphere test sample position for transmittance or reflectance measurement. Adapted from [152] 39
3.22 Electron beam interacting with a sample to generate secondary electrons and x-rays. Adapted from [155]. 40
3.23 Flowchart of typical SEM measurement. 41

4.1 Device architecture: Single-side-textured 2T Perovskite/c-Si tandem cell with RJ and rear ITO (reference device) [156]. 43
4.2 Optimizing the thickness of MgF_2. 45
4.3 Flowchart of 2-Steps measures towards optimizing 2T tandem devices. 46
4.4 Device architecture: Single-side-textured 2T Perovskite/c-Si tandem cell with RJ and rear IWO (optimized with TCO-RJ) [156]. 47
4.5 Contour plots: Single-side-textured 2T Perovskite/c-Si tandem with IWO_IWO configuration. 49
4.6 Device architecture: Single-side-textured 2T Perovskite/c-Si tandem cell with *(p/n)*nc-SiO_x:H as RJ and rear IWO (TCO-free optimized RJ with oxidic layers) [156]. 50
4.7 Contour plots: Single-side-textured 2T Perovskite/c-Si tandem with *(p/n)*nc-SiO_x:H_IWO configuration. 51
4.8 Device architecture: Single-side-textured 2T Perovskite/c-Si tandem cell with *(p/n)*nc-Si:H as RJ and rear IWO (TCO-free optimized RJ with non-oxidic layers) [156]. 52
4.9 Device architecture: Single-side-textured 2T Perovskite/c-Si tandem cell with *(p/n)*nc-SiO_x:H as RJ and rear IWO (TCO-free optimized RJ with nc-Si:H/ nc-SiO_x:H) [156]. . . 53
4.10 Device architecture: Single-side-textured 2T Perovskite/c-Si tandem cell with *(p/n)*nc-SiO_x:H as RJ and rear IWO (TCO-free optimized RJ with nc-SiO_x:H/nc-Si:H) [156]. . . . 54
4.11 Optimizing Front-ITO thickness: Front-ITO vs Implies Photocurrent density. 56
4.12 Optimizing C60 thickness: C60 vs Implies Photocurrent density. 57
4.13 Device architecture: Double-side-textured 2T Perovskite/c-Si tandem cell with RJ and rear ITO (reference device). 58
4.14 Device architecture: Double-side-textured 2T Perovskite/c-Si tandem cell with RJ and rear IWO (optimized with TCO-RJ). 58
4.15 Contour plots: Double-side-textured 2T Perovskite/c-Si tandem with IWO_IWO configuration. 59
4.16 Device architecture: Double-side-textured 2T Perovskite/c-Si tandem cell with *(p/n)*nc-SiO_x:H as RJ and rear IWO (TCO-free optimized RJ with oxidic layers). 61
4.17 Contour plots: Double-side-textured 2T Perovskite/c-Si tandem with *(p/n)*nc-SiO_x:H_IWO configuration. 62

4.18 Device architecture: Double-side-textured 2T Perovskite/c-Si tandem cell with *(p/n)*nc-Si:H as RJ and rear IWO (TCO-free optimized RJ with non-oxidic layers) [156]. 63
4.19 Device architecture: Double-side-textured 2T Perovskite/c-Si tandem cell with *(p/n)*nc-SiO_x:H as RJ and rear IWO (TCO-free optimized RJ with nc-Si:H/ nc-SiO_x:H) [156]. . . 64
4.20 Device architecture: Double-side-textured 2T Perovskite/c-Si tandem cell with *(p/n)*nc-SiO_x:H as RJ and rear IWO (TCO-free optimized RJ with nc-SiO_x:H/nc-Si:H). 65
4.21 Device architecture: Single-side-textured 2T Perovskite/c-Si tandem cell with *(p/n)*nc-SiO_x:H as RJ and rear IWO (optimized 2T tandem device with TCO-free optimized oxidic RJ layers) [156]. 67
4.22 Device architecture: Double-side-textured 2T Perovskite/c-Si tandem cell with *(p/n)*nc-SiO_x:H as RJ and rear IWO (optimized 2T tandem device with TCO-free optimized oxidic RJ layers) [156]. 68

5.1 Flowchart of depositing (*i*)a-Si:H) layers. 72
5.2 Schematics illustrate symmetrical passivation of (a) *i*-layers and (b) *i*-1 layers with n-contact, on the surface of a (100) c-Si wafers. 73
5.3 Effective minority carrier lifetime of *i*-1 layer with various *n*-contacts. 73
5.4 Effective minority carrier density and i-V_{oc} comparison of *i*-1 layer with distinct *n*-contacts. 74
5.5 Schematics illustrate symmetrical passivation of (a) bilayer (*i*-1 & *i*-2) and (b) bilayer (*i*-1 & *i*-2) with *n*-contact, on the surface of a <100> c-Si wafers. 75
5.6 Effective minority carrier lifetime of *i*-1 layer with various *n*-contacts. 75
5.7 Effective minority carrier density and i-V_{oc} comparison of *i*-1 & *i*-2 layers with distinct n-contacts. 76
5.8 Schematics illustrate symmetrical passivation of (a) *i*-1+ HPT+*i*-2 and (b) *i*-1+HPT+ *i*-2 with various *n*-contact, on the surface of (100) c-Si wafers. 77
5.9 Minority carrier lifetime measurements of bilayer (*i*-1 + HPT + *i*-1) with intermediate HPT and different *n*-layers. 77
5.10 Effective minority carrier density and i-V_{oc} comparison of *(*i-1 + HPT + *i*-2) layers with distinct *n*-contacts. 78
5.11 Schematics illustrate symmetrical passivations : (a) (*i*-1) + *p*-contact, (b) (*i*-1+ *i*-2) + *p*-contact and (c) (*i*-1+ HPT + *i*-2) + *p*-contact , on the surface of a <100> c-Si wafers. . 78
5.12 Minority carrier lifetime measurements using *p*-contacts with various *i* (*i*-1 & *i*-2) layers. 79
5.13 Effective minority carrier density and i-V_{oc} comparison of *i*-layers with distinct *p*-contacts. 80
5.14 Effective lifetime (τ_{eff}) of flat (100)c-Si samples with symmetrical passivation: *i*-1 (10 nm), *i*-1 (5 nm) + *i*-2 (5 nm), *i*-1 (5 nm) + HPT + *i*-2 (5 nm) and different (*n*)-layers (a-Si:H (6 nm), nc-Si:H (20 nm),nc-SiO_x:H (60 nm). 80
5.15 Effective lifetime (τ_{eff}) of flat (100)c-Si samples with symmetrical passivation: *i*-1 (10 nm), *i*-1 (5 nm) + *i*-2 (5 nm), *i*-1 (5 nm) + HPT + *i*-2 (5 nm) and different (*p*)-layers (nc-Si:H (5 nm), nc-SiO_x:H (16 nm). 81
5.16 Thickness of doped nc-SiO_x:H layer (nm) vs Activation Energy,E_a (meV). 82
5.17 Thickness of doped nc-SiO_x:H layer (nm) vs Dark Conductivity, σ_d (S/cm). 83
5.18 A process flowchart of SHJ solar cell fabrication w/ the highlighted bottom device' architecture. 84
5.19 Front (a) and rear (b) side of a Single-side-textured Single-junction SHJ solar cell. . . . 86
5.20 J-V Parameters of Single-side-textured SHJ solar cells fabricated by 60 nm (*n*)nc-SiO_x:H (60 nm) layers with distinct (*p*)nc-SiO_x:H layers. 87
5.21 J-V Parameters of Single-side-textured SHJ solar cells fabricated by 60 nm (*p*)nc-SiO_x:H (60 nm) layers with distinct (*n*)nc-SiO_x:H layers. 88
5.22 Contour plot of optically simulated Single-side-textured 2T tandem device w/ doped Odixic layers as RJ : (best FF in optimal thickness range). 89
5.23 Contour plot of optically simulated Single-side-textured 2T tandem device w/ doped Odixic layers as RJ : (average FF in optimal thickness range). 89
5.24 EQE curves of Single-side-textured SHJ solar cells fabricated by 60 nm (*n*)nc-SiO_x:H layers with distinct (*p*)nc-SiO_x:H layers. 90
5.25 EQE curves of Single-side-textured SHJ solar cells fabricated by 60 nm (*p*)nc-SiO_x:H layers with distinct (*n*)nc-SiO_x:H layers. 90

5.26 J-V Parameters of Single-side-textured SHJ solar cells fabricated by 10 nm (*p*)nc-Si:H layers with distinct (*n*)nc-Si:H layers. 92
5.27 J-V Parameters of Single-side-textured SHJ solar cells fabricated by 20 nm (*p*)nc-Si:H layers with distinct (*n*)nc-Si:H layers. 93
5.28 J-V Parameters of Single-side-textured SHJ solar cells fabricated by 60 nm (*n*)nc-Si:H layers with distinct (*p*)nc-Si:H layers.). 94
5.29 EQE curves of Single-side-textured SHJ solar cells fabricated by 10 nm (*p*)nc-Si:H layers with distinct (*n*)nc-Si:H layers. 95
5.30 EQE curves of Single-side-textured SHJ solar cells fabricated by 20 nm (*p*)nc-Si:H layers with distinct (*n*)nc-Si:H layers. 96
5.31 EQE curves of Single-side-textured SHJ solar cells fabricated by 60 nm (*n*)nc-Si:H layers with distinct (*p*)nc-Si:H layers. 96
5.32 Contour plot of optically simulated Single-side-textured 2T tandem device w/ doped Non-odixic layers as RJ (average FF). 97
5.33 Contour plot of optically simulated Single-side-textured 2T tandem device w/ doped Non-odixic layers as RJ : (best FF in optimal thickness range). 97
5.34 J-V Parameters of Single-side-textured SHJ solar cells fabricated by 30/5 nm (*p*)nc-Si:H /(*p*)nc-SiO_x:H layers with distinct (*n*)nc-Si:H layers. 98
5.35 EQE curves of Single-side-textured SHJ solar cells fabricated by 30/5 nm (*p*)nc-Si:H /(*p*)nc-SiO_x:H layers with distinct (*n*)nc-Si:H layers. 99
5.36 Contour plot of optically simulated Single-side-textured 2T tandem device w/ doped Oxidic/Non-oxidic layers as RJ : (best FF in optimal thickness range). 100
5.37 Contour plot of optically simulated Single-side-textured 2T tandem device w/ doped Oxidic/Non-oxidic layers as RJ : (average FF in optimal thickness range). 100
5.38 Sample M16993's cross-section as shown in with a closer view of a finger (a), while (b) shows an enlarged picture of Ag, (c) and (d) show the (*i*)a-Si:H (5 + 5 nm)/(*n*)nc-SiO_x:H (60 nm)/*(p)*nc-SiO_x:H (60 nm) layers stacks. 101
5.39 Sample M17956's cross-section as shown in with a closer view of a finger (a), while (b) shows an enlarged picture of Ag, (c) and (d) show the *(*i)a-Si:H (5 + 5 nm)/*(*n)nc-Si:H (40 nm)/*(p)*nc-Si:H (30 nm) layers stacks. 102

1

Introduction

'All energy is ultimately derived from the sun and harvesting it directly through solar power seems to be the best way to transition to renewable energy.'

-Peter Rive

1.1. Solar Energy: Bearer of Clean Energy

Transitioning from mainstream energy sources to renewable alternatives has been a tough challenge in the 21st century, and in which global leaders have promised several long-term goals to reduce carbon emissions but tremendous effort is still required to achieve these targets [1]. Tackling global warming and the energy crisis needs a more substantial contribution from renewable energy sources. For instance, for global electricity generation, only 26% comes from renewable sources with slim 10% from nuclear power in the year 2019 [2].

Globally, more than 260 GW of new renewable energy capacity was built in 2020, shattering the previous record by more than 50%. Even while hydropower generation has declined by 27.2% since 2011 (from 68.4% to 41.2%), wind and solar electricity generation have increased by 25% and 25.3%, showing increases of 16.6% and 5.4% over the past few years respectively. Global solar PV installations hit 117 GW in 2021, a spike of 10% over 2020 [3]. Figure 1.1 depicts the production of renewable net capacity from 2000 to 2020 [3].

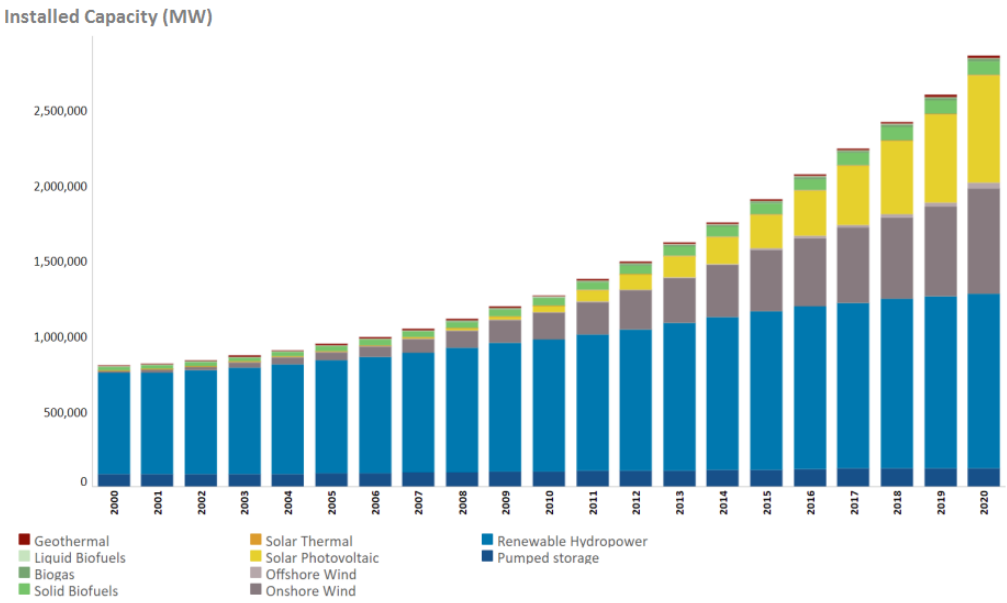

Figure 1.1: Globally installed renewable energy capacity bar chart (2000-2020). Adapted from [2].

According to the International Renewable Energy Agency (IRENA), renewable energy sources have surpassed conventional energy sources in terms of adding electricity to the grid over the past several years [3]. In 2022, 26.74% of generating capacity came from renewable energy sources in the US [2]. China had a 25% jump from the year 2021 to 2022 for renewable energy generation with a plan to attain 156 gigawatts of wind turbines and solar panels by the end of 2022 [4]. European Union plans to extend capacity to 320 gigawatts of solar power by 2025 to reduce dependency on external energy supplies. And definitely, solar power contributes a major portion of this renewable energy spectrum with nearly 60% [4].
The corporate sector, as shown in figure 1.2, continues to expand by adding 12 million new employees in the renewable energy sectors, with 3.98 million of those positions going to PV technology [5]. This clearly demonstrates the importance to invest in solar energy research to tackle the current energy crisis.

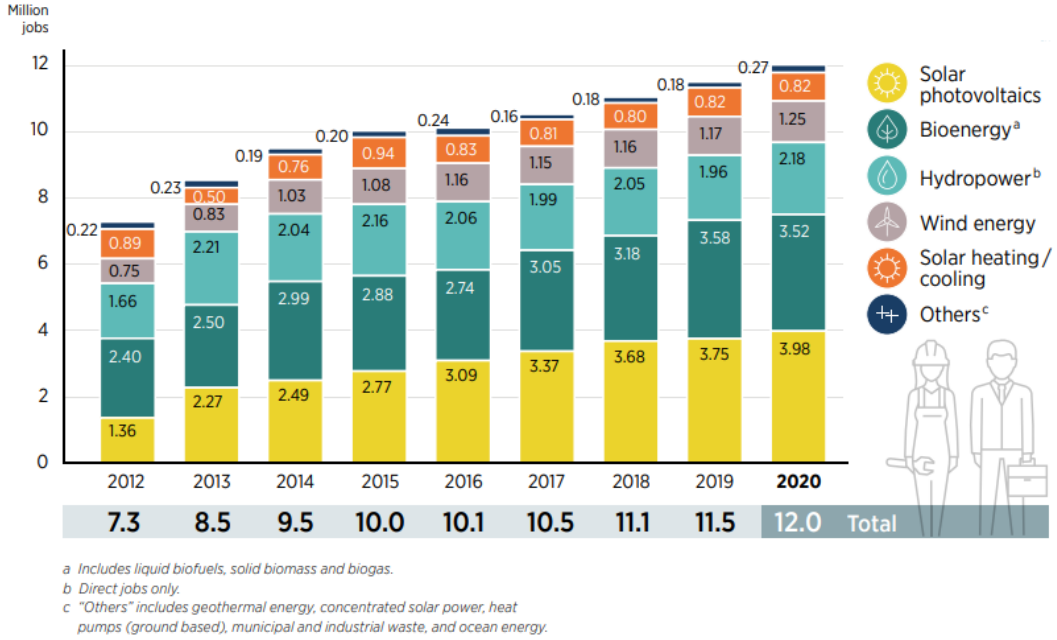

Figure 1.2: Worldwide employment in renewable energy technology sectors (2012-20). Adapted from [2].

1.2. Fundamentals of Solar Cells

1.2.1. Semiconductor Materials:

Sufficient photon energy (E_{ph}) is necessary to generate an electron-hole pair. Photons have relatively little momentum, with $p = E_{ph}/c$ (light speed, $c = 3 \times 10^8$ m/s) [6]. In a direct band gap semiconductor (GaAs, CdS, ZnS, CdSe etc), E_{ph}) must be at least equal to the band gap energy (E_G) in order to produce an electron-hole pair. It is not necessary to impart much momentum to the electron. In an indirect band gap semiconductor (Si, Ge, AlAs, GaP etc), an electron experiences a large shift in momentum for a E_{ph} to generate an electron-hole pair. This is due to the fact that in an indirect band gap semiconductor, the maximum energy of the valence band (VB) occurs at a different value of momentum from the minimum in the conduction band (CB). A lattice vibration also referred to as a ”phonon,” (energy in the form of heat) is used as a mediator to let an electron interact with a photon in order to gain energy. It’s a drawn-out and sluggish process since it needs the intersection of three different things: an electron, a photon, and a ”phonon”. In contrast to a direct band gap semiconductor, the maximum of VB and the minimum of CB occur at the same value of momentum. The recombination of electrons and holes follows the same reasoning. A direct band gap semiconductor has a substantially higher radiative recombination rate than an indirect band gap semiconductor [7, 8, 9].

1.2.2. Generation:

In solid-state physics, the generation process is the mechanism through which two electrons are generated. Gaining energy electrons transit from the VB to the CB and leave a hole behind. The flow of charge carriers in VB and CB determines the conductivity of the material as they are closest to the Fermi level (highest energy level of an electron at absolute zero temperature).
Figure 1.3 (a) illustrates, the band gap, the distance an electron must traverse to conduct from the VB to the CB in an atomic structure. CB is made up of electrons in the innermost shell, whereas VB is made up of valence electrons in the outermost shell. VB and CB overlap in conductors. As a result of this overlap, valence electrons are essentially allowed to move into the CB to participate part in conduction. Poor conduction is seen in insulators since the electrons of VB are isolated from CB by a wide band gap, or "forbidden" gap (E_G or $\Delta E > 3.2$ eV). This "forbidden" gap (E_G or $\Delta E \leq 3.2$ eV) in semiconductors is sufficiently tiny to be crossed by any sort of excitation. The energy needed to travel from VB to CB can be obtained through thermal energy, such as the photon from direct sunlight in the case of photovoltaic cells. Above zero degrees Kealvin, the energy required for silicon and germanium are 1.1 eV and 0.7 eV, respectively. This difference of energy under light from electrons and holes gives an estimation of the implied open circuit voltage. The creation of electron-hole pairs during illumination when light energy is greater than the bandgap is shown in the schematic 1.3 where (a) shows different types of materials, (b) generation, and (c) fermi level positions of different semiconductors [7, 10].

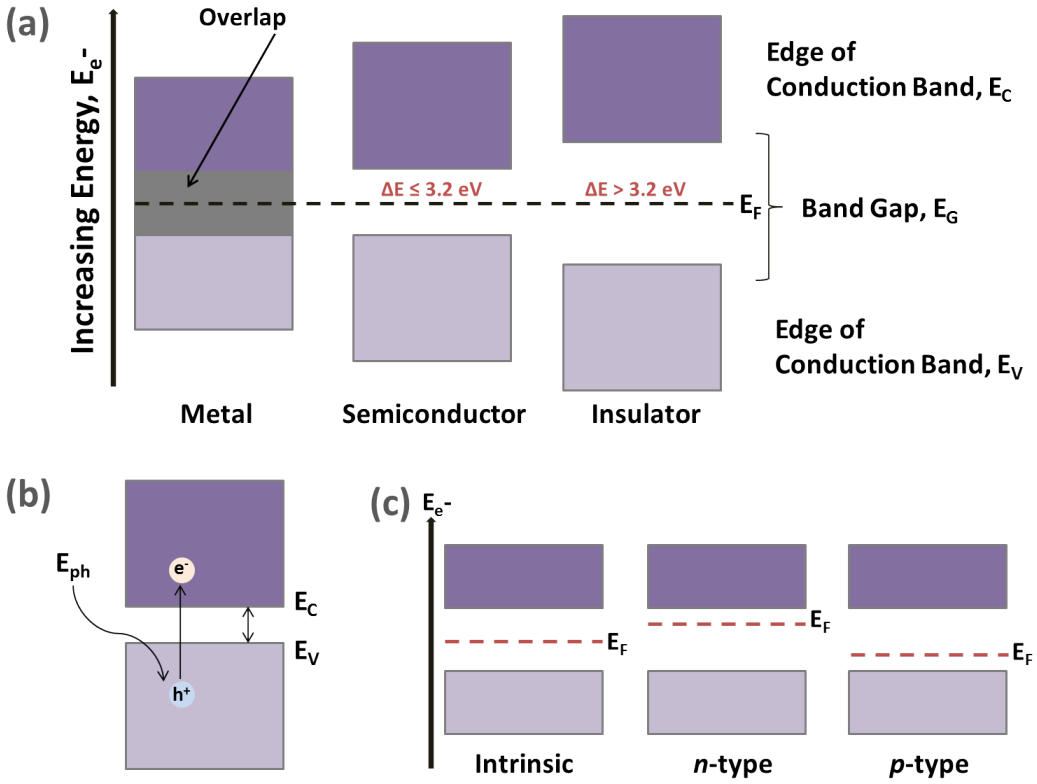

Figure 1.3: Schemetic describes (a) different types of materials, (b) generation and (c) fermi level positions.

.

1.2.3. Recombination:

The shift from non-equilibrium to thermal equilibrium is called recombination where an electron transit from the conduction to the valence band and releases the photon energy. Effective carrier lifetime, open circuit voltage, solar cell efficiency, etc. can be affected by the recombination mechanism.

Recombination can occur in three different ways: (i) Radiative (band to band), (ii) Auger, and (iii) Trap Assisted (SRH) [11, 10].

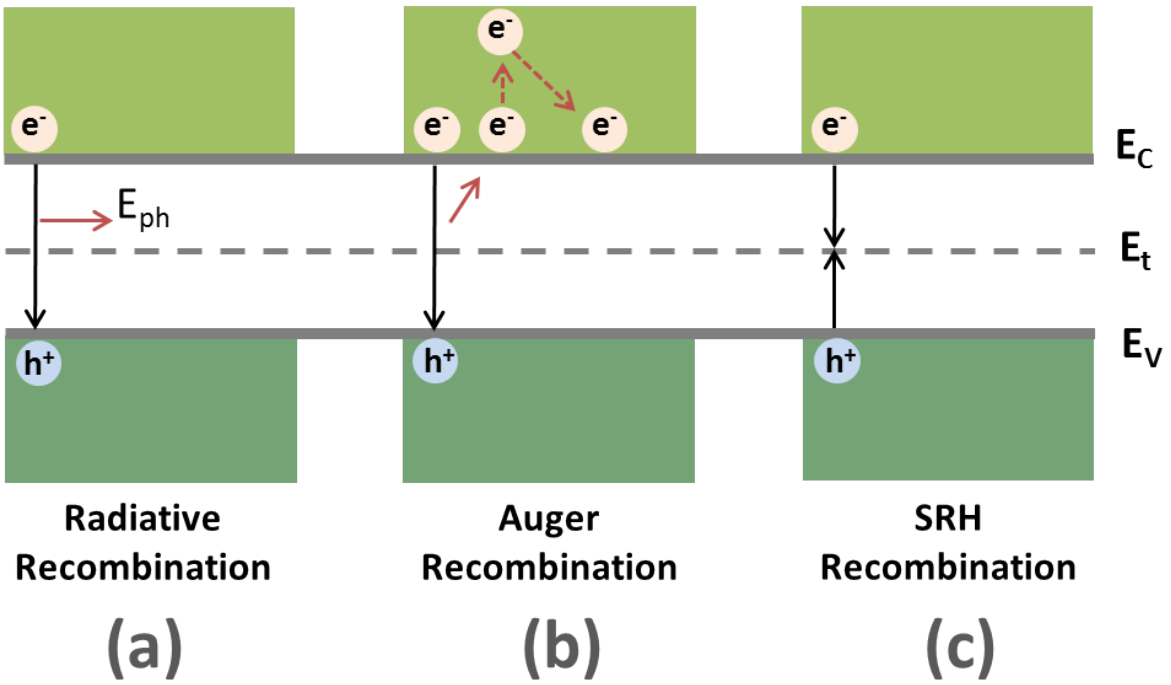

Figure 1.4: The schematics (a),(b), and (c) demonstrate the types of recombination.

.

(i). Radiative (band to band) Recombination :

The Radiative (band to band) recombination mechanism, as in 1.4 (a), is basically happening in direct bandgap semiconductors where an electron move from CB to VB to recombine with a hole and releases a photon inside the material where $E_{ph} = E_G$.

(ii). Auger Recombination :

Auger recombination is non-radiative recombination, shown in 1.4 (b). During electron-hole recombination, the thermal energy from the emitted photons is transferred to another charge carrier. It causes either a hole to move to the lower VB or an electron to move to the higher CB shell.

(iii). Shockley-Read-Hall (SRH) :

A two-step transition of an electron from the conduction band to the valence band is known as trap-assisted or Shockley-Read-Hall (SRH) recombination, and it occurs when an electron and a hole interact in a trap. It's crucial to know that a "trap" is a constraint on the mobility of electrons and holes. Due to the absence of an electron in the defect state, positive electrical charges form, which draw the electron. An electron is trapped in the first step. This trapped electron enters VB in the subsequent step and recombines with a hole. 1.4 (c) shows the schematic. The prominent recombination centers are the areas that lie between CB and VB.

1.3. Solar Cell's Working Principle :

In order to alter the electrical properties of intrinsic Si wafers, impurity atoms are added. Three electrons are available on Boron (5)'s bonding shell, allowing it to create three covalent bonds with Si (14) atoms in a crystal. While the dopant (Boron) atom is stable at absolute zero with its missing bond, normal temperature provides enough thermal energy to force an electron into this gap. When this occurs, the atom that donates the electron now has a hole in the crystal that can be filled by another atom. p-type Si is produced when movable holes with a positive electric charge are present.
Some Si (14) atoms in the crystal can be replaced by phosphorous (15), which then acts as a dopant atom. Each dopant atom has the potential for four covalent connections. The fifth electron, which is not

used in covalent bonding, is very closely bound to the dopant atom and is made free to move within the crystal by the thermal energy present at ambient temperature. Because the dopant atoms' individual negative electric charges make one electron available, the resulting crystal material is n-type silicon.

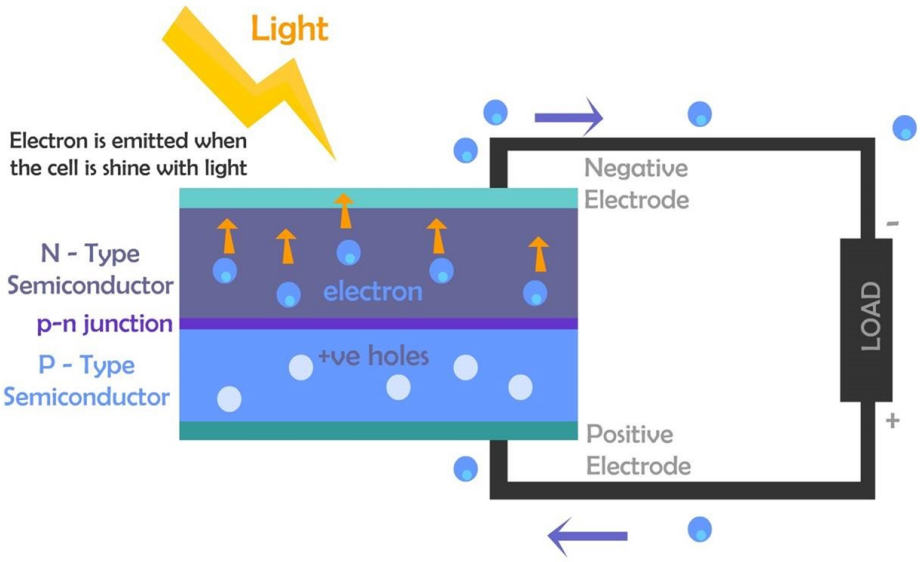

Figure 1.5: Solar cell basic working principle. Adapted from [12].

Doping creates a significant amount of free mobile electrons on the n-type side with a fewer electrons on the p-type side. In a similar fashion, doping produces a significant number of free mobile holes on the p-type side. Free electrons and holes are influenced by this built-in electric field with the electrons being attracted towards the positively charged phosphorous ions in the *n*-layer and negatively charged boron ions in the *p*-layer. In this manner, a P-N junction or depletion region is produced. They successfully combine to create a barrier. This barrier prevents electrons from moving from the *n*-layer to the *p*-layer. When a process reaches equilibrium, a junction point with a divided electric field on both sides is generated. By acting as a diode, this electric field forces electrons to drift from the *p*-layer to the *n*-layer. These electrons and holes are spread evenly throughout the volume in the absence of electric charge. Free electrons diffuse into the *p*-layer due to random thermal motion and leave a hole close to the n-to-p contact.

Figure 1.5 illustrates, how an electron can be energized by a photon breaking its covalent bond, and move to the *n*-layer, when light shines on a P-N junction solar cell [46]. Electrons are drawn to n-type materials by the electric field, whereas holes are drawn to p-type materials. Current passes through the junction as a result of this charge separation. .Electrons move from the *n*-layer to the *p*-layer and produce current when connected to an electric wire.
In a nutshell, the illumination of light causes the electron-hole pair to transition from the excitons to the plasmons state (bound to unbound state). The separation of the charge carriers occurs afterward, and the charge carriers are ultimately collected via an external circuit [13, 14, 15].

1.3.1. Perovskite Solar Cells:

Materials having a hybrid organic-inorganic structure or Perovskites (PVK) that share the mineral calcium titanium oxide's ($CaTiO_3$) crystal structure. The standard chemical formula for this crystal structure is ABX_3, which can be seen in figure 1.6, where **A** and **B** are cations and **X** is an anion. Here,

- **A** represents organic cations : Methylammonium ($CH_3NH_3^+MA^+$) or Formamidinium ($CH(NH_2)_2^+$)).
- **B** represents metal cations: ((Pb_2^+ or Sn_2^+), and
- **X** represents halide (Cl^-, Br^-, or I^-) [16].

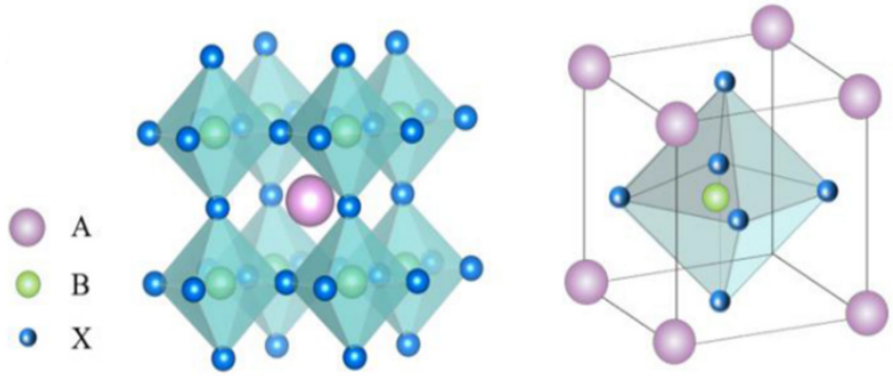

Figure 1.6: Crystal structure of a 3D Perovskite. Adapted from [16].

Due to its semi-transparency and high optical absorption coefficients, it has drawn a lot of interest. Additionally, having substantial charge-carrier mobilities, improved optical properties, binding energy, better dielectric constant, as well as frequent collection and transport of charge carriers, results in high V_{oc} and J_{sc}, which eventually leads towards higher efficiency [17]. Despite these significant benefits, this technology shows minimal compatibility with the environment and needs more research before it can be commercialized [17].

1.3.2. Silicon Heterojunction Solar Cells:

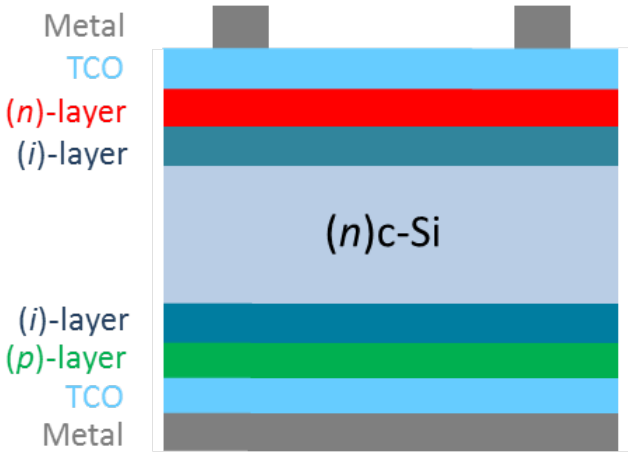

Figure 1.7: Device architecture of single-junction (rear-junction) SHJ solar cell.

Contrary to homojunction structures with equal bandgap semiconductor materials, SHJ solar cells use various bandgap materials. (*i*)a-Si:H/c-Si or heterojunction interface can significantly impact the overall efficiency of the solar cell. It is because depositing two semiconductors with different bandgap (c-Si 1.1 eV and (*i*)a-Si:H 1.5–2.0 eV) (*i*)a-Si:H layers significantly passivate the surface dangling bonds. When compared to the theoretical efficiency limit of 29.43% [18] of crystalline silicon (c-Si) solar cells, the recent efficiency record of 26.81% by Hao Lin et al.([19]) indicates considerable improvement. Researchers demonstrated that it is possible to go above SHJ's typical V_{oc} (750 mV) [19, 20]. The highest V_{oc} for homojunction solar cells is recorder 700 mV [21]. The choice of SHJ solar cells as the bottom cell for the multijunction tandem application was influenced by effective passivating contacts, improved optoelectronic properties of nanocrystalline window layers to reduce reflection loss at the interfaces of TCO/doped layers [22, 23], and low-temperature coefficients or the ability to perform better at higher temperatures which offer the solar cells' overall efficiency [24].

1.3.3. PVK/c-Si Tandem Solar Cells: Paving the Way of High Efficiency

Sunlight is composed of a lot of photons containing certain energy, E_{ph}= hv = hc/λ (h is the plank constant,v is the frequency of the electromagnetic radiation, c is the velocity of light and λ is the wavelength of incident light). Wavelength is inversely proportional to the frequency, (λ = c/f). The short wavelength of a photon (in Gamma-ray for example), has larger momentum and high frequency. In space, the solar spectrum is more like the radiation of a black body and covers different wavelengths. The Earth's surface can absorb selected sunlight, regulated by the atmosphere at a certain wavelength (290 nm – 3000 nm) including the wavelength range of visible light (380 nm – 750 nm) and the Infrared range starts from (780 nm - 1 mm).

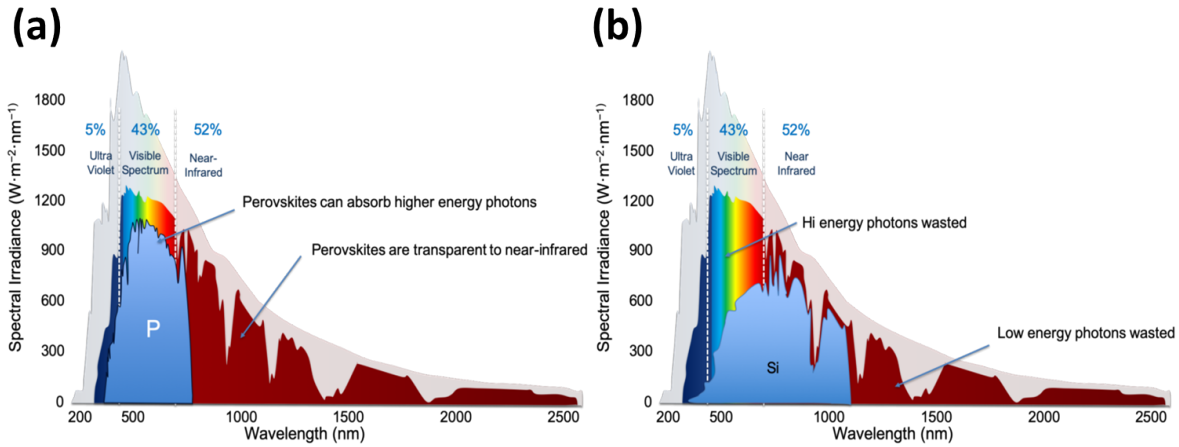

Figure 1.8: Spectral irradiance absorbance of Perovskite (P) and Silicon (Si) are shown in (a) and (b) respectively. Adapted from [25].

Considering all of the logic and physics behind it, scientists and researchers proved that, solar cells made with materials like Perovskite with wide bandgap (1.2-2.3 eV), short wavelength range (300-850 nm, Fig. 1.8 a) can absorb photons with high frequency and high energy can be used as a top cell. While harvesting energy in the long wavelength range (400-1100 nm, Fig. 1.8 b). solar cells made by narrow bandgap materials (0.6-1.5 eV) like Si can absorb photons with low frequency and less energy is an ideal choice for a bottom cell. Each cell responds to a different wavelength range of the solar spectrum, as shown in Fig. 1.8 [26]. Stacking them together increases the possibility to yield higher overall power conversion efficiency (PCE).

By stacking one on top of the other one of two absorbers, multijunction or tandem solar cells (TSCs) are fabricated. The goal is to combine wide and narrow bandgap subcells such that when illuminated light hits the top cell's (wide bandgap, transparent, SQ limit 33%) absorber with high energy photons [27] and the bottom cell's (narrow bandgap, opaque, SQ limit 29.4%) absorber [28] with low energy photons, a high output direct current can potentially be produced. Tandem device topologies with four and two terminals, respectively, are shown in Fig. 1.9 [29].

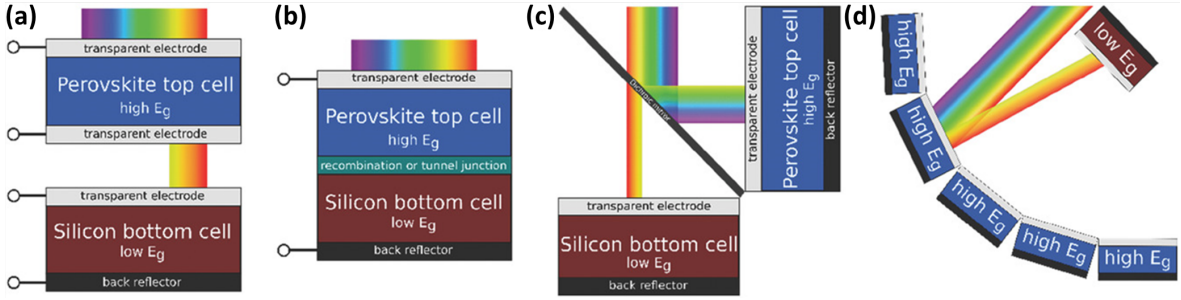

Figure 1.9: Perovskite/Silicon tandem architectures : (a). Four-terminal (4T), (b). Two-terminal (2T); (c). Four-terminal optical spectral splitting; and (d). Four-terminal reflective tandem device . Adapted from [30].

(i). Two-terminal Tandem Cells (2T):

Monolithic 2T tandem devices that are electrically and optically coupled, connected by tunnel junctions, and fabricated on top of one another, as shown in [Fig. 1.9(b)]. When a gadget is referred to as ”monolithic,” it signifies that all of its components are combined to create a single chip that can convert a bigger portion of solar irradiance into electricity. Direct fabrication reduces the number of processing steps as well as contact layer requirements. Less contact or window layers can enhance the current generation and reduce parasitic absorption. The maximum current that can be produced by any of these sub-cells Some disadvantages include the requirement for current matching between two sub-cells, and lower device lifetime due to perovskite top cells' lower stability when compared to c-Si bottom cells [29, 31, 32].

(ii) Four-terminal Tandem Cells (4T):

The two sub-cells were individually fabricated to form a 4T solar cell, where they are optically connected. It offers a number of device structures, including mechanically stacked (Fig. 1.9(a)], spectral splitting (Fig. 1.9(c)) and reflective tandems (Fig. 1.9(d)). Current matching is not required, maintenance is simple, and a longer device lifetime by replacing defective cells, are the key benefits of these devices. There are some downsides, including they do consume more electrode materials and exterior electronics for interconnecting, fabrication processes for fabricating two unique cells individually, and higher parasitic absorption by the conductive glass substrate of perovskite top cells [33, 34, 31, 32].

Potential tandem combinations are PVK (1.7 eV)/c-Si (1.2 eV), PVK (1.7 eV)/CIGS (1.1 eV), and PVK (1.8 eV)/PVK (1.25 eV) with comparatively low PCE (device of 1 cm^2 active area),is the main reason to choose PVK/c-Si combination [35]. Over the last few years most of the perovskite/c-Si tandem devices, that show efficiency records, have either silicon heterojunction (SHJ) or silicon homojunction solar cells as a bottom device. Table 1.1 represents an overview of two terminal perovskite/c-Si tandem devices which have been investigated in the past few years (till 2022). The term 'HIT' refers to the heterojunction configuration with thin intrinsic buffer layers. the thin film layers are deposited on the c-Si absorber with low-temperature RF-PECVD deposition.

However, S. Mariotti, et al. and E. Aydin, et al. (2023) announced a new efficiency record of 32.50% and 33.70% efficiency with single-side-textured and double-side-textured 2T PVK/c-Si, where SHJ was the bottom cell, further details are not given [36, 37]. This is the obvious argument for selecting the SHJ solar cell to be optimized as a bottom device.

Table 1.1: List of recent studies of silicon solar cells with tandem current, open circuit voltage, fill factor, power conversion efficiency order by publication date

Author	Publication Date	Bottom Cell	TRJ	Area [cm^2]	J_{sc} [mA/cm^2]	V_{oc} [V]	FF [%]	PCE [%]	Ref.
Bacha et al.	2022, Jun	HIT	ITO	-	15.38	1.98	88.60	27.00	[38]
Tockhorn et al.	2022, Mar	HIT	ITO	1	19.56	1.92	79.40	29.80	[39]
Kohnen et al.	2021, May	HIT	ITO	1	17.81	1.94	80.89	27.90	[40]
Al-Ashouri et al.	2020, Dec	HIT	ITO	1.064	19.26	1.90	79.52	29.10	[41]
Schulze et al.	2020, May	HIT	ITO	0.25	17.70	1.77	80.30	25.10	[42]
Chen et al.	2020, Apr	HIT	ITO	0.42	19.20	1.82	75.30	26.10	[43]
Bett et al.	2019, Sep	HIT	ITO	0.25	14.60	1.83	74.30	19.90	[44]
Kohnen et al.	2019, May	HIT	ITO	1	17.81	1.78	78.64	25.00	[45]
Mazzarella et al.	2019, Feb	HIT	ITO	1.10	19.00	1.79	74.60	25.20	[46]
Hou et al.	2019, Jan	HIT	ITO	0.13	15.95	1.83	70.00	20.40	[47]
Chen et al.	2018, Oct	HIT	ITO	0.42	17.80	1.80	79.40	25.40	[48]
Jost et al.	2018, Oct	HIT	ITO	0.81	18.50	1.76	78.50	25.50	[49]
Bush et al.	2018, Aug	HIT	ITO	1	18.40	1.77	77.00	25.00	[50]
Sahil et al.	2018, Jun	HIT	nc-Si	1	19.50	1.79	73.10	25.20	[51]
Zheng et al.	2018, Jun	Homo	none	4	16.10	1.68	78.00	20.50	[52]
Sahil et al.	2018, Feb	HIT	nc-Si	0.25	16.80	1.75	77.50	22.00	[53]
Wu et al.	2017, Oct	Homo	ITO	1	17.60	1.75	73.80	22.50	[54]
Bush et al.	2017, Feb	HIT	ITO	1	18.10	1.65	79.00	23.60	[55]
Werner et al.	2016, Sep	Homo	ZTO	1.43	15.30	1.64	64.80	16.00	[56]
Werner et al.	2016, Jul	HIT	IZO	1.43	16.40	1.72	73.10	20.50	[57]
Werner et al.	2015, Dec	HIT	IZO	0.17	15.80	1.69	79.90	21.20	[58]
Werner et al.	2015, Dec	HIT	IZO	1.22	16.10	1.70	76.70	19.20	[58]
Albrecht et al.	2015, Oct	HIT	ITO	0.16	14.00	1.76	77.30	18.10	[59]

1.3.4. Challenges With single-side-textured SHJ Bottom Cells

Since high-quality PVKs are often fabricated by spin-coating or spraying onto the substrate, flat-front SHJ bottom cells are the best option for 2T tandem applications. Based on the locations of the electron transport layer (ETL) and hole transport layer (HTL), PVKs can be divided into two architectures:

- **(i):** As illustrated in Fig. 1.10 (a), the layers of the "Inverted" (p-i-n) structure are stacked as "ETL (doped *n*-layer)-intrinsic-HTL(doped *p*-layer)".
- **(ii):** While in the "Conventional" (n-i-p) structure, layers are stacked as "HTL(doped *p*-layer)-intrinsic-ETL(doped *n*-layer)," shown in Fig. 1.10 (b).

On the other hand, SHJ solar cells also have two types of structures:

- **(i):** Rear junction SHJ solar cell's *n*-layer (surface field layer) is deposited on the front and *p*-layer (emitter layer) is deposited on the rear side of the wafer as '*n*-layer-intrinsic-*p*-layer'
- **(ii):** In contrast, front Junction (FJ) SHJ solar cell's *p*-layer (emitter layer) is deposited on the front and *n*-layer (surface field layer) is deposited on the rear side of (100) c-Si as '*p*-layer-intrinsic-*p*-layer'.

For 2T tandem, 'p-i-n' PVKs need to be deposited on a rear junction SHJ bottom cell, as fig. 1.10 1.10 (a), and n-i-p' PVKs need to be deposited on a FJ SHJ bottom cell, fig. 1.10(b). Recent studies have shown that "p-i-n" architecture has superior PCEs of PVKs when paired with a single-side textured RJ SHJ bottom cell[60, 46]. While the 'n-i-p' arrangement demonstrates high J_{sc} and efficiency for low bandgap single-junction PVK, the 'p-i-n' configuration is preferable for the fabrication of tandem devices with both flat and textured c-Si bottom cells [35, 61]. Owing to the thin front *n*-layer, parasitic absorption can be significantly dropped [35]. This led to the decision in this thesis to first optically optimize the 2T tandem device using 'p-i-n' PVK/RE SHJ tandems. Following that, Single-side textured single junction RE SHJ was electrically investigated for further tandem application.

A 2T 'p-i-n' perovskite/RJ SHJ device is made by depositing the rear-HTL (p-type) layer of the top cell over the front-TCO layer of the bottom cell. In a two-step recombination mechanism, top-rear- HTL and bottom-front-TCO layers will form the recombination junction and the majority of charge carriers will recombine in this junction (holes from the top-rear-HTL with electrons from the bottom-front-TCO layer or vice versa. By means of a transparent tunnel connection, a combination of low reflectivity, low lateral conductivity, and high vertical conductivity drives electron movement past the barrier. This might increase light absorption in the bottom cell while lowering parasite uptake [62, 63]. Without recombination, top- rear-HTL would form a reverse p-n junction with the front *n*-layer of the bottom cell, reducing the built-in voltage (V_B) or photovoltage. ITO is often used as the recombination layer. Although it can increase parasitic absorption and poor refractive index matching with PVK/c-Si cell result in high reflectance at the interface[64].

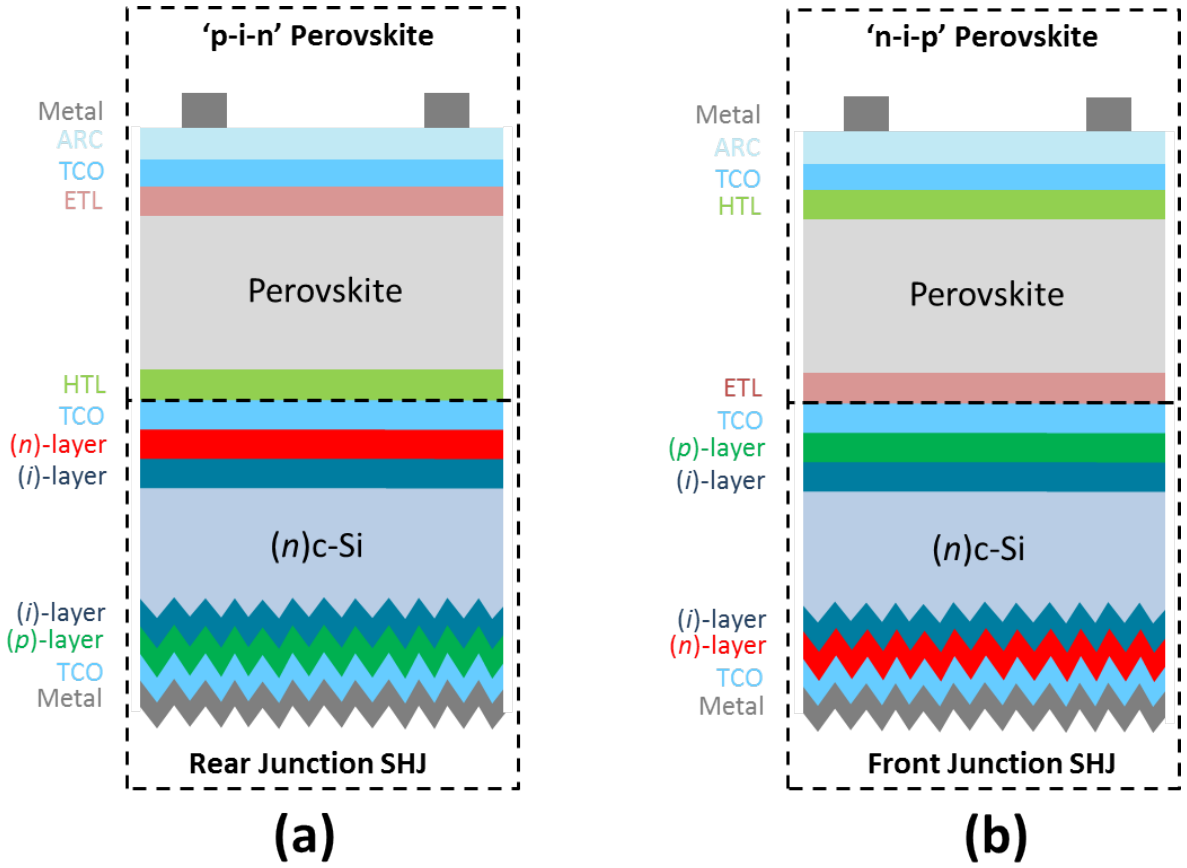

Figure 1.10: Device architecture of 2T Perovskite/c-Si Tandem solar cells: (a) 'p-i-n' Perovskite/Rear junction SHJ and (b) 'n-i-p' Perovskite/Front emitter SHJ configurations.

In comparison to c-Si, some doped materials for instance, (*p/n*)nc-Si:H or (*p/n*)nc-SiO_x:H, have similar refractive indexes. In order to establish a monolithic 2T PVK/c-Si that is devoid of TCO, combining with the top-cell's HTL it can form a p-n junction with the bottom-cell's *n*-layer. Despite possibly having higher absorption than ITO, (*p*)nc-Si:H or (*p*)nc-SiO_x:H layers may mitigate reflection loss in the relevant NIR spectrum [53, 65]. Once materials with matching refractive indices have been chosen to create a device, the thickness must be tuned to minimize interference loss in this interfacial. However, the proposed *p*-layer exhibits high vertical but low lateral charge carrier transport across the recombination junction and may increase recombination rate [53, 65]. Whether the top cell's HTL deposited on an n-type ITO or p-type underlayer from the bottom cell, can be compatible with various device architectures.

Reflection loss may rise depending on the layer stack selection of the top cell, making the bottom cell the current limiter. Before fabricating optically optimized SHJ bottom cells, it was crucial to inves-

tigate different *i*-layers for better passivation which leads to better cell performance. In particular, it is critical to optimize the doped contact stacks to provide better band bending between c-Si/(*i*)a-Si:H, minimized current losses, and decreased contact resistivity at the TCO/doped layers interface. While comparing with (111)c-Si surface, (100)c-Sic-Si surface is more susceptible to epitaxial growth [66]. Crystallographic orientations reveal (111)c-Si has one dangling bond per atom and Si-atom needs to create one bond in the developing plane. while (100)c-Sic-Si has two broken dangling bonds & silicon atom needs to form two bonds with a certain angle[67]. Frequent transformation of(100)c-Si to c-Si(100-(2x1) dimers configuration also can encourage further epitaxial growth [67]. Diffusion length of adatoms (atom lies on the surface of c-Si) can encourage higher epitaxial growth [66].

Moreover high bulk series resistance R_B, ($R_B = \Delta V_F/\Delta I_F$, where V_F refers to forward voltage dropped across the diode and I_F is the forward current flowing through the diode) might be detrimental towards high effective carrier lifetime of an *i*-layer. The series resistance is related to the defect inside the *i*-layer and can reduce short-circuit current as well as fill factor. Growing a highly H-diluted layer directly on (100) surface will lead to detrimental epitaxial growth, this is the reason why we have an *i*-1 layer with pure SiH_4, the H-diluted *i*-2 layer afterward.

1.4. Research Outline

In this study, optical modeling of monolithic 2T tandem devices with TCO-free recombination junctions and a partial 'proof of concept' are combined. With an overview of the conceptual foundations of solar energy and outlining any challenges (section 1.3.4) to be overcome for this master thesis, a research proposal wraps up **chapter 1**. The underlying knowledge of atomic growth and passivation mechanisms of passivating layers, characteristics of doped layers, and a conceptual understanding of recombination junctions are the main topics of **chapter 2**. The prerequisite tools and characterization methods for monolithic 2T tandem (optical) and RE SHJ solar cells (optoelectrical) are introduced in **chapter 3**. In the following two chapters, the research's key findings are discussed as :

- **Chapter 4**: Optical simulations of single-junction and monolithic 2T Perovskite/c-Si tandem served as the foundation for this research. Starting with an optical simulation of a two-terminal tandem device, the goal was to allow more light to be transmitted to the bottom cell by using different TCOs and replace this TCO with doped nc-Si:H/nc-

1.5. Research Proposal

To optimize single-side-textured RE SHJ for PVK/c-Si monolithic 2T tandem devices, while considering main challenges and areas of concern (section 1.4) the research objective and research questions are also defined. A detailed workflow is included in the Appendix.

The objective of this research can be described as:
Optimizing SHJ bottom cells for monolithic 2T Perovskite/c-Si tandem applications with TCO-free recombination junctions.

Based on the identified main challenges towards fabricating PVKs/c-Si tandem solar cells, two main research questions of this research are defined below as the most relevant for contributing in providing scientific value in this field. In order to support answering the research questions in a detailed manner, sub-questions (SQ) are also defined.

1. Optical properties of monolithic 2T PVKs/c-Si solar cells with TCO-free recombination junctions.

   - **SQ-1A:** How do the monolithic 2T devices perform with TCO-free recombination junction in the comparison of various traditional TCO layers with single-side-textured SHJ bottom cells?
   - **SQ-1B:** How do devices perform with double side textured top and bottom devices? What are the performance differences between the single-side-textured and double-side-textured monolithic 2T tandem devices?

2. Can the proposed TCO-free recombination junction transport charge carriers efficiently?

   - **SQ-2A:** How does the thickness of a doped can affect the electrical properties of doped layers? How do these doped layers perform under temperature-dependent dark IV measurement
   - **SQ-2B:** How to efficiently passivate the flat (100) c-Si surface?
   - **SQ-2C:** How do the SJ cells perform electrically with the optimized optical parameters for the 2T tandem application?

Collaboration between the partner universities (TU Delft and TU Eindhoven) is necessary to utilize optically adjusted data for PVKs and manufacture a monolithic 2T PVK/c-Si solar cell in order to achieve these research goals. The research questions are carefully evaluated and prioritized, for instance, research question 1 has been chosen as the initial significant question to be addressed since the monolithic 2T devices had been initially optically optimized as with TCO and TCO-free recombination junction layers. Following those optimized data, the experimental part was carried out. Although some more intriguing investigations, for instance optically optimized single and double-side-textured 4T tandem devices, are not included in this study, due to time limits and resource constraints in the lab. Nevertheless, these parts are briefly mentioned in the appendix.

2

Fundamentals

This chapter covers literature reviews on different material characteristics of SHJ solar cells. Particularly, hydrogenated intrinsic amorphous silicon layers (a-Si:H) for better chemical passivation and doped layers (nc-SiO_x:H and nc-Si:H) that could be used as recombination junctions (RJs) are covered.

2.1. SHJ solar cells: Traditional and Proposed Architecture

Due to the low fabrication temperatures (160-200 °C) [68], few process steps, possible higher open circuit voltage of 750 mV [69, 20], good infrared response [70], SHJ solar cells have been gaining attention due to it's potential for achieving high power conversion efficiencies of single-junction and tandem solar cells during the past several years.

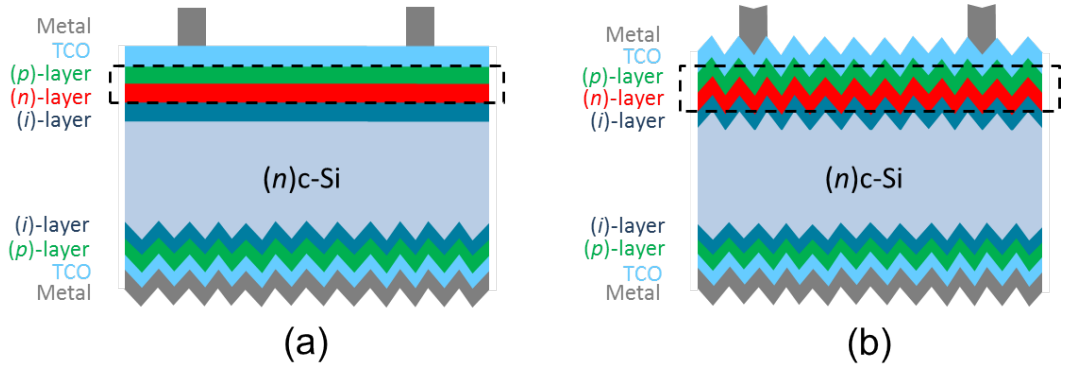

Figure 2.1: Device architecture of (a) front-side-flat and (b) double-side-textured single-junction SHJ solar cell with proposed doped oxidic layers as RJ.

Recent studies demonstrate that employing SHJ as the bottom cell in tandem reached an efficiency of 33.2% from KAUST [71, 38, 37]. Typical SHJ solar cells are created by stacking various layers in a specified order. Thanks to the effective passivating contact structures of (*i*)a-Si:H layers on the main absorber ensure the improvements of optoelectrical properties of the SHJ solar cells [72]. Previously optimized hole-selective back-contacts confirm the rear-junction of SHJ solar cells with better electrical characteristics and increased charge carrier transmission [15, 73]. One of the primary objectives of this study is to enhance the optical properties of tandem solar cells by using TCO-free recombination junctions (RJs). Due to this, doped nc-Si:H layers are deposited rather than doped a-Si:H layers, because doped nc-Si:H layers can be highly doped to facilitate efficient collection of charge carriers [15]. Figure 2.1 (a) depicts a front-side-flat and 2.1 (b) depicts a double-side-textured single-junction SHJ solar cell with proposed RJ. The reason

for choosing to develop front-side-flat SHJ solar cells is that the SHJ cells serve as substrates for solution-processed perovskite top cells. A flat surface can ensure a conformal coverage of the perovskite absorber [55, 41, 46].

In a tandem device, the inter-layers are often constructed of TCO, which often contains indium. Indium needs to be reduced for realizing mass production of SHJ solar cells [74].

2.2. Hydrogenated Amorphous Silicon

Wafer-based Crystalline silicon (c-Si) and Amorphous silicon (a-Si:H) thin film solar cells (typical substrates include glass, metal, etc.) are the two primary forms of solar cells. There are two basic variants of c-Si: single or monocrystalline silicon, which is made up of continuous crystals or uniform forms of crystal development, and polycrystalline silicon, which is made up of numerous discrete silicon crystals. Amorphous silicon (a-Si:H), on the other hand, is merely ”non-crystalline” silicon because it lacks a tetrahedral structure in the atoms that create unsatisfied valences or dangling bonds on an immobilized silicon atom. It’s good to note that the minority carrier lifetime in a solar cell could be reduced by dangling bonds, which act as recombination centers. Doped a-Si:H can be formed [75]. In order to create the passivation layer between the doped thin film materials and the active layer for SHJ solar cells, (*i*)a-Si:H passivating layer is a crucial material.

2.2.1. Atomic composition of (*i*)a-Si:H

The two most distinct sorts of materials are those that are crystalline and those that are non-crystalline, or amorphous. In contrast to c-Si, which refers to an even and distinct arrangement of atoms with highly acute melting points [76, 77], a-Si is a non-crystalline form with an absence of a symmetrical atomic pattern that has a melting point throughout a wide temperature range.

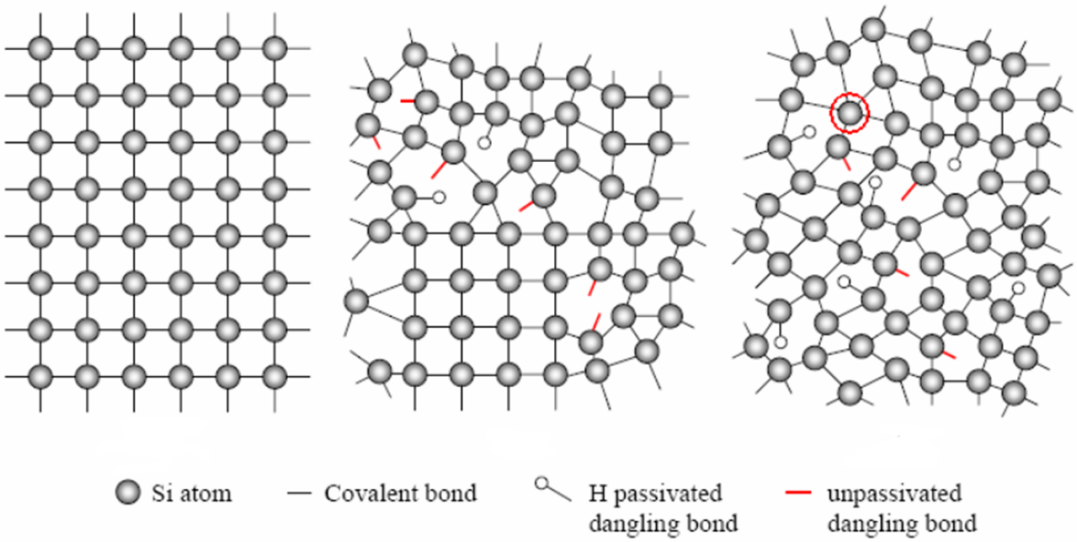

Figure 2.2: A schematic illustrating of the atomic composition (a) crystalline silicon (c-Si), (b) hydrogenated nanocrystalline silicon (µc-Si:H), and (c) hydrogenated amorphous silicon (a-Si:H). Adopted from [78].

Hydrogenated amorphous silicon (a-Si:H) is considered as a standard photovoltaic material used as a passivation layer over the active material. However, this was not always the case. Due to unstable bonding, poor photoconductivity, and challenging doping difficulties, a-Si was suffering. In 1969, scientists Alexander, Sterling, and Chittick produced hydrogenated amorphous silicon

(a-Si:H) by silane gas (SiH_4) precursor [79, 80]. After ten years of study, it was discovered that a-Si:H possesses superior electrical characteristics [81, 82].

The non-identical angles and lengths between the bonds in the random and short-range order of a-Si:H are easily broken at high temperatures. Some Si atoms only have cohesive links with three other Si atoms, leading to defects known as dangling bonds. These dangling bonds are acting as the recombination centers that induces a high charge carrier recombination rate, for instance, Shockley-Read-Hall (SRH) recombination, which happens when atoms have an impurity, in the bulk of a-Si:H or the interface of a-Si:H and the active material. By introducing 5% to 15% of hydrogen content it is possible to passivate these defects in the a-Si by reducing the defect density around from $10^{19} cm^{-3}$ to $10^{16} cm^{-3}$ [83]. The dilution ratio In some cases, they have the tendency to covalent bonds with five other Si atoms, which is referred to as a floating bond. These unsatisfied bonds are passivated or the flaws are reduced using hydrogen atoms [84].

The microstructure of a-Si:H and hydrogen content are all directly impacted by the circumstances of a-Si:H deposition. Fourier Transform Infrared Spectroscopy (FTIR) is the technique used most frequently to determine the Si:H bonding configurations and microstructure of a-Si:H. The preponderance of monohydride molecules (MHs or Si-H: 2000 cm-1 [85]), which corresponded to low stretching mode, can produce a more compact and less defective atomic structure in the amorphous layer, according to studies by Meddeb et al [86, 87]. Section 2.2.2 contains a comprehensive explanation of the effects of the various radicles. Here, the microstructure factor (R*) is used to calculate the proportion of mono or multi-hydrogen hydride that can be present by dividing the FITR intensities at 2090 cm-1 modes by the sum of the intensities at 2000 cm-1 and 2090 cm-1 modes, where better passivation properties and lower R* are associated with a reduced fraction of microvoids [86]. Figures 2.2 (a), (b), and (c) exhibit c-Si with a long-range symmetrical arrangement of tetrahedral structure, nanocrystalline silicon, and a-Si:H.

In summary, to passivate dangling bonds and make amorphous silicon atoms more stable, hydrogen gas must be introduced. Hydrogen gas is the most lightweight and easiest to collide with Si:H radicles, and it may be used to produce hydrogenated amorphous silicon layers on c-Si surface.

2.2.2. Growth mechanism of (*i*)a-Si:H

For a few decades, radio frequency plasma-enhanced chemical vapor deposition (RF-PECVD) has been the most popular and acceptable method for depositing the (*i*)a-Si:H layer on the c-Si from silane (SiH_4) precursor and Hydrogen (H_2) gas [88]. In the EKL cleanroom, the deposition chamber 3 (DPC3) of PECVD (AMIGO) is dedicated for depositing *i*- layer, section 3.4.3 of Chapter 3 provides a detailed explanation of the RF-PECVD procedure. The majority of spontaneous reactions take place in a vacuumed chamber when energetic electrons and molecules of the silane gas clash. Among all other forms of species, SiH_3 is the dominating species when power and pressure are less than 10 W/cm^2 and 10 Pa [88, 89]. Any gas that has a high concentration of molecules or ionized atoms is the fourth state of matter called plasma. Radicals, several unpaired electrons in highly reactive atoms, ions, or molecules, are produced in molten process gases as well as on surfaces exposed to plasma. In their research, Matsuda et al. [90] and Gallagher et al. [91] described the so-called physisorbed condition of SiH_3 and its propensity to adsorb all over the surface that is nearly fully hydrogenated, despite the fact that SiH_3's probability of a surface reaction, β is irrespective of the substrate temperature [90].

The formation of (*i*)a-Si:H from SiH_4 with plasma ignition can be explained in the following manner

- For instance, neutral radicals are produced when plasma electrons collide with SiH_4 molecules (SiH_3, SiH_2, SiH, Si, H).
- Transported and dispersed to the surface of the developing films are produced radicals, mostly SiH_3.
- Physisorption accompanied with abstraction and adhesion of Hydrogen.
- Si-Si bonds and a number of stable silane gas molecules are developed [92].

– Direct abstraction of hydrogen results in the formation of a dangling bond and the molecular SiH_4.
– (*i*)a-Si:H films on the c-Si surface as a result of SiH_3 radicles interacting with the film surface and subsequently adhering to dangling bonds shown in figure 2.3 [92].

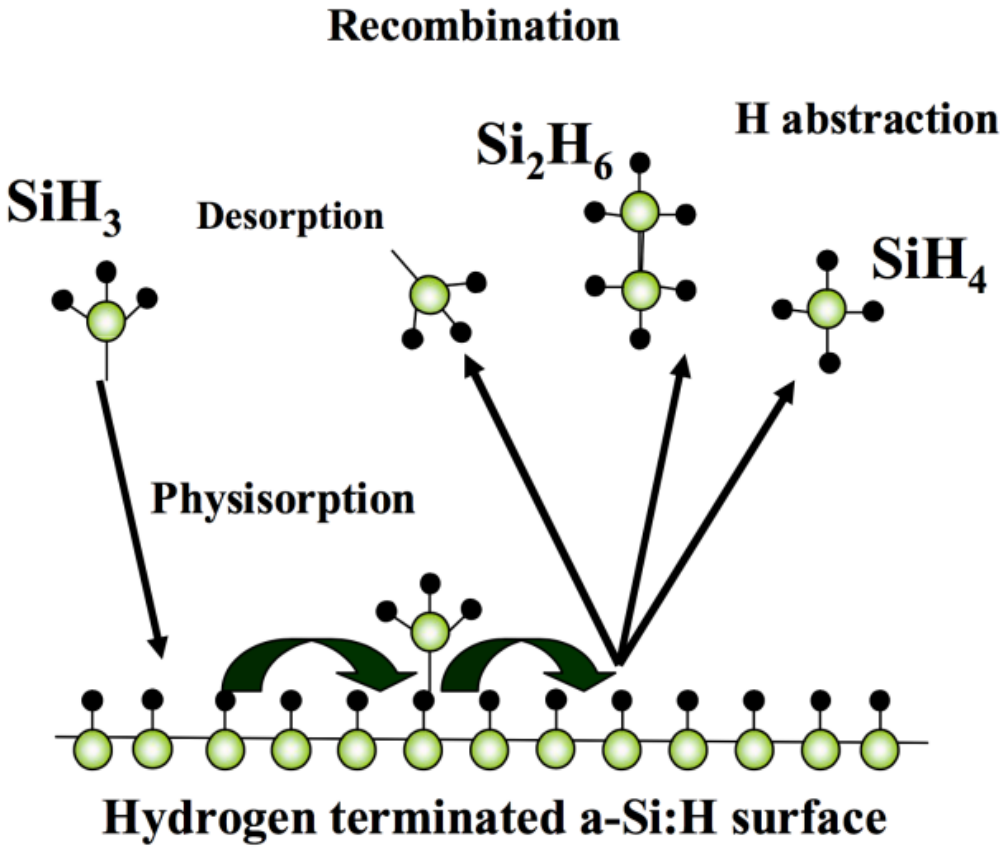

Figure 2.3: The schematic illustrates the interaction between SiH_3 and the c-Si growing surface. Adopted from [88].

In so-called physisorbed condition, so to speak SiH_3 diffuses over the surface until it either adheres to a surface dangling bond or removes a hydrogen atom from the surface to generate SiH_4 and a surface dangling bond. Respectively low deposition temperatures (about 200 °C), which greatly reduce thermal energy, are to account for this phenomenon. The formation of the film requires at least two SiH_3 radicals. The development of the film is aided by chemical absorption on a surface-dangling link. In this case, the surface first creates a dangling bond that later permits a different radical to deposit there, leading to the development of the film. Due to the instability of three-center Si-H-Si, the 'insertion' reaction of SiH_3 takes place on the surface bonds of strained Si-Si insertion.

The influence of various radicals on the growth process of (*i*)a-Si:H

– The SiH_3 radical can remove a hydrogen atom from the surface to create dangling bonds and silane gas.
– Chemical absorption on a dangling bond results from the removal of a hydrogen atom from the surface, which aids in the film's development.
– Si_2H_6 synthesis.
– Removing something from a physisorbed condition.

– (*i*)a-Si:H films are developed on c-Si surface with the help of interaction between the film and SH_3 radicals as shown below:

$$H + SiH_4 \longrightarrow H_2 + SiH_3 \tag{2.1}$$

The insertion reaction is dependent on Si-Si bonds on the a-Si: H surface and substrate temperature, T_s. At low temperatures, the surface contains abundant SiH_3 radicals with the activation energy (0.7- 0.9 eV) stated by Kessels et al. which enhances the reaction probability, β [93]. In actuality, many radical species, including SiH_2, SiH, Si, also contribute to the development of the film and the quality of the deposited of material, depending on their chemical characteristics and/or activation energies. For instance, SiH_2 radicals can produce extremely faulty layers by speeding up the production of polysilane Si_2H_6, as expressed in chemical reaction equation 2.1, but the resulting polysilane species may also result in a film that grows with poor quality [87, 94, 95].

Growth mechanism of (*i*)a-Si:H on c-Si surface

Polished thin c-Si on both sides provides a flat, ground surface for growing thin films. Usually, 270 μm c-Si<100> substrates can be textured by the etching process it can be 250 μm thick c-Si<111> oriented double-sided textured pyramid surface, which is the most typical c-Si surface for SHJ devices considering its outstanding light trapping properties.

The majority of scientific studies use c-Si wafers with a double-sided textured surface [96, 97, 98, 67, 66]. It was crucial to conduct some preliminary research on epitaxial growth on c-Si<100> surfaces since single-sided textured wafers were used in this study. According to prior research, c-Si<111> surfaces have one dangling bond per surface atom while c-Si<100>(unreconstructed) & c-Si<100>-(2x1) (reconstructed) surfaces also has one dangling bond per Si atom dangling bonds, as demonstrated by S. De Wolf and R. Hamers et al., as in figure 2.4 [67], increasing the likelihood of epitaxial development. Epitaxial growth is detrimental and we want to avoid it. The detrimental epi-growth mechanism on the c-Si<111> surface necessitates a higher thermal budget than that of the c-Si<100> surface [99], while in this study, we focused on the low thermal budget. Equation 2.2 determines the dilution ratio of the flow of hydrogen gas. In a previous study, it was found that the <100> c-Si surface is prone to detrimental epitaxial growth even at a lower hydrogen dilution ratio [62].

$$\text{Dilution Ratio} = \frac{\text{Flow rate of Hydrogen}(H_2)}{\text{Flow rate of silane}(SiH_4)} \tag{2.2}$$

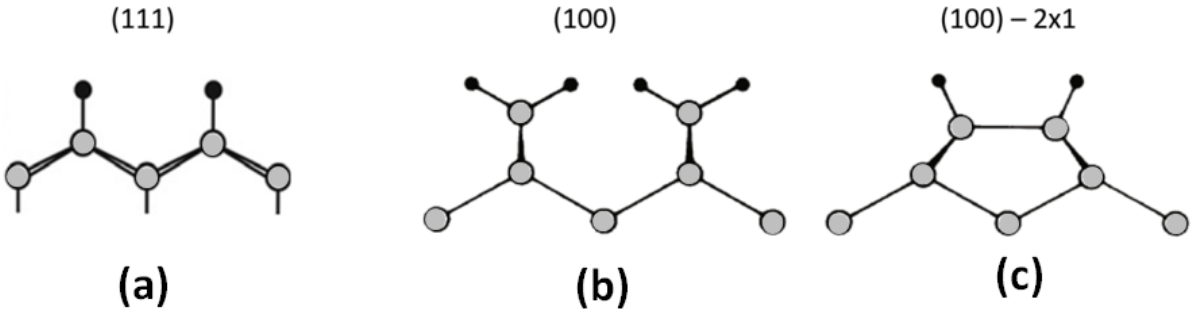

Figure 2.4: Atomic growth on various c-Si surface orientations: (a) <111>; (b) <100> (unreconstructed); and (c) <100> (- 2x1) (reconstructed). Adopted from [92].

To sum up, the most suitable method for achieving good film growth is to use hydrogenated amorphous silicon (a-Si:H) produced from SiH_3 radicals in silane plasma with robust epitaxial growth on the c-Si<100> surface while atomic hydrogen can also dissolve the dangling bonds [100].

Passivation mechanisms

Regarding silicon solar cells, the technique called surface passivation inhibits electrons and holes on the wafer surface from abruptly recombining. The passivation of dangling bonds, which is necessary to improve the device's performance (higher V_{oc}, efficiency for instance), as surface recombination will otherwise lessen the anticipated collection of charge carriers. Chemical and field effect passivation can be used to accomplish this by ensuring a higher effective lifetime of the charge carriers (τ_{eff}) [97, 101, 102]. Figure 2.5 illustrating the surface passivation of the c-Si surface.

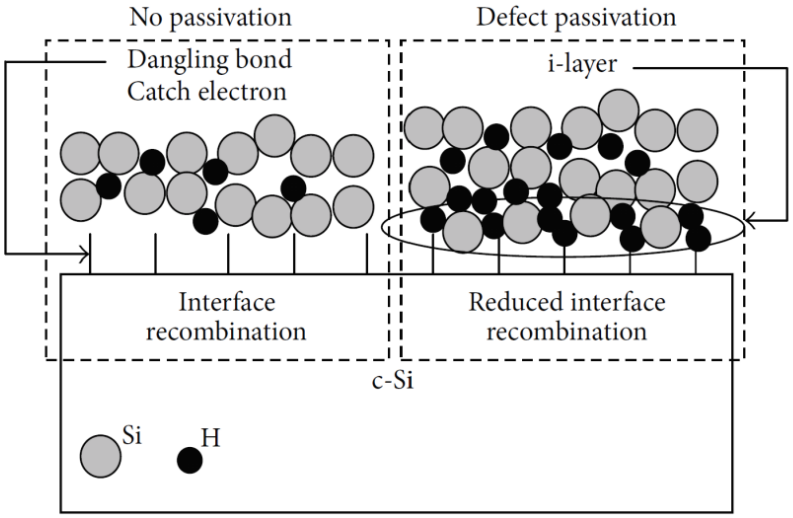

Figure 2.5: The schematic of the surface passivation process on c-Si surfaces. Adopted from [95].

- Chemical Passivation: Saturation of dangling bonds essentially results in the passivation of surface states. This most often used passivation technique for SHJ solar cells aims to lessen the number of dangling bonds. For this research, RF-PECVD was used to deposit 10 nm hydrogenated intrinsic bilayers on top of the active material, sandwiching HPT between two intrinsic layers [20, 103]. Bilayer applications with HTP, according to earlier studies, provide superior passivation quality [104, 68, 105]. To improve electrical properties (J_{sc}, FF, V_{oc} etc.) and reduce parasitic absorption of the solar cells, the intrinsic layer's thickness (10–12 nm) was verified [88].
- Field-effect Passivation: It is the process of deliberately reducing the minority carrier density (electrons or holes) by depositing doped layers [106]. In order for this to occur, a surface electric field must be created that repels the minority carriers and reduces the amount of recombination that can occur at the interface.

2.3. Doper Layers:(*n*)/(*p*)nc-Si:H

Contrary to a-Si, nc-Si contains smaller crystalline flakes in the amorphous phase. Although it comes from the same group of porous silicon with paracrystalline or an amorphous crystal structure, nc-Si is more stable and preferred in thin film applications due to its lower hydrogen concentration [107]. With a greater capacity for absorption, nc-Si:H doped with boron (B_2H_6) or phosphorus (PH_3) had a better probability of minimizing spectral loss. In general, nc-Si:H is more transparent than a-Si:H due to the a-Si:H tissue that is hydrogen-rich, which enlarges

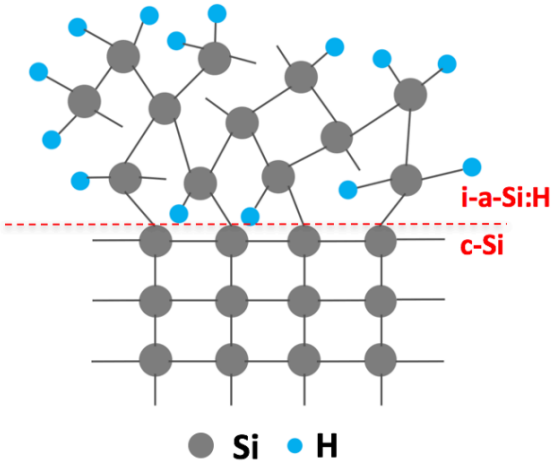

Figure 2.6: Schematic of chemical passivation at c-Si/*(i)*a-Si:H interface. Adopted from [84]

the bandgap of the material and makes the film more transparent. Therefore, it can reduce the parasitic absorption as compared to std a-Si:H layers [107].

Combining amorphous silicon and nanocrystalline silicon grains with a mean grain size of 3-5 nm results in hydrogenated nanocrystalline silicon, which provides some excellent optoelectrical properties such as less parasitic absorption loss absorption, higher carrier mobility, and better conductivity [108, 109].

2.3.1. Atomic Structure

nc-Si:H microstructure consists of a few tens nanometers large nanocrystals in the amorphous matrix (a-Si: H), where H atoms are located in this network for dangling bond passivation. Depending on deposition parameters this material can be amorphous or highly crystalline. Figure 2.7 shows the crystalline state (e.g. cracks and gaps) of the material on the left side and on the right, a complete amorphous state is visible [110].

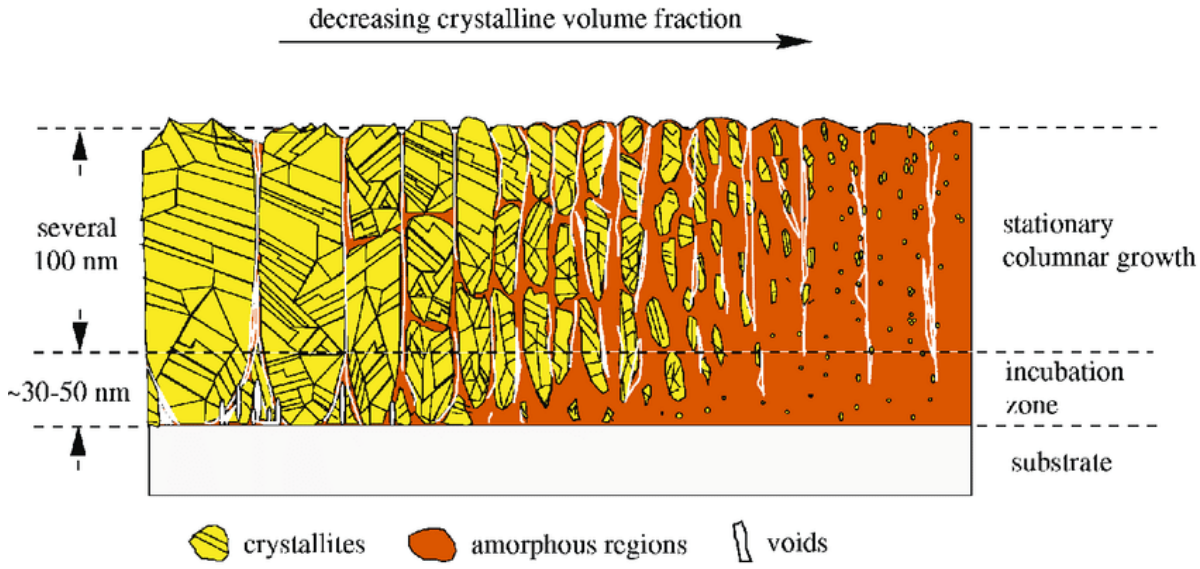

Figure 2.7: Atomic structure of nc-Si:H: crystalline phase on the left (yellow) and amorphous silicon on the right (orange). Adopted from [110].

2.3.2. Growth Mechanism

The amorphous matrix essentially encases the nc-Si:H film deposition. PECVD uses high-density SiH_4 (as a source of Si) plasma that has been diluted in H_2 to deposit a doped nc-Si:H layer. In order to grow films, several conditions must be met, such as low substrate temperature, spontaneous growth, processing pressure, electrode spacing, low-pressure plasma processing, RF power, and most crucially, H_2 dilution of the source gases [111, 112]. Figure 2.9 demonstrated the growth of nc-Si:H films in four stages with hydrogen-induced crystallization [113, 114, 115].

- Incubation: In the first stage, an incubation/amorphous layer with a few nanometers of thickness is developed. This layer mainly controls the transformation to the nanocrystalline phase. Various treatments make it to the next stage of growth: nucleation.
- Nucleation: In this stage, the nucleation of nanocrystal starts [116, 117].
- Nano-growth: Next, the nanocrystalline stage progresses till the growth is stable. The thickness contains different crystalline fractions as this growth takes place in a cone-shaped manner. In this growth process, H destroys the strained Si-Si bonds in the a-Si:H film by forming Si-H-Si bond configurations. This helps the growth from amorphous to nanocrystalline phase [118].
- Stationery-growth: Nanocrystals are already developed.

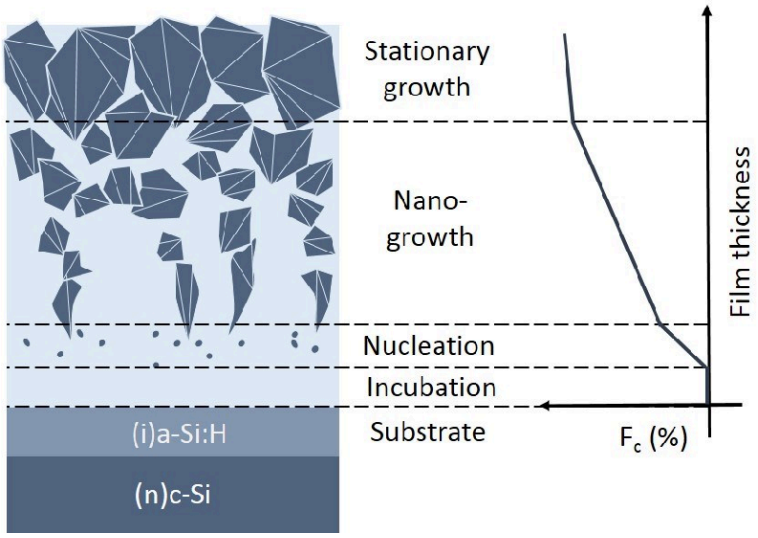

Figure 2.8: Growth mechanism of nc-Si:H. Adopted from [119].

2.4. Doped Layers: (*n*)/(*p*)nc-SiO_x:H

Hydrogenated nanocrystalline silicon oxide (nc-SiO_x:H) is an oxygen alloy of nc-Si:H, which offers tunable optical properties: absorption coefficient α(λ), refractive index n(λ) and electrical properties: conductivity (σ). Doped nc-SiO_x:H, used as a window layer in silicon heterojunction (SHJ) solar cells, is an ideal substitute for the doped amorphous silicon layer (a-Si:H) to reduce parasitic absorption loss. Because of their greater absorption coefficient, a-Si:H window layers (widegap emitter layers in solar cells) in a SHJ solar cell may lead to parasitic absorption, which directly affects the solar cell's EQE as well as current density. nc-SiO_x:H, the higher-bandgap material with improved conductivity and transparency, maybe a solution to lessen this optical loss [120, 121, 122, 123, 84, 124]. Lower activation energy (E_{act}) in nc-SiO_x:H than in a-Si:H can emphasize the overall J-V parameters (J_{sc}, V_{oc} and FF) of a SHJ solar cell. Phosphorus (PH_3) doped nc-SiO_x:H exhibits a wide processing window for realizing a higher conductivity when compared to Boron (B_2H_6) doped nc-SiO_x:H thin film layers [84]. The (*n*)/(*p*)nc-SiO_x:H material is a superior replacement for the TCO of SHJ solar cells due to its tunable optical properties [73].

2.4.1. Atomic Structure

It has been demonstrated through prior research that silicon heterojunction (SHJ) solar cells with thin inherent buffer layers can increase cell efficiency. Thin film layers made of nc-SiO_x:H instead of nc-Si:H can be utilized as windows through which light can easily penetrate the main absorber, crystalline silicon (c-Si), due to its higher transparency [122, 125]. Due to the fact that doped nc-SiO_x:H is less conductive and has a higher contact resistance (ρ_c) (since it contains oxygen). According to the traditional nucleation theory, growth and nucleation are what determine crystal sizes and atomic volume [126, 123]. The density and size can be used to explain whether a crystallite is nano (10 nm) or micro (>10 nm) crystalline [111]. Figure 2.9 shows an amorphous matrix with nano and microcrystalline phases [123].

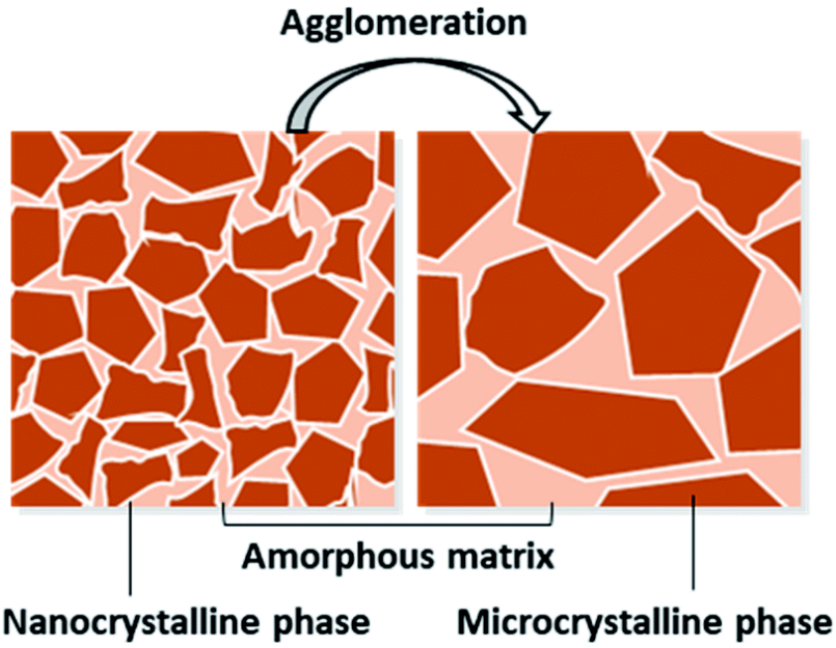

Figure 2.9: Schematic of an amorphous matrix with nano- and microcrystalline phases. Adapted from [123].

2.4.2. Growth Mechanism

SiH_4, H_2, PH_3 (diluted in H_2 by 1%), and CO_2 are precursor gases used to deposit hydrogenated nc-SiO_x:H. An amorphous incubation layer can delay the formation of the nanocrystal in the nc-SiO_x:H. nc-SiO_x:H. However, CO_2 plasma treatment and relatively thin nc-Si:H seed layers are employed to prompt nucleation of nanocrystals [127, 9].

The growth of a-SiO_x:H: H thin film layers by RF-PECVD is interesting. In the incubation stage, an incubation/amorphous layer a-SiO_x:H with a few nanometers of thickness is developed. This layer mainly controls the transformation to the nanocrystalline phase. Various treatments make it to the next stage of growth which is nucleation. Earlier research by L. Mazzarella et al. and S. Kirner et al. reveal that CO_2 plasma treatment or ultra-thin nc-Si:H seed layer can narrow down the incubation layer to enhance nanocrystal nucleation [116, 117, 128, 127]. Following that, the growth becomes stagnant as the nanocrystalline phase gradually rises. Typically, crystal formation during the stationary growth stage takes the form of a cone. Film thickness affects this particular proportion of crystalline cones, shown in figure 2.8 [129, 130].

2.5. Transparent Conducting Oxides

In contrast to conventional solar cells, SHJs have a particular form of architecture as p/i/n/i/n or n/i/n/i/p stack, wrapped with TCO and a metallic grid. Here, the front TCO basically used as an anti-reflection (AR) coating and charge carrier transport layer whereas the rear TCO is used to increase internal reflection and shield doped layers from metallization damage. [131]. TCOs are materials with a good combination of better optoelectrical properties, which makes them essential in the field of research on solar cells. Just as other doped materials, n and p-type TCOs can be found, depending on the prevailing charge carriers. n-type TCOs such as Indium Tin Oxide (ITO), Aluminum Doped Zinc Oxide (AZO), and Indium Tungsten Oxide (IWO) are the most often employed in contemporary PV research due to their wide bandgap and excellent optical and electrical performance [132, 133].

2.5.1. Optical and Electrical properties of TCOs

After the metallic layer, the very first layer of an SHJ solar cell stack is the AR coating, here it is a TCO layer. Similar to other materials, the band structure of the core material affects the optical characteristics of TCO. The entire light bending capacity or so-called refractive index, of the active layer of a SHJ solar cell is determined by TCOs in conjunction with the other doped thin film layers. Considering that, the front TCO layer, here is ITO (n-type semiconductor with a band gap range of 3.5 to 4.3 eV), the suggested thickness of 75 nm was previously optimized in the PVMD research group in TUDelft. On the other hand, a SHJ solar cell's back side has a TCO thickness that has been doubled, in this example to 150nm, in order to maximize infrared response [132]. The conductivity (σ), basically depends on total charge carrier concentration (N), elementary charge (e) and mobility of the charge carrier (μ), can be described as $\sigma = N.e.\mu$. Ideally, TCOs with higher charge carrier mobility and lower charge carrier concentration should be used in solar cell application [132, 134].

2.5.2. Recombination Junction (RJ)

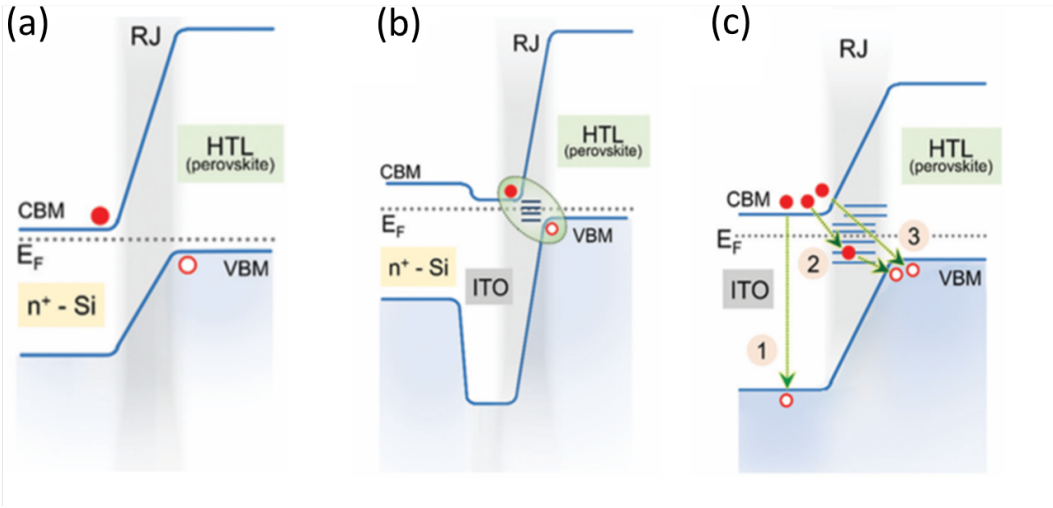

Figure 2.10: Band diagrams of the interface between perovskite/c-Si silicon tandem solar cell: (a) without and (b)with an ITO as RJ, whereas (c) represents a closer image of the tunneling region to observe different recombination mechanisms such as : (1) Local, (2) Trap-assisted and (3) Direct tunneling. Adopted from [64].

As the two p-n (n-p-n-p) junctions join together in series in a tandem solar cell, a third p-n junction is created at the junction point under a reverse bias state with the opposite polarity. In a reversed bias condition, the flow of current will be blocked as it moves in the other direction. Therefore, the

conduction band of an n-type semiconductor will be extensively filled with electrons if we employ two heavily doped layers in the junction point, while the valance band of a p-type semiconductor will be heavily filled with holes. Depletion width, which is inversely correlated to effective doping, enables electrons to pass over the impermissible barrier through recombination with holes from the valence band of the adjacent p-type material or HTL. Electrons naturally travel downhill whereas holes move higher. If an electron travels in the traditional manner, there is a significant barrier preventing it from reaching the p-side. By increasing the doping, the junction gets steeper and the depletion region is reduced, allowing carriers to tunnel from one side of the junction to the other. Higher doping conditions in the reverse bias state allow current to pass.

Figure 2.10 (a) and (b) depict the band diagrams of a 2T tandem device without and with ITO interface, whereas, (c) is an enlarged image of RJ area [64]. Tunneling via this junction is achievable with heavy doping and low voltage, and high current will flow in reverse bias [73]. Since the maximum current in reverse bias is inversely or proportionally correlated with the exponential function of doping, it is proportional to doping. An ideal tunnel junction allows all of the current that is generated in the cell to travel through it without encountering any additional resistance. ITO is typically employed as the electrode in single junction c-Si solar cells as well as the intermediate layer in multijunction solar cells [135]. However, this extremely expensive material also has a number of optoelectrical flaws, including parasitic absorption at higher wavelengths, poor matching of the bottom cell's refractive indices, and high interface reflectance. These issues could be remedied by employing highly doped thin film layers as RJs instead of ITO.

In summary, RJ is nothing more than a tunnel diode at the intersection of two sub-cells, derived from the concept of current matching in the tandem devices. The efficiency of the cell can be decreased by charge carrier recombination or an accumulation of charges close to the RJ in the space between two subcells of a PIN configuration. Contrary to standard RJ, it is feasible to prevent trapping-related field loss at the junction With trap-assisted recombination tunneling. This supports the efficient photocurrent generation which leads to achieving better performance of a multijunction device. Along with non-oxidic thin film layers, highly doped nc-SiO_x:H films can play a significant role as a RJ and be a better alternative to ITO. These doped nc-Si: H-based thin-film layers, including its oxidic alloy, allow tunable light management of the tandem devices. This can eventually lead to optimized tandem device performance [73, 136, 63].

3

Instrumentation of SHJ Solar Cells: Fabrication and Characterization

The numerous instrumentation based on the optical simulation (for two-terminal and single-junction solar cells) and electrical simulation tools, as well as characterization techniques for single-side-textured SHJ solar cells, have been highlighted in this chapter. A brief overview based on the flowcharts and measuring techniques are provided.

3.1. Optimal Simulation Tool: GenPro4

The optical simulation-tool 'GenPro4' software is basically a library of Matlab (developed by the PVMD group of TU Delft) that plays a curtail part of this hybrid research project. The software uses the combination of wave and ray optics to analyze optical properties while completely disregarding the electrical properties of multilayer solar cells. Considering the interference effect (scattering and trapping of light at the interfaces) the fraction of incident light absorption on different layers the implied photocurrent density, J_{sc} and the generation profile (reflection and parasitic loss) are calculated. More details can be found in the paper by Santbergen et al. (add ref GenPro4_ and GenPro4_manual [137]). The optical simulation system for 2T tandem devices and single-junction SHJ solar cells are depicted in the flowchart in fig. 3.1.

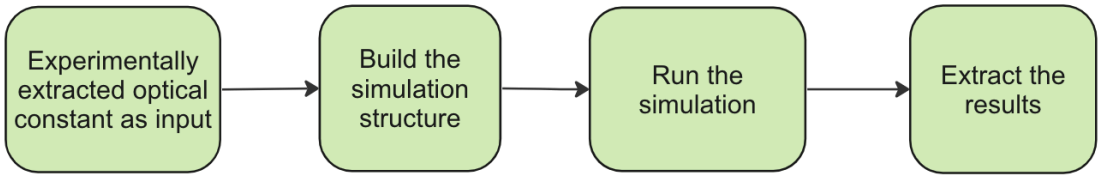

Figure 3.1: The optical simulation system of 2T tandem devices and single-junction SHJ solar cells are depicted in a flowchart.

3.1.1. Optical Properties

GenPro4 uses thick layers and a refractive index of wavelengths to estimate reflectance, absorptance, and transmittance in solar cell materials by reducing the structure of the cell to a 1-D multilayer structure. The theory is expressed by the equation T + R + A = 1, where T is the amount of light that is transmitted, R is the number of photons that are reflected, and A is the amount of light that is absorbed rather than reflected by a substance. Since solar cells are opaque and have zero transmittance, T is also zero. The extinction coefficient, also known as the degree of

absorption loss, is determined by the formula N = n + ik, where n is the complex refractive index, i is the square root of -1, n is the refractive index, and k is the material's extinction coefficient. The majority of the time, k > 0 (light is absorbed). n and k are both wavelength-dependent. This approach provides a better and faster computation of the properties. Different optical formulas (e.g. Fresnel equations, Snell's law, Lambert-Beer law) are used to model flat interfaces [137]. GenPro4 considers discrete propagation for flat surfaces and can also simulate for textured surfaces using wave effects like diffraction interference with scalar scattering model [137]. This is very helpful as textured interfaces are used in real cells to reduce reflection.

3.2. Experimental Simulation Tools: Dark Conductivity of Doped Layers

Optimize the thickness of doped layers and doped layers with intrinsic layers is done by following :

- Cleaning Corning Eagle XG glasses with an ultrasonic cleaner.
- In the EKL lab, RF-CVD AMIGO was used to deposit the doped layers and the (*i*)a-Si:H/doped layer stack.
- The EKL laboratory's RF-PVD PROVAC was used to deposit metallic layers.
- As a follow-up procedure, the ESP lab underwent 30 minutes of annealing at 130 °C.

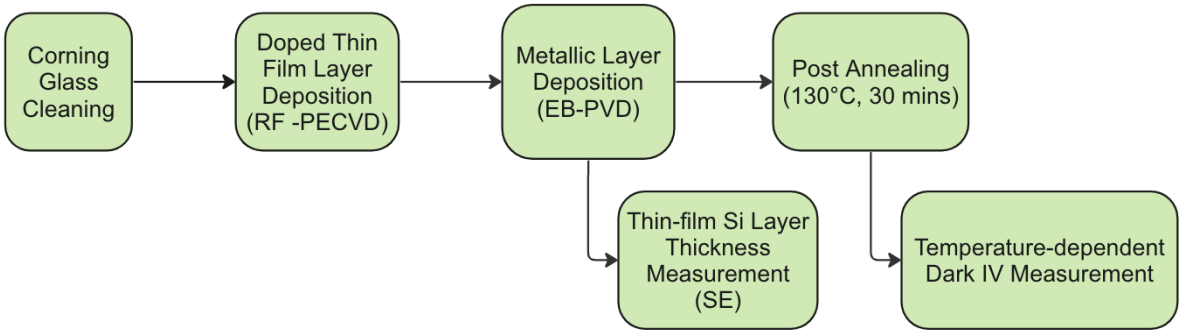

Figure 3.2: Flowchart of doped layers investigation.

3.2.1. Ultrasonic Cleaner: Corning Eagle XG

Ultrasonic cleaners use cavitation (vacuum-like scrubbing process with microscopic implosions) to clean materials using mechanical vibrations to produce sound waves in a cleaning solution. This process is highly effective for cleaning delicate things and can be cleaned in a proper uniform manner.

3.2.2. Electron Beam- Physical Vapor Deposition(EB-PVD)

Metal evaporation is a well-known technique for metallization and in this process, the material is heated up to its melting point and this evaporation spray is targeted towards the subject in a high vacuum container (typically under 10^{-3} to 10^{-6} Pa) and then metal attaches to the substrate material in a cooler temperature [138]. The schematic of PROVAC PRO500S is shown in Fig. 3.3 supports two methods for the metal evaporation process: electron beam and resistive (thermal) evaporation [139], and the flowchart 3.23 shows the steps of the electron beam evaporation procedure in a nutshell. RF-PECVD by tool Amigo (details discussed in 3.3.3) was used to deposit thin film layers on top of the chronic glass and then the metallic layers were deposited on top of this precursor. Due to its low melting point of 660.32°C, aluminum is a suitable material for this operation. In this research work Al 99.99% with slugs 5x5x15 mm was used for this metallization process.

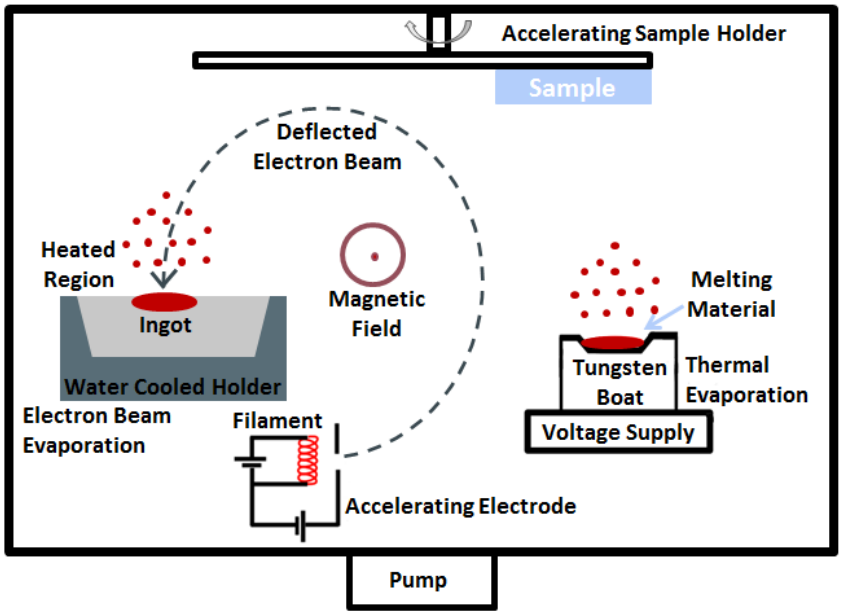

Figure 3.3: Metal evaporation system in PVDM group with electron beam evaporation (left) and resistive evaporation (right). Adapted from [139].

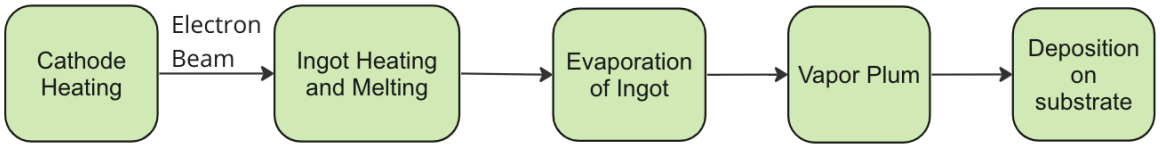

Figure 3.4: Flowchart of EM-PVD metal deposition process.

3.2.3. Dark Conductivity and Activation Energy

Dark current measurements were carried out for various doped layers deposited on plain glass, both with and without intrinsic layers. A conductive metallic layer was deposited by using the electron beam evaporation method.

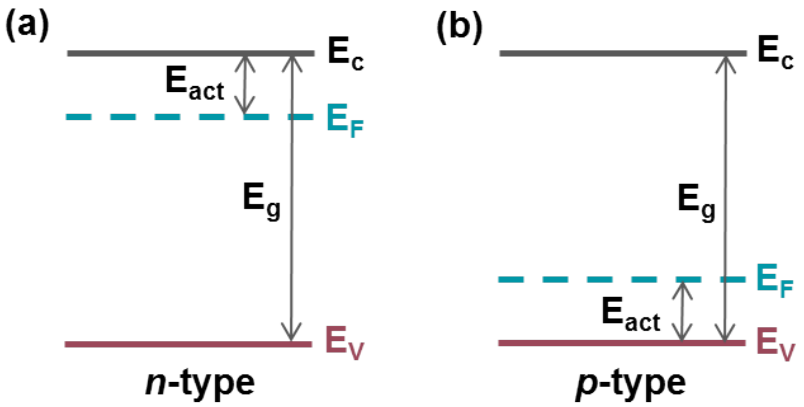

Figure 3.5: Definition of activation energy of *n*-type (a) and *p*-type (b) materials.

The activation energy (E_A, energy between Fermi level $E_F$and valence bond E_V presented in fig-

ure **??**) represents the doping efficiency of p-type material and plays a significant role in tunneling probability and hence the measurement of device performance is dependant on this. Dark conductivity (σ_d) is measured using equation 3.17, where q is the elementary charge, p is hole density, n is electron density (both under thermal equilibrium), μ_p is hole mobility and μ_n is electron mobility.

$$\sigma_d = q(n\mu_n + p\mu_p) \tag{3.1}$$

$$p = N_V exp(\frac{E_V - E_F}{K_B T}) \tag{3.2}$$

$$n = N_C exp(\frac{E_F - E_C}{K_B T}) \tag{3.3}$$

Equations 3.18 and 3.19 represent hole and electron density respectively as Fermi level dependent where N_V and N_C are the effective densities of the valence band and conduction band. As dark conductivity is temperature dependent, this can be measured for different temperatures using equation 3.20, where d is the distance between electrodes, I is measured current and V is measured voltage, t is deposited layer thickness and l is electrode length. And activation energies can be determined from these obtained $\sigma_d(T)$ values using equation 3.21 (σ_o is a pre-exponential factor).

$$\sigma_d(T) = \frac{dl}{tlV} \tag{3.4}$$

$$\sigma_d(T) = \sigma_o exp(-\frac{E_{act}}{K_B T}) \tag{3.5}$$

E_A is finally measured from the slope of the fitted line by plotting $ln(1/\sigma_d(T))$ over $1/K_B T$ (an example figure 3.6). An illustration of a sample measuring setup for activation energy and dark conductivity is depicted in figure 3.7. I-V curve was measured for temperatures between 130°C and 45°C with applied voltage 10V at the sample (presented at figure 3.6) [140]. Doped layers are deposited on corning glasses and coplanar-shaped contacts are formed by hard masking using evaporating Al. Annealing below 130 °C is done in the air for about 30 minutes to facilitate good contacts between doped layers and Al contact in this work.

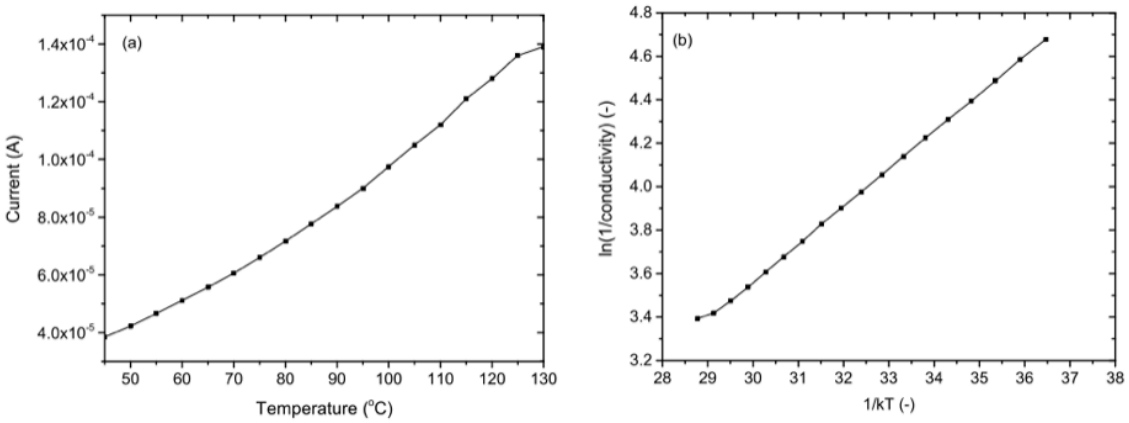

Figure 3.6: (a) Dark current at 10V and (b) conductivity, measured at various temperatures. Adapted from [140].

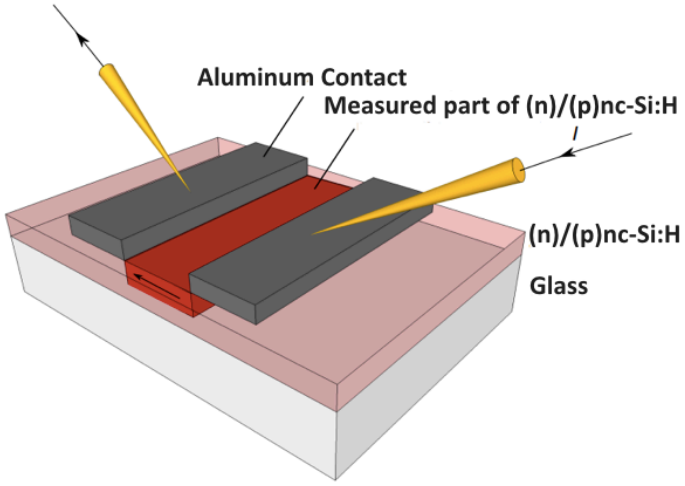

Figure 3.7: An illustration of a sample measuring setup for Activation Energy and Dark Conductivity. Adapted from [139].

3.3. Characterization of Doped Layer

The following methods were used to characterize doped layers:

- Before the annealing procedure, the layer's thickness was measured using Spectroscopic Ellipsometry (SE).
- In order to quantify the activation energy of the solar cells, a dark current measurement was performed.

In this chapter's parts 3.4.1 and 3.4.2, the operational ideas are fully presented.

3.4. Experimental Simulation Tools: Fabrication of Single-Junction SHJ Solar Cells

To fabricate single-side-textured single-junction SHJ solar cells boxes of 25 double-sided polished Float Zone (FZ) n-type <100> oriented c-Si wafers, with the thickness, diameter, and resistivity of (280±20 μm), (99.7 - 100.3 mm), and (3±2 Ωcm) respectively, were used. To shield the substrate from the texturing process, Silicon Nitride (SiN_x) was deposited on one side of the wafer using Novellus. A dedicated flowchart, depicted in figure 3.8, was followed to fabricate the single-side-textured single junction FBC-SHJ solar cells.

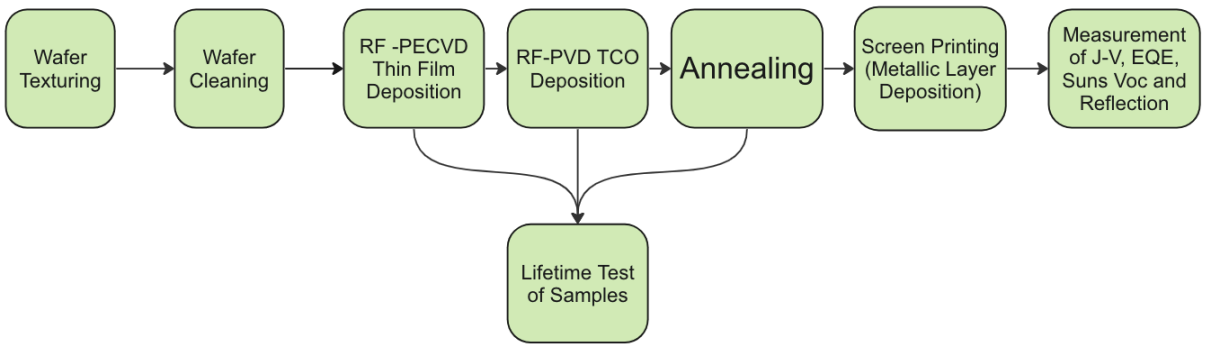

Figure 3.8: Flowchart to fabricate single-side-textured single-junction SHJ solar cells.

The steps of the flowchart are outlined as follows:

- A ∼200 nm thick SiN_x was deposited on one side of the wafers.
- 5% TMAH treatment was employed to texture the other side of the <100> c-Si wafers.
- Submersion in BHF for the deletion of SiN_x.
- The wafers were then cleaned through a wet-chemical cleaning procedure.
- The (*i*)a-Si:H and doped layer-stacks were deposited by 'RF-PECVD' Amigo in the EKL laboratory.
- ITO is deposited at room temperature on the deposited doped layer's stack, on both sides of the wafers by using the RF sputtering tool (Zorro) in EKL.
- As a post-treatment, annealing (heating), was done at 180°C temperature for 5 minutes using the Oven in the ESP lab.
- Solar cells were completed with Silver (Ag) Screen printing on both the front and rear sides.

This chapter also contains sections 3.2.1 through 3.2.5 that go into great detail about the texturing process, dissolving SiNx, RE-PECVD operating principle, sputtering, and screen printing mechanism.

3.4.1. Wafer Texturing

The double-sided polished <100> oriented c-Si wafers were coated with a 200 nm thick SiN_x layer, which serves as an etching mask for the subsequent texturing process, in order to fabricate the single-side-textured SHJ solar cells. The anisotropic etching method is adopted to texturize wafers by dipping them in a hot (75 ± 2°C) alkaline etching solution [5% tetramethylammonium hydroxide (TMAH, $((CH_3)4NOH)$] for 15 minutes. This alkaline etching solution is made by combining; 1L of 25% TMAH (SIGMA-ALDRICH) and 120 mL ALKA-TEX.8 (GP Solar) and 4L de-ionized (DI) water. ALKA-TEX.8 helps with increasing bath lifetime and decreasing the texture time.

As a result, we obtain a <111> oriented textured random upright pyramid on the rear surface of about several microns (0.5 µm to 2.1 µm) in size (add ref GP 92). This structure allows a longer optical path in the wafer. This increases absorption and minimizes reflection losses and hence, the optical advantage is observed [10].

3.4.2. Wafer Cleaning

Both planar and textured c-Si surfaces can suffer from contamination and defects. After post-texturing, this surface becomes larger for defects with higher contamination probability. This is a hindrance to the performance of the solar cell. This cleaning is targeted towards purging the contaminants (e.g. organics, metals) and smoothing out nano-roughness from wafer texturing. Also, oxides are cleaned from the c-Si surface and the dangling bonds are passivated partially. This cleaning process is called the nitric acid oxidation cycle (NAOC) and includes a full cycle of wet chemical oxidation and hydrofluoric (HF) dip. The steps are stated below.

- Organic contaminants are removed by dipping the single-side-textured wafers into HNO_3 (99% concentrated) for 10 minutes at room temperature.
- Following step is to use de-ionized (DI) water to rinse it out for ∼5 minutes.
- Next, metal contaminants are removed by dipping them into HNO_3 (69.5% concentrated) for 10 minutes at (110±5 °C). De-ionized (DI) water is used to rinse them once more for ∼5 minutes.
- In the last step, the surface dangling bonds are substantially passivated, and the native oxide layers are cleaned from the surface by a hydrofluoric dip with Maragoni (0.55% HF) for ∼5 minutes. A shorter or longer period is avoided in order to not leave the wafer dirty or increase roughness [139].

This complete NAOC cycle is repeated three times for single-side-textured wafer [141]. The wafer is then immediately placed into the vacuum chamber of the RF-PECVD equipment (Amigo) for processing in order to prevent re-oxidation.

3.4.3. Radio Frequency Plasma-Enhanced Chemical Vapor Deposition (RF-PECVD)

For radio frequency (RF) plasma-enhanced vapor deposition (PECVD), the AMIGO machine (Elettrorava, S.P.A) was used for the deposition of intrinsic and doped layers. The device has separated deposition chambers that safeguard from cross-contamination, which can be seen in figures 3.9 (depict the full system) and 3.10 the chambers from a top view respectively.

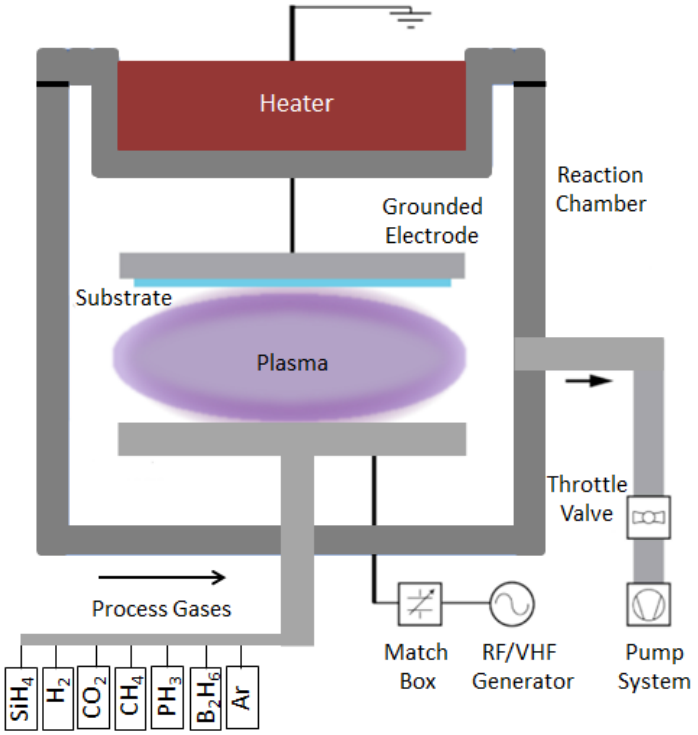

Figure 3.9: Schematic of RF-PECVD deposition system. Adapted from [10].

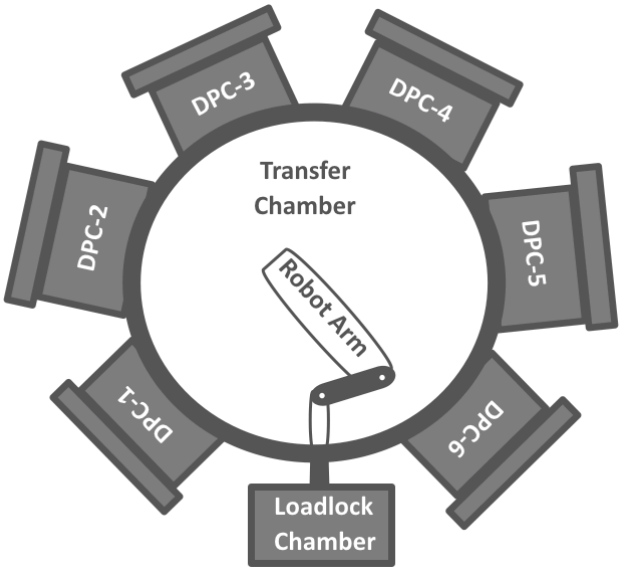

Figure 3.10: Top view of RF-PECVD tool (Amigo) in PVMD group depicting six deposition chambers connected with pumps for vacuum transfer and thin-films deposition.

Samples are loaded in a PECVD load-lock chamber (LLC) after treatments in an ultra-high vacuum (UHV). Next, the samples are placed into DPC (specific reaction chambers with UHV), and gas precursors are injected based on deposition purposes. Silane (SiH_4) and hydrogen (H_2) are used for the deposition of (*i*)a-Si:H and diborane (B_2H_6) and phosphine (PH_3) dopant gases are used for doped layers. Also methane (CH_4) and carbon dioxide (CO_2) help with the carbon and oxygen gases in deposition layers. The atoms and molecules of the gases introduced in the UHV reaction chamber are ionized and turned into plasma via an energy source which is the oscillating electric field between two capacitively-coupled electrodes regulated through an RF signal of 13.56 MHz [10]. This accelerates the electrons and they collide with gas molecules and generate various molecules (e.g. ions, neutral atoms, radicals). Positive and negative particles help with layers growth via interaction with the material as neutral and others create a plasma sheet [131]. For single-side-textured SHJ solar cells, *i*-layer, *n*-type and *p*-type depositions were done using the RF-PECVD's DPC_3, DPC_2 and DPC_1 chambers respectively. The entire deposition process is outlined in a flowchart in fig. 3.11

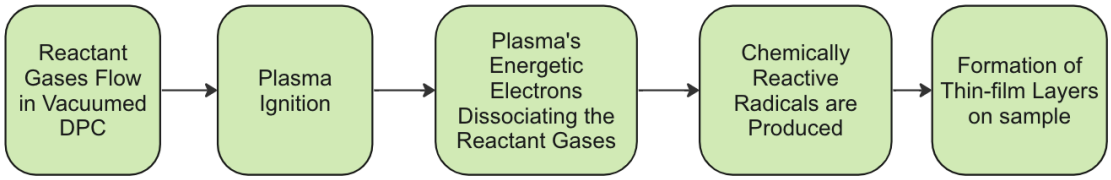

Figure 3.11: Flowchart of RF-PECVD deposition process.

This process is relatively simple and provides some advantages such as;

- Deposition can be done at low temperatures (<200 °C) [10] as an electric field energy source is used instead of thermal sources.
- A variety of films can be deposited as different gas precursors are available and the possibility of mixing gas flows. Also,
- The final films are of high quality with proper adhesive to materials with surface coverage and uniformity [10].

The pressure and temperature in reaction chambers, gas flow rates, and RF generation of power to fuse in the plasma can be adjusted based on various needs of the deposition providing sufficient flexibility in the process [142, 143, 144, 145].

3.4.4. Radio-frequency Magnetron Sputtering

Radio-frequency (RF) magnetron sputtering (a type of physical vapor deposition (PVD) method) is used to deposit the TCO layers and metal contacts in solar cells. Figures 3.12 depict a typical chamber of an RF-magnetron sputter and 3.13 shows the top view of the tool. It is a simple one-step deposition process with high power [146] where:

- Atoms and released electrons are sputtered from the target (cathode) when RF power is applied via highly energetic inert Argon (Ag) gas particles. These particles then deposit on the substrate after sputtering. They also collide with Ar atoms to generate ions and loose electrons aiding the plasma environment. The transparent coating oxide with specific indium tin (ITO) was sputtered by the tool Zorro (Polyteknik). The target for this ITO deposition is a mixture of 90 wt.% In_2O_3 and 10 wt.% SnO_2.

Before using the refined ITO sputtering recipe on the actual devices, the sheet resistance by the linear four-probe system CMT-SR2000NW of CR10K and anticipated thickness was assessed by the Spectroscopic Ellipsometry (SE) from the ESP lab (explained in detail in section 3.4.1). Previously optimized recipes served as a reference to fit with the new anticipated recipe for both

of these measurements. Lower sheet resistance was confirmed, and the ITO target was checked by examining the predicted layer's thickness. The goal of the entire process was to determine whether any recipe modifications were required.
Flowchart 3.14 shows the sputtering procedure in a nutshell.

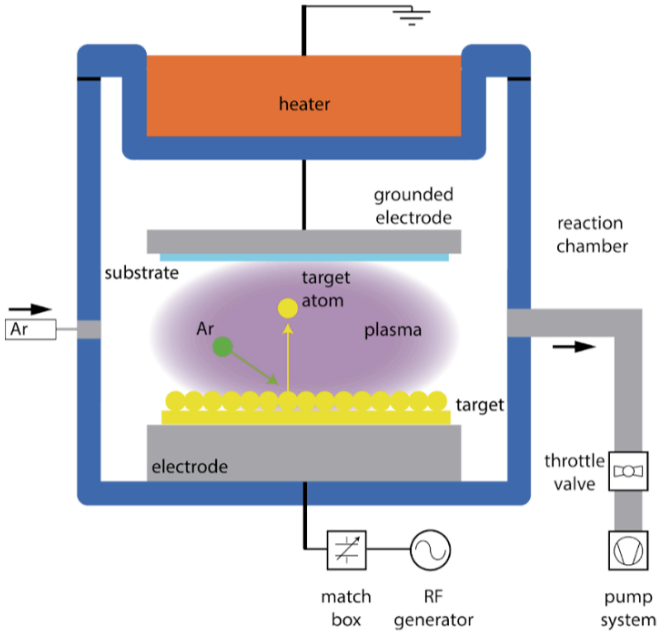

Figure 3.12: A traditional magnetron sputtering system. Adapted from [108].

.

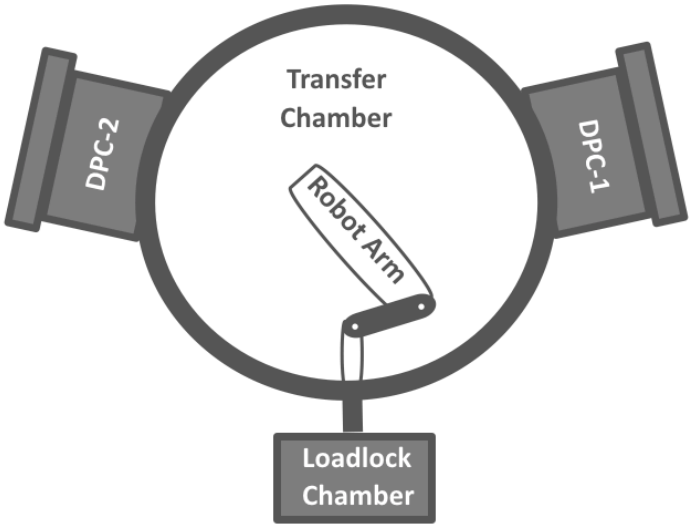

Figure 3.13: Top view of RF-PVD sputtering tool (Zorro) developed by PVMD group depicting two deposition chambers connected with pumps for vacuum transfer and TCO deposition.

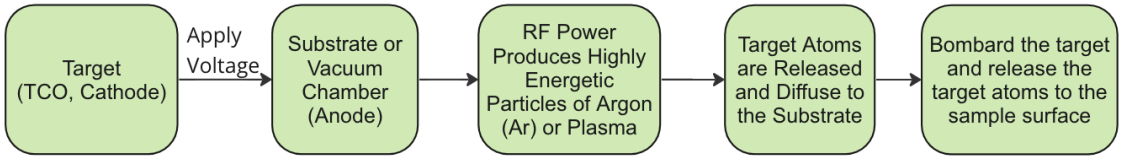

Figure 3.14: Flowchart of RF-PVD deposition process.

3.4.5. Screen printing

Screen printing is used in this project for the deposition of metal contacts. This is an important factor when it comes to the performance of the fabricated solar cells [22]. In screen printing, a squeegee is used to sweep a liquid, viscous, polymer-based metallic paste (for this project, silver, Ag from DuPontTM) across the surface of a screen. At low temperatures, contact formation is possible with this paste.
The squeegee is made of a thin-wire mesh that is interlaced with specific openings for grid patterning (busbars). The paste is then printed on the substrate (with deposited thin film layers) after passing through the opening (mask) of the screen. Following that the SHJ solar cell is heated in an oven at 170°C for 30 minutes after screen printing to enable the development of the metal connections. In ref. [97], the mechanism is described in more depth. Fig. 3.15 depicts a traditional schematic representation of the screen printing system.

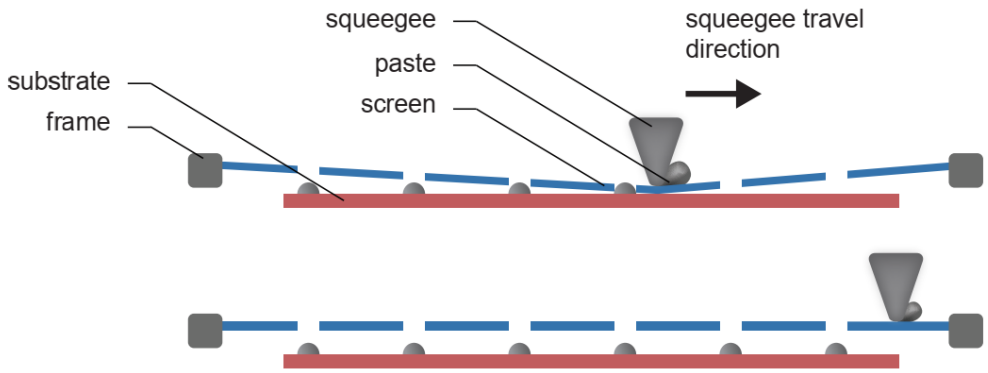

Figure 3.15: A traditional screen printing system (The top part represents the process and the bottom part denotes the end). Adapted from [147].

3.5. Characterization of Single Junction SHJ Solar Cells

The characterization of single-junction SHJ solar cells could be described in two steps. Using a lifetime tester, the minority carrier lifetime was evaluated following RF-PECVD of intrinsic and doped layers and a complete SHJ solar cell characterization process was done as follows:

- Prior to and following TCO sputtering, the Sinton WCT-120 photoconductance lifetime tester was used to assess the lifetime of the minor carrier density.
- The solar simulator from the ESP lab, a AAA class Wacom WXS-90S-L2, was used to test the J-V properties of the solar cells.
- An EQE measurement device manufactured in-house was used to determine the EQE of a single junction SHJ solar cell. A Suns-Voc-150 (Sinton) illumination-voltage meter was used to measure SunsVoc.
- A UV-Vis-NIR spectroscopy was used to determine the reflectance loss of the solar cells.

In this chapter's sections 3.4.1 to 3.4.5, the operational concepts for solar cell measurements are fully presented.

3.5.1. Photoconductance Lifetime Tester

Passivation quality of solar cell layers, effective charge carrier lifetime (τ_{eff}), implied open circuit voltage (i-V_{OC}) and reverse biased saturation current (J_0) are characterized using the photoconductance lifetime tester.

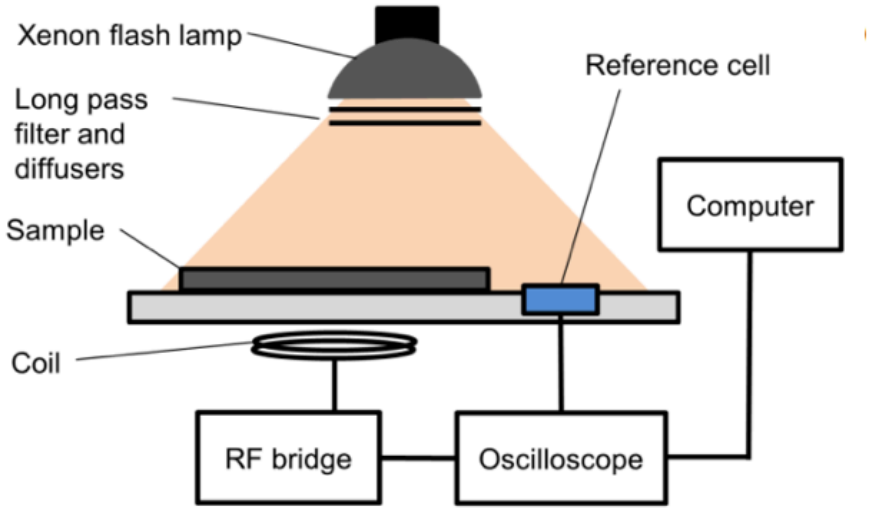

Figure 3.16: Depiction of photoconductance lifetime tester. Adapted from [148].

Sinton WCT-120 photoconductance lifetime tester is used in this work (depicted in figure 3.16). The test sample is placed on a stage at uniform and constant temperature. A light intensity detector (a photodiode) is also present on top of that stage and below the stage near the wafer, a coil is integrated in an inductive fashion to the RF bridge. The samples are illuminated by using a flash lamp from above with preset measurement setting the time period. This illumination generates photoconductance in the sample and introduces additional charge carriers and hence increased conductance. The coil measures this conductivity and τ_{eff}, i-V_{OC} and J_0 are estimated using the optical models [149].

$$\sigma_L = q\Delta p(\mu_n + \mu_p) \tag{3.6}$$

Equation 3.1 represents the photoconductivity (σ_L) in *n*-type semiconductors due to additional minority carriers/holes where q is electron charge, Δp is excess carrier density, μ_n and μ_p are electron and hole mobility. This enables us to calculate the excess charge density (Δp). There are couple of modes that can be used for this measurement: 1. quasi-steady-state-photoconductance (QSSPC) mode 2. transient photoconductance decay (Transient PCD) mode. The mode can be adjusted by the decay time constant of the light source (flash lamp) and a short time constant is set for QSSPC mode (for samples with minority charge carrier lifetime τ_{eff} < 200μs) and long time constant is set for PCD mode (for samples with minority charge carrier lifetime τ_{eff} > 200μs). Equation 3.2 represents τ_{eff} where $G(t)$ is the generation rate calculated from photodiode. For QSSPC mode, $\frac{\partial \Delta p}{\partial t}$ is negligible as $G(t) >> \frac{\partial \Delta p}{\partial t}$ as illumination change rate is very slow. For PCD mode, $G(t)$ is approximated to 0 as light is used only to excite carriers and is off during the measurement.

$$\tau_{eff} = \frac{\Delta p}{G(t) - \frac{\partial \Delta p}{\partial t}} \tag{3.7}$$

τ_{eff} (measured as a function of minority carrier density) value is measured at $10^{15} cm^{-3}$ minority carrier density as this is the recommended value for measuring surface recombination [139]. This value is similar to the injection level under one sun condition. Shockley-Read Hall (SRH) recombination along with detects can occur below this value and Auger and radiative recombination is observed above this, depicted by figure 3.17 [83].

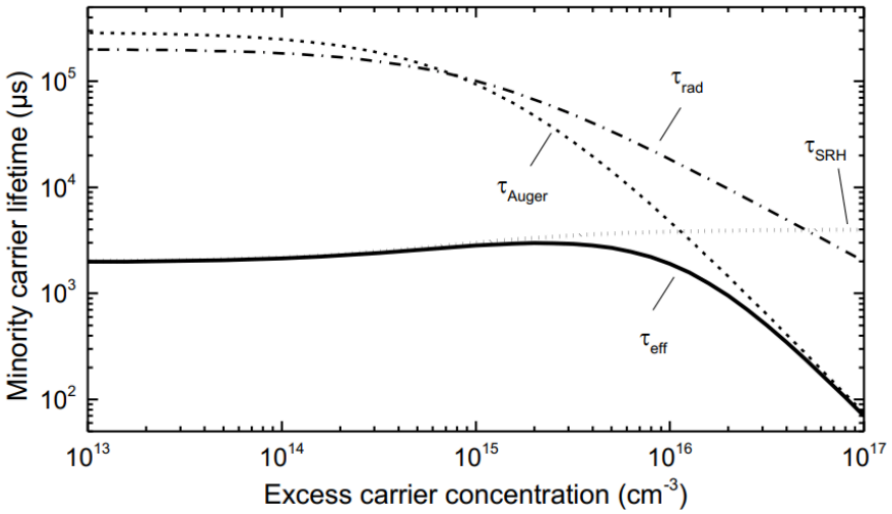

Figure 3.17: Minority carrier density (MCD) as a function of concentration for different recombination mechanisms. Adapted from [84].

Equation 3.8 represents the calculation of i-V_{OC} based on MCD, where N_D is the concentration of donors. Passivation qualities of the intrinsic *(i)*a-Si:H layers and damages occurred while SHJ fabrication (ITO sputtering) process are measured using lifetime measurement in this work.

$$iV_{OC} = \frac{K_B T}{q} \ln\left(\frac{\Delta p(N_D + \Delta p)}{n_i^2}\right) \tag{3.8}$$

3.5.2. Spectroscopic Ellipsometry

Figure 3.18 shows a traditional setup of Spectroscopic Ellipsometry (SE) which is used for measuring changes in light polarization by reflection or transmission when light interacts with sample in test and provides with useful data (e.g. sample layer thickness, optical constants) [150]. Polarized light (passing unpolarized light through polarizer) hits the sample and then this elliptically polarized light is analysed by the polarization analyzer. The setup measures amplitude ratio (φ) and phase difference (Δ) between p- and s- polarized waves and then optical constants and layer thickness is calculated by fitting collected data using optical models. Physical parameters are obtained by using Code-Lorentz for a-Si:H layers from this calibrated data [99]. A structural overview for physical properties characterization through SE measurements is depicted in figure 3.23.

Layer thickness measurement was done using this technique for deposition rate verification and uniformity in layers by J.A. Woollam Co., M-2000DI in this work. Only the front flat surface of the SHJ is checked by this technique, due to the rear side is a rough surface, SE cannot be used for checking film thickness on a textured surface (size of a few μm).

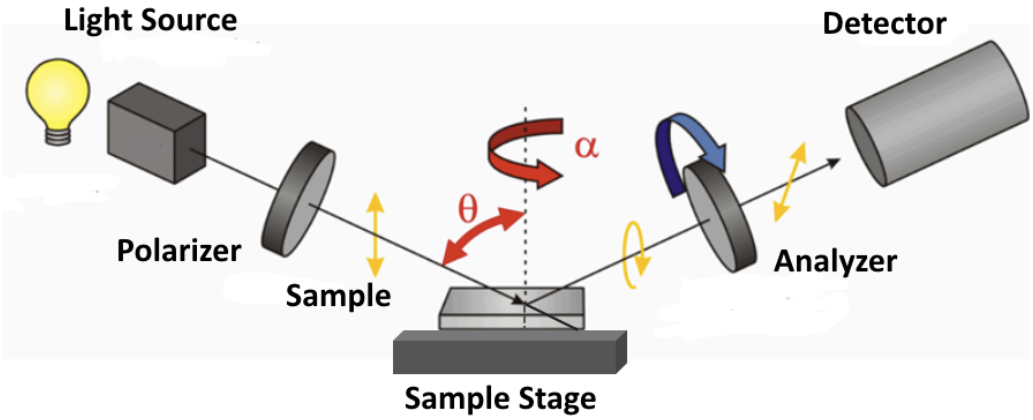

Figure 3.18: Spectroscopic Ellipsometry setup with the light source, polarizer, polarization analyzer, and detector. Adapted form [151].

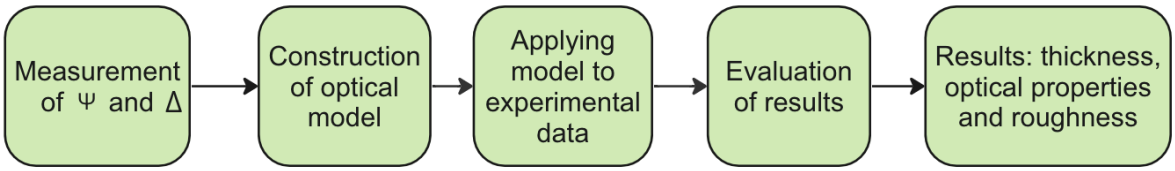

Figure 3.19: Steps for characterizing physical properties with SE measurements.

3.5.3. J-V Measurements

Wacom WXS- 90S-L2 solar simulator (AAA class) is used for J-V measurement in this project with traditional parameters (1000 W/m^2 irradiance, AM 1.5 spectrum and 25 °C solar cell temperature). Two reference solar cells are used for calibration and a halogen and a xenon lamp were used for the simulation of the AM 1.5 spectrum. The V_{OC} equation is represented in 3.9. and J_{ph} is similar to short circuit current density when the cell is in short circuit mode (presented in equation 3.10).

$$V_{OC} = \frac{k_B T}{q} ln(\frac{J_{ph}}{J_0} + 1) \tag{3.9}$$

$$J_{SC} \approx J_{ph} \tag{3.10}$$

Figure 3.20 shows the current-voltage characteristic (J-V curve) from the measurement. Key parameters (V_{OC}, J_{SC}, FF, and η) from the solar cell characterization are presented in the equations below. This provides guidance on resistances and influences the fill factor. The slope on the J_{SC} side is an illustration of shunt resistance (R_{SH}). In this work, no shunt resistance-related issue occurred in the cell due to high R_{SH} which confirms the higher FF of the devices Higher levels of the series resistance (R_S) limit the FF of the devices in comparison to the (R_{SH}), which is shown by the slope at the V_{OC} side. The fill factor and efficiency of the device are determined using equations 3.11 and 3.12.

$$FF = \frac{J_{mpp} V_{mpp}}{J_{SC} V_{OC}} \tag{3.11}$$

$$\eta = \frac{J_{SC} V_{OC} FF}{P_{in}} \tag{3.12}$$

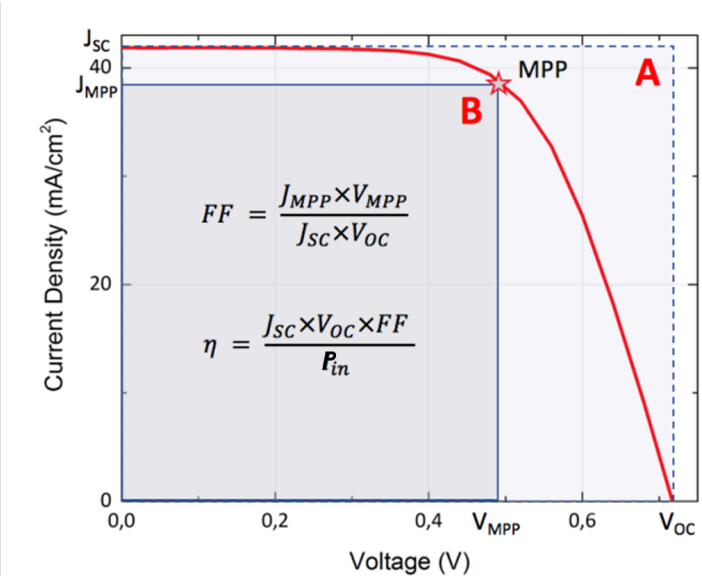

Figure 3.20: A typical J-V curve with the required equations regarding solar cell efficiency and fill factor. Adapted from [84].

3.5.4. EQE

External quantum efficiency (EQE) is the fraction of electron-hole pairs photogenerated in the absorber layer over total photons incidents on the cell defined by the equation 3.8 below where $I_{ph}(\lambda)$ is photogenerated current and $\Psi_{ph,\lambda}$ is spectral photon incident on the cell. EQE provides insight into optical and electrical losses for the fabricated solar cell and as this is a fraction, the value ranges from 0 to 1.

$$EQE(\lambda) = \frac{I_{ph}(\lambda)}{q\Psi_{ph,\lambda}} \tag{3.13}$$

A Xenon lamp as a light source, a calibrated photodiode, and a current meter were used to build the EQE measurement setup. Monochromators were used to convert the light source input to narrow wavelength bands of photons of monochromatic light rays as EQE measurement requires this. The light was also kept as stable as possible for consistent Ψ_x on the reference and test sample (solar cell). A photodiode with known EQE (known $EQE^{r}ef(\lambda)$) is used for the calculation of $\Psi_{ph,\lambda}$ using equation 3.9. EQE measurement is done of the sample post calibration and $EQE(\lambda)$ is measured and using equation 3.10, $J_{SC,EQE}$ is calculated. For calculating $\phi_{ph,\lambda}^{AM1.5}$, equation 3.11 used where h is Planck constant, c is speed of light and $P_{ph,\lambda}^{AM1.5}$ is power density.

$$\Psi_{ph,\lambda} = \frac{I_{ph}^{ref}(\lambda)}{qEQE^{ref}\lambda} \tag{3.14}$$

$$J_{SC} = -q\int_{\lambda 1}^{\lambda 2} EQE(\lambda)\phi_{ph,\lambda}^{AM1.5}d\lambda \tag{3.15}$$

$$\phi_{ph,\lambda}^{AM1.5} = \frac{P_{ph,\lambda}^{AM1.5}\lambda}{hc} \tag{3.16}$$

The wavelength of 300 to 1200 nm is used for EQE measurement of the fabricated SHJ solar cell in this work as below 300 nm wavelength, the power density of AM1.5 is negligible, and above 1200 nm is not absorbed in c-Si. Internal Quantum Efficiency (IQE) is measured using the reflectance (R) from EQE measurement and by UV-Vis-NIR spectroscopy (described in the next

section). Equation 3.12 defines IQE, where $R(\lambda)$ is the reflectance at a wavelength and $1 - R(\lambda)$ is effective absorbance.

$$IQE(\lambda) = \frac{EQE(\lambda)}{1 - R(\lambda)} \tag{3.17}$$

3.5.5. UV-Vis-NIR Spectroscopy

Analysis of the optical properties (e.g. absorptions, transmissions, and reflections) of sample materials in ultraviolet, visible, and near-infrared regions of the spectrum was done by Ultraviolet-Visible-Near-Infrared spectroscopy (UV-Vis-NIR) characterization technique. Reflectance (R) of the fabricated solar cells was measured through a LAMBDA 1050+ UV-Vis-NIR spectrophotometer (PerkinElmer) (figure 3.21) in this work, which gives insight into photons lost in reflection. In this process, the input light (light of two different types of wavelengths: tungsten lamp / visible-NIR range and deuterium D2 light / UV light) is filtered by a monochromator to convert into a monochromatic light before illuminating the samples. This output light from the monochromator illuminates a reference and the test sample. The position of the sample determines the type of optical property to be measured.

- Absorbance can be measured by placing the sample inside the cavity (integrating sphere with inner walls made of highly reflective material (e.g. barium sulfate ($BaSO_4$).
- Transmittance can also be measured by placing the sample on the front side of the integrating sphere (figure 3.21). The equation can also be used to determine the transmittance where the Spectral Absorbance (A) + Reflectance (R) + Transmittance (T) = 1.
- Reflectance is measured by placing the sample on the rear side of the integrating sphere (figure 3.21).

All wavelengths of 300 nm to 1200 nm are scanned for measuring reflectance for this work.

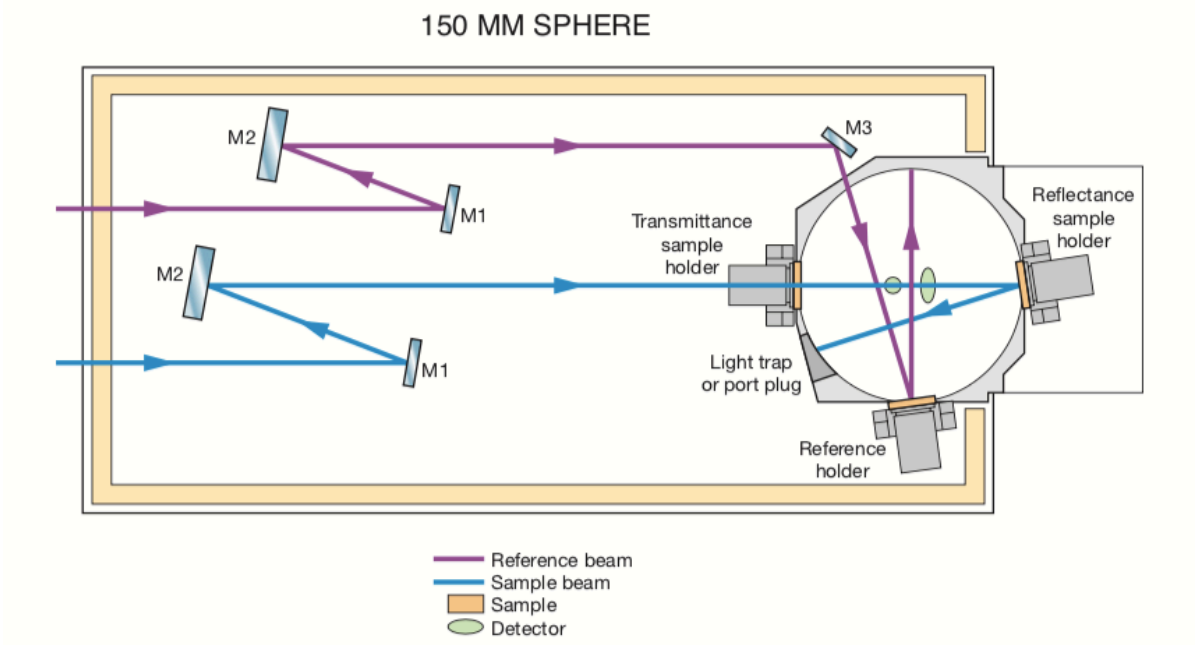

Figure 3.21: Optical design of a UV-Vis-NIR spectrometer with a 150 mm integrating sphere test sample position for transmittance or reflectance measurement. Adapted from [152]

3.5.6. SunsVoc

The Suns-Voc-150 (Sinton) illumination-voltage tester measures the SunsVoc of the SHJ solar cells, after metallization, employing input from Wacom's short circuit current (J_{SC}) measurement

results. Voltage is measured using the slow decay flash lamp with a pseudo-I-V curve and series resistance (R_S) does not affect the obtained I-V curve. This process gives an estimation of the upper limit of open circuit voltage (V_{OC}), pseudo fill factor (pFF). The V_{OC} further can be measured from Wacom and the pFF can be compared to J-V measurement's FF to gain insight into losses resulting from the R_S by using Eq. 3.18 [153]. The maximum power point (MPP) of the solar cell is indicated in Eq. 3.18 by the subscript 'mpp'. The solar cells or PV modules must be working at MPP in order for PV systems to operate as efficiently as possible.

$$R_{S,SunsVoc} = (pFF - FF)\frac{V_{OC}J_{SC}}{J_{mpp}^2} \tag{3.18}$$

3.5.7. SEM

Scanning electron microscopy is widely used in research work due to its large depth of field and high resolution providing an optimized magnification compared to traditional optical microscopes [154]. This is possible as this machine uses an electromagnet instead of a lens. The electron beam is used to scan the sample for image generation (figure 3.22). Upon hitting the sample, these electrons generate secondary, back-scattered electrons and characteristic X-rays, and then the detector collects these particles, and Fig. 3.23 represents the workflow of the machine.

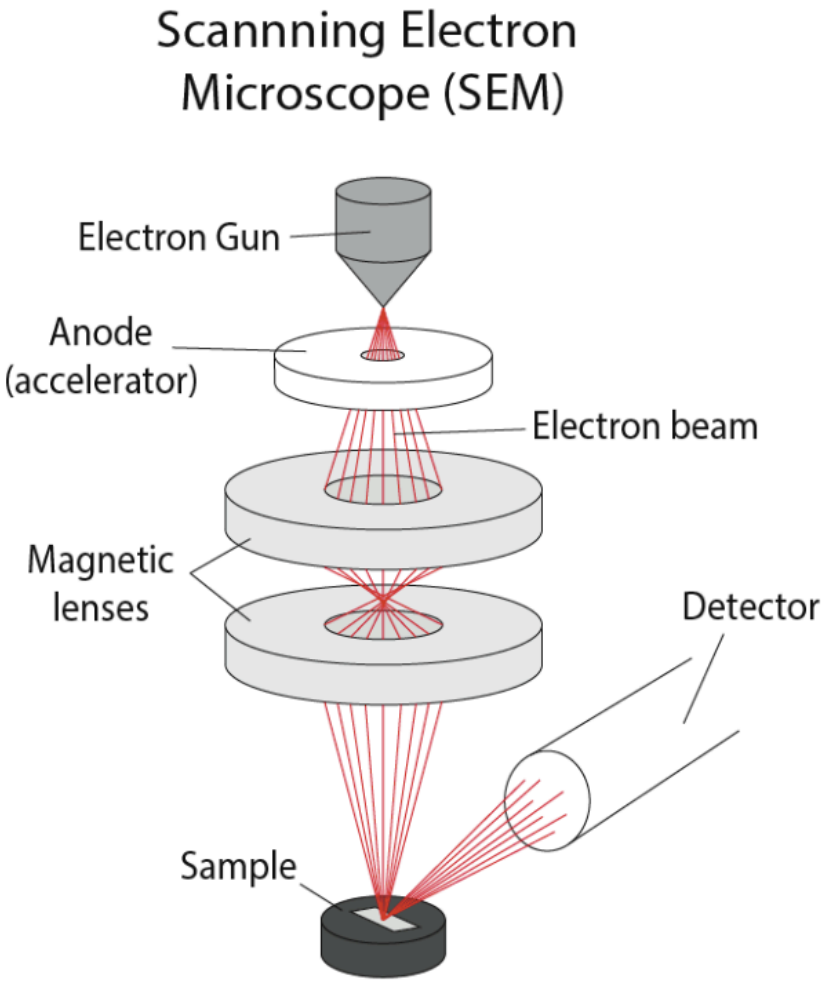

Figure 3.22: Electron beam interacting with a sample to generate secondary electrons and x-rays. Adapted from [155].

Hitachi Regulus 8230 in EKL100 was used in this project. The optimized sample's cross-section

was examined using this machine by observing the micro-structure of the doped layers underneath the ITO layer. Also, layer thickness was compared with the expected thickness from the prepared recipes. It is quite challenging to distinguish the difference between (*i*)a-Si:H and the other thin film layers.

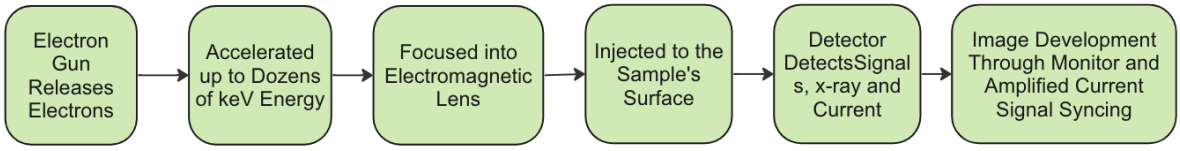

Figure 3.23: Flowchart of typical SEM measurement.

The possible methods for obtaining a clear image include : (i) placing photoresist on top of the sample before cutting it (if BHF does not attack Ag, photoresist need not be on top)→(ii) cutting the sample→(iii) wet etching in, for instance, BHF 1:7 for about a minute→(iv) rinsing in water, and→(v) SEM inspection. The purpose is to create topography contrast so that the interfaces between the different materials are better visible. In SEM topography contrast is more easy to detect than material contrast.

4

Optical Simulation

This chapter examines a variety of optical simulations of the 2T Perovskite/c-Si tandem solar cells. Based on a fabricated 2T tandem solar cell ([86]), the optical simulation model was built with the refractive indices of composing layers and absorbers as inputs. Figure 4.1 illustrates the device layout of a monolithic two-terminal, single-side-textured reference cell with the absorption curve where the ITO layer functioned as a recombination junction layer (RJ) and the resultant photocurrent density $J_{imp,tandem}$ is 18.30 mA/cm^2.

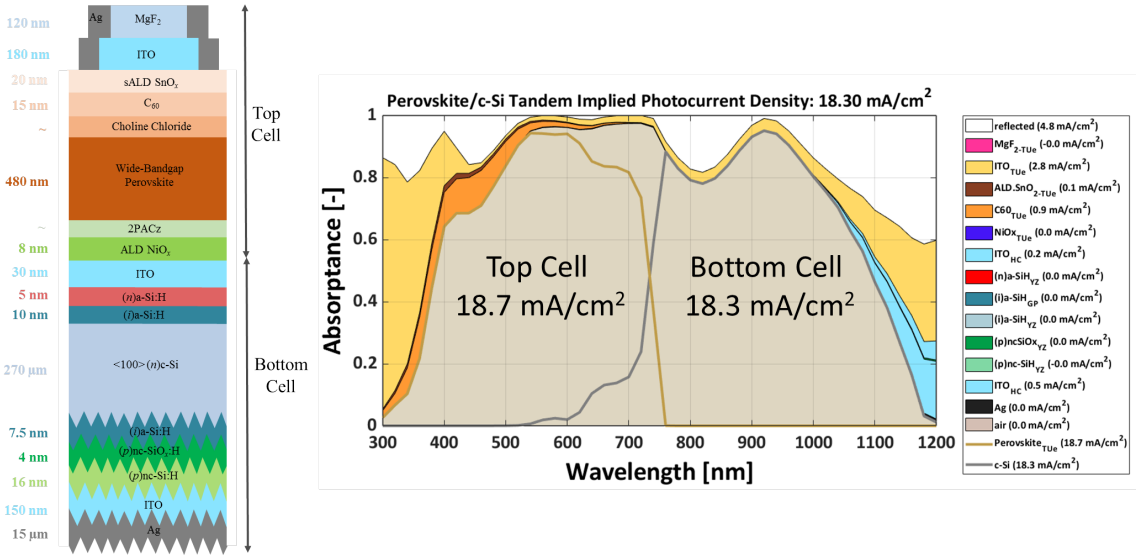

Figure 4.1: Device architecture: Single-side-textured 2T Perovskite/c-Si tandem cell with RJ and rear ITO (reference device) [156].

Simulations are performed by utilizing different RJ topologies and the TCO layers of the bottom device. The idea was to use distinct doped Si-based layers to replace the intermediate ITO layer, which is used as a recombination junction layer, in order to reduce the optical loss in the junction of the two different cells.

4.1. Previously Optimized Tandem and Some Intro.

The 2T Perovskite/c-Si tandem solar cell produced by the partner institutions of TUDelft and TU/e emerged as the inspiration for this work ([86]). From this initial experiment, thickness variables

and optical constants were considered for designing a two-terminal tandem device that used ITO as the back TCO layer and the recombination junction layer. General facts on the software GenPro4 can be found in Chapter 3 section 3.1. The project's optimized top two layers for optimizing the anti-reflection effect, specifically, the MgF_2 and top-ITO layer were optimized to be 120 nm and 180 nm, respectively, shown in Fig.4.1. The current limiter, however, was the bottom cell which requires further improvement to enhance the performance of tandem solar cells. In this project, we intend to examine a number of potential recombination junction (RJ) layers to replace ITO to possibly tune the reflectance that originates from the intermediate interfaces between the perovskite top cell and the c-Si bottom cell, thus allowing more light to be transmitted into the bottom cell. Several layers were used for composing the RJs, namely, ITO, AZO, IWO, doped nc-SiO_x:H, and doped nc-Si:H.
The goal was to employ several standard TCO layers and particular doped layers as a recombination junction after adjusting the thickness of each layer in order to maximize the implied photocurrent density of the SHJ bottom cell. Typically, for a given thickness ITO and IWO has better conductivity compared to AZO. IWO offers higher transparency. However AZO has advantages over ITO, including lower cost, greater abundance, high thermal stability, layer flexibility, and lack of toxicity. While ITO and IWO contain indium, which is expensive, AZO is composed of aluminum and zinc, two common and inexpensive materials. Considering all possible advantages, all of these materials were used to optically analyze the performance in the 2T tandem devices as RJ and rear TCO (back reflector).

4.1.1. Layers of 2T Tandem Device: Brief Intro.

(i). Layers of the Top-Cell

– **MgF_2:** Anti-reflective coating (ARC) frequently reduces reflection loss when making solar cells. Less reflection occurs at the surface when the optical thickness of the dielectric material is optimized. The predicted refractive index (n) of ARC, in an ideal situation, should be equal to the square root of the index of the adjacent materials. MgF_2, which has a relatively low index at visible wavelengths (1.38 for 300 to 1200 nm wavelength range), is the most often used as an ARC due to its proper refractive index matching between the solar cell and the air.

  Configurations to optically optimize MgF_2 thickness in the range of 0 to 200 nm :

  ◊ **Cell1: ITO (30 nm)/*(n)*a-Si:H (5 nm)**/*(i)*a-Si:H/ c-Si/*(i)*a-Si:H/*(p)*nc-SiO_x/*(p)*nc-Si:H/ITO.
  ◊ **Cell2: IWO (30 nm)/*(n)*a-Si:H (5 nm)**/*(i)*a-Si:H/ c-Si/*(i)*a-Si:H/*(p)*nc-SiO_x/*(p)*nc-Si:H/ITO.
  ◊ **Cell3: ITO (30 nm)/*(n)*nc-Si:H (20 nm)**/*(i)*a-Si:H/ c-Si/*(i)*a-Si:H/*(p)*nc-SiO_x/*(p)*nc-Si:H/ITO.
  ◊ **Cell4: ITO (30 nm)/*(n)*nc-SiO_x:H (40 nm)**/*(i)*a-Si:H/ c-Si/*(i)*a-Si:H/*(p)*nc-SiO_x/*(p)*nc-Si:H/ITO.

Table 4.1: Optimizing MgF_2 Thickness from different cell configurations:

Cell	$J_{imp,tandem}$ (mA/cm^2)	MgF_2 (nm)	$J_{imp,tandem}$ (mA/cm^2)	MgF_2 (nm)
Cell1	17.76	0-200	18.55	120
Cell2	17.72	0-200	18.75	120
Cell3	17.75	0-200	18.55	120
Cell4	17.66	0-200	18.56	120

To optimize the thickness simulation loop was run (0-200 nm range). We present in Fig.4.2 the simulated implied photocurrent density (J_{imp}) 18.55 mA/cm^2 of the tandem solar cells with Cell3 configuration with the optimized MgF_2 thickness (120 nm).

– **Front-ITO:** The initial 180 nm thickness of front-ITO layer was optically re-optimized for optimized 2T tandem devices. It is good to know that the electrons gathered in the top ETL (C60) can travel to the metal electrode thanks to the lateral conductivity of the top ITO.

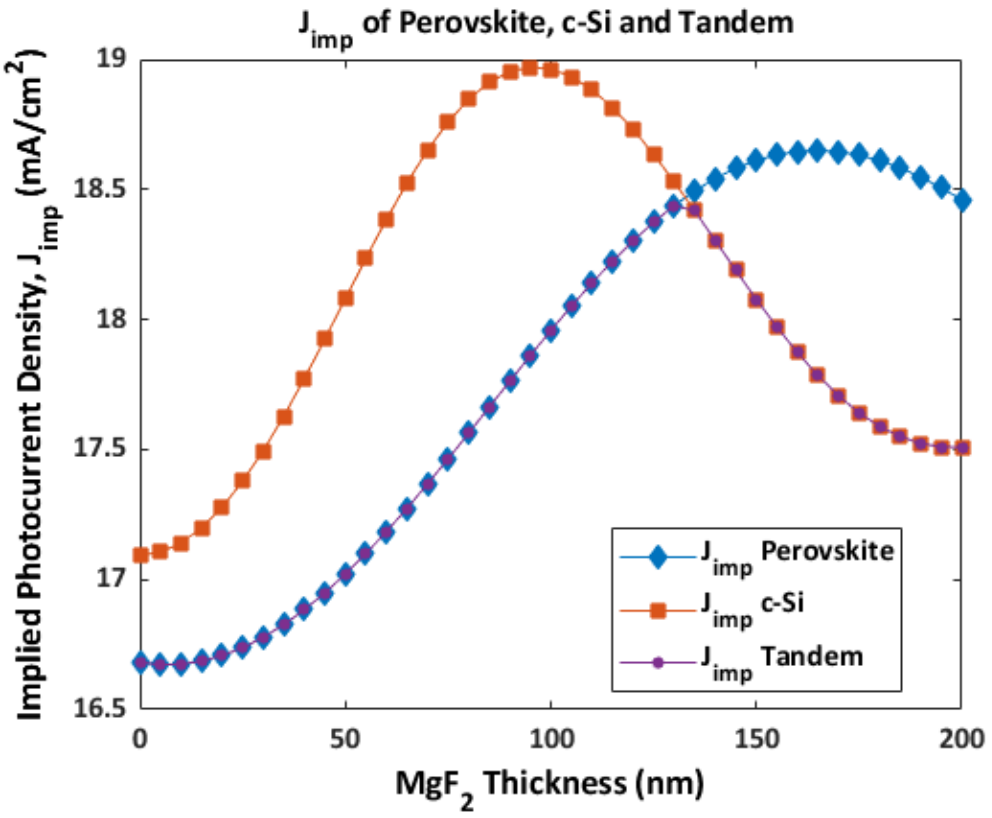

Figure 4.2: Optimizing the thickness of MgF_2.

- **sALD SnO_x:** The sALD SnOx layer's thickness (20 nm) was optimized by TUE, it effectively acts as a buffer layer to shield against the damage caused by ITO sputtering.
- **C60:** 10 nm C60 layer works as the top cell's ETL [86].
- **Choline Chloride:** Choline Chloride modified perovskite films and reduced charge carrier recombination to increase the quality of SnOx ETL and encourage the extraction of interface charges [157]. Despite the fact that there is no thickness assumed.
- **Perovskite:** The thickness of the perovskite was tuned at 480 nm. In the wide bandgap top cell, this serves as the primary absorber.
- **2PACz:** A better power conversion efficiency is provided by a [2-(9H-Carbazol-9-yl)ethyl]Phosphonic Acid (2PACz) anode, (HTL of the top cell). For optical simulation, the thickness is assumed to be zero.
- **ALD NiO_x:** Without Nickel oxidic (NiO_x) layer (8 nm), 2PACz layer (HTL) may experience sputtering damage which could lead to low shunt resistance for the top cell. By increasing lateral resistance in the interface, an undoped NiO_x exhibits superior tandem device performance [158].

(ii). Layers of the Bottom Cell

- **RJ-ITO:** As a recombination layer in a multi-junction solar cell, Indium Tin oxidic (ITO) is employed because of its higher transparency and proper band alignment with adjacent cells. It promotes high PCE of Perovskite/c-Si tandem devices by decreasing the junction damage to an n-type c-Si solar cell with a front-side tunnel oxidic passivating electron contact. For 2T tandem cells and single-junction SHJ solar cells, ITO thickness was 30 nm and 75 nm, respectively [132]. In this work, AZO and IWO are also used as RJ layers.
- ***(n)*a-Si:H:** As electron transport layers (ETL), n-type amorphous silicon thin films are employed in SHJ solar cells. The optimal thickness is 5 nm [86].

- ***(n)*nc-Si:H:** Improvements in optoelectrical properties are the main need for recombination layers. Introducing doped silicon layers to recombination junctions as tunnel junctions are recommended in this work. The optical simulation was used to find the ideal thickness of the RJ layer for the 2T tandem device.
- ***(p)*nc-Si:H:** The *(p)*nc-Si:H is added on top of *(n)*nc-Si:H or *(p)*nc-SiO_x:H/*(n)*nc-Si:H forming the RJ to replace TCO [46]. The optimal thickness of RJ layers was optically tuned.
- ***(n)*nc-SiO_x:H:** As reported in the literature, *(n)*nc-SiO_x:H with proper refractive index and thickness can effectively transmit light into the bottom cell [46]. The optical simulation was performed to determine the optimal layer thickness for a RJ.
- ***(p)*nc-SiO_x:H :** The *(p)*nc-SiO_x:H is added on top of *(n)*nc-SiO_x:H or *(p)*nc-Si:H/*(n)*nc-SiO_x:H forming the RJ to replace TCO.
- ***(i)*a-Si:H** A very thin layer of intrinsic amorphous silicon can be employed to passivate surface dangling bonds. The ideal thickness is between 6 and 10 nm, which has good passivation [84]. For better performance, two 5 nm intrinsic amorphous silicon layers with HPT were employed [86].
- **c-Si:** In the optical simulation, c-Si wafers with single- and double-sided textures and thicknesses of 270 and 260 µm respectively, were used.
- **Rear-ITO:** The optimal thickness of rear-ITO is 150 nm ([132]).
- **Rear electrode (Ag):** The silver coating's thickness was determined as 15 µm.

For a better understanding of the optical property match, a plot with wavelength-dependent refractive indexes (n) and the extinction coefficients(k) of the above materials can be seen in the appendix (fig. 1).

4.2. Single-side-textured 2T Tandem Solar Cells

Single-side-textured Perovskite/c-Si 2T tandem devices using doped thin film Si layers and standard TCO layers as RJ. Two measures were taken in order to optically optimize the 2T devices as shown in 4.3. (i). initially, only tuning the RJ while keeping the same TCO on the rear and all other layers of the tandem device, and (ii). then, the entire monolithic tandem device was optimized to achieve the maximum matched implied tandem current density. Section 4.2.1 discusses the effect of various TCO layers used as RJ and at the rear side of the tandem devices, section 4.2.1 discusses the effect of various TCO-free doped nc-Si:H layers used as RJ, section 4.2.3 discusses the effects while inserting an oxidic or non-oxidic layer in *(p)*nc-Si:H/*(n)*nc-Si:H or *(p)*nc-SiO_x:H/*(n)*nc-SiO_x:H layer stacks as RJ and 4.2.4 summarises the outcomes of the 2T Tandem with conventional and proposed RJ layers.

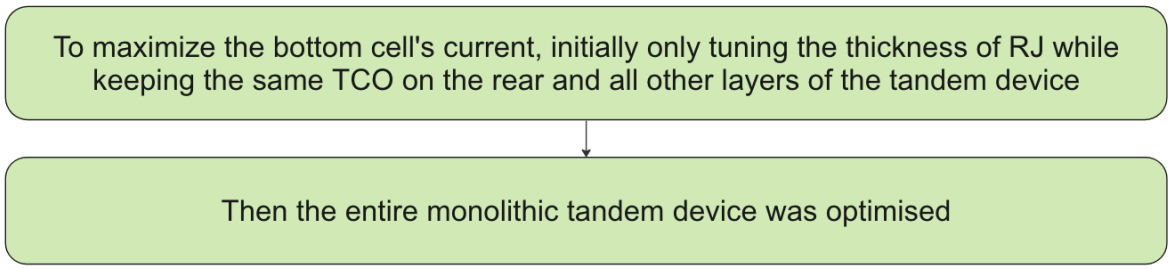

Figure 4.3: Flowchart of 2-Steps measures towards optimizing 2T tandem devices.

4.2.1. Optimizing Various Combinations RJ and Rear-TCO Layers

In this study, apart from using ITO at the RJ and rear side of the device, two other varieties of TCO (IWO, AZO) were used to determine which TCO layer optically performs better for the various tandem devices. All nine possible combinations with different TCO arrangements are roughly listed here :

1. RJ ITO (30/15 nm) with Rear ITO (150 nm)
2. RJ ITO (30/22 nm) with Rear IWO (150 nm)
3. RJ ITO (30/15 nm) with Rear AZO (150 nm)
4. RJ IWO (30/20 nm) with Rear ITO (150 nm)
5. RJ IWO (30/35 nm) with Rear IWO (150 nm)
6. RJ IWO (30/20 nm) with Rear AZO (150 nm)
7. RJ AZO (30/20 nm) with Rear ITO (150 nm)
8. RJ AZO (30/25 nm) with Rear IWO (150 nm)
9. RJ AZO (30/15 nm) with Rear AZO (150 nm)

The simulation results of the IWO_IWO (30/150 nm) configuration in Fig.4.4, which shows each layer's absorptance as a function of wavelength. The light brown area of the absorbance curve reflects the photon absorption of the two main absorbers, Perovskite for the top cell and c-Si for the bottom cell, with corresponding implied photocurrent densities of 18.7 mA/cm^2 and 18.8 mA/cm^2 respectively. From the reference device of Fig.4.1 it is clear that the bottom cell limits the current flow while replacing the ITO layers (both RJ-ITO and rear-ITO) with more transparent IWO layers to allow more current in the bottom cell. With the initial thickness of 30/150 nm for the IWO/Rear-TCO, the simulation loop was applied in the range of 0-180 nm (for RJ-IWO) and 0-190 nm (for rear-IWO) thickness to optimize the possible optimum thickness from the contour plots as in Fig. 4.5. With the optimized RJ thickness, the bottom device results in 18.80 mA/cm^2 J_{imp} with 4.7 mA/cm^2 and 4.1 mA/cm^2 of reflection and parasitic loss respectively. In comparison with the reference device Fig. 4.1, these optical losses were 4.8 mA/cm^2 and 4.5 mA/cm^2 respectively, which results in 0.40 mA/cm^2 increment of current flow. Finally, the RJ thickness was optimized (35 nm) while keeping all other parameters unchanged, which results J_{imp} of 18.70 mA/cm^2 as shown in Fig.4.4.

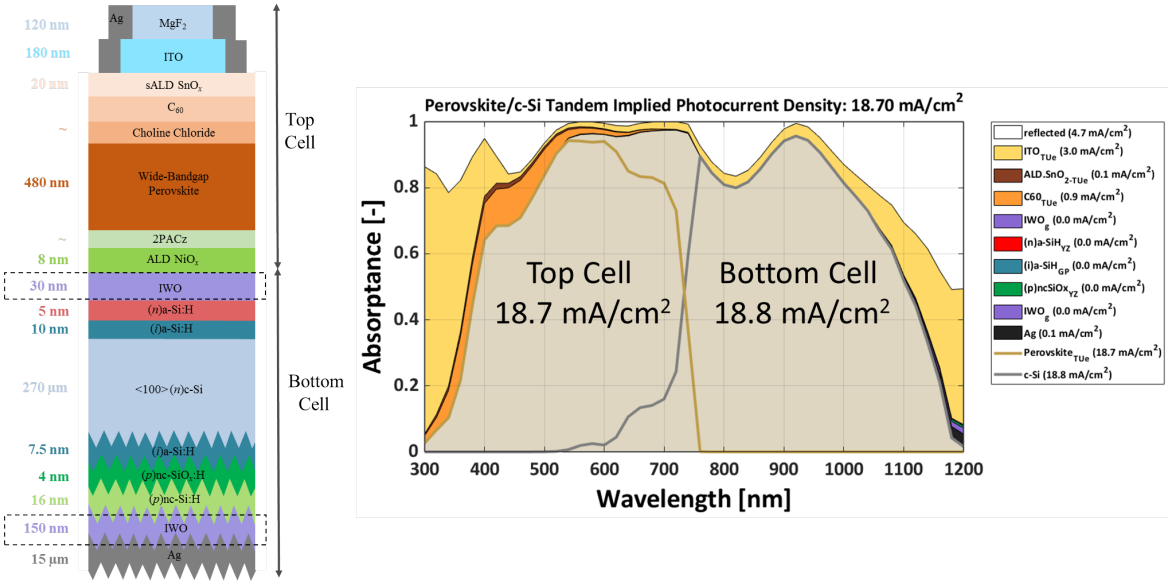

Figure 4.4: Device architecture: Single-side-textured 2T Perovskite/c-Si tandem cell with RJ and rear IWO (optimized with TCO-RJ) [156].

Other than the targeted photon energy absorption by the two main absorbers of the tandem device, certain reflection losses are indicated in the white area, and additional major parasitic absorption losses for all remaining 16 layers are also represented in different colors in the graph. The main optical limits of the cell were thus determined. The cell has four primary optically potential weaknesses, as shown in Fig.4.4 of the 2T tandem devices with IWO_IWO configuration:

- The front (350-500 nm) and in the interface of Perovskite/c-Si tandem (700-900 nm) wavelength range are two causes of the increased reflectance losses (4.7 mA/cm^2, white area).
- The front-ITO has significant parasitic absorption is (3.0 mA/cm^2, yellow area).
- A significant parasitic absorption in the C60 layer (0.9 mA/cm^2, orange area).
- The front ETL sALD SnOx and rear electrode (Ag) show 0.1 mA/cm^2 parasitic loss (in the dark brown and black area).

A similar pattern was followed to optimize all of the previously mentioned nine configurations and the outcomes are mentioned in 4.2. As an ETL or RJ layer as well as a back-reflector (rear-TCO), devices with IWO optically perform better than AZO and ITO, which results in the SHJ bottom cell no more the current limiter in the 2T tandem devices. For further research, this finding was taken into consideration while optimizing single-side-textured 2T devices with proposed RJ layers and also for the optically optimized complete 2T tandem devices with various configurations.

Table 4.2: Optical outcomes of 2T Perovskite/c-Si tandem with TCO-RJ: Single-side-textured devices.

RJ	Thickness (nm)	Rear TCO	Thickness (nm)	Implied Photocurrent Density				
				Tandem Current J_{Tandem} (mA/cm^2)	Perov. Top cell J_{Perov} (mA/cm^2)	SHJ Bot cell J_{c-Si} (mA/cm^2)	Refl. Loss J_{Refl} (mA/cm^2)	Parasitic Loss $J_{parasitic}$ (mA/cm^2)
ITO (Ref)	30	ITO (Ref)	150	18.30	18.7	18.3	4.8	4.5
ITO	15	ITO	150	18.65	18.6	18.8	4.4	4.7
ITO	22	IWO	150	18.69	18.7	18.8	4.7	4.2
ITO	15	AZO	150	18.65	18.6	18.7	4.6	4.7
IWO	20	ITO	150	18.66	18.7	18.8	4.4	4.4
IWO	30	IWO	150	18.70	18.7	18.8	4.7	4.1
IWO	20	AZO	150	18.66	18.7	18.7	4.4	4.6
AZO	25	AZO	150	18.67	18.7	18.7	4.4	4.6
AZO	25	IWO	150	18.70	18.7	18.7	4.7	4.2
AZO	15	AZO	150	18.65	18.6	18.7	4.3	4.7

4.3. Intro. of Various Combinations of TCO-free RJ in the 2T Tandem Devices

1. nc-SiO$_x$:H layers as RJ with Various Rear-TCO Layers (see in section 4.3.1)
2. nc-Si:H layers as RJ with Various Rear-TCO Layers (see in section 4.3.2)
3. nc-Si:H/nc-SiO$_x$:H layers as RJ with Various Rear-TCO Layers (see in section 4.3.3)
4. nc-SiO$_x$:H/nc-Si:H layers as RJ with Various Rear-TCO Layers (see in section 4.3.3)

4.3.1. Optimizing Doped nc-SiO$_x$:H Layers as RJ with Various Rear-TCO

In order to decrease reflection loss at interfaces between two sub-cells of the single-side-textured tandem devices, *(p)*nc-SiO$_x$:H/*(n)*nc-SiO$_x$:H is used to replace the *(n)*a-Si:H/ITO in the tandem device (see Figure 4.6). In the simulation, the thicknesses of both doped nc-SiO$_x$:H layers were varied aiming at minimizing the intermediate reflection losses, thus maximizing the light coupling into the bottom cell. Apart from only using ITO at the rear side of the device, two other variations of TCO (IWO, AZO) were used in the device's bottom part to compare performance. To form a RJ at the junction of two devices, the ITO layer from the recombination junction is replaced by *(p)*nc-nc-SiO$_x$:H or *(p)*nc-Si:H layer, and the *(n)*a-Si:H layer is replaced by *(n)*nc-SiO$_x$ or *(n)*nc-Si:H layer, as shown in Fig. 4.6 and 4.8. The simulated thickness range for the *(p)*nc-SiO$_x$ and *(p)*nc-Si:H layer was 0 to 180 nm and for the *(n)*nc-SiO$_x$ and *(n)*nc-Si:H layer was 0 to 190 nm.

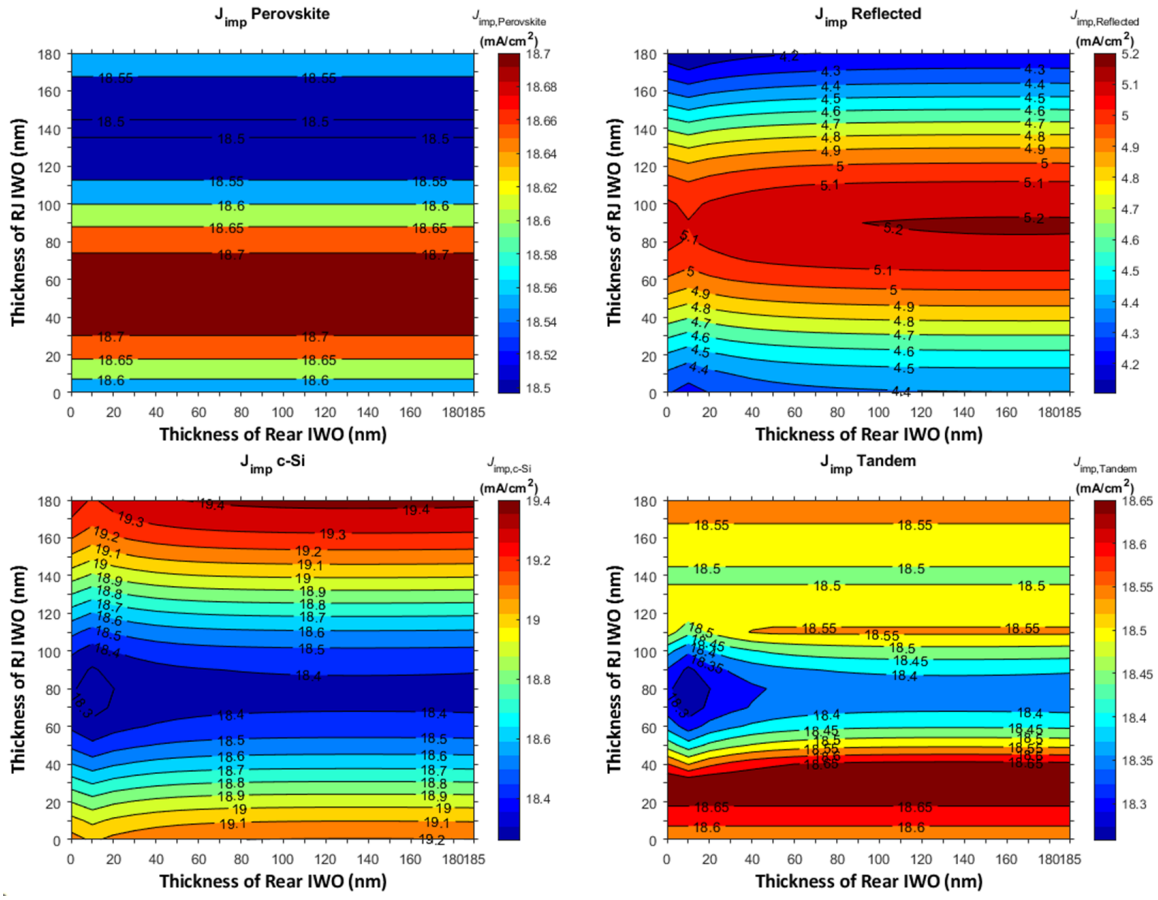

Figure 4.5: Contour plots: Single-side-textured 2T Perovskite/c-Si tandem with IWO_IWO configuration.

With doped oxidic layers in the recombination junction, several TCO layers were employed in the back side including:

(i) (*p*/*n*)nc-SiO_x:H varied from (0-180 nm)/(0-190 nm) with Rear-ITO (150 nm)
(ii) (*p*/*n*)nc-SiO_x:H varied from (0-180 nm)/(0-190 nm) with Rear-IWO (150 nm)
(iii) (*p*/*n*)nc-SiO_x:H varied from (0-180 nm)/(0-190 nm) with Rear-AZO (150 nm)

Initially, the simulation was with 30 nm thickness of the (*p*/*n*)nc-SiO_x:H layers while keeping all other parameters constant. For the optimal thickness of (*p*/*n*)nc-SiO_x:H layers, the contour plots were made (see in Fig. 4.7) to identify the best thickness range. Among all of the above-mentioned combinations, (*p*/*n*)nc-SiO_x:H of (30/30 nm) with rear-IWO of 150 nm, see in Fig. 4.6, shows better performance with 0.15 mA/cm^2 boost up of resultant tandem implied photocurrent density ($J_{imp,tandem}$) from the reference cell (see Fig.4.1) with 18.45 mA/cm^2.

The bottom device is no longer the current limiter although the 2T tandem device still experiences some reflection loss and parasitic absorption loss, for instance, compared with the reference ITO_ITO configuration:

– There are larger reflection losses (3.3 mA/cm^2, white area) in the front (350–550 nm) and the Perovskite/c–Si tandem interface (780–940 nm) wavelength ranges. This loss is reduced by 1.5 mA/cm^2.
– The front ITO layer's major parasitic absorption is higher (2.9 mA/cm^2, yellow region).
– The loss in the C60 layer (0.9 mA/cm^2, orange area) remains the same.

– SnO_x layer's parasitic absorption loss is now 0.1 to 0.4 mA/cm^2, clay area) and Rear electrode shows 0.1 mA/cm^2 parasitic loss (black ara).

Although with the optimized thickness of the RJ layers (30/30 nm) the overall tandem current increased (18.45 mA/cm^2) and the bottom device is no longer the current limiter (20.3 mA/cm^2), still the top cell and bottom cell experience unmatched current generation for the less current generation in the top-cell (18.5 mA/cm^2). A similar approach was followed for the rest of the mentioned combinations and the results are listed below in 4.3.

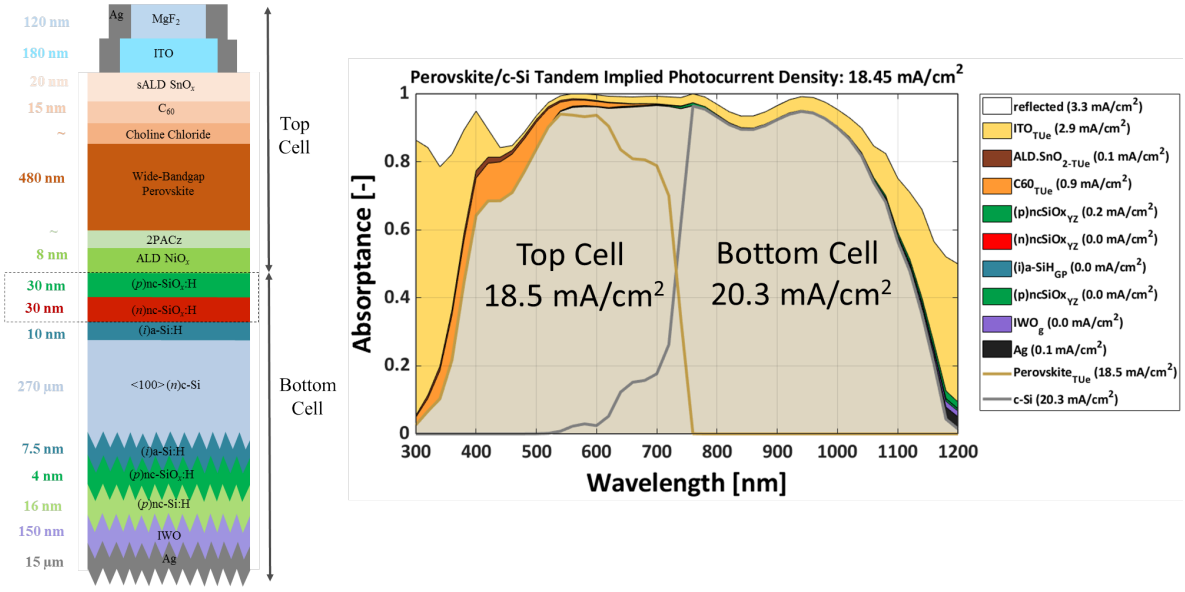

Figure 4.6: Device architecture: Single-side-textured 2T Perovskite/c-Si tandem cell with *(p/n)*nc-SiO_x:H as RJ and rear IWO (TCO-free optimized RJ with oxidic layers) [156].

Table 4.3: Optical outcomes of 2T Perovskite/c-Si tandem with TCO-free Oxidic layers as RJ : Single-side-textured devices.

RJ	Thickness (nm)	Rear TCO	Thickness (nm)	Implied Photocurrent Density: Tandem Current J_{Tandem} (mA/cm^2)	Perov. Top cell J_{Perov} (mA/cm^2)	SHJ Bot cell J_{c-Si} (mA/cm^2)	Refl. Loss J_{Refl} (mA/cm^2)	Parasitic Loss $J_{parasitic}$ (mA/cm^2)
(*p*)/(*n*)nc-SiO_x:H	30/30	ITO	150	18.45	18.5	20.1	3.2	4.6
(*p*)/(*n*)nc-SiO_x:H	30/30	IWO	150	18.45	18.5	20.3	3.3	4.2
(*p*)/(*n*)nc-SiO_x:H	30/20	AZO	150	18.45	18.56	20.0	3.1	4.8

In conclusion, the bottom cell's optical performance significantly improves when doped oxidic layers are used as the tandem's RJ in place of ITO at the recombination junction. Because of the optimized interference effect at interfaces between the two absorbers, the bottom absorber could absorb more light, which led to a significant decrease in front reflection loss, especially the reflection losses from the intermediate interfaces. Taking that as inspiration, research was done to improve the tandem current while keeping the other layers constant (apart from RJs), and the resultant $J_{imp,tandem}$ is 18.66 mA/cm^2 with a 58/70 nm thickness of *(p)*nc-SiO_x:H/*(n)*nc-SiO_x:H combination where the $J_{imp,tandem}$ = 18.90 mA/cm^2(see in the appendix 2).

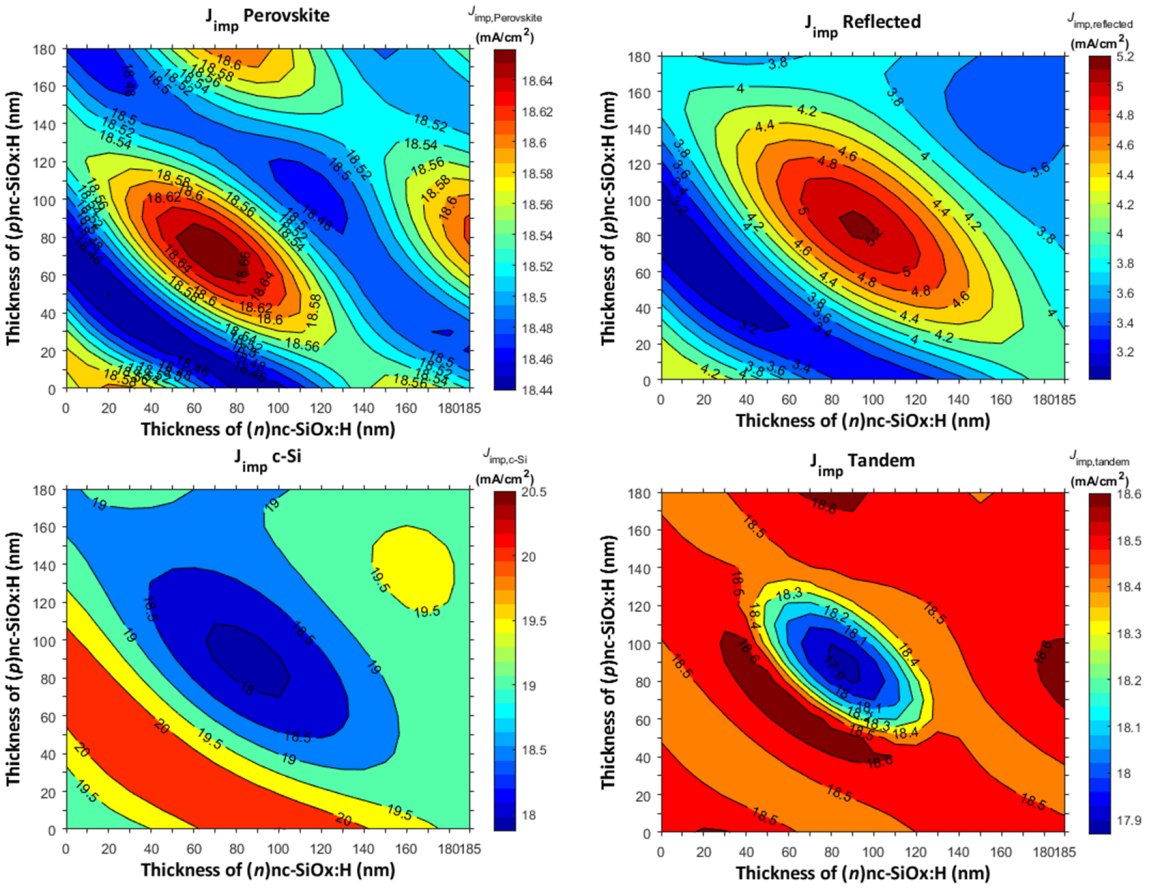

Figure 4.7: Contour plots: Single-side-textured 2T Perovskite/c-Si tandem with *(p/n)*nc-SiO_x:H_IWO configuration.

4.3.2. Optimizing Doped nc-Si:H Layers as RJ with Various Rear-TCO

The same pattern was continued in section 4.3.1. The sole difference is that doped non-oxidic layers, rather than doped oxidic layers, were used as RJ (highlighted in the enclosed black rectangle). The goal was to compare the performance of the devices with doped oxidic RJ. In order to compare performance, the device's bottom component was constructed using all three types of TCO (ITO, IWO, and AZO). The simulated thickness range of (*p*/*n*)nc-Si:H layers was followed by (0-190 nm)/(0-180 nm) respectively. With doped non-oxidic layers in the recombination junction, several TCO layers were employed in the back side including:

(i) (*p*/*n*)nc-Si:H varied from (0-180 nm)/(0-190 nm) with Rear-ITO (150 nm)

(ii) (*p*/*n*)nc-Si:H varied from (0-180 nm)/(0-190 nm) with Rear-IWO (150 nm)

(iii) (*p*/*n*)nc-Si:H varied from (0-180 nm)/(0-190 nm) with Rear-AZO (150 nm)

In comparison to the ITO_ITO configuration, all three mentioned combinations showed better performance. Overall implied tandem photocurrent density ($J_{imp,tandem}$) was boosted up from 18.30 mA/cm^2 to 18.50 mA/cm^2 with all proposed configurations and none of the cells are current limiter (see in Fig. 4.8) Especially the device with the rear IWO shows less parasitic loss (4.3 mA/cm^2) than the other combinations. A brief overview of all of the outcomes can be seen in table 4.4.

The bottom device is not the current limiter with this new pattern of RJ configuration, although the 2T tandem device still experiences some reflection loss and parasitic absorption loss, for instance, compared with the reference ITO_ITO configuration:

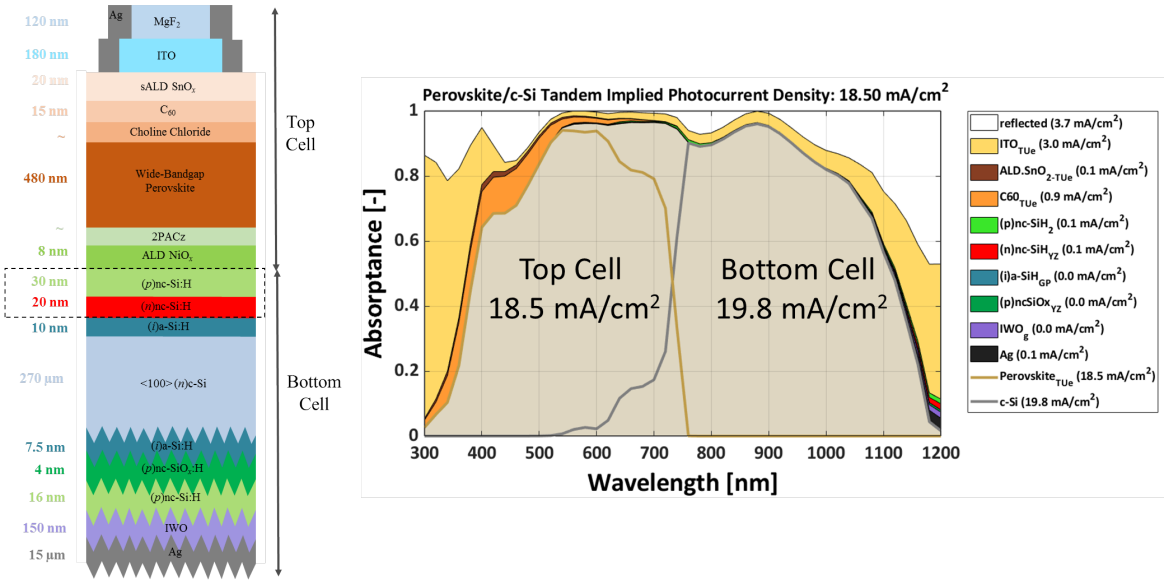

Figure 4.8: Device architecture: Single-side-textured 2T Perovskite/c-Si tandem cell with *(p/n)*nc-Si:H as RJ and rear IWO (TCO-free optimized RJ with non-oxidic layers) [156].

- There are larger reflection losses (4.3 mA/cm^2, white area) in the front (350–550 nm) and the Perovskite/c–Si tandem interface (780–940 nm) wavelength ranges. This loss is reduced by 0.5 mA/cm^2.
- The front ITO layer's major parasitic absorption is higher (3.0 mA/cm^2, yellow region).
- The loss in the C60 layer (0.9 mA/cm^2, orange area) remains the same.
- SnO_x layer's parasitic absorption loss is 0.1 mA/cm^2, (clay area) and Rear electrode shows 0.1 mA/cm^2 parasitic loss (black area).

Although with the optimized thickness of the RJ layers (30/30 nm) the overall tandem current increased (18.50 mA/cm^2) and the bottom device is no longer the current limiter (19.8 mA/cm^2), still the top cell and bottom cell experience unmatched current generation for the less current generation in the top-cell (18.5 mA/cm^2). A similar approach was followed for the rest of the mentioned combinations and the results are listed below in 4.3.

Table 4.4: Optical outcomes of 2T Perovskite/c-Si tandem with TCO-free non-oxidic layers as RJ: Single-side-textured devices.

RJ	Thickness (nm)	Rear TCO	Thickness (nm)	Implied Photocurrent Density: Tandem Current J_{Tandem} (mA/cm^2)	Perov. Top cell J_{Perov} (mA/cm^2)	SHJ Bot cell J_{c-Si} (mA/cm^2)	Refl. Loss J_{Refl} (mA/cm^2)	Parasitic Loss $J_{parasitic}$ (mA/cm^2)
(*p*)/(*n*)nc-Si:H	30/20	ITO	150	18.50	18.5	19.7	3.5	4.7
(*p*)/(*n*)nc-Si:H	30/20	IWO	150	18.50	18.5	19.8	3.7	4.3
(*p*)/(*n*)nc-Si:H	30/20	AZO	150	18.50	18.5	19.6	3.5	4.8

Overall the bottom cell's optical performance significantly improves when doped non-oxidic Si layers are used as the tandem's RJ in place of ITO at the recombination junction. Although the matching refractive index of the non-oxidic Si materials with the c-Si (offers higher conductivity

for their low bandgap (Eg) and activation energy (Ea) than the oxidic Si layers) has a significant effect at interfaces between the two absorbers leads to an improved implied photocurrent density $J_{imp,tandem}$ from the reference ITO_ITO configuration, in some cases, the overall current generation in less than the conventional RJ-TCO layers and the oxidic Si RJ layers.

4.3.3. Optimization of Doped nc-Si:H/nc-SiO$_x$:H RJ Layers with Various Rear TCOs

Getting inspired by the prior research, by R. Santbergen et. al, the concept of introducing **'inter-layer'** in a multijunction device is applied here [159]. Moreover, it is shown in prior research that the bilayer *p*-contact with the combination of low activation energy (E_a) and wide energy bandgap (E_g) materials are crucial for the effective hole collection in SHJ solar cells. However, considering the thickness-dependent (E_a) it is important to optimize the newly inserted layer's thickness for a better collection of holes in the SHJ solar cells [15]. In addition, comparing the optical outcomes of the previous two sections (4.3.1, 4.3.2) it is also clear that (*p*)nc-SiO$_x$:H materials, for their wide E_g and transparency, can offer an effective RJ.

From an electrical perspective, this combination leads towards reduced contact resistivity which can result in higher V_{oc} and FF of the solar cell [15, 73]. In the mentioned prior research, to increase the device's FF the low Ea material (*p*)nc-Si:H) can play a crucial role in contact with the ITO. To design the device with TCO-free RJ, the positions were tuned to investigate the lowest possible optical losses. Considering the previously optimized thickness of (*p*)nc-SiO$_x$:H of 4 nm [15], inserting a thinner (*p*)nc-SiO$_x$:H or (*p*)nc-Si:H, while keeping the other two layer unchanged, to establish an effective bi-layer *p*-contact was aimed to this work. This is because of comparing the outcomes with and without bilayer *p*-contact in the application of RJ of the proposed TCO-free 2T tandem devices. Although the inserted layer's thickness was optically optimized for the 2T device.

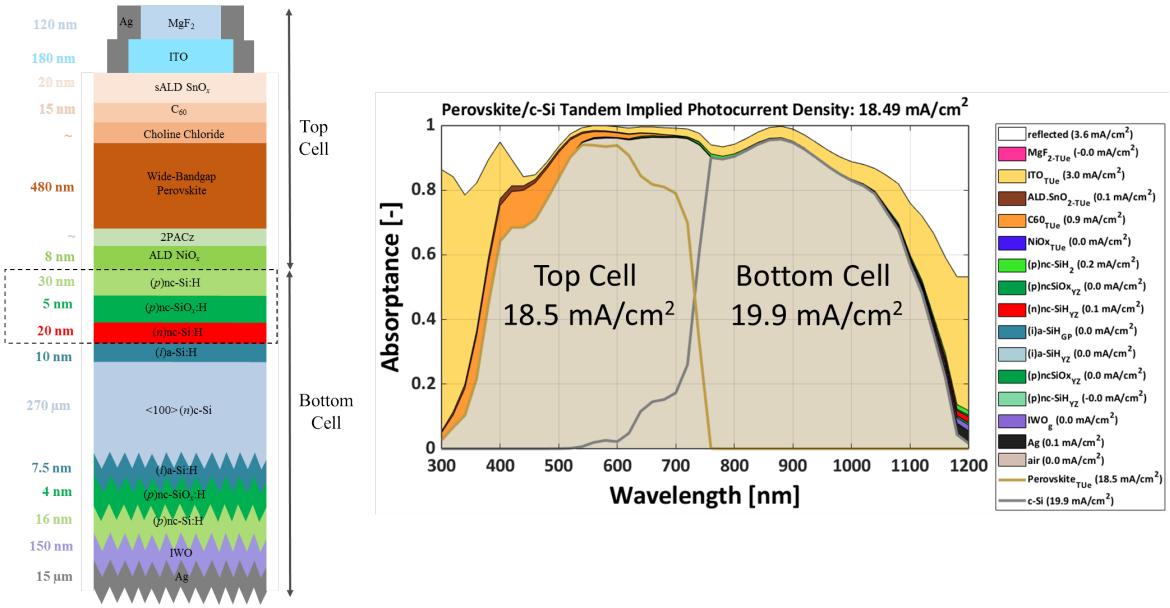

Figure 4.9: Device architecture: Single-side-textured 2T Perovskite/c-Si tandem cell with *(p/n)*nc-SiO$_x$:H as RJ and rear IWO (TCO-free optimized RJ with nc-Si:H/ nc-SiO$_x$:H) [156].

The overall optimization process leads in two different ways, where firstly a (*p*)nc-SiO$_x$:H was inserted in between two nc-Si:H layers as :

(i) (*p*/*n*)nc-Si:H with an Inserted (*p*)nc-SiO$_x$:H (5-50 nm) with Rear-ITO (150 nm)

(ii) (*p*/*n*)nc-Si:H with an Inserted (*p*)nc-SiO$_x$:H (5-50 nm) with Rear-IWO (150 nm)

(iii) (*p*/*n*)nc-Si:H with an Inserted (*p*)nc-SiO$_x$:H (5-50 nm) with Rear-AZO (150 nm)

To optically optimize these combinations, with an initial 5 nm thin (*p*)nc-SiO$_x$:H was inserted in on the top of (*n*)nc-Si:H layer to for a bi-layer *p*-contact. Following that, the simulated thickness was optimized for an effective RJ. The device with (*p*)nc-Si:H/(*p*)nc-SiO$_x$:H/(*n*)nc-Si:H_IWO configuration, implied photocurrent density ($J_{imp,tandem}$) is 18.49 mA/cm^2, shown in Fig. 4.9, where the SHJ bottom device shows $J_{imp,c-Si}$ = 19.90 mA/cm^2. The reflection loss was effectively reduced until 0.5 mA/cm^2 with the parasitic loss in the range of (4.8-4.4 mA/cm^2) observed in all mentioned combinations. A brief summary can be seen from the table 4.5.

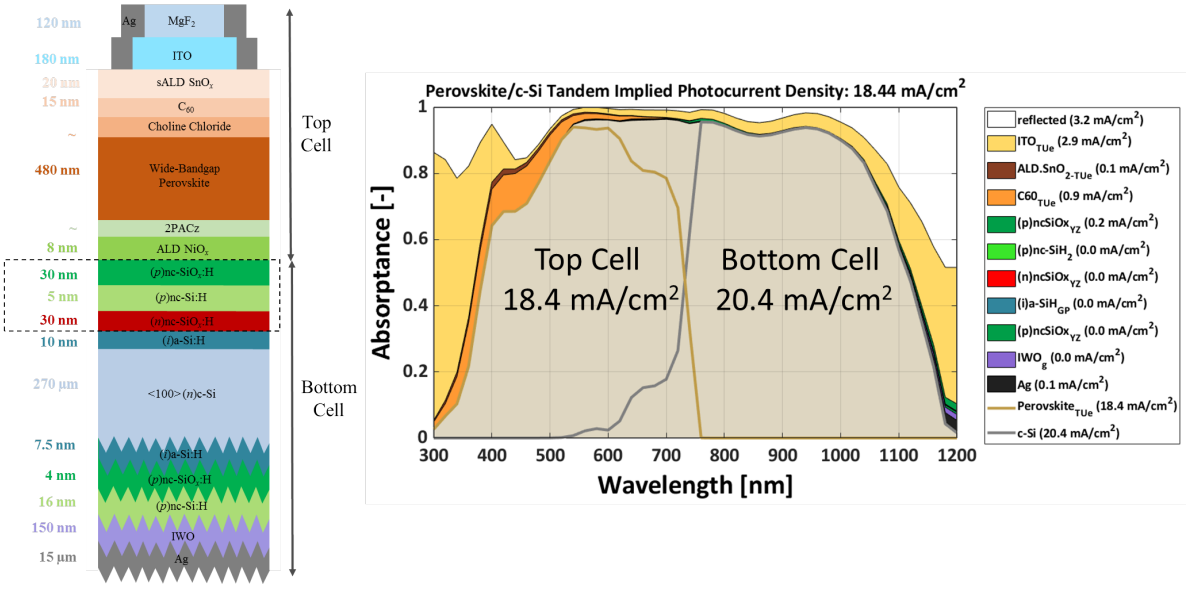

Figure 4.10: Device architecture: Single-side-textured 2T Perovskite/c-Si tandem cell with *(p/n)*nc-SiO$_x$:H as RJ and rear IWO (TCO-free optimized RJ with nc-SiO$_x$:H/nc-Si:H) [156].

Table 4.5: Optical outcomes of 2T Perovskite/c-Si tandem with TCO-free Non-oxidic/Oxidic layers as RJ: Single-side-textured devices.

RJ	Thickness (nm)	Rear TCO	Thickness (nm)	Implied Photocurrent Density: Tandem Current J_{Tandem} (mA/cm^2)	Perov. Top cell J_{Perov} (mA/cm^2)	SHJ Bot cell J_{c-Si} (mA/cm^2)	Refl. Loss J_{Refl} (mA/cm^2)	Parasitic Loss $J_{parasitic}$ (mA/cm^2)
(*p*)/(*n*)nc-Si:H w/ (*p*)nc-SiO$_x$:H	30/5/20	ITO	150	18.49	18.5	19.8	3.4	4.7
(*p*)/(*n*)nc-Si:H w/ (*p*)nc-SiO$_x$:H	30/5/20	IWO	150	18.49	18.5	19.9	3.5	4.4
(*p*)/(*n*)nc-Si:H w/ (*p*)nc-SiO$_x$:H	30/5/20	AZO	150	18.49	18.5	19.7	3.3	4.8
(*p*)/(*n*)nc-SiO$_x$:H w/ (*p*)nc-Si:H	30/5/30	ITO	150	18.44	18.4	20.2	3.0	4.6
(*p*)/(*n*)nc-SiO$_x$:H w/ (*p*)nc-Si:H	30/5/30	IWO	150	18.44	18.4	20.4	3.2	4.2
(*p*)/(*n*)nc-SiO$_x$:H w/ (*p*)nc-Si:H	30/5/30	AZO	150	18.44	18.4	20.0	3.0	4.8

Subsequently a (*p*)nc-Si:H was inserted in between two nc-SiO$_x$:H layers as :

(i) (*p*/*n*)nc-SiO$_x$:H with an Inserted (*p*)nc-Si:H (5-40 nm) with Rear-ITO (150 nm)

(ii) (*p*/*n*)nc-SiO$_x$:H with an Inserted (*p*)nc-Si:H (5-40 nm) with Rear-IWO (150 nm)

(iii) (*p*/*n*)nc-SiO$_x$:H with an Inserted (*p*)nc-Si:H (5-40 nm) with Rear-AZO (150 nm)

The same trend was followed to optically optimize the mentioned combinations, with an initial 5 nm thin (*p*)nc-Si:H was inserted in on the top of (*n*)nc-SiO$_x$:H layer for the formation of bi-layer *p*-contact. The simulated thickness was optimized for an effective RJ. The device with (*p*)nc-SiO$_x$:H/

(*p*)nc-Si:H/(*n*)nc-SiO_x:H_IWO implied photocurrent density ($J_{imp,tandem}$) of 18.44 mA/cm^2 can be seen in Fig.4.10, where the SHJ bottom device shows $J_{imp,c-Si}$ = 20.40 mA/cm^2. The reflection loss was effectively reduced in the range of 1.0-1.8 mA/cm^2 and the parasitic loss remains similar for all of the proposed configurations (4.3-4.9 mA/cm^2), compared with ITO_ITO configuration. A brief summary can be seen from the table 4.5.

In summary, comparing the configurations with single *p*-contact, it is suggested to insert bi-layer *p*-contact that offers better optical performance while reducing the reflection loss of around 1.1 mA/cm^2 from the reference ITO_ITO configuration. Moreover, the bottom cell generates more current by absorbing more light in the c-Si absorber with these configurations.

4.3.4. Comparison Among Different RJs and Rear TCOs: Single-side-textured Perovskite/c-Si 2T Tandem Solar Cells

(i). Optical Analysis of Single-side-textured 2T Tandem Devices: (with initial RJ thickness)

Table 4.6: Summarizing optical outcomes of Single-side-textured 2T Perovskite/c-Si tandem (with initial RJ thickness) devices.

RJ	Thickness (nm)	Rear TCO	Thickness (nm)	Implied Photocurrent Density				
				Tandem Current J_{Tandem} (mA/cm^2)	Perov. Top cell J_{Perov} (mA/cm^2)	SHJ Bot cell J_{c-Si} (mA/cm^2)	Refl. Loss J_{Refl} (mA/cm^2)	Parasitic Loss $J_{parasitic}$ (mA/cm^2)
ITO (Ref)	30	ITO (Ref)	150	18.30	18.7	18.3	4.8	4.5
ITO	15	ITO	150	18.65	18.6	18.8	4.4	4.7
ITO	22	IWO	150	18.69	18.7	18.8	4.7	4.2
ITO	15	AZO	150	18.65	18.6	18.7	4.6	4.7
IWO	20	ITO	150	18.66	18.7	18.8	4.4	4.4
IWO	30	IWO	150	18.70	18.7	18.8	4.7	4.1
IWO	20	AZO	150	18.66	18.7	18.7	4.4	4.6
AZO	25	AZO	150	18.67	18.7	18.7	4.4	4.6
AZO	25	IWO	150	18.70	18.7	18.7	4.7	4.2
AZO	15	AZO	150	18.65	18.6	18.7	4.3	4.7
(*p*)/(*n*)nc-SiO_x:H	30/30	ITO	150	18.45	18.5	20.1	3.2	4.6
(*p*)/(*n*)nc-SiO_x:H	30/30	IWO	150	18.45	18.5	20.3	3.3	4.2
(*p*)/(*n*)nc-SiO_x:H	30/20	AZO	150	18.45	18.5	20.0	3.1	4.8
(*p*)/(*n*)nc-Si:H	30/20	ITO	150	18.50	18.5	19.7	3.5	4.7
(*p*)/(*n*)nc-Si:H	30/20	IWO	150	18.50	18.5	19.8	3.7	4.3
(*p*)/(*n*)nc-Si:H	30/20	AZO	150	18.50	18.5	19.6	3.5	4.8
(*p*)/(*n*)nc-Si:H w/ (*p*)nc-SiO_x:H	30/5/20	ITO	150	18.49	18.5	19.8	3.4	4.7
(*p*)/(*n*)nc-Si:H w/ (*p*)nc-SiO_x:H	30/5/20	IWO	150	18.49	18.5	19.9	3.5	4.4
(*p*)/(*n*)nc-Si:H w/ (*p*)nc-SiO_x:H	30/5/20	AZO	150	18.49	18.5	19.7	3.3	4.8
(*p*)/(*n*)nc-SiO_x:H w/ (*p*)nc-Si:H	30/5/30	ITO	150	18.44	18.4	20.2	3.0	4.6
(*p*)/(*n*)nc-SiO_x:H w/ (*p*)nc-Si:H	30/5/30	IWO	150	18.44	18.4	20.4	3.2	4.2
(*p*)/(*n*)nc-SiO_x:H w/ (*p*)nc-Si:H	30/5/30	AZO	150	18.44	18.4	20.0	3.0	4.8

Table 1 shows the overall optical analysis of all previously mentioned proposed configurations of the single-side-textured 2T tandem devices where the initial thickness of RJ was considered as 30 nm. The reason is that it is well established in various research previously and works for all types of discussed materials. With this approach, it was possible to optimize the SHJ bottom cell as no longer the current limit device for the 2T tandem applications. More specifically the proposed devices with TCO-free RJ optically perform better while reducing the interference effect in between the interlayer of the two sub-cells.

(ii). Optical Analysis of Single-side-textured 2T Tandem Devices: (with optimized RJ thickness)

To optimize the simulated RJ Thickness, the simulation loop was applied for a certain thickness range for the proposed layers (mentioned in 4.3.1-4.3.3). With the optical outcome contour plots were created to optically analyze the possible simulated thickness range of the RJ layers. Finally, the optically optimal RJ thickness was established. In all cases SHJ solar call was considered to be not the current limiter and the thickness of the al other layers remained the same. Table 2 shows an overall summary of all of the proposed configurations. It is clearly shown that the proposed devices with TCO-free RJ layers offer similar or in some cases better optical performance for having these materials a matched refractive index value with c-Si.

(iii). Thickness Optimization of Front-ITO and C60 Layer

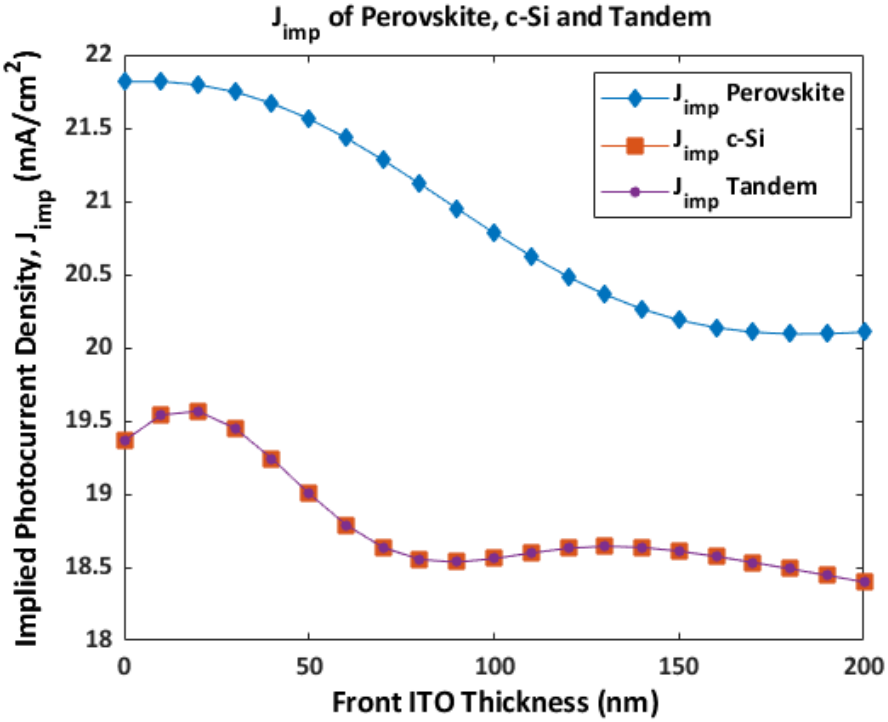

Figure 4.11: Optimizing Front-ITO thickness: Front-ITO vs Implies Photocurrent density.

From the optical analysis, it is clear that the front-iTO and C60 layers offer the maximum parasitic loss in the range of 2.8-3.0 mA/cm^2 and 0.9 mA/cm^2 respectively. We re-evaluated these layers' thickness to reduce the loss to generate more current by allowing more light to pass through to reach the bottom cell. Fig. 4.11 suggests the simulated thickness of front-ITO as 20 nm which is quite non-realistic as this layer should have a thickness in the range of 100-200 nm for ensuring sufficient lateral conductivity. A similar trend was observed while optimizing the simulated optimal thickness of C60 layer which is 1 nm (see in Fig. 4.12). Since the realistic thickness range should be 10-20 nm. Finally, it was decided to apply the lowest minimal thickness in the realistic range for both of these layers.

4.4. Double-side-textured 2T Tandem Solar Cells

As previously discussed in section 4.3, all eighteen different configurations are repeated in this section applying a new pattern '**Double-side-textured**'. To be more specific, the previously used 270 μm thick c-Si absorber now changes with 260 μm thick while initially keeping all thickness parameters unchanged. Later, based on optimal results from contour plots, optimized simulated

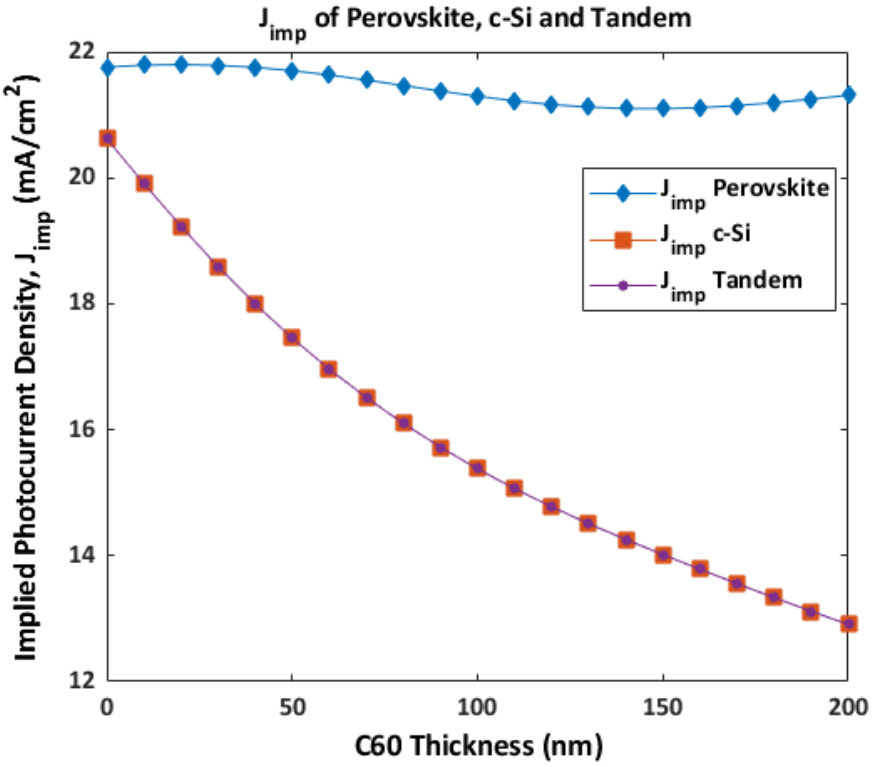

Figure 4.12: Optimizing C60 thickness: C60 vs Implies Photocurrent density.

thickness for RJ was applied to achieve the highest current generation. Following that, in the final stage, the complete devices were fully optically optimized with the current matching between the two sub-cells. From the Fig. 4.13 and 4.14, it is clear that this new pattern of the device allows more light to pass through the thin film layers to reach the bottom cell's active layer that offers higher implied photocurrent density ($J_{imp,tandem}$). Section 4.4.1, the optical analysis of all of the possible configurations using TCO layers (ITO, IWO, and AZO) as RJ and back-reflector are discussed. Section 4.5 is all about TCO-free configurations and their possible arrangements and 4.6 is summarizing the results of all double-side-textured configurations. Here Fig. 4.13 is the reference device with ITO_ITO configuration. Indeed in this case the bottom device is not the current limiter, although all possible alternate options of the ITO layer and the proposed TCO-free RJ layers were introduced to optimize the optical outcomes and compare the losses with single-side-textured devices.

4.4.1. Optimization of Various Recombination Junction and Rear TCOs

Three usual types of TCOs (ITO, IWO, and AZO) were used in nine different layouts as the RJ and the back reflector. The proposed layouts are :

1. RJ ITO (30/60 nm) with Rear ITO (150 nm)
2. RJ ITO (30/65 nm) with Rear IWO (150 nm)
3. RJ ITO (30/55 nm) with Rear AZO (150 nm)
4. RJ IWO (30/75 nm) with Rear ITO (150 nm)
5. RJ IWO (30/78 nm) with Rear IWO (150 nm)
6. RJ IWO (30/75 nm) with Rear AZO (150 nm)
7. RRJ AZO (30/55 nm) with Rear ITO (150 nm)
8. RJ AZO (30/75 nm) with Rear IWO (150 nm)
9. RJ AZO (30/65 nm) with Rear AZO (150 nm)

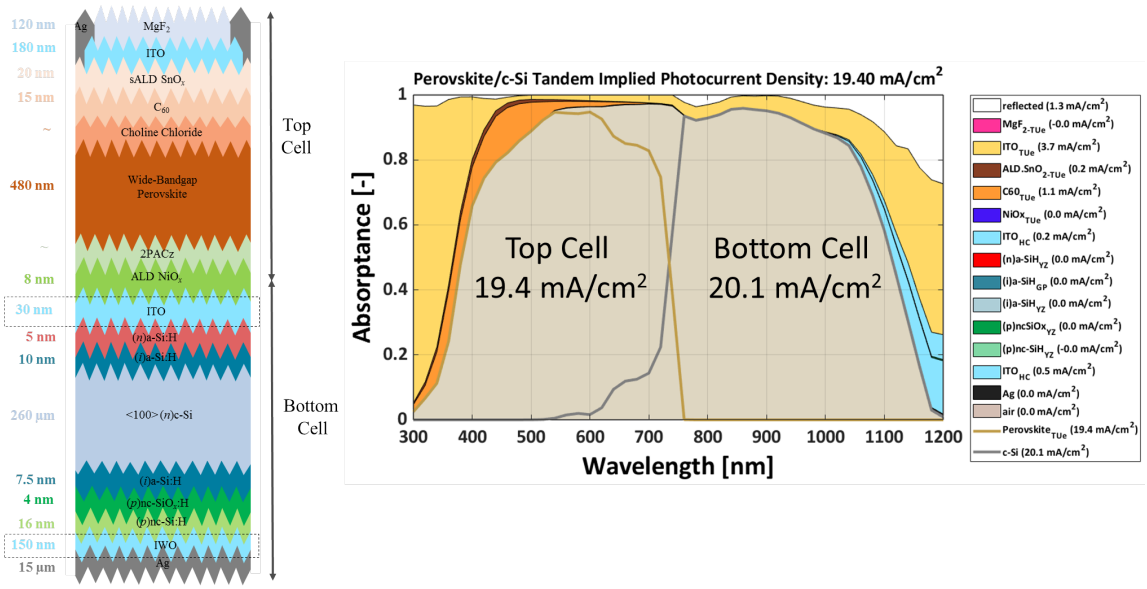

Figure 4.13: Device architecture: Double-side-textured 2T Perovskite/c-Si tandem cell with RJ and rear ITO (reference device).

Among them Fig. 4.14 shows the IWO_IWO configuration with the resultant absorbance curve. Here the simulation was performed in the range of 0-180 nm to optimize the thickness of RJ layer (30 nm) from the contour plots shown in Fig. 4.15.Although IWO_IWO configuration doesn't show the best implied photocurrent density ($J_{imp,tandem}$ = 19.38 mA/cm^2) comparing to ITO_ITO device ($J_{imp,tandem}$ = 19.40 mA/cm^2), the bottom cell generated ($J_{imp,c-Si}$) 20.40 mA/cm^2. This result indicates that the 2T device needs to be re-optimized to enhance the tandem implied photocurrent density. Compared with the single-side-textured device with a similar configuration, the parasitic absorption of the front-ITO is increased by 1.1 mA/cm^2, and the reflection loss is reduced by 3.3 mA/cm^2.

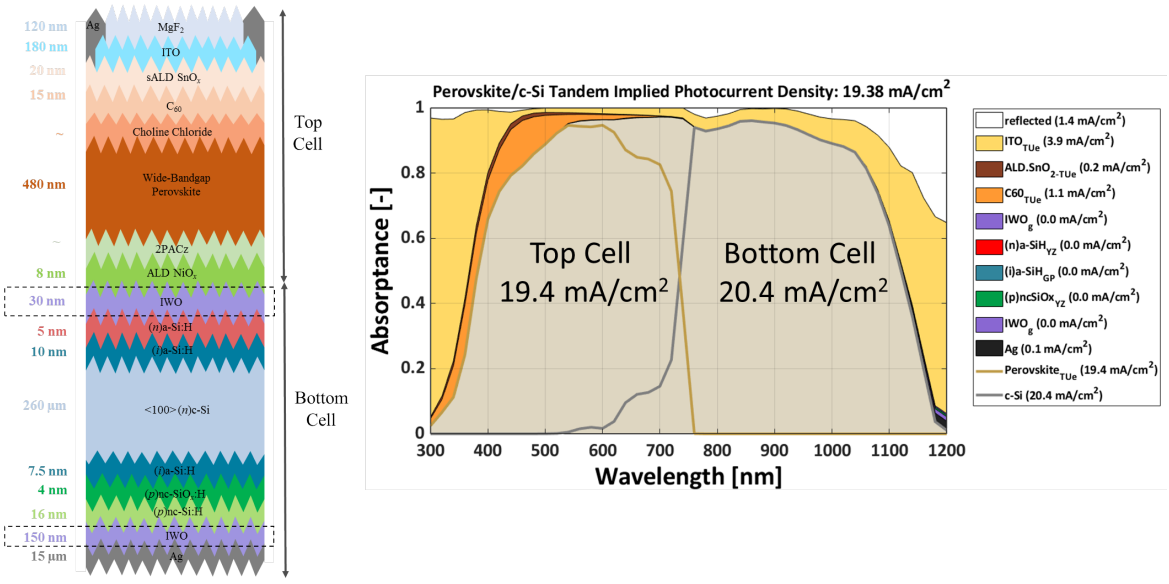

Figure 4.14: Device architecture: Double-side-textured 2T Perovskite/c-Si tandem cell with RJ and rear IWO (optimized with TCO-RJ).

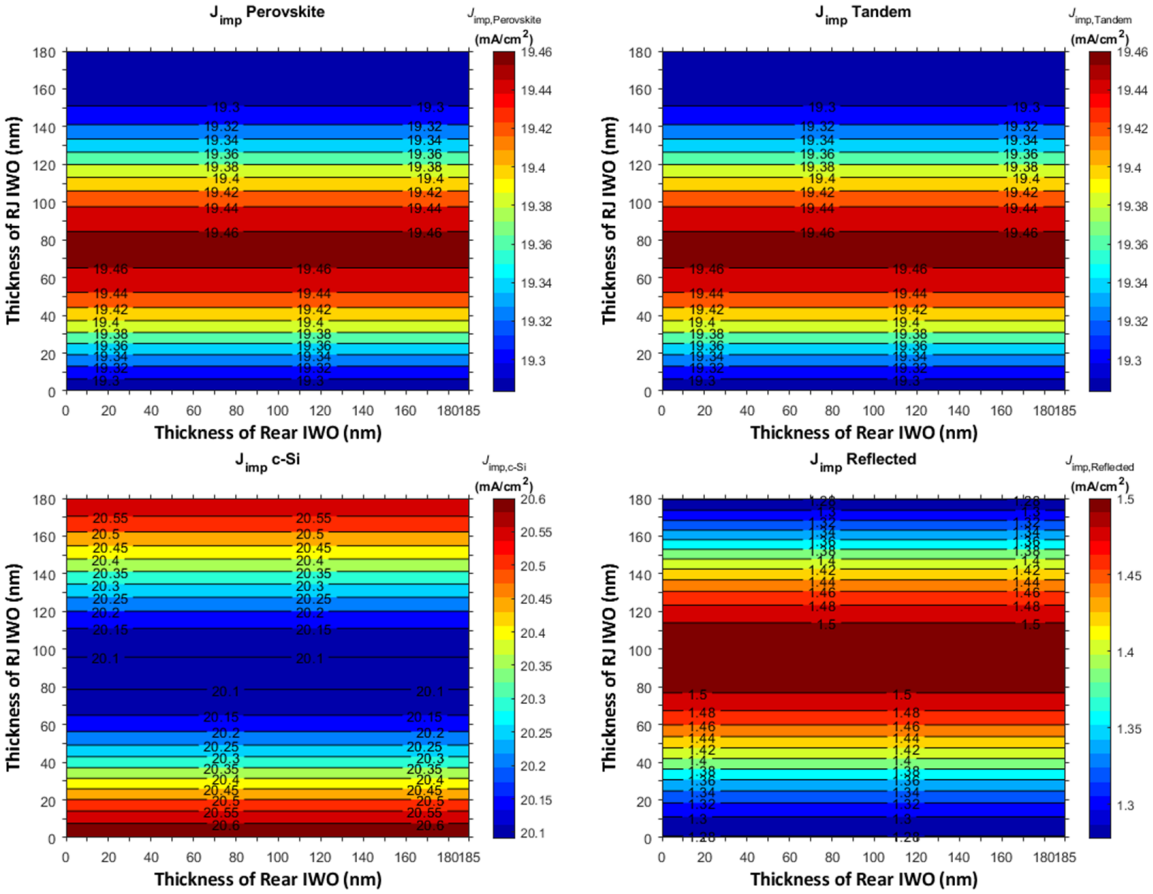

Figure 4.15: Contour plots: Double-side-textured 2T Perovskite/c-Si tandem with IWO_IWO configuration.

The overall analysis can be described as:

- Reflection loss (1.4 mA/cm^2, white area) can be seen in the front (350–380 nm) and the Perovskite/c–Si tandem interface (750–850 nm) wavelength ranges.
- The front ITO layer's major parasitic absorption loss (3.9 mA/cm^2, yellow region).
- The absorption loss in the C60 layer is (1.1 mA/cm^2, orange area).
- The rear electrode (Ag) has a parasitic absorption loss of 0.1 mA/cm^2 (black area)

The parasitic absorption loss of the SnOx layer (clay region) in the top cell is (0.2 mA/cm^2) and the same loss was noticed while using ITO or AZO as RJ in the configurations. The overall summary of the optical outcome is shown in table 4.7.

4.5. Intro. of Various Combinations of TCO-free RJ in the 2T Tan- dem Devices

In this section, same as in section 4.3, all possible TCO-free RJ layer configurations were introduced in the double-side-textured pattern. The Idea was to investigate the optical loss in detail with different scenarios to optimize the 2T tandem device. Depending on the materials property, the proposed TCO-free RJ configurations can be categorized into main 4 parts as:

1. nc-SiO$_x$:H layers as RJ with Various Rear-TCO Layers (see in section 4.5.1)

Table 4.7: Optical outcomes of 2T Perovskite/c-Si tandem with TCO-RJ: Double-side-textured devices.

RJ	Thickness (nm)	Rear TCO	Thickness (nm)	Implied Photocurrent Density				
				Tandem Current J_{Tandem} (mA/cm^2)	Perov. Top cell J_{Perov} (mA/cm^2)	SHJ Bot cell J_{c-Si} (mA/cm^2)	Refl. Loss J_{Refl} (mA/cm^2)	Parasitic Loss $J_{parasitic}$ (mA/cm^2)
ITO	30	ITO	150	19.40	19.4	20.1	1.3	5.8
ITO	30	IWO	150	19.40	19.4	20.1	1.4	5.5
ITO	30	AZO	150	19.40	19.4	20.1	1.2	5.8
IWO	30	ITO	150	19.38	19.4	20.3	1.2	5.8
IWO	30	IWO	150	19.38	19.4	20.4	1.4	5.3
IWO	30	AZO	150	19.38	19.4	20.2	1.2	5.6
AZO	30	ITO	150	19.40	19.4	20.1	1.2	5.8
AZO	30	IWO	150	19.40	19.4	20.3	1.3	5.5
AZO	30	AZO	150	19.40	19.4	20.1	1.2	5.9

2. nc-Si:H layers as RJ with Various Rear-TCO Layers (see in section 4.5.2)
3. nc-Si:H/nc-SiO$_x$:H layers as RJ with Various Rear-TCO Layers (see in section 4.5.3)
4. nc-SiO$_x$:H/nc-Si:H layers as RJ with Various Rear-TCO Layers (see in section 4.5.3)

4.5.1. Optimizing Doped nc-SiO$_x$:H Layers as RJ with Various Rear-TCO

The three possible configurations with this configuration are:

(i). (*p*/*n*)nc-SiO$_x$:H (30/30 nm) with Rear-ITO (150 nm)

(ii). (*p*/*n*)nc-SiO$_x$:H (30/30 nm) with Rear-IWO (150 nm)

(iii). (*p*/*n*)nc-SiO$_x$:H (30/30 nm) with Rear-AZO (150 nm)

Among all of these configurations, (*p*/*n*)nc-SiO$_x$:H_IWO configuration, shown in Fig. 4.16, results better-implied photocurrent density in the bottom cell ($J_{imp,c-Si}$ = 20.8 mA/cm^2). However, the implied photocurrent density ($J_{imp,perovskite}$ = 19.2 mA/cm^2) of the top cell, limits the tandem photocurrent density to 19.19 mA/cm^2. Initially, the RJ thickness of both of these layers was 30 nm. Following that a simulation loop with 0-180 nm and 0-190 nm, for the (*p*/*n*)nc-SiO$_x$:H respectively, was applied to generate contour plots (see in Fig. 4.17) for finding possible optimized thickness ranges. Finally (*p*/*n*)nc-SiO$_x$:H layers with 60/80 nm thickness with 150 nm thick IWO back reflector were applied to perform the simulation which results $J_{imp,tandem}$ = 19.39 mA/cm^2 (shown in the appendix 3).

From the absorption curve of Fig. 4.16 the important losses can be highlighted as:

– Reflection loss (1.3 mA/cm^2, white area) can be seen in the front (350–380 nm) and the Perovskite/c–Si tandem interface (750–850 nm) wavelength ranges.
– The front ITO layer's major parasitic absorption loss (3.8 mA/cm^2, yellow region).The absorption loss in the C60 layer is (1.1 mA/cm^2, orange area).

(*p*)nc-SiO$_x$:H layer also shows 0.4 mA/cm^2 parasitic loss which is unchanged for all types of back reflectors in the configurations. For it's high transparency the IWO back reflector, the back electrode (Ag) shows 0.1 mA/cm^2 absorption loss. The overall summary of all optical analyses is shown in table 4.8.

4.5.2. Optimizing Doped nc-Si:H Layers as RJ with Various Rear-TCO

Three different configurations in this category are :

Table 4.8: Optical outcomes of 2T Perovskite/c-Si tandem with TCO-free Oxidic layers as RJ : Double-side-textured devices.

RJ	Thickness (nm)	Rear TCO	Thickness (nm)	Tandem Current J_{Tandem} (mA/cm^2)	Implied Photocurrent Density Perov. Top cell J_{Perov} (mA/cm^2)	SHJ Bot cell J_{c-Si} (mA/cm^2)	Refl. Loss J_{Refl} (mA/cm^2)	Parasitic Loss $J_{parasitic}$ (mA/cm^2)
(*p*)/(*n*)nc-SiO$_x$:H	30/30	ITO	150	19.19	19.2	20.6	1.0	5.8
(*p*)/(*n*)nc-SiO$_x$:H	30/30	IWO	150	19.19	19.2	20.8	1.1	5.6
(*p*)/(*n*)nc-SiO$_x$:H	30/30	AZO	150	19.19	19.2	20.6	1.0	5.9

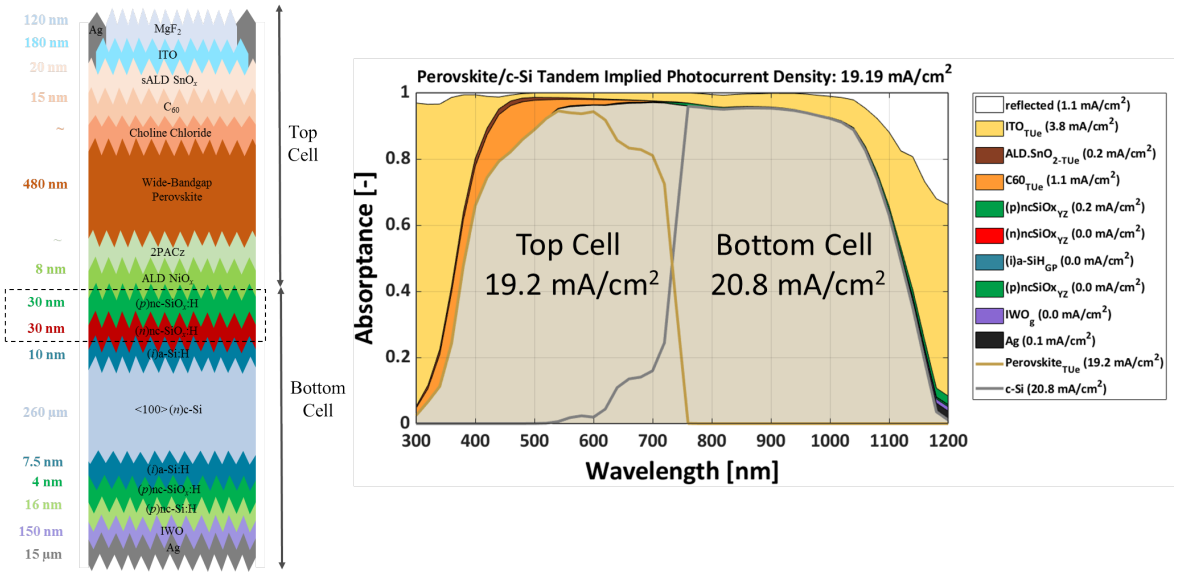

Figure 4.16: Device architecture: Double-side-textured 2T Perovskite/c-Si tandem cell with *(p/n)*nc-SiO$_x$:H as RJ and rear IWO (TCO-free optimized RJ with oxidic layers).

(i) (*p*/*n*)nc-Si:H (30/20 nm) with Rear-ITO (150 nm)

(ii) (*p*/*n*)nc-Si:H (30/20 nm) with Rear-IWO (150 nm)

(iii) (*p*/*n*)nc-Si:H (30/20 nm) with Rear-AZO (150 nm)

The main purpose of this experiment is to compare the optical outcome of two different patterns (single-side-textured and double-side-textured) of devices while using the same materials to build the RJ. Among all the mentioned above configurations, (*p*/*n*)nc-Si:H_IWO (with 30/20_30 nm thickness) is the optimized device configuration considering the optical outcomes. From the absorption curve of Fig. 4.18 the important losses can be highlighted as:

– Reflection loss (1.1 mA/cm^2, white area) can be seen in the front (350–380 nm) and the Perovskite/c–Si tandem interface (750–850 nm) wavelength ranges.

– The front ITO layer's major parasitic absorption loss (3.8 mA/cm^2, yellow region). The absorption loss in the C60 layer is (1.1 mA/cm^2, orange area).

Top cell's (*p*)nc-SiO$_x$:H layer and the bottom cell's RJ layers (*p*/*n*)nc-Si:H also shows 0.2 mA/cm^2, 0.2 mA/cm^2 respectively. The 0.1 mA/cm^2 parasitic loss remains the same for all types of back reflectors in the configurations. A possible reason could the higher transparency of rear-IWO and the high transparency the IWO back reflector. The overall summary of mentioned configurations with the optical outcomes is shown in table 4.9.

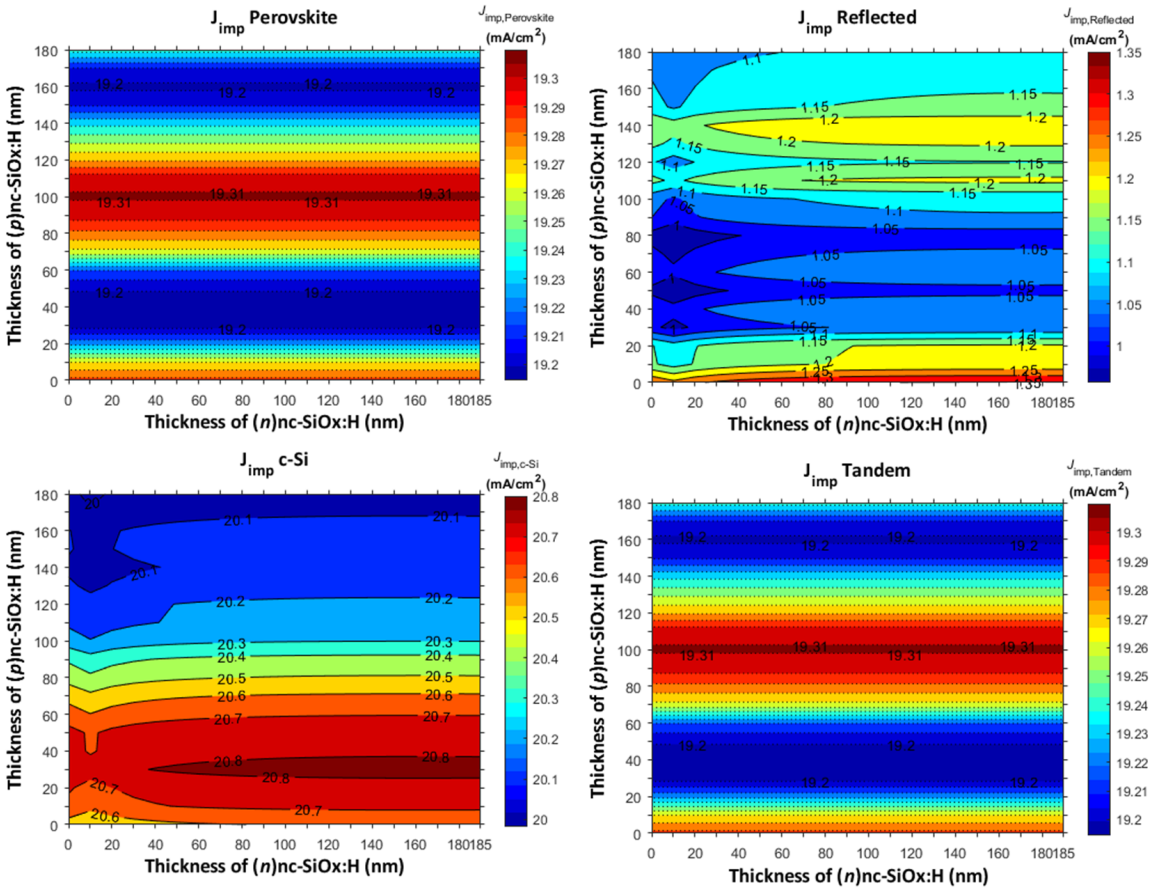

Figure 4.17: Contour plots: Double-side-textured 2T Perovskite/c-Si tandem with *(p/n)*nc-SiO_x:H_IWO configuration.

Table 4.9: Optical outcomes of 2T Perovskite/c-Si tandem with TCO-free Non-oxidic layers as RJ: Double-side-textured devices.

RJ	Thickness (nm)	Rear TCO	Thickness (nm)	Tandem Current J_{Tandem} (mA/cm^2)	Implied Photocurrent Density Perov. Top cell J_{Perov} (mA/cm^2)	SHJ Bot cell J_{c-Si} (mA/cm^2)	Refl. Loss J_{Refl} (mA/cm^2)	Parasitic Loss $J_{parasitic}$ (mA/cm^2)
(*p*)/(*n*)nc-Si:H	30/20	ITO	150	19.22	19.2	20.6	1.0	5.9
(*p*)/(*n*)nc-Si:H	30/20	IWO	150	19.22	19.2	20.7	1.1	5.7
(*p*)/(*n*)nc-Si:H	30/20	AZO	150	19.22	19.2	20.5	1.0	6.0

4.5.3. Optimization of Doped nc-Si:H/nc-SiO_x:H RJ Layers with Various Rear TCOs

As previously mentioned in section 4.3.3 that the motivation of using bilayer p-contact is for the application of the combination of low activation energy (E_a) and wide energy bandgap (E_g) materials together as it is crucial for the effective hole collection in SHJ solar cells. The same trend was followed in this section with a different device pattern (double-side-textured) to compare optical properties, same aim as the last two sections (4.5.1, 4.5.2).

The overall optimization process leads in two different ways, where firstly a majority of oxidic Si layers were combined with non-oxidic Si layers and vice versa. By inserting (*p*)nc-SiO_x:H in

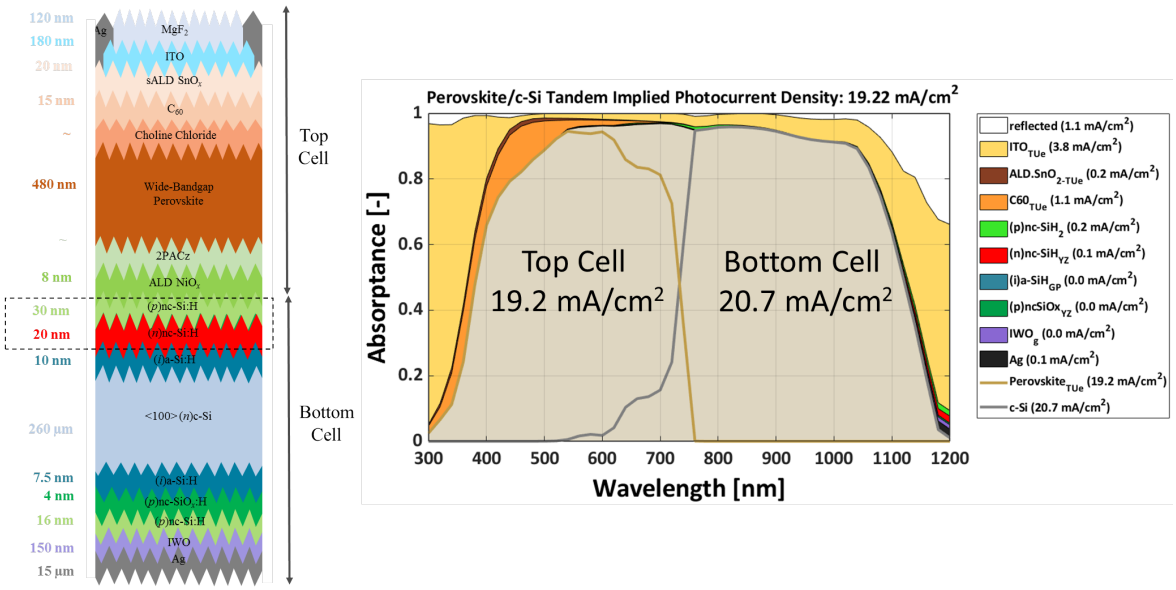

Figure 4.18: Device architecture: Double-side-textured 2T Perovskite/c-Si tandem cell with *(p/n)*nc-Si:H as RJ and rear IWO (TCO-free optimized RJ with non-oxidic layers) [156].

between two nc-Si:H layers the possible configurations can be listed as:

(i) (*p*/*n*)nc-Si:H with an Inserted (*p*)nc-SiO_x:H (5 nm) with Rear-ITO (150 nm)

(ii) (*p*/*n*)nc-Si:H with an Inserted (*p*)nc-SiO_x:H (5 nm) with Rear-IWO (150 nm)

(iii) (*p*/*n*)nc-Si:H with an Inserted (*p*)nc-SiO_x:H (5 nm) with Rear-AZO (150 nm)

Among all the mentioned above configurations, (*p*/*n*)nc-Si:H with an Inserted (*p*)nc-SiO_x:H (5 nm)_IWO (150 nm) is the optimized device configuration considering the optical outcomes. From the absorption curve of Fig. 4.19 the major optical losses can be highlighted as:

– Reflection loss (1.1 mA/cm^2, white area) can be seen in the front (350–380 nm) and the Perovskite/c–Si tandem interface (750–850 nm) wavelength ranges.

– The front ITO layer's major parasitic absorption loss (3.7 mA/cm^2, yellow region). The absorption loss in the C60 layer is (1.1 mA/cm^2, orange area).

(*p*/*n*)nc-Si:H layers also show 0.2 and 0.1 mA/cm^2 parasitic loss respectively, which is unchanged for all types of back reflectors in the mentioned configurations. For its high transparency, the IWO and AZO layers as the back reflector and the back electrode (Ag) show 0.1 mA/cm^2 absorption loss. The resultant implied photocurrent density ($J_{imp,tandem}$) is 19.21 mA/cm^2. A short summary of mentioned configurations with the optical outcomes is shown in table 4.10.

Subsequently, a (*p*)nc-Si:H was inserted in between two nc-SiO_x:H layers and the possible configurations can be listed as:

(i) (*p*/*n*)nc-SiO_x:H with an Inserted (*p*)nc-Si:H (50 nm) with Rear-ITO (150 nm)

(ii) (*p*/*n*)nc-SiO_x:H with an Inserted (*p*)nc-Si:H (50 nm) Rear-ITO (150 nm)

(iii) (*p*/*n*)nc-SiO_x:H with an Inserted (*p*)nc-Si:H (50 nm) with Rear-AZO (150 nm)

Among all the mentioned above configurations, (*p*/*n*)nc-SiO_x:H with an Inserted (*p*)nc-Si:H (5 nm)_IWO (150 nm) is the optimized device configuration considering the optical outcomes. From the absorption curve of Fig. 4.20 the major optical losses can be highlighted as:

– Reflection loss (1.1 mA/cm^2, white area) can be seen in the front (350–380 nm) and the Perovskite/c–Si tandem interface (750–850 nm) wavelength ranges.

– The front ITO layer's major parasitic absorption loss (3.8 mA/cm^2, yellow region). The absorption loss in the C60 layer is (1.1 mA/cm^2, orange area).

*(*p)nc-SiO$_x$:H and (*n*)nc-Si:H layers also show 0.1 and 0.001 mA/cm^2 (however the (*n*)nc-Si:H layer's 0.001 mA/cm^2 parasitic loss is not displayed, but from the GenPro4's aplot: J_{imp} > 0.001, mA/

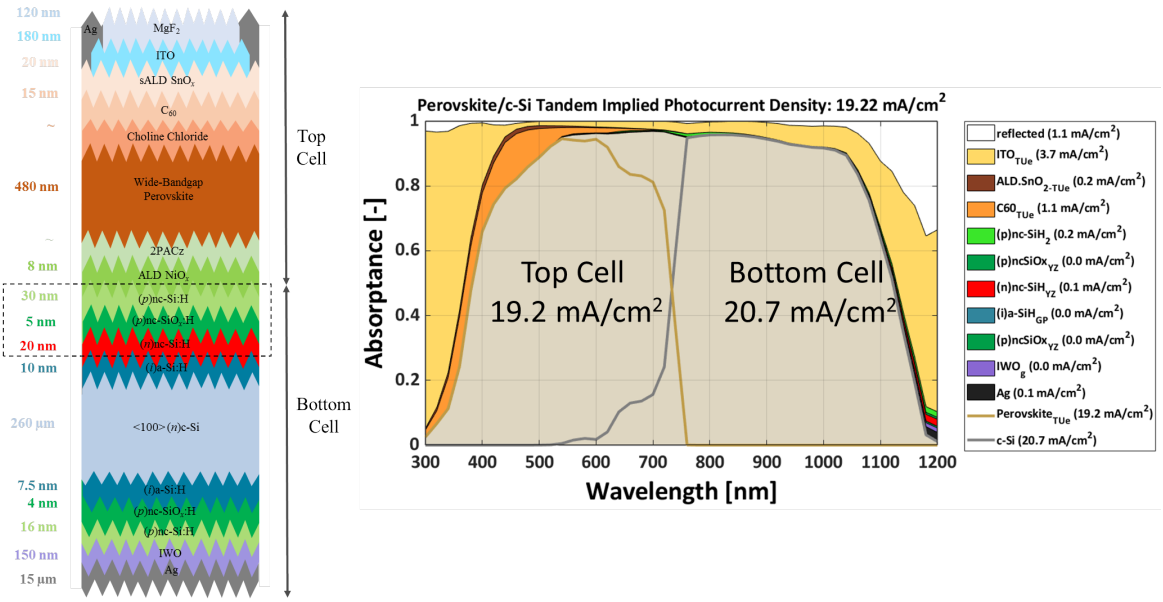

Figure 4.19: Device architecture: Double-side-textured 2T Perovskite/c-Si tandem cell with *(p/n)*nc-SiO$_x$:H as RJ and rear IWO (TCO-free optimized RJ with nc-Si:H/ nc-SiO$_x$:H) [156].

Doped oxidic layers with a non-oxidic intermediary layer perform better when compared to two different types of doped oxidic and non-oxidic layer combinations. It is important to note that while identical performance can be seen with a thin doped oxidic intermediary layer (5 nm), in this situation a thicker doped non-oxidic intermediary layer (50 nm) is required.

Table 4.10: Optical outcomes of 2T Perovskite/c-Si tandem with TCO-free Non-oxidic/Oxidic layers as RJ: Double-side-textured devices.

RJ	Thickness (nm)	Rear TCO	Thickness (nm)	Implied Photocurrent Density: Tandem Current J_{Tandem} (mA/cm^2)	Perov. Top cell J_{Perov} (mA/cm^2)	SHJ Bot cell J_{c-Si} (mA/cm^2)	Refl. Loss J_{Refl} (mA/cm^2)	Parasitic Loss $J_{parasitic}$ (mA/cm^2)
(*p*)/(*n*)nc-Si:H w/ (*p*)nc-SiO$_x$:H	30/5/20	ITO	150	19.22	19.2	20.6	1.0	5.8
(*p*)/(*n*)nc-Si:H w/ (*p*)nc-SiO$_x$:H	30/5/20	IWO	150	19.22	19.2	20.7	1.1	5.6
(*p*)/(*n*)nc-Si:H w/ (*p*)nc-SiO$_x$:H	30/5/20	AZO	150	19.22	19.2	20.5	1.0	5.9
(*p*)/(*n*)nc-SiO$_x$:H w/ (*p*)nc-Si:H	30/5/30	ITO	150	19.18	19.2	20.7	1.0	5.8
(*p*)/(*n*)nc-SiO$_x$:H w/ (*p*)nc-Si:H	30/5/30	IWO	150	19.18	19.2	20.8	1.1	5.6
(*p*)/(*n*)nc-SiO$_x$:H w/ (*p*)nc-Si:H	30/5/30	AZO	150	19.18	19.2	20.6	0.9	5.9

4.5.4. Comparison Among Different RJs and Rear TCOs: Single-side-textured Perovskite/c-Si 2T Tandem Solar Cells

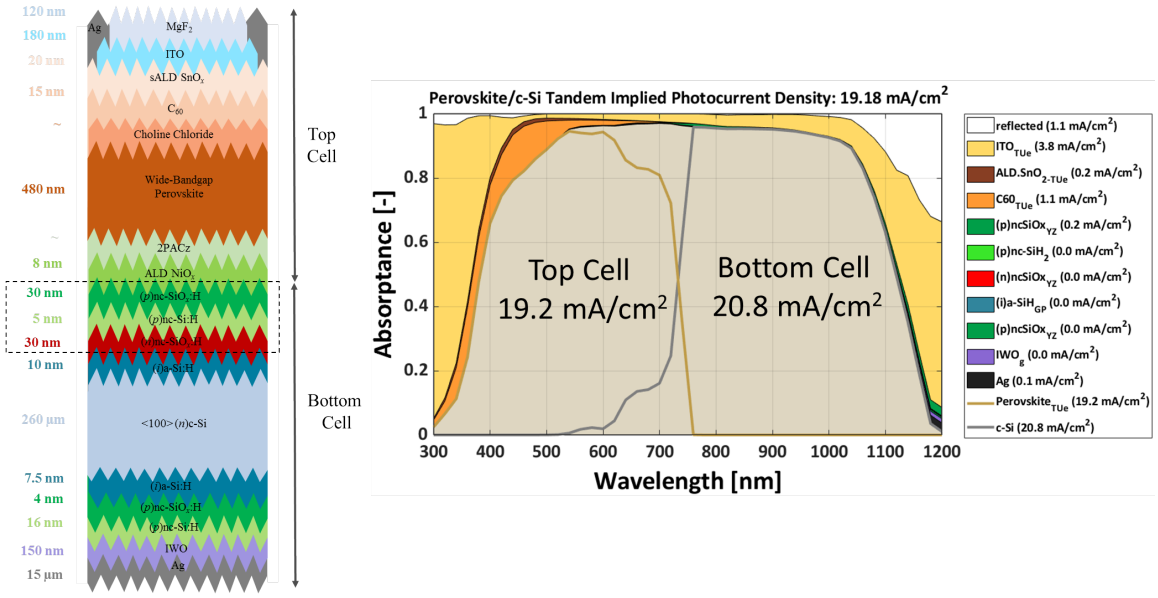

Figure 4.20: Device architecture: Double-side-textured 2T Perovskite/c-Si tandem cell with *(p/n)*nc-SiO_x:H as RJ and rear IWO (TCO-free optimized RJ with nc-SiO_x:H/nc-Si:H).

(i). Optical Analysis of Double-side-textured 2T Tandem Devices: (with initial RJ thickness)

Table 4.11: Summarizing optical outcomes of Double-side-textured 2T Perovskite/c-Si tandem devices (with initial RJ thickness).

RJ	Thickness (nm)	Rear TCO	Thickness (nm)	Tandem Current J_{Tandem} (mA/cm^2)	Implied Photocurrent Density: Perov. Top cell J_{Perov} (mA/cm^2)	SHJ Bot cell J_{c-Si} (mA/cm^2)	Refl. Loss J_{Refl} (mA/cm^2)	Parasitic Loss $J_{parasitic}$ (mA/cm^2)
ITO	30	ITO	150	19.40	19.4	20.1	1.3	5.8
ITO	30	IWO	150	19.40	19.4	20.1	1.4	5.5
ITO	30	AZO	150	19.40	19.4	20.1	1.2	5.8
IWO	30	ITO	150	19.38	19.4	20.3	1.2	5.8
IWO	30	IWO	150	19.38	19.4	20.4	1.4	5.3
IWO	30	AZO	150	19.38	19.4	20.2	1.2	5.6
AZO	30	ITO	150	19.40	19.4	20.1	1.2	5.8
AZO	30	IWO	150	19.40	19.4	20.3	1.3	5.5
AZO	30	AZO	150	19.40	19.4	20.1	1.2	5.9
(*p*)/(*n*)nc-SiO_x:H	30/30	ITO	150	19.19	19.2	20.6	1.0	5.8
(*p*)/(*n*)nc-SiO_x:H	30/30	IWO	150	19.19	19.2	20.8	1.1	5.6
(*p*)/(*n*)nc-SiO_x:H	30/30	AZO	150	19.19	19.2	20.6	1.0	5.9
(*p*)/(*n*)nc-Si:H	30/20	ITO	150	19.22	19.2	20.6	1.0	5.9
(*p*)/(*n*)nc-Si:H	30/20	IWO	150	19.22	19.2	20.7	1.1	5.7
(*p*)/(*n*)nc-Si:H	30/20	AZO	150	19.22	19.2	20.5	1.0	6.0
(*p*)/(*n*)nc-Si:H w/ (*p*)nc-SiO_x:H	30/5/20	ITO	150	19.22	19.2	20.6	1.0	5.8
(*p*)/(*n*)nc-Si:H w/ (*p*)nc-SiO_x:H	30/5/20	IWO	150	19.22	19.2	20.7	1.1	5.6
(*p*)/(*n*)nc-Si:H w/ (*p*)nc-SiO_x:H	30/5/20	AZO	150	19.22	19.2	20.5	1.0	5.9
(*p*)/(*n*)nc-SiO_x:H w/ (*p*)nc-Si:H	30/5/30	ITO	150	19.18	19.2	20.7	1.0	5.8
(*p*)/(*n*)nc-SiO_x:H w/ (*p*)nc-Si:H	30/5/30	IWO	150	19.18	19.2	20.8	1.1	5.6
(*p*)/(*n*)nc-SiO_x:H w/ (*p*)nc-Si:H	30/5/30	AZO	150	19.18	19.2	20.6	0.9	5.9

The optical outcomes of eighteen various double-sided textured devices are all displayed in the appendix (table 3). Compared to TCO-free recombination junction devices, tandem implied photocurrent density is 0.18 mA/cm^2 higher when the standard TCO layer is used in the recombination junction and as the rear reflector. Aiming to increase the implied photocurrent density of the c-Si bottom device, which was accomplished with 0.70 mA/cm^2 greater photocurrent density than utilizing the conventional TCO layers in the recombination junction, is something that should be mentioned.

(ii). Optical Analysis of Double-side-textured 2T Tandem Devices: (with optimized RJ thickness)

Table 4.13 shows the optimal thickness of the traditional and TCO-free recombination junction layers. The proposed 2T tandem device with TCO-free recombination junction layers shows the highest tandem implied photocurrent density as 19.46 mA/cm^2, which is very similar to the ITO_ITO configuration device's 19.40 mA/cm^2. Having proper refractive index matching with the two absorbers (perovskite and c-Si), using nc-SiO_x:H or nc-Si:H to build the RJ reflection loss is reduced by 0.2 mA/cm^2. By tuning the thicknesses of these intermediate layers, the interference effect can be optimized.

One of the recommended devices has a reflection loss of 1.1 mA/cm^2 and a bottom cell current density of 20.80 mA/cm^2 due to the usage of IWO as the back reflector and doped oxidic layers as TRJ in the tunnel junction.

4.6. Perovskite/c-Si 2T Tandem Device: Pre and Post Optimization

The c-Si bottom cell functioned as the current limiter in the first device with an ITO_ITO layout, as shown in Fig.4.1. Given this, the objective of the project was to enhance the current generation SHJ bottom cell by lowering the parasitic absorption loss and the reflection loss of the two terminal devices. In the recombination junction, if ITO can be replaced by several doped layers, it is possible to increase the implied photocurrent density of the bottom cell. This is quite obvious from observing all device performances of eighteen different single-side-textured devices and eighteen different double-side-textured devices. But now the current limiter is the top cell. The two major top cell layers, ITO and C60, are often the driving forces behind the creation of the perovskite top cell current limiter. However tables in the appendix (2 and 3) show maximizing the tandem current of the 2T devices while keeping all layers thickness constant, represented in tables 4.12 and 4.13 as **'pre'**, where the data from complete optimized 2T devices with maximum current matching are represented as **'post'** optimization. As a final step, the total 2T device was In sections 4.6.1 and 4.6.2, several potential settings that result in the maximum tandem photocurrent density of single-side-textured and double-sided-textured devices are discussed.

4.6.1. (*p*)/(*n*)nc-SiO_x:H as RJ with Rear IWO : Single-side-textured

The (*p*)/(*n*)nc-SiO_x_IWO configuration with a single-side-textured was formerly produced by MgF_2 (120 nm)/ ITO_TUe (180 nm)/ ALD SnO_{2TUe} (20 nm)/ C60 (15 nm)/ Choline Chloride (∼)/ Perovskite (480 nm)/ 2PACz (∼)/ NiO_{xTUe} (8 nm)/ (*p*)nc-SiO_x:H (60 nm)/ (*n*)nc-SiO_x:H (80 nm)/ (*i*)a-Si:H (10 nm)/ c-Si (260 µm)/ (*i*)a-Si:H (7.5 nm)/ (*p*)nc-SiO_x:H (4 nm)/(*p*)nc-Si:H (16 nm)/ IWO_g (150 nm)/ Ag (15 µm). The resultant tandem implied photocurrent density, which can be seen in Fig. 4.16, is 19.39 mA/cm^2.

Following that several simulations, the optically optimal thickness parameters are : The (*p*)/(*n*)nc-SiO_x_IWO device with a single side of texturing was formerly produced by MgF_2 (100 nm)/ ITO_TUe (108 nm)/ ALD SnO_{2TUe} (6 nm)/ C60 (10 nm)/ Choline Chloride (∼)/ Perovskite (558 nm)/ 2PACz (∼)/ NiO_{xTUe} (6 nm)/ (*p*)nc-SiO_x:H (65 nm)/ (*n*)nc-SiO_x:H (45 nm)/ (*i*)a-Si:H (10 nm)/ c-Si (270 µm)/ (*i*)a-Si:H (7.5 nm)/ (*p*)nc-SiO_x:H (4 nm)/(*p*)nc-Si:H (16 nm)/ IWO_g (150 nm)/ Ag (15 µm). The resulting tandem implied photocurrent density, which can be seen in Fig. 4.21, is 19.79 mA/cm^2.

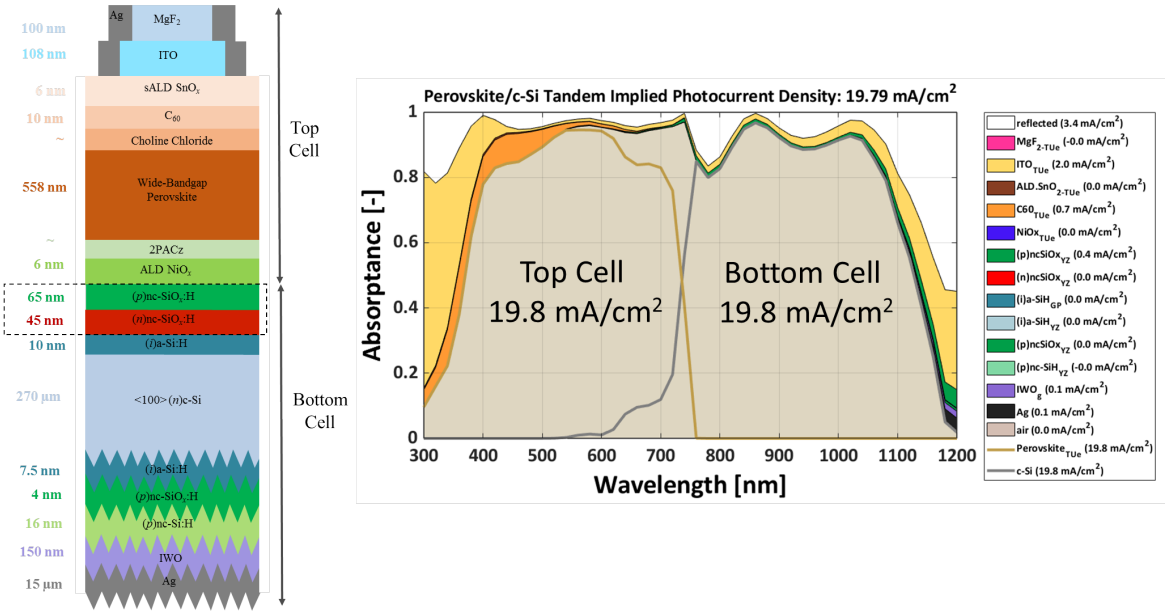

Figure 4.21: Device architecture: Single-side-textured 2T Perovskite/c-Si tandem cell with *(p/n)*nc-SiO_x:H as RJ and rear IWO (optimized 2T tandem device with TCO-free optimized oxidic RJ layers) [156].

4.6.2. (*p*)/(*n*)nc-SiO_x:H as RJ with Rear IWO : Double-side-textured

The (*p*)/(*n*)nc-SiO_x:H_IWO configuration with a single-side-textured was formerly produced by MgF_2 (120 nm)/ ITO_TUe (180 nm)/ ALD SnO_{2TUe} (20 nm)/ C60 (15 nm)/ Choline Chloride (~)/ Perovskite (480 nm)/ 2PACz (~)/ NiO_{xTUe} (8 nm)/ (*p*)nc-SiO_x:H (60 nm)/ (*n*)nc-SiO_x:H (80 nm)/ (*i*)a-Si:H (10 nm)/ c-Si (260 µm)/ (*i*)a-Si:H (7.5 nm)/ (*p*)nc-SiO_x:H (4 nm)/(*p*)nc-Si:H (16 nm)/ IWO_g (150 nm)/ Ag (15 µm). The resultant tandem implied photocurrent density, which can be seen in Fig. 4.16, is 19.39 mA/cm^2.

Following that several simulations, the optically optimal thickness parameters are : The (*p*)/(*n*)nc-SiO_x:H_IWO configuration with a Double-side-textured was formerly produced by MgF_2 (100 nm)/ ITO_TUe (100 nm)/ ALD SnO_{2TUe} (6 nm)/ C60 (10 nm)/ Choline Chloride (~)/ Perovskite (558 nm)/ 2PACz (~)/ NiO_{xTUe} (20 nm)/ (*p*)nc-SiO_x:H (80 nm)/ (*n*)nc-SiO_x:H (40 nm)/ (*i*)a-Si:H (10 nm)/ c-Si (260 µm)/ (*i*)a-Si:H (7 nm)/ (*p*)nc-SiO_x:H (5 nm)/(*p*)nc-Si:H (19 nm)/ IWO_g (120 nm)/ Ag (15 µm). The resultant tandem implied photocurrent density, which can be seen in Fig. 4.22, is 20.57 mA/cm^2. The tandem implied photocurrent density is 1.31 mA/cm^2 higher than the previous devices, and both of the cells are generating similar implied photocurrent density. The absorption curve from the optical simulation is in Figure 4.22.

Summary:

The findings of the devices with the same configuration but distinct thickness parameters of the single-side-textured and double-side-textured 2T tandem devices are displayed in Tables 4.12 and 4.13 respectively. Initially, the idea was to increase the bottom cell's current since it functioned as the two-terminal tandem device's current limiter. After going through some possible modifications in RJ, the bottom cell is no longer a current limiter. However, the top call became the current limiter device in 2T tandem. While comparing among conventional TCOs, for its optoelectrical property (proper refractive index matching with the main absorbers, higher transparency, and electron mobility) IWO performs better both as RJ and the back reflector. The 2T devices with *p*/*n* configurations, thicker n layers with relatively less thick *p*-layer optically perform better for both oxidic and non-oxidic RJ. The devices with **bilayer *p*-contact/*n*-layer** combinations (between **(*p*)nc-Si:H/(*p*)nc-SiO_x:H/(*n*)nc-Si:H** and **(*p*)nc-SiO_x:H/(*p*)nc-Si:H/(*n*)nc-Si:H**) the last one works slightly better by reducing reflection loss.

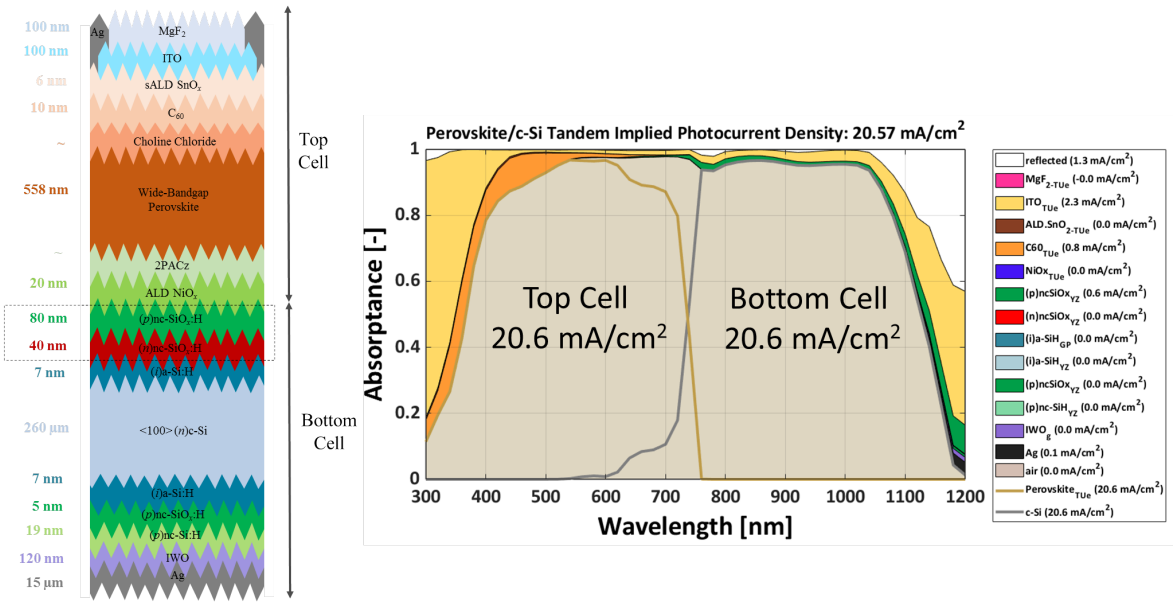

Figure 4.22: Device architecture: Double-side-textured 2T Perovskite/c-Si tandem cell with *(p/n)*nc-SiO_x:H as RJ and rear IWO (optimized 2T tandem device with TCO-free optimized oxidic RJ layers) [156].

With necessary modifications, tandem implies photocurrent density for both single-side-textured and double-side-textured devices was further improved by current matching between the two devices, thanks to GenPro4. The front ITO and C60 layers in the top cell and lower front reflection loss of all devices with TCO-free RJ are from 2.8 to 1.9 mA/cm^2 and 0.9 to 0.7 mA/cm^2 respectively, which has a great impact to improve the overall $J_{imp,tandem}$. In single-side-textured and double-side-textured devices with TCO-free dopes oxidic layers as RJ layers, the highest tandem implied photocurrent density (J_{imp}) are 19.66 mA/cm^2, and 20.57 mA/cm^2. Considering the loss analysis and results, single-side-textured TCO-free devices might be the optimum choice for this type of monolithic 2T tandem application. The improvement (significant loss reduction) while introducing nc-SiO_x:H or nc-Si:H materials instead of ITO was possible for their proper refractive index matching with the two absorbers (perovskite and c-Si). Considering a textured interface that leads to reduced reflection loss and allows more light to enter the device, double-side-textured devices were also optimized. However, the mismatch of wavelength-dependent refraction index among the materials induces parasitic absorption. To reduce the mentioned losses, optimizing the interference effect at the interfaces of the layers of the proposed 2T configurations it is possible to boost up the tandem current generation.

The balanced incident photon absorption in both Ultraviolet-visible (UV-Vis, ~ 300 to 800 nm) and near-infrared (NIR, ~ 800 to 1200 nm) range can be emphasized while reducing losses in between the interfaces of the device. However current matching between two sub-cells is crucial to designing an advanced 2T tandem device. The suboptimal matching of refractive index (n) at interfaces, more specifically in the intermediate interfaces between two sub-cells can lead to significant reflection loss. For better absorption guided light management with advanced optical simulations can offer reduced two main optical losses, parasitic absorption and reflection losses, which can enhance light coupling into the two sub-cell.

Table 4.12: Summarizing optical outcomes of Single-side-textured 2T Perovskite/c-Si tandem devices (with current matching).

				Implied Photocurrent Density of Single-side-textured Devices				
RJ	Thickness (nm) Pre | Post	Rear TCO	Thickness (nm) Pre | Post	Tandem Current J_{Tandem} (mA/cm^2) Pre | Post	Perov. Top cell J_{Perov} (mA/cm^2) Pre | Post	SHJ Bot cell J_{c-Si} (mA/cm^2) Pre | Post	Refl. Loss J_{Refl} (mA/cm^2) Pre | Post	Parasitic Loss $J_{parasitic}$ (mA/cm^2) Pre | Post
ITO	15 | 25	ITO	150 | 150	18.65 | 19.40	18.6 | 19.4	18.8 | 19.4	4.4 | 4.1	4.7 | 3.5
IWO	35 | 28	IWO	150 | 150	18.71 | 19.50	18.71 | 19.5	18.7 | 19.5	4.8 | 4.2	4.1 | 3.2
AZO	15 | 25	AZO	150 | 150	18.65 | 19.40	18.6 | 19.4	18.7 | 19.4	4.3 | 4.0	4.7 | 3.7
(*p*)/(*n*)nc-SiO$_x$:H	60/70 | 25/90	ITO	150 | 110	18.66 | 19.76	18.7 | 19.8	18.7 | 19.8	4.1 | 3.3	4.9 | 3.5
(*p*)/(*n*)nc-SiO$_x$:H	60/70 | 65/45	IWO	150 | 150	18.65 | 19.79	18.7 | 19.8	18.9 | 19.8	4.2 | 3.4	4.6 | 3.2
(*p*)/(*n*)nc-SiO$_x$:H	60/70 | 26/85	AZO	150 | 120	18.64 | 19.76	18.6 | 19.8	19.0 | 19.8	3.7 | 3.1	5 | 3.7
(*p*)/(*n*)nc-Si:H	30/70 | 35/37	ITO	150 | 120	18.63 | 19.75	18.6 | 19.8	18.8 | 19.8	4.0 | 3.2	4.8 | 3.6
(*p*)/(*n*)nc-Si:H	30/75 | 35/44	IWO	150 | 120	18.63 | 19.78	18.6 | 19.8	18.8 | 19.8	4.4 | 3.6	4.5 | 3.3
(*p*)/(*n*)nc-Si:H	30/70 | 35/32	AZO	150 | 120	18.63 | 19.72	18.7 | 19.7	18.6 | 19.7	4.0 | 3.1	4.9 | 3.8
(*p*)/(*n*)nc-Si:H w/ (*p*)nc-SiO$_x$:H	30/50/20 | 38/5/25	ITO	150 | 150	18.66 | 19.74	18.7 | 19.7	18.7 | 19.7	4.0 | 3.2	5.1 | 3.6
(*p*)/(*n*)nc-Si:H w/ (*p*)nc-SiO$_x$:H	30/50/20 | 38/5/30	IWO	150 | 150	18.66 | 19.77	18.7 | 19.8	18.8 | 19.8	4.2 | 3.5	4.7 | 3.1
(*p*)/(*n*)nc-Si:H w/ (*p*)nc-SiO$_x$:H	30/40/20 | 35/5/29	AZO	150 | 150	18.62 | 19.74	18.6 | 19.7	19.0 | 19.7	3.7 | 3.1	5.1 | 3.8
(*p*)/(*n*)nc-SiO$_x$:H w/ (*p*)nc-Si:H	28/40/28 | 35/20/40	ITO	150 | 150	18.72 | 19.78	18.7 | 19.8	18.8 | 19.8	4.0 | 3.1	4.8 | 3.6
(*p*)/(*n*)nc-SiO$_x$:H w/ (*p*)nc-Si:H	30/40/30 | 35/26/35	IWO	150 | 150	18.73 | 19.79	18.7 | 19.8	18.8 | 19.8	4.3 | 3.5	4.3 | 3.3
(*p*)/(*n*)nc-SiO$_x$:H w/ (*p*)nc-Si:H	40/40/30 | 35/22/35	AZO	150 | 150	18.72 | 19.77	18.7 | 19.8	18.7 | 19.8	4.0 | 3.0	4.9 | 3.8

Table 4.13: Summarizing optical outcomes of Double-side-textured 2T Perovskite/c-Si tandem devices (with current matching).

				Implied Photocurrent Density of Double-side-textured Devices				
RJ	Thickness (nm) Pre | Post	Rear TCO	Thickness (nm) Pre | Post	Tandem Current J_{Tandem} (mA/cm^2) Pre | Post	Perov. Top cell J_{Perov} (mA/cm^2) Pre | Post	SHJ Bot cell J_{c-Si} (mA/cm^2) Pre | Post	Refl. Loss J_{Refl} (mA/cm^2) Pre | Post	Parasitic Loss $J_{parasitic}$ (mA/cm^2) Pre | Post
ITO	40 | 39	ITO	150 | 150	19.45 | 20.48	19.4 | 20.5	19.9 | 20.5	1.4 | 1.3	5.8 | 4.1
IWO	78 | 70	IWO	150 | 150	19.47 | 20.60	19.5 | 20.6	20.1 | 20.6	1.5 | 1.6	5.4 | 3.5
AZO	65 | 39	AZO	150 | 150	19.53 | 20.48	19.5 | 20.5	19.5 | 20.5	1.4 | 1.3	5.9 | 4.1
(*p*)/(*n*)nc-SiO$_x$:H	70/80 | 78/40	ITO	150 | 150	19.39 | 20.53	19.4 | 20.5	20.0 | 20.5	1.2 | 1.1	5.8 | 4.1
(*p*)/(*n*)nc-SiO$_x$:H	60/80 | 80/40	IWO	150 | 120	19.39 | 20.57	19.4 | 20.6	20.2 | 20.6	1.3 | 1.3	5.6 | 3.8
(*p*)/(*n*)nc-SiO$_x$:H	60/80 | 75/40	AZO	150 | 90	19.39 | 20.52	19.4 | 20.5	20.1 | 20.5	1.1 | 1.1	5.9 | 4.2
(*p*)/(*n*)nc-Si:H	40/70 | 43/40	ITO	150 | 150	19.41 | 20.55	19.4 | 20.5	19.9 | 20.5	1.2 | 1.2	5.9 | 4
(*p*)/(*n*)nc-Si:H	40/80 | 40/30	IWO	150 | 150	19.41 | 20.58	19.4 | 20.6	20.1 | 20.6	1.3 | 1.4	5.7 | 3.8
(*p*)/(*n*)nc-Si:H	40/80 | 41/41	AZO	150 | 150	19.40 | 20.54	19.4 | 20.5	19.8 | 20.5	1.3 | 1.1	6 | 4.2
(*p*)/(*n*)nc-Si:H w/ (*p*)nc-SiO$_x$:H	40/5/60 | 40/15/30	ITO	150 | 150	19.41 | 20.55	19.4 | 20.6	20.0 | 20.6	1.2 | 1.2	5.8 | 4
(*p*)/(*n*)nc-Si:H w/ (*p*)nc-SiO$_x$:H	40/5/60 | 45/15/30	IWO	150 | 120	19.41 | 20.59	19.4 | 20.6	20.2 | 20.6	1.3 | 1.3	5.6 | 3.8
(*p*)/(*n*)nc-Si:H w/ (*p*)nc-SiO$_x$:H	40/5/60 | 40/15/30	AZO	150 | 150	19.41 | 20.52	19.4 | 20.5	20.0 | 20.5	1.2 | 1.1	5.9 | 4.2
(*p*)/(*n*)nc-SiO$_x$:H w/ (*p*)nc-Si:H	30/50/30 | 80/5/40	ITO	150 | 150	19.46 | 20.52	19.5 | 20.5	19.9 | 20.5	1.2 | 1.1	5.8 | 4.1
(*p*)/(*n*)nc-SiO$_x$:H w/ (*p*)nc-Si:H	30/50/30 | 75/5/50	IWO	150 | 150	19.46 | 20.55	19.5 | 20.6	20.0 | 20.6	1.3 | 1.3	5.6 | 3.8
(*p*)/(*n*)nc-SiO$_x$:H w/ (*p*)nc-Si:H	30/50/30 | 75/5/39	AZO	150 | 150	19.46 | 20.52	19.5 | 20.5	19.8 | 20.5	1.2 | 1.1	5.9 | 4.2

5

Optimizing single-junction SHJ solar cells

While the maximum V_{oc} of homojunction cells can be attained at approximately 700 mV [21], SHJ solar cells can transcend this value to approximately 750 mV [20, 69]. However flat (100)c-Si surface is prone to detrimental epitaxial growth during the deposition of (*i*)a-Si:H layers [143]. Highly hydrogen-diluted *i*-layers could promote this growth. Dangling bonds originate from a network's abrupt discontinuous expansion, which can eventually create traps near the heterojunction interface (c-Si/(*i*)a-Si:H). Surface recombination velocity (SRV) describes defect density. High SRV may lessen photo-generated carriers. This recombination loss can be reduced by effectively passivating the c-Si surface with (*i*)-Si:H, and significantly enhance the effective lifetime for minority charge carriers.
SHJ solar cells feature superior chemical passivation thanks to the (*i*)a-Si:H passivating layers deposited on the c-Si surface [69]. Optimizing intrinsic passivation layers, which were deposited with ideal thicknesses of 7–10 nm on either side of the absorber (c–Si), was one of the most essential steps in the fabrication of high-efficiency solar cells. This chapter focuses on fabricating single-junction devices experimentally in order to investigate their electrical properties. Firstly, various (*i*)a-Si:H passivation strategies for flat (100) c-Si surfaces were explored; then the electrical properties of doped layers were investigated via dark conductivity and activation energy tests. Lastly, solar cells with various RJs as suggested in Chapter 4 (Fig. 5.18) located at the flat front side were fabricated.

The necessary deposition parameters of various (*i*)-layers are shown in table 5.1. The rate of deposition is thickness over time, hence the anticipated deposition time was determined by the necessary thickness.

Table 5.1: Deposition parameters of numerous intrinsic and doped layers.

Parameters	Variations	Units
Substrate Temperature	160	$^{\circ}C$
Pressure inside the Chamber	0.7-2.2	mbar
RF Power	3-6	W
Dilution Ratio	0-3	-
Duration	29-81	sec

Film deposition is a fully automated process. Before utilizing the optimized recipe, the time is computed into the input Excel spreadsheet using optically optimized thickness, and the load and

tune capacitor values are updated after conditioning of the chambers (a process to prepare the chambers for further deposition). Equation 5.1 is the ratio of the flow rate of H_2 to that of SiH_4.

$$\text{Dilution Ratio} = \frac{\text{Flow Rate } (H_2)}{\text{Flow Rate } (SiH_4)} \tag{5.1}$$

5.1. Passivation Optimization

Investigations were done to further enhance passivation quality with different *i*a-Si:H layers:

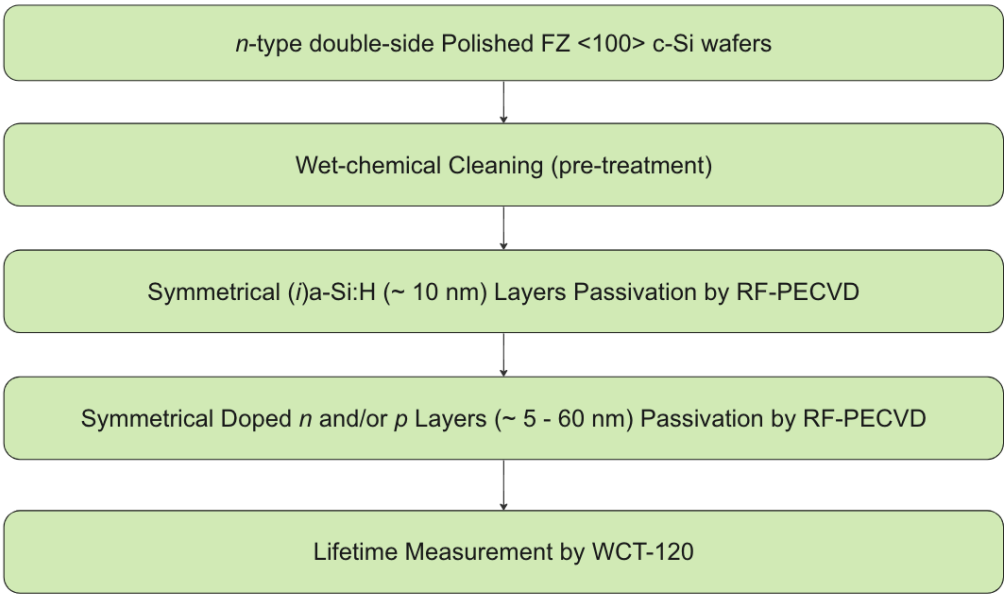

Figure 5.1: Flowchart of depositing (*i*)a-Si:H) layers.

Following investigations were done to further enhance passivation quality with different (*i*)a-Si:H layers:

- 5.1.1 Symmetrical monolayer passivation, (***i*-1**) [160].
- 5.1.2 Symmetrical bilayer passivation, **(*i*-1 + *i*-2)** layer [161, 162], and
- 5.1.3 Symmetrical bilayer passivation with intermediate HPT **(*i*-1 + HPT + *i*-2)** [86] were investigated.

In addition to *i*-layer/*n*-contact, section 5.1.4 represents various passivation of *i*-layers/*p*-contact combination. All of the possible *i*-layers/*p*-contact layer stack combinations are covered in this part and are thoroughly examined and explored. Figure 5.1 represents the process flow chart of symmetrical *i*-layer passivation. Additional research was done on the doped layer's properties, dark IV, and activation energy measurement, covered in section 5.2.

5.1.1. Symmetrical Monolayer Passivation (*i*-1 Layer)

Optimizing numerous intrinsic layers is the main focus of 5.1's experimental methodology section including prior-deposition conditions, film-deposition, characterization, and optimization of these intrinsic layers. In Fig. 5.2, the schematic for the symmetrical passivation of the *i*-layer is depicted. In the first step of this experiment, which is detailed in table 5.2, a pure 40 sccm Silane (SiH_4) plasma induced symmetrical *i*-1 layer with a thickness of 10 nm was deposited under the deposition conditions of 160°C, 0.7 mbar, 3 W, and 13.56 MHz, optimized high-performance deposition conditions by a master student in the earlier study [86].

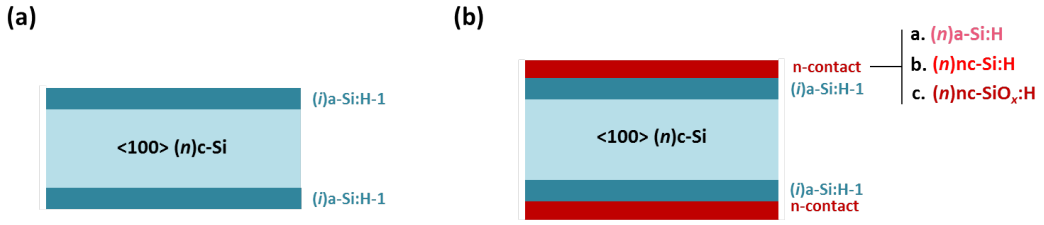

Figure 5.2: Schematics illustrate symmetrical passivation of (a) *i*-layers and (b) *i*-1 layers with n-contact, on the surface of a (100) c-Si wafers.

i. Prior-deposition Conditions

Prior to the fabrication of single-junction SHJ solar cells, several intrinsic layers were optimized with n-type double-sided polished TOPSIL FZ (100) silicon wafers having the resistivity and thickness of (3±2 Ωcm) and thickness (280 ± 20 µm), respectively. To achieve the optimum result, the c-Si surface must be completely free of contamination with low-defect density, it undergoes the wet-chemical wafer cleaning technique (see Chapter 3 section 3.4.2), just before the thin film deposition.

ii. Film Deposition

Following section 5.1.1 (i), wafers are immediately loaded into the Load Lock Chamber (LLC) of the AMIGO to thin film deposition by RF-PECVD following wet-chemical cleaning in CR100 of EKL (Else Kooi Lab). Once all samples have been loaded, the pressure in the LLC is manually adjusted to match the vacuum condition in the deposition chamber (DPC). Chapter 3 goes into great detail on the RF-PECVD process step-by-step.

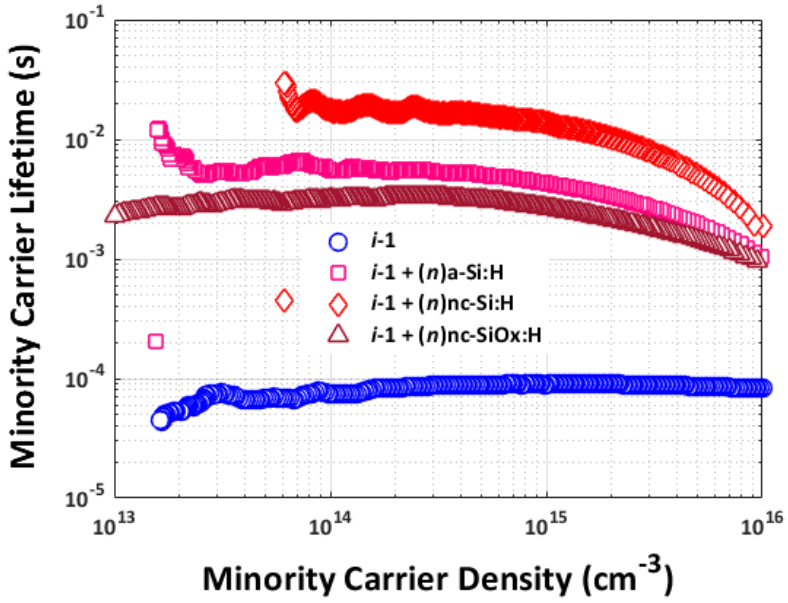

Figure 5.3: Effective minority carrier lifetime of *i*-1 layer with various *n*-contacts.

iii. Experimental Results

It is important to note that there was no additional hydrogen supply, meaning the (*i*)a-Si: H layer was only deposited using silane gas, yielding an effective charge carrier lifetime (τ_{eff}) 0.71 ms.

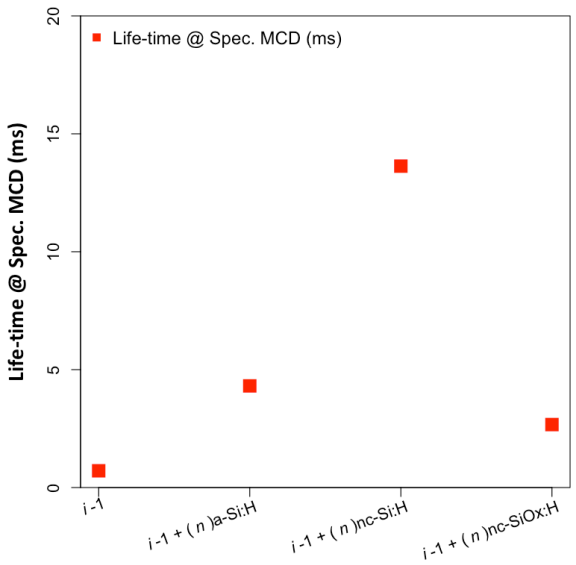

Figure 5.4: Effective minority carrier density and i-V_{oc} comparison of *i*-1 layer with distinct *n*-contacts.

It is known from previous research, at MCD = $10^{15}cm^{-3}$, surface recombination and injection level are dominant (under a one-sun situation)[139], MCD < $10^{15}cm^{-3}$ SRH recombination can be dominent [83], while MCD > $10^{15}cm^{-3}$ favors Auger and radiative recombination.
Monolayer samples deposited on different *n*-contact show a consistent range of injection levels ($10^{13.9}$ to $10^{14.6}$ cm) with higher (τ_{eff}), whereas without *n*-contact the injection level in consistent from ($10^{13.5}$ to 10^{16} cm) with low (τ_{eff}) (see in Fig. 5.3). A quick overview of minority carrier density per layer can be seen in Fig. 5.4.

i-1 + (*n*)nc-Si:H exhibits the highest minority carrier lifetime and implied open circuit voltage i-V_{oc} of any of these *i*-layer samples. Depositing doped *n*-contact [(*n*)a-Si:H (6 nm), (*n*)nc-Si:H (20 nm) or (*n*)nc-SiO_x:H (60 nm) layer] on *i*-1 layer creates strong depletion of holes. This subsequently reduces the trap-assisted recombination (SRH) at the nc-Si:H (or a-Si:H)/c-Si interface [163, 164, 83]. The (τ_{eff}) of a monolayer sample (without the *n*-contact) results (τ_{eff}) and i-V_{oc} of 0.71 ms and 688 mV respectively. While depositing a (n)a-Si:H (6 nm), (n)nc-Si:H (20 nm), or (n)a-Si:H (60 nm) layers on top of a 10 nm *i*-1, resultant (τ_{eff}) and i-V_{oc} are 4.31 ms, 13.63 ms, 2.67 ms and 713 mV, 742 mV, 708 mV respectively.

Summary

The reduction of recombination in low injection scale ($10^{13}cm^{-3}to10^{14}cm^{-3}$) to high injection scale ($10^{15}cm^{-3}to10^{16}cm^{-3}$) leads to an impressive improvement of (τ_{eff}) (0.71 to 13.63 ms). Figure 5.3 illustrates the exhibit of improved i-V_{oc} for this series, which ranges from 708 to 742 mV.

5.1.2. Symmetrical Bilayer Passivation (*i*-1 and *i*-2)

The bilayer deposition schematic is shown in Fig. 5.5 where (a) represents the bilayer passivation (*i*-1 and *i*-2) and (b) represent several *n*-contacts [(*n*)a-Si:H (6 nm), (*n*)nc-Si:H (20 nm) or (*n*)nc-SiO_x:H (60 nm) layer], deposited on *i*-1 and *i*-2 layers with various thickness. This symmetrical bilayer passivation is a **two-step** deposition strategy where on a flat (100)c-Si surface :

– ***i*-1 :** It is the first layer of intrinsic amorphous silicon. This ultra-thin (~5 nm) intrinsic layer can be deposited with pure silane plasma ignition for around 29 sec under a deposition pressure of 0.7 mbar.

– ***i*-2 :** On top of *i*-1, another ultra-thin (5 nm) intrinsic layer *i*-2 was deposited with a higher hydrogen dilution ratio (3) for around 32 sec under 1.4 mbar.

The advantage of the bilayer over the s (*i*)a-Si:H layer is that the (*i*)a-Si: H-2 can supply more hydrogen H_2 during its deposition to the c-Si/(*i*)a-Si: H interface, therefore benefiting the passivation quality [161].

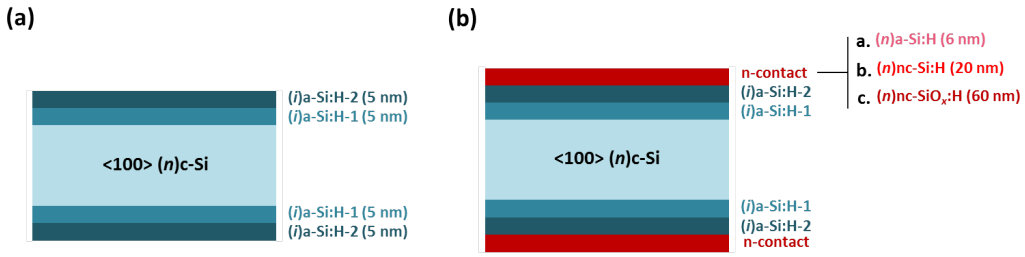

Figure 5.5: Schematics illustrate symmetrical passivation of (a) bilayer (*i*-1 & *i*-2) and (b) bilayer (*i*-1 & *i*-2) with *n*-contact, on the surface of a <100> c-Si wafers.

i. Film Deposition

There is a slightly changed in deposition parameter to deposit *i*-2 layer (5 nm), more specifically the hydrogen H_2 dilution ratio is increased from 0-3 with 1.4 mbar pressure (see table 5.5), however, to deposit the *i*-1 layer all deposition parameters remained the same as before.

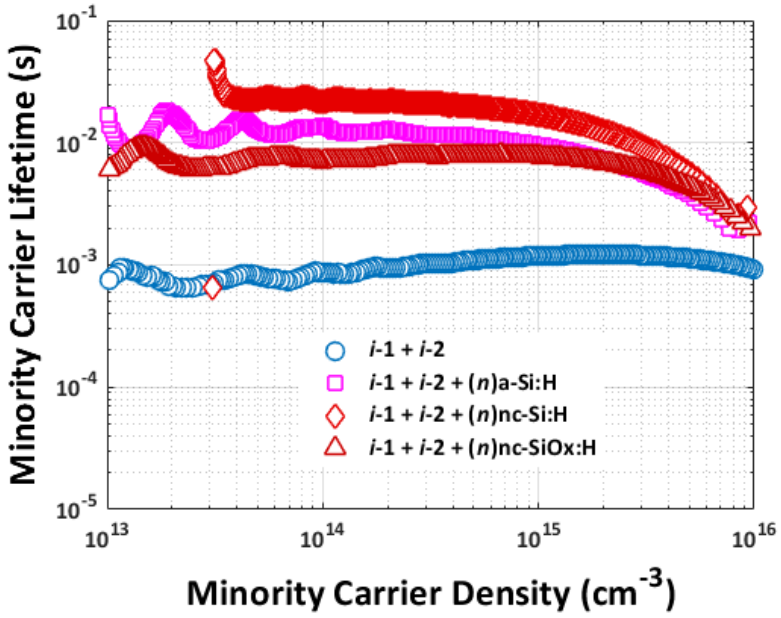

Figure 5.6: Effective minority carrier lifetime of *i*-1 layer with various *n*-contacts.

ii. Experimental Results

In comparison to monolayer deposition, bilayer deposition has an increased effective charge carrier lifetime (τ_{eff}) because of the additional 30 sccm H_2 supply. The FF and i-V_{oc} are indicated as 16.87 ms and NaN mV, respectively.
While depositing *n*-layers on the top of bilayer *i*-layers, a consistent range of injection level ($10^{13.6}$

to $10^{14.9}$ cm) with higher (τ_{eff}) can be observed from Fig. 5.6, while growing bilayers without *n*-contact the range is from $10^{14.2}$ to $10^{13.5}$ cm with a lower (τ_{eff}). A quick overview of minority carrier density per layer can be seen in Fig. 5.7. Several *n*-contacts were placed on top of the *i*-bilayer to assess the results, following the same pattern as monolayer deposition. The bilayer sample without any *n*-contact results (τ_{eff}) and i-V_{oc} of 1.18 ms and 704 mV respectively. While depositing a (*n*)a-Si:H (6 nm), (*n*)nc-Si:H (20 nm), or (*n*)a-Si:H (60 nm) layers on top of a 10 nm *i*-1, resultant (τ_{eff}) and i-V_{oc} are 9.56 ms, 16.87 ms, 7.69 ms and 776 mV, NaN, 734 mV respectively. *i*-bilayer with (*n*)nc-Si:H sample reached 16.87 ms (τ_{eff}). While the *i*-bilayer was being deposited between (*n*)nc-Si:H and c-Si, see Fig 5.6 and 5.7, a very high minority charge carrier lifetime and minority charge carrier density. This establishes the increased passivation of dangling bonds as well as the fact that more H_2 assisted (with a dilution ratio of 3) in supplying hydrogen to the a-Si:H/c-Si interface.

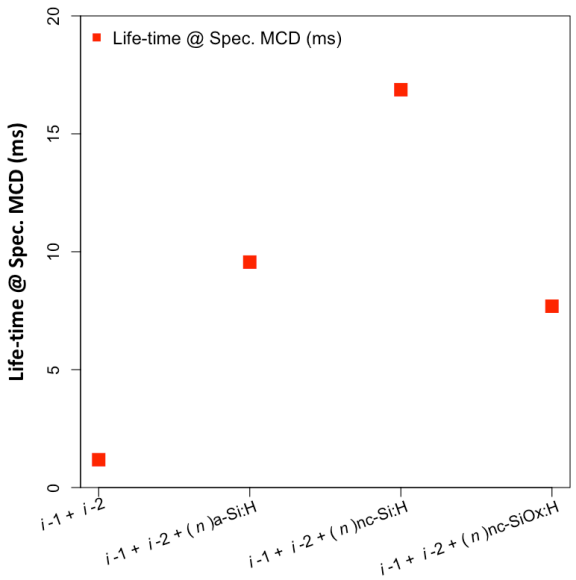

Figure 5.7: Effective minority carrier density and i-V_{oc} comparison of *i*-1 & *i*-2 layers with distinct n-contacts.

Summary

Depositing a 20 nm thin (*n*)nc-Si:H layer on top of two thin bilayer samples, (5 + 5 nm of *i*-1 and *i*-2 layers), with different H_2 dilution ratio shows a significant improvement of (τ_{eff} = 16.87 ms) over the results of the *i*-1 (10 nm) layer without additional H_2 (τ_{eff} = 13.63 ms). Because of the different deposition conditions of the *i*-2 layer (with more H_2) allows more H_2 incorporation into the *i*-1 the resultant i-V_{oc} also improved from 742 mV to NaN (very high value) for this same sample. Moreover, comparing the samples with two other types of *n*-contact (a-SiO_x:H andnc-SiO_x:H) the sample with (*n*)nc-Si:H layer shows the highest τ_{eff}. This is because the bias voltage is the highest during the deposition ofnc-SiO_x:H, which means the highest ion bombardment happens during the film deposition which can be prone to more defect near c-Si/(*i*)a-Si:H interface.

5.1.3. Symmetrical Bilayer Passivation with Intermediate HPT (*i*-1 + HPT + *i*-2).

In order to passivate the recombination centers, HPT works by causing hydrogen radicals to diffuse into the layer and to the (*i*)a-Si:H/c-Si interface. It is worth noting that HPT may induce etching of the film. In this experiment, the thickness remained constant with bilayer samples, due to the rather short (200 sccm) HPT applied, to investigate the performance and compare with different types of passivating layers (monolayer and bilayer).

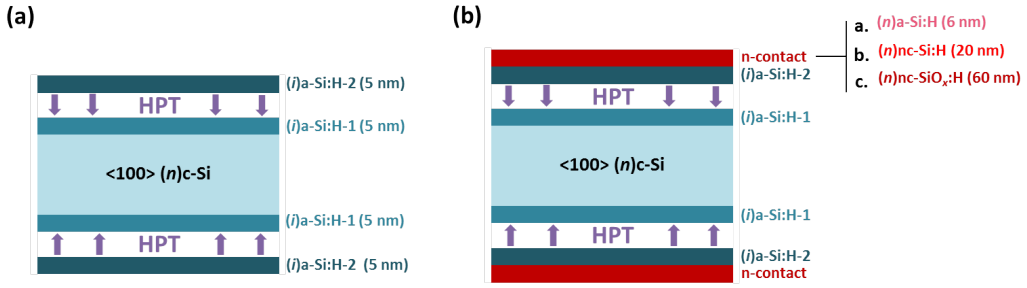

Figure 5.8: Schematics illustrate symmetrical passivation of (a) *i*-1+ HPT+*i*-2 and (b) *i*-1+HPT+ *i*-2 with various *n*-contact, on the surface of (100) c-Si wafers.

i. Film Deposition

Similar to bilayer *i*-layer deposition conditions, the intermediate Hydrogen Plasma Treatment (HPT) was examined with a specific deposition condition (see in table 5.5).

ii. Experimental Results

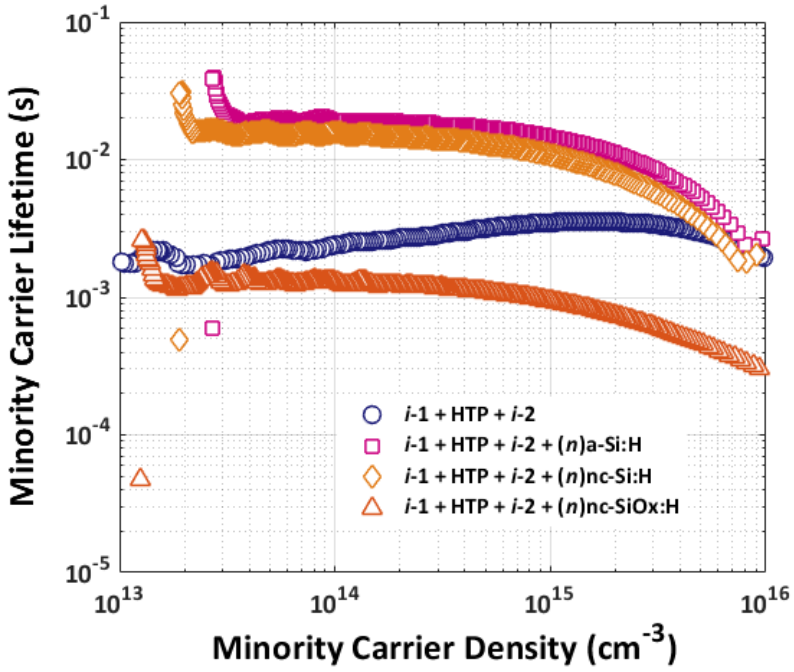

Figure 5.9: Minority carrier lifetime measurements of bilayer (*i*-1 + HPT + *i*-1) with intermediate HPT and different *n*-layers.

Minority carrier lifetime measurements of bilayers (*i*-1 & *i*-1) with intermediate HPT and various *n*-layers are shown in Fig. 5.9. With a consistent range of injection level (10^{14} to 10^{16} cm), growing bilayers with intermediate hydrogen plasma treatment (*i*-1 + HPT + *i*-2) without any *n*-contact clearly results better than the bilayer samples without HPT. The *i*-1 + HPT + *i*-2 sample without the *n*-contact results (τ_{eff}) and i-V_{oc} of 3.48 ms and 726 mV respectively. While depositing a (*n*)a-Si:H (6 nm), (n)nc-Si:H (20 nm), or (*n*)a-Si:H (60 nm) layers on top of a 10 nm *i*-1, resultant (τ_{eff}) and i-V_{oc} are 14.62 ms, 10.81 ms, 0.94 ms and 789 mV, 768 mV, 676 mV respectively.

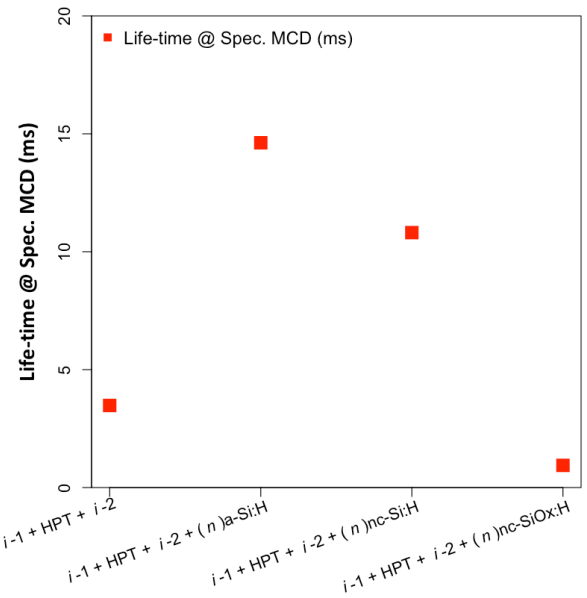

Figure 5.10: Effective minority carrier density and i-V_{oc} comparison of *(*i-1 + HPT + *i*-2) layers with distinct *n*-contacts.

Summary

The *i*-1 + HPT + *i*-2 sample (τ_{eff}) without the *n*-contact results (τ_{eff})and i-V_{oc} of 3.48 ms and 726 mV respectively. While depositing a (*n*)a-Si:H (6 nm), (*n*)nc-Si:H (20 nm), or (*n*)a-Si:H (60 nm) layers on top of a 10 nm *i*-1, resultant (τ_{eff}) and i-V_{oc} are 14.62 ms, 10.81 ms, 0.94 ms and 789 mV, 768 mV, 676 mV respectively. Applying HPT of (200 sccm) shows better improvement for the *i*-layer with (*n*)a-Si:H layer of τ_{eff} = 14.62 ms than the bilayer sample τ_{eff} = 9.56 ms.

5.1.4. Symmetrical Passivation of *i*-layers with *p*-contact

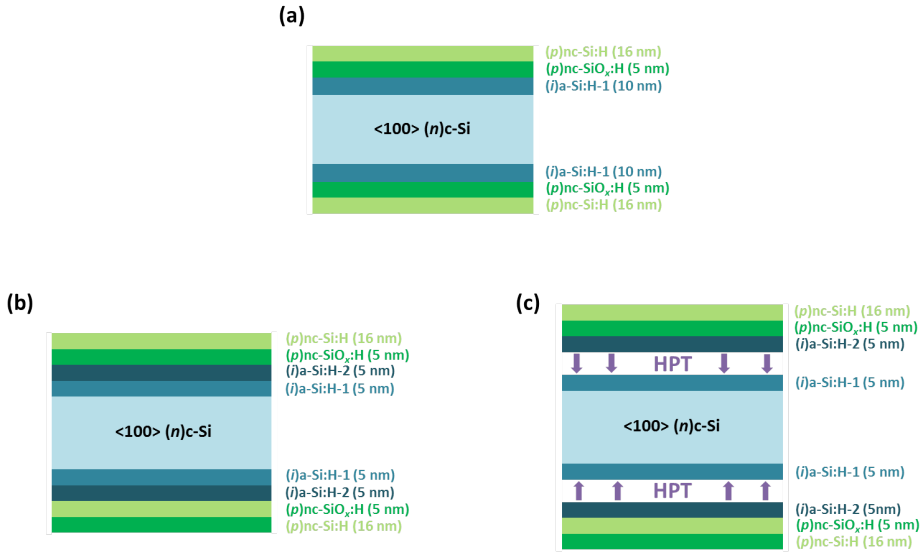

Figure 5.11: Schematics illustrate symmetrical passivations : (a) (*i*-1) + *p*-contact, (b) (*i*-1+ *i*-2) + *p*-contact and (c) (*i*-1+ HPT + *i*-2) + *p*-contact , on the surface of a <100> c-Si wafers.

i. Literature Review

By incorporating each variation of the *i*-layers passivation with *p*-contact, mentioned in the previous section, to investigate the effective charge carrier lifetime and i-V_{oc} employ it for the manufacturing of crystalline silicon SHJ solar cells. Note, the passivation optimization of *i*/*p*- contact stack is to fabricate front junction bottom cells, which can be further combined with nip perovskite top cells forming 2T tandem devices.

ii. Film Deposition

In order to investigate the effective charge carrier lifetime and i-V_{oc}, samples were prepared and investigated with pre-optimized parameters, see in table 5.4. The schematic of the samples can be seen in Fig.5.12 where (a). describes the schematic of bilayer *p*-contact with an *i*-1 layer passivation, (b). represents the schematic of bilayer *i*-layer passivation (*i*-1 + *i*-2) layers, and (c). represents the schematic of *p*-contact and bilayer *i*-layer passivation with intermediate HPT (*i*-1 + *i*-2 layers).

iii. Experimental Results :

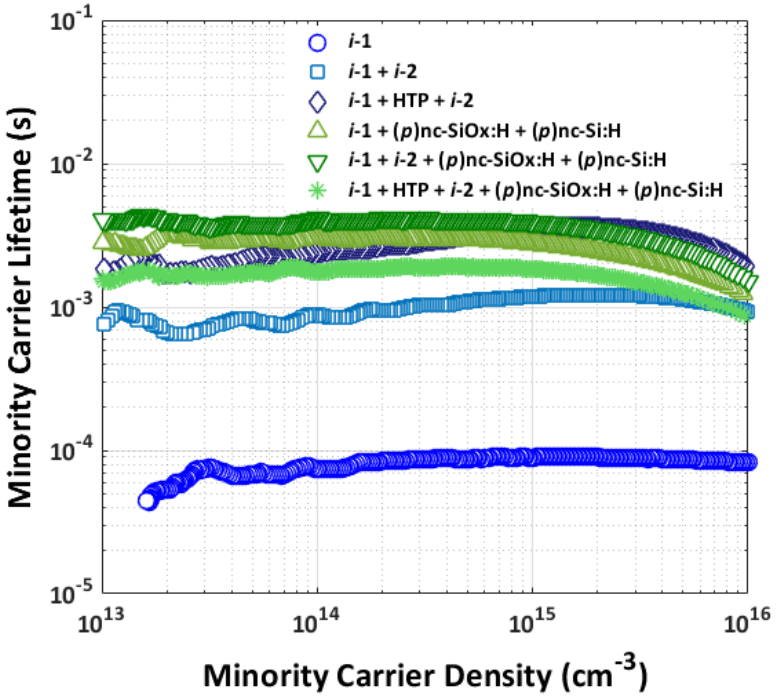

Figure 5.12: Minority carrier lifetime measurements using *p*-contacts with various *i* (*i*-1 & *i*-2) layers.

The higher injection takes place in the range of 10^{14} to 10^{15} cm^{-3} is dominated by SRH recombination, where the excess charge carrier concentrations injected under the forward bias conditions have a large enough lifetime to modify the electrostatics of majority carriers in the quasi-neutral regions [165].

Compared with the other two samples with (*i*-1)/*p*-contact and (*i*-1 + HPT + *i*-2)/*p*-contact, the sample of the bilayer (*i*-1 + (*i*-2)/ with bilayer *p*-contact shows better τ_{eff} and i-V_{oc} of 3.92 ms and 721 mV respectively, as shown in Fig 5.12 and 5.13. *i*-1/*p*-contact, (*i*-1 + *i*-2)/*p*-contact and (*i*-1 + HPT + *i*-2)/*p*-contact

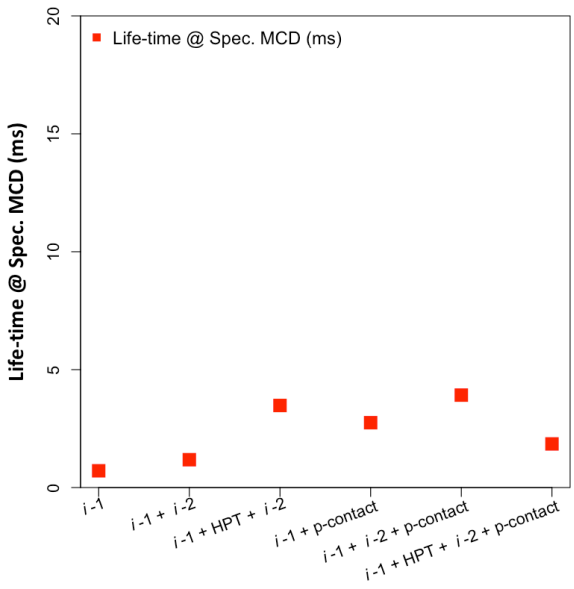

Figure 5.13: Effective minority carrier density and i-V_{oc} comparison of *i*-layers with distinct *p*-contacts.

Summary :

Overall, samples with symmetrical passivation of (*i*-1 + *i*-2)/*p*-contact stacks combination shows better results with highest τ_{eff} and i-V_{oc} as 3.92 ms and 721 mV respectively.

5.1.5. Summary of *i*-layer Passivation:

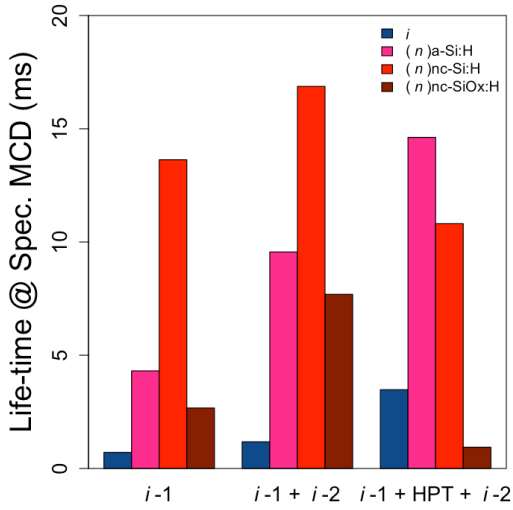

Figure 5.14: Effective lifetime (τ_{eff}) of flat (100)c-Si samples with symmetrical passivation: *i*-1 (10 nm), *i*-1 (5 nm) + *i*-2 (5 nm), *i*-1 (5 nm) + HPT + *i*-2 (5 nm) and different (*n*)-layers (a-Si:H (6 nm), nc-Si:H (20 nm),nc-SiO_x:H (60 nm).

In a nutshell, comparing among (*i*-1)/*n*-contact, (*i*-1 + (*i*-2)/*n*-contact and (*i*-1 + HPT + *i*-2)/*n*-contact samples, (*i*-1 + (*i*-2)/*n*-contact sample shows highest τ_{eff} and i-V_{oc} as 16.87 ms and NaN respectively. As mentioned in the earlier discussion, comparatively thicker contact, (*n*)a-Si:H (6

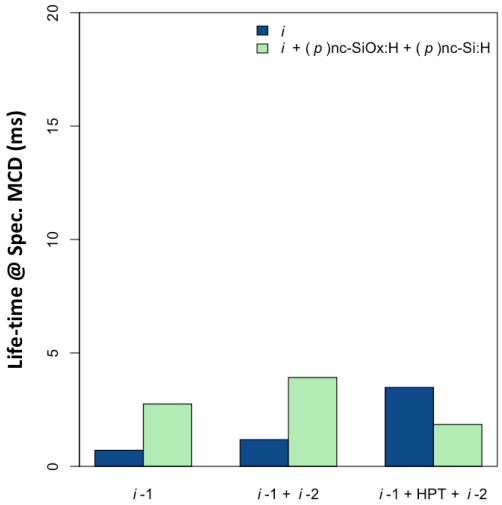

Figure 5.15: Effective lifetime (τ_{eff}) of flat (100)c-Si samples with symmetrical passivation: *i*-1 (10 nm), *i*-1 (5 nm) + *i*-2 (5 nm), *i*-1 (5 nm) + HPT + *i*-2 (5 nm) and different (*p*)-layers (nc-Si:H (5 nm), nc-SiO$_x$:H (16 nm).

nm), (*n*)a-Si:H (20 nm), (*n*)nc-SiO$_x$:H (60 nm), was deposited on top of *i*-layers. The reasons are : (a) comparing with (*n*)a-Si:H, (*n*)nc-Si:H needs to reach a specific thickness to assure the crystal growth and (b) we want to test if a thicker *n*-layer (which is optically beneficial for the 2T tandem application, see in chapter 4) can have good passivation quality.
In a similar pattern, bilayer *p*-contact of (*p*)nc-SiO$_x$:H (5 nm)/(*p*)cn-Si:H (16 nm) layer stacks electrically works better in the rear junction. The FF can be improved when depositing the low E_a material (*p*)nc-Si:H on top of ITO [15]. The highest τ_{eff} and i-V_{oc} as 3.92 ms and 721 mV respectively. However, The combination works better for all samples with *i*/*n*-contact combinations perform better than those with *i*/*p*-contact combinations, see in Fig 5.14 and 5.15. The possible reasons could be : (a) attributed to defect formation in the *i*-layer as a result of shifting the Fermi level due to the overlaying *p*-layer stack [166, 167, 168, 169] and (b) excessive annealing effect of read side *i*/*p* stack while depositing the front side layer stacks [166, 167]. It is important to further investigate the deposition conditions of the *p*-layer stack for better passivation quality.

5.2. Optimizing Doped nc-SiO$_x$:H Layers

i. Activation Energy

To investigate the electrical properties of doped nc-SiO$_x$: H layers activation energy (E_a) and dark conductivity (σ_d) measurements were performed. For *n*-layers it it preferred to have lower E_a, whereas for the *p*-layers both wider bandgap (E_G) and lower E_a are considered [84]. The E_a indicates doping of the layer, which affects the selective transport of charge carriers [170]. material doping efficiency and influences tunneling probability. The energy difference can be expressed as:

- Fermi Level to Conduction band, $E_a = E_C - E_F$, for *n*-type material, and
- Fermi Level to Valence band, $E_a = E_F - E_V$ for *p*-type material.

The E_a of optimized layers must be measured in order to assess device performance properly. Lower activation energy is usually correlated with better conductivity. Doped layers were deposited on corning glasses to study dark IV characteristics, and a post-annealing process (> 130 °C) was used to enhance crystallinity by reordering ions and surface roughness. Corresponding

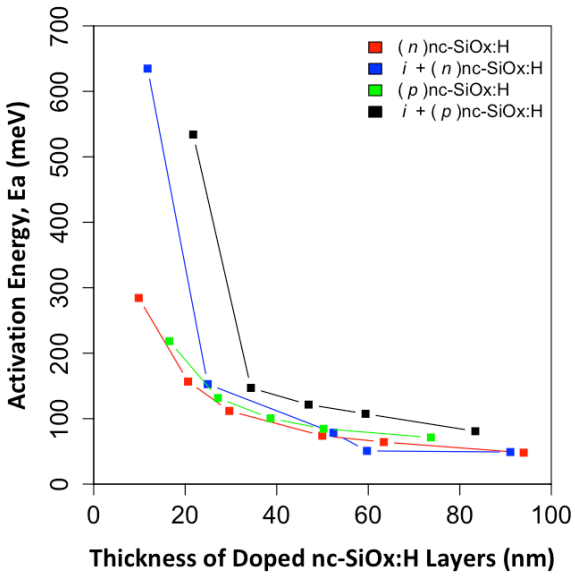

Figure 5.16: Thickness of doped nc-SiO_x:H layer (nm) vs Activation Energy,E_a (meV).

conductivity σ_d of the prepared samples (10-100 nm) were determined over the substrate temperature range of (130°C to 60°C), with bias voltage 100 V, 10 V, and 1 V (voltage decrease with increasing conductivity of the films).

The thickness-dependent Ea curves are shown in Fig. 5.16 for four different types of nc-SiO_x:H samples in two main categories, such as, **monolayer samples:** *n*-layers (in red), and *p*-layers (in green), and, **bilayer samples:** *i*/*n*-layers (in blue) and *i*/*p*-layers (in black). *n*-layers samples with a thickness of 9.84 nm, 20.63 nm, 29.64 nm, 49.95 nm, 63.4 nm and 93.96 nm show the E_a of 284.39 meV, 156.68 meV, 111.81 meV, 73.86 meV, 65.92 meV and 48.03 meV respectively. The thickest sample 93.96 nm shows the lowest

ii.Dark Conductivity :

Conductivity is the ability of a substance to allow the flow of an electric current. Dark conductivity (σ_d) can be defined as:

$$\sigma_d = q(n\mu_n + p\mu_p) \tag{5.2}$$

Equation 5.2 shows that the σ_d depends on the total charge carrier density and mobility, μ_n or μ_p [84].

The thickness-dependent σ_d curves are shown in Fig. 5.17 for four different types of nc-SiO_x:H samples, measured in two main categories, such as **monolayer samples:** *n*-layers (in red), and *p*-layers (in green), and, **bilayer samples:** *i*/*n*-layers (in blue) and *i*/*p*-layers (in black). The c-Si/*i*a-Si:H interface's field-effect passivation is related to the E_a or σ_d of doped silicon layers. The investigation of this electrical attribute is necessary because it affects the selective transport of charge carriers and thus the performance of solar cells as introduced before. Fig. reveals higher conductivity (3.6E-06 - 3.5E-01 S/cm) when monolayer samples with *n*-contact (10-50 nm) samples were optimized compared to *p*-contact samples (4.8E-08 - 6.7E-02 S/cm). The bilayer samples with *i*/*i*-contact layer stacks also followed the same trend. The thickness range (50-100 nm) does not exhibit substantial variation among σ_d, aside from the*n*-layers' increased conductivity. A summary of thickness dependent E_a and σ_d measurement can be seen in the table 5.2

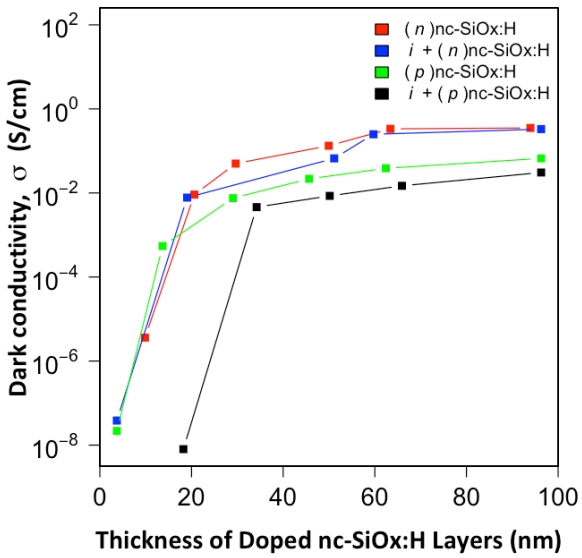

Figure 5.17: Thickness of doped nc-SiO$_x$:H layer (nm) vs Dark Conductivity, σ_d (S/cm).

Table 5.2: Activation Energy (E$_a$) and Dark Conductivity (σ_d) of nc-SiO$_x$ and *i*/nc-SiO$_x$ layers

Layers	E$_a$ (meV)	DarkConductivity (S/cm)	Thickness (nm)
(*n*)nc-SiO$_x$	284.39	3.62E-06	9.84
(*n*)nc-SiO$_x$	156.68	9.14E-03	20.63
(*n*)nc-SiO$_x$	111.81	5.00E-02	29.64
(*n*)nc-SiO$_x$	73.86	1.33E-01	49.95
(*n*)nc-SiO$_x$	65.92	3.30E-01	63.4
(*n*)nc-SiO$_x$	48.03	3.51E-01	93.96
i/(*n*)nc-SiO$_x$	622	3.99E-08	11.77
i/(*n*)nc-SiO$_x$	165.1	1.08E-03	24.91
i/(*n*)nc-SiO$_x$	79.25	6.86E-02	52.38
i/(*n*)nc-SiO$_x$	56.45	1.90E-01	59.72
i/(*n*)nc-SiO$_x$	49.22	3.34E-01	91.05
(*p*)nc-SiO$_x$	218.33	5.44E-04	16.5
(*p*)nc-SiO$_x$	131.6	7.53E-03	27.14
(*p*)nc-SiO$_x$	100.55	2.1E-02	38.64
(*p*)nc-SiO$_x$	84.51	3.86E-02	50.23
(*p*)nc-SiO$_x$	71.29	6.65E-02	73.7
i/(*p*)nc-SiO$_x$	652.25	2.22E-10	21.74
i/(*p*)nc-SiO$_x$	147.01	4.60E-03	34.96
i/(*p*)nc-SiO$_x$	121.43	8.53E-03	46.96
i/(*p*)nc-SiO$_x$	107.42	1.48E-02	59.41
i/(*p*)nc-SiO$_x$	80.81	3.07E-02	83.43

Collecting electrons at a-Si:H/c-Si interface is followed by trap-assisted or direct tunneling in the conduction band as ITO is *n*-type-like. However, poor doping concentration reduces Ea thus the Schottky barrier, which can hinder electron collection to the electrode, forms in the *n*-type/ITO interface. Transport mechanisms of the *n*-type/ITO interface can be direct tunneling, thermionic emissions, trap-assisted, or direct tunneling.
Similarly, collecting holes at the a-Si:H/c-Si interface is followed by trap-assisted or direct tunneling or thermionic emission, whereas the efficient collection can be manipulated by the size of the energy barrier, the conductivity of ITO and the band bending induced by c-Si [170]. This means holes must tunnel through the so-called band-to-band tunneling in the *p*-layer/ITO interfaces. Band gap, doping concentration, and work function mismatch can affect the device's FF. Prior reveals that for high doping concentration of *p*-layer, which results in low E_a, TCO' work function is not decisive for hole collection [23]. A better match of work function may be achieved with moderated doping and thickness tuning [171]. Overall it is important to optimize the thickness-dependent doping concentration of the doped layer for better performance of the device.

5.3. Optimizing Single-side-textured single-junction SHJ Solar Cells for TCO-free RJ Layers

The fabrication and electrical properties optimization of single-side-textured SHJ solar cells are covered in this section. Single-side-textured SHJ solar cells can be constructed as either a rear junction (with rear emitter) or a front junction (with front emitter) device, as was previously discussed in chapter 1, section 1.3.4. Due to the greater optical response of front *n*-contact [61] of top cell that may lead to higher PCE, [51, 55], monolithic 2T tandem solar cells are typically developed with the 'p-i-n' configuration of the top cell and rear junction bottom cell, see Fig. 5.18. Considering the high purity of FZ wafers, these wafers were chosen to fabricate single-junction SHJ solar cells. A detailed fabrication process is introduced in chapter 3, followed by the deposition parameters mentioned in tables 5.3, 5.5, and 5.4.

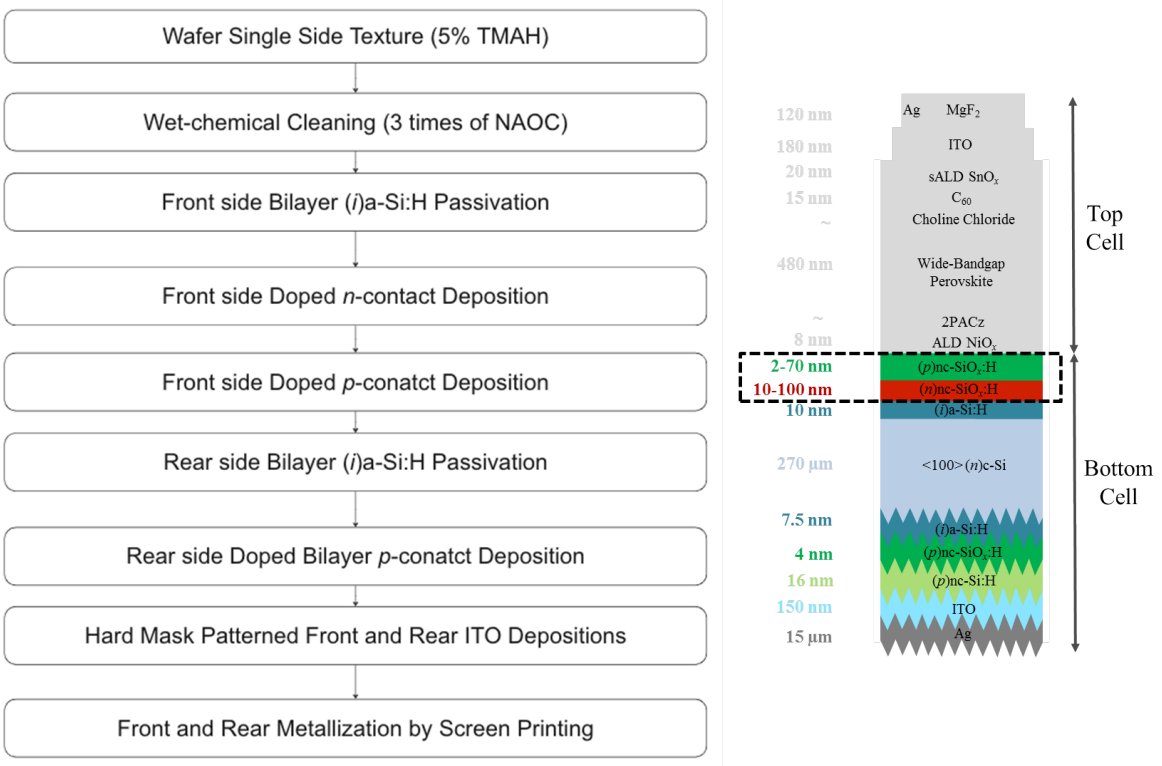

Figure 5.18: A process flowchart of SHJ solar cell fabrication w/ the highlighted bottom device' architecture.

Table 5.3: Deposition parameters of doped Si layers.

Parameters	Variations	Units
Substrate Temperature	180	$^{\circ}C$
Pressure inside the Chamber	0.6-2.7	mbar
RF Power	4-13	W
Dilution Ratio	100-212	-
Duration	81-3630	sec

Table 5.4: Deposition parameters of ITO layers

Layer	T_S [$^{\circ}C$]	Argon [sccm]	Pressure [mbar]	Power [W]	Frequency [MHz]	Area [inch]	Thickness [nm]
ITO	25	45	2E-2	130	13.56	4	75-150

Table 5.5: Deposition parameters of Single-side-textured Single-junction SHJ solar cells (front layers stacks)

Layer	T_S [$^{\circ}C$]	SiH_4 [sccm]	B_2H_6 (200ppm in H_2) [sccm]	PH_3 (2% in H_2) [sccm]	CO_2 [sccm]	H_2 [sccm]	Pressure [mbar]	Power [W]	Frequency [MHz]
(i-1)a-Si:H	160	40	-	-	-	-	0.7	3	13.56
(*i*-2)a-Si:H	160	10	-	-	-	30	1.4	3	13.56
HPT	160	-	-	-	-	200	2.2	6	13.56
(*n*)a-Si:H	180	40	-	11	-	-	0.6	4	13.56
(*n*)nc-SiO_x:H	180	1	-	1.2	1.6	100	2.7	11	13.56
(*n*)nc-Si:H	180	1	-	1.2	-	100	2.7	11	13.56

Table 5.6: Deposition parameters of Single-side-textured Single-junction SHJ solar cells (rear layers stacks)

Layer	T_S [$^\circ C$]	SiH_4 [sccm]	B_2H_6 (200ppm in H_2) [sccm]	PH_3 (2% in H_2) [sccm]	CO_2 [sccm]	H_2 [sccm]	Pressure [mbar]	Power [W]	Frequency [MHz]
(i-1)a-Si:H	160	40	-	-	-	-	0.7	3	13.56
(i-2)a-Si:H	160	10	-	-	-	30	1.4	3	13.56
HPT	160	-	-	-	-	200	2.2	9	13.56
HPT	160	1.2	-	-	-	120	4	13	40.68
(*p*)nc-SiO_x:H	180	0.8	10	-	1.4	170	2.2	11	13.56
(*p*)nc-Si:H	180	0.8	10	-	-	-	2.2	13	13.56

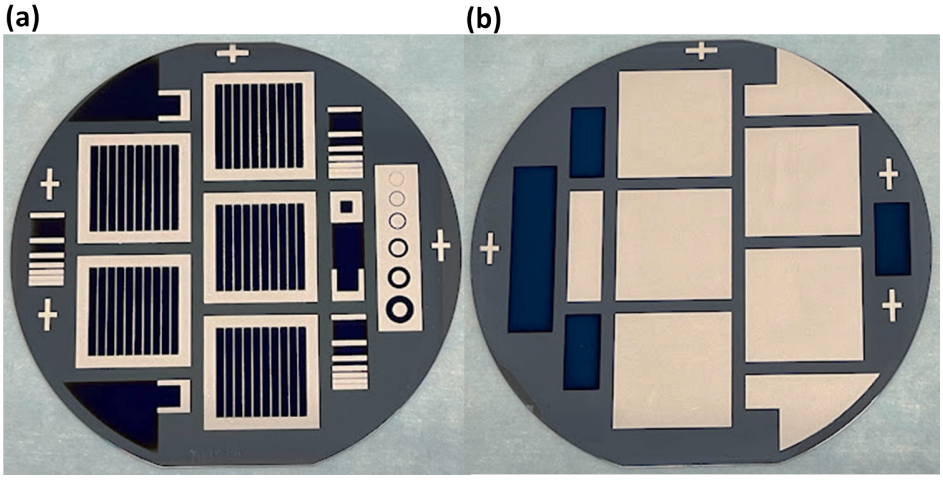

Figure 5.19: Front (a) and rear (b) side of a Single-side-textured Single-junction SHJ solar cell.

5.4. Single-junction SHJ Solar Cells with Oxidic RJ

The outcomes of the single-junction SHJ solar cells are discussed in this section. The front side was optically optimized, more specifically, the previously optimized (*n*)a-Si:H layer was replaced with (*n*/*p*)nc-SiO_x:H, to form the *n*-contact or RJ, in order to build TCO-free monolithic 2T tandem SC. More charge carriers can tunnel through recombination (good recombination) thanks to this (*n*/*p*)nc-SiO_x:H junction, which is meant to increase recombination [73]. While the rear side was pre-optimized with respect to 2T tandem applications.

5.4.1. J-V measurement

i. Comparison Among Distinct (*p*)nc-SiO$_x$:H Layers

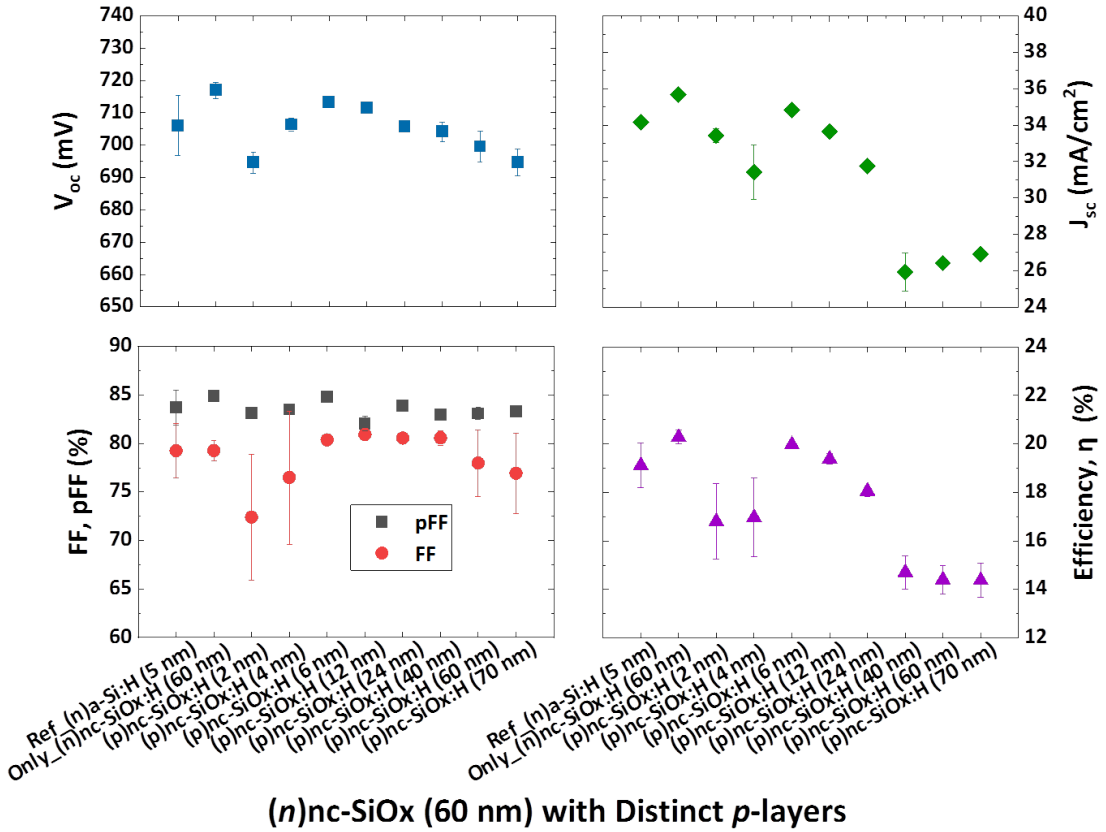

Figure 5.20: J-V Parameters of Single-side-textured SHJ solar cells fabricated by 60 nm (*n*)nc-SiO$_x$:H (60 nm) layers with distinct (*p*)nc-SiO$_x$:H layers.

The illuminated J-V characteristics are measured from the finished single-side-textured SHJ solar cells. Bilayer passivation was used to create all cells, as was previously mentioned. The front side of solar cells fabricated with (*n*)nc-SiO$_x$:H (60 nm) layers with distinct (*p*)nc-SiO$_x$:H layer demonstrated in Fig.5.20. Here the first two samples, prepared with (*n*)a-Si:H and (*n*)nc-SiO$_x$:H (w/o (*p*)nc-SiO$_x$:H layer on top of (*n*)nc-SiO$_x$:H layer), only are presented as references.
The mentioned thicknesses are taken from the optical simulation of 2T device (see Fig. 5.23 and 5.22). The gradually decreasing trend of J_{sc}, in the range of 33.42 to 26.91 mA/cm^2 with the increasing thickness of (*p*)nc-SiO$_x$:H layer was investigated. Eventually, the efficiency also gradually decreases from 16.81% to 14.38% by following the same trend. However, achieving the highest FF is the most challenging as it is considerably the prominent limiting factor to fabricating high-efficiency solar cells. The highest average FF is 78.2% and the highest FF is 81% for the sample with 12 nm (*p*)nc-SiO$_x$:H (12 nm). The ΔFF is defined as the difference between pFF measured from SunsV_{oc} and FF were measured from illuminated J-V characterization, more specifically ΔFF = pFF - FF, where the greater the ΔFF means the higher value of the charge carriers' resistivity (R_s). For the optimized sample with (*p*)nc-SiO$_x$:H layer (6 nm), ΔFF = 4.4%, is more highly resistive for charge carriers transportation, which may cause the reduction of J_{sc} from that device. However, FF can also be limited by high $Rs_{SunsVoc}$ (0.56 Ωcm^2).

Minority carrier lifetime was determined in single-junction solar cells in three steps: after RF-PECVD, after RF-PVD, and after annealing. The results were 7.79 ms→3.92 ms→5.58 ms for the flat side and 7.9 ms→3.90 ms→5.58 ms for the textured side. The shorter minority carrier lifetime suggests that the defect rate rose following the sputtering of the ITO layer. Traces (see Fig. 5.38)

that are diffused into doped layers or c-Si absorbers have the potential to reduce shunt resistance and have an impact on total V_{oc} and FF.

ii. Comparison Among Distinct (*n*)nc-SiO$_x$:H Layers

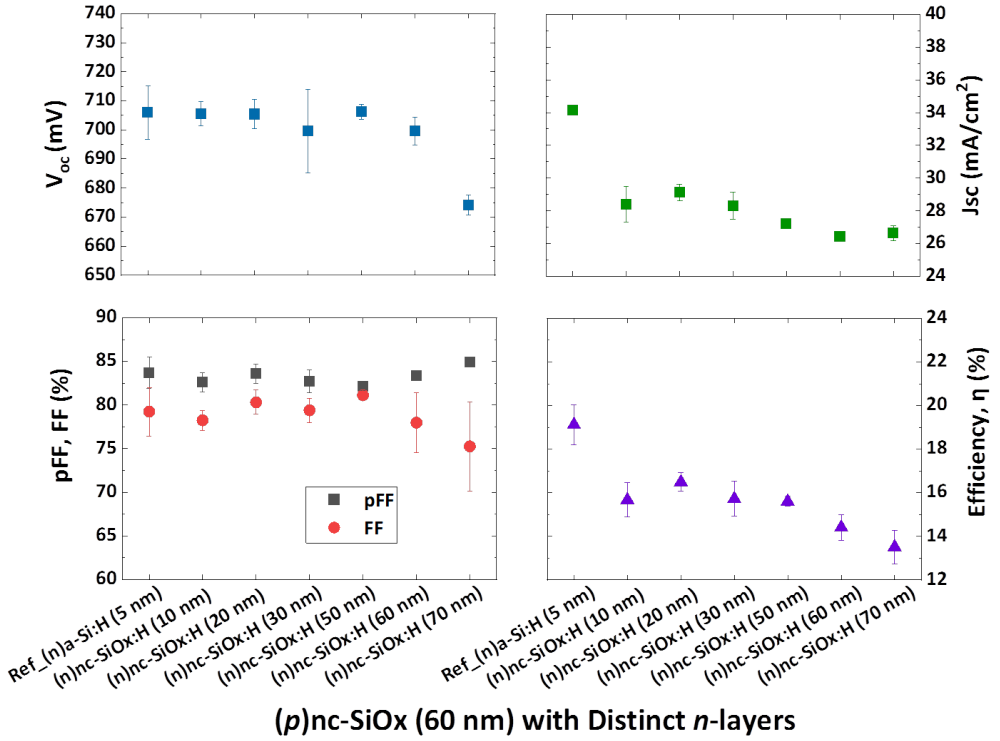

Figure 5.21: J-V Parameters of Single-side-textured SHJ solar cells fabricated by 60 nm (*p*)nc-SiO$_x$:H (60 nm) layers with distinct (*n*)nc-SiO$_x$:H layers.

In this part, the J-V parameters of single-side-textured SHJ solar cells were fabricated by (*p*)nc-SiO$_x$:H (60 nm) layers with distinct (*n*)nc-SiO$_x$:H layers. A similar trend was followed to choose the thickness parameters of RJ layers, which are taken from the optical simulation of 2T device (see Fig. 5.23 and 5.22). While manufactured with the optically optimal thickness rang and optically simulated single-junction solar cell with 20 nm (*n*)nc-SiO$_x$:H layer (Fig. 5.21) V_{oc} achieves 705.4 mV, with an average of 699.6 mV. The J_{sc}, FF, and efficiency are 29.11 mA/cm^2, 80.31%, and 16.49% respectively. The measured V_{oc}, J_{sc}, FF and efficiency are in the range of (699.6-706.2 mV), (26.42-29.11 mA/cm^2), (77-81.12%) and (14.41-16.49%) respectively, as shown in Fig. 5.21. The higher ΔFF is noted in the range of ΔFF = 9.65% to 1.02% where the optimized sample of this series of experiments, which is (*n*)nc-SiO$_x$:H layer that is 20 nm, shows ΔFF= 3.3% also indicates the increasing value of R_s which leads to a low FF of the device. With an exception the sample with 70 nm thick (*n*)nc-SiO$_x$:H layer, which results in comparatively low J-V parameters (V_{oc} = 674.8 mV and FF = 75.25%), thicker *n*-layer shows better performance compared to thicker *p*-layer samples. However, FF can also be limited by pretty $Rs_{SunsVoc}$ (0.88 Ωcm^2).

Fig.5.21 shows that, the device with thin (*n*)nc-SiO$_x$:H layer that is 20 nm, deposited in between (*i*)-layers and thick (*p*)nc-SiO$_x$:H layer of 60 nm, performs the best among all other combinations. The results are shown in table 5.7. Before depositing window layers, buffer layers were deposited on the substrate to form a heterojunction structure and surface passivation. The measured effective carrier lifetime for the flat side is 3.65 ms→6.53 ms and for the textured side is 3.52 ms→6.53 ms following TCO deposition and post-annealing operation, which may have an influence on the resultant J-V parameters. The resultant J_{sc} is 29.11 mA/cm^2 of the device showing 4.87 mA/cm^2 less current than the optically simulated J_{imp}, which is 33.89 mA/cm^2. As mentioned

before, samples with a thicker *n*-layer could effectively reduce the ITO sputtering damage. The J-V parameters of optimized samples are shown in 5.7.

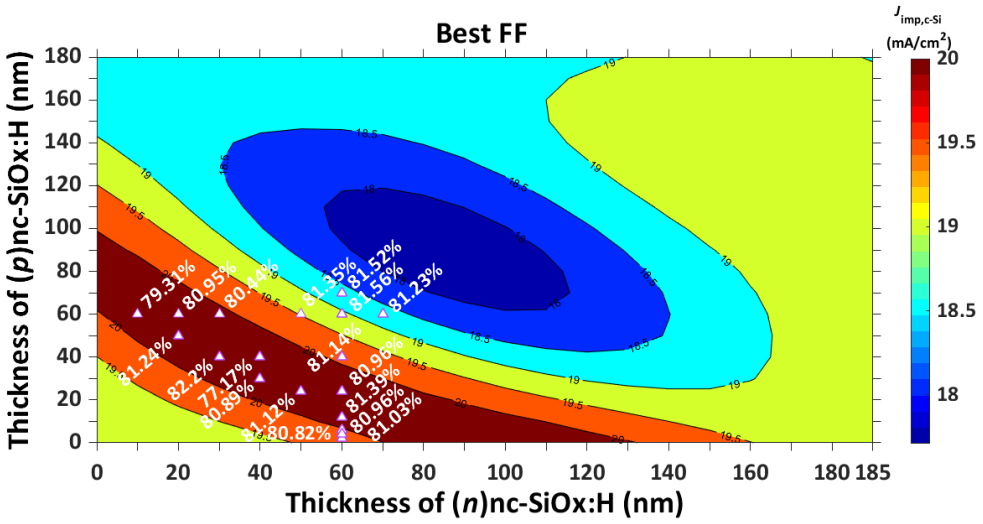

Figure 5.22: Contour plot of optically simulated Single-side-textured 2T tandem device w/ doped Odixic layers as RJ : (best FF in optimal thickness range).

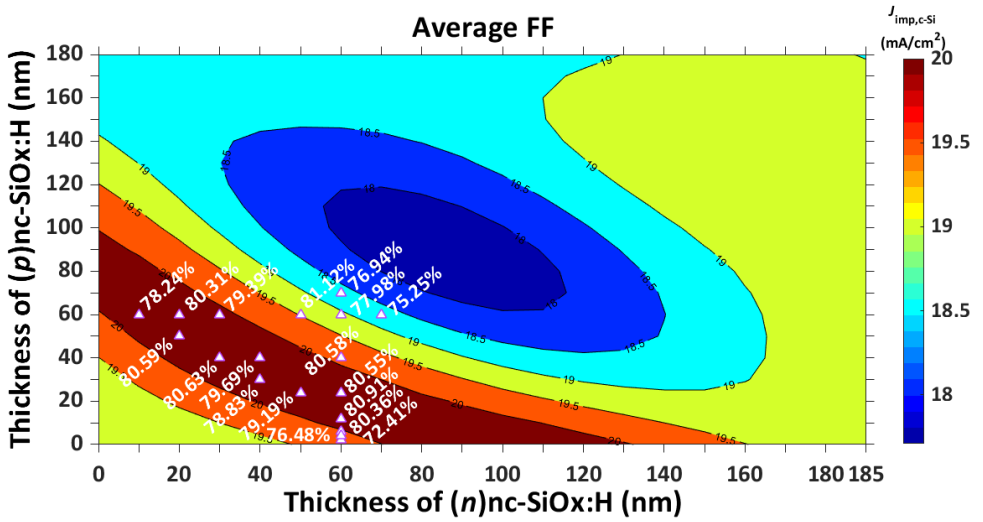

Figure 5.23: Contour plot of optically simulated Single-side-textured 2T tandem device w/ doped Odixic layers as RJ : (average FF in optimal thickness range).

Table 5.7: Optimized J-V data of Single-side-textured SHJ solar cells fabricated by 60 nm (*n*)nc-SiO_x:H (60 nm) layers with distinct (*p*)nc-SiO_x:H layers.

Sample	V_{oc} [mV]	J_{sc} mA/cm²	FF [%]	pFF [%]	η [%]	$Rs_{SunsVoc}$ [Ω cm²]	$J_{se,EQE}$ mA/cm²	J_{imp} mA/cm²
*(p)/(n)*nc-SiO_x:H (6/60 nm)	>713	35	>80	85	20	0.56	33.85	35.58
*(p)/(n)*nc-SiO_x:H (60/20 nm)	>705	>29	>80.3	84	17	0.88	30.34	33.89

5.4.2. EQE Measurement

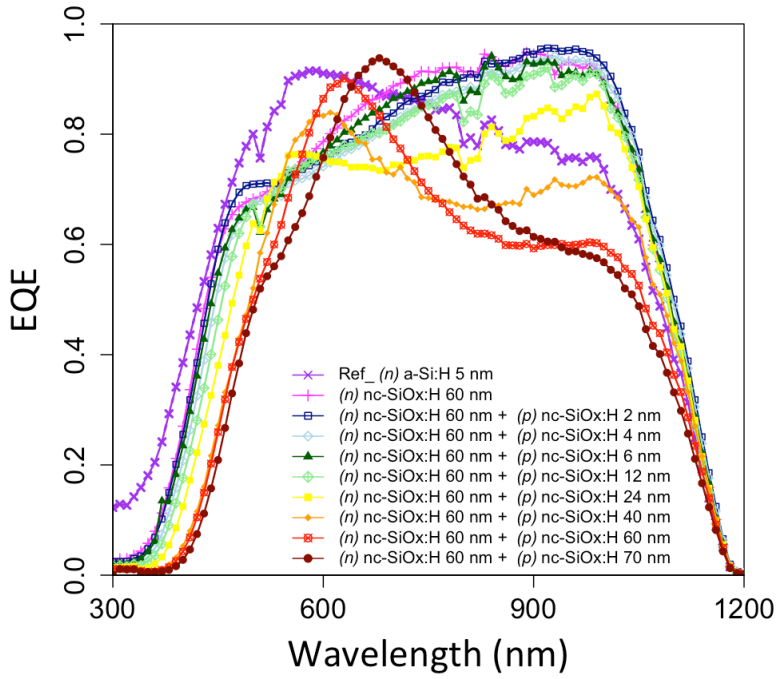

Figure 5.24: EQE curves of Single-side-textured SHJ solar cells fabricated by 60 nm (*n*)nc-SiO_x:H layers with distinct (*p*)nc-SiO_x:H layers.

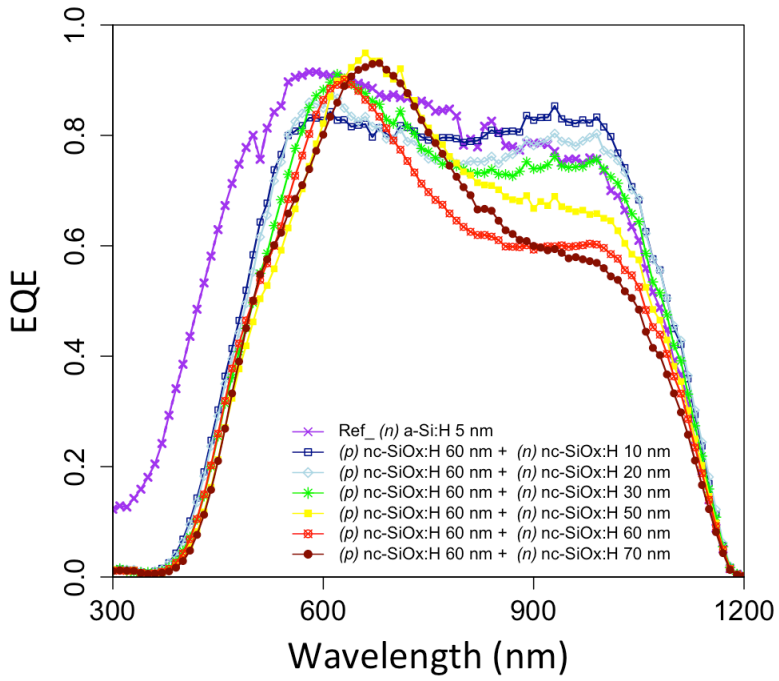

Figure 5.25: EQE curves of Single-side-textured SHJ solar cells fabricated by 60 nm (*p*)nc-SiO_x:H layers with distinct (*n*)nc-SiO_x:H layers.

To effectively explain the resultant J_{sc} of a solar cell, it is important to perform the EQE as well as the reflectance (R) measurement. It is because, EQE is measured considering the device's effect of optical losses, for instance, transmission as well as the reflection loss. It calculates the overall amount of photogenerated charge carriers that the solar cell absorbs under illumination (this number varies depending on the material and wavelength). Therefore $J_{sc,EQE}$ is the wavelength-dependent current density.

While measuring the EQE, short circuit current density $J_{sc,EQE}$ was simultaneously measured for a certain device, which changes with the layer's thickness. Samples from Fig. 5.24 show that, while keeping the *n*-layer constant 60 nm thicker, the thin *p*-layers (2-6 nm) has better infrared response > 800 nm which is gradually decreasing with a thicker layer. When the thickness of the (*p*)nc-SiO_x:H layers are varied in the range of (2-70 nm), solar cells exhibit J_{sc} in the range of (26-35 mA/cm^2) while maintaining the (*n*)nc-SiO_x:H layer at 60 nm. Which has an influence on cell's EQE (amount of photogenerated free charge carriers or electrons under illumination conditions). A similar trend was followed to vary *p*-layers to measure the EQE in NIR. While combining with a thicker *p*-layer, in contrast of the previous samples, a comparatively thick *n*-layers (10-20 nm) shows better response > 800 nm, shown in Fig. 5.25.

Summary

Single-junction SHJ solar cell structure was also optically simulated to compare with electrically optimized results. Optically stimulated single-junction solar cell, which has the same thickness parameters, shows 35.58 mA/cm^2 is > 1 mA/cm^2 from the experimental result, (see in appendix Fig. 8). This proves that the cells are not only electrically functional but also align with the optical simulations to produce the same results which is the 'proof of concept' for the proposed devices discussed in chapter 4.

The contour plots in Fig. 5.22 and 5.23 show optically ideal *p*-layer and *n*-layer thickness ranges for the TCO-free RJ layers of 2T tandem devices. Getting an idea regarding thickness parameters from these plots, single-junction devices that have undergone electrical testing, and the samples' FF mentioned in these plots. The average FF for the majority of the cells is higher than 80%, as can be observed, while the thickest cell, (*p*)/(*n*)nc-SiO_x:H (40/30 nm), has the highest FF of 82.20%. This can demonstrate that the thicker oxidic *p*-layers are more compatible with slightly thin highly conductive *n*-layers to function as an efficient RJ with a good recombination rate for having a possibly similar population of charge carriers in these window layers. This also indicates a possible realistic optical analysis of a single-junction device.

Additionally, it can guarantee compatibility between the proposed 2T tandem devices with TCO-free RJ and those with conventional TCO RJ layers. From this series of experiments, the device with the thinnest (*p*)nc-SiO_x:H layer, 6 nm, deposited on top of the thickest (*n*)nc-SiO_x:H layer, 60 nm, performs the best among all thickness combinations. While using the wider bandgap material (*p*)nc-SiO_x:H in RJ, V_{oc} may reduced due to the metallization contamination, and FF may be dropped for insufficient volume fraction of crystalline growth compared to the dominant incubation for poor surface passivation and higher contact resistance in the interlayer interfaces.

Field-effect passivation near the *p*-contact/ITO interface could be attributed to work functions' mismatch, low activation energy of thin *p*-layer, and type of TCO, that leads towards lowering the FF. For single-junction devices tuning the thickness of (*p*)nc-SiO_x:H layer in the range of 6-12 nm may enhance the transport, however, to fabricate 2T solar cell, it is strongly advised to follow the suggested optically optimized thickness for better cell performance.

5.5. Single-junction SHJ Solar Cells with Non-oxidic RJ

5.5.1. J-V measurement

In this section, the illuminated J-V characteristics of single-side-textured SHJ solar cells are discussed where the cells are fabricated with non-oxidic layers, more specifically (*p*)nc-Si:H (10 nm) layer was deposited on distinct *(n)*-Si:H layers (20 nm,40 nm,60 nm,80 nm,100 nm). The reason to investigate these two layers is to electrically investigate the *n*-contract for the monolithic 2T tandem application.

i.Comparison Among Distinct (*n*)nc-Si:H Layers

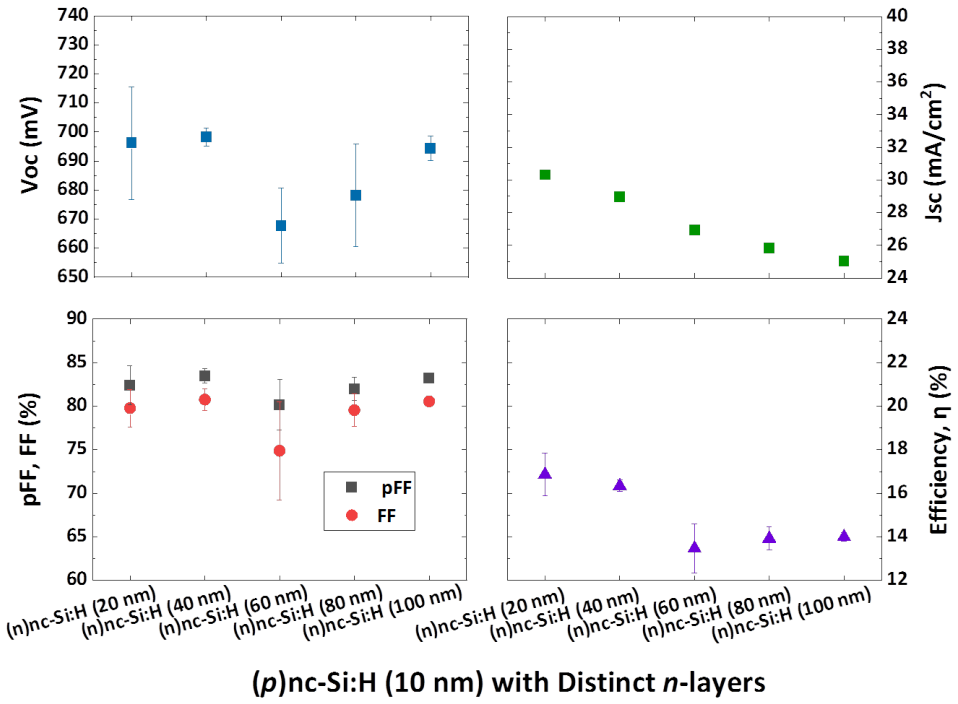

Figure 5.26: J-V Parameters of Single-side-textured SHJ solar cells fabricated by 10 nm (*p*)nc-Si:H layers with distinct (*n*)nc-Si:H layers.

Data demonstrated in Fig.5.26, which shows that the device with thin (*p*)nc-Si:H layer that is 10 nm, deposited on the top of 40 nm(*n*)nc-Si:H layer, performs the best among all other thickness combinations. V_{oc} achieves 699 mV, with an average of 687 mV. The J_{sc} is 29 mA/cm^2, with the average of 27.4 mA/cm^2 and optically optimized as 34.4%. FF is 81% with an average of 79% , pFF is 83.5%, with an average of 82.2% and efficiency is 16.3% with the average of 15%.

With an increasing thickness of *n*-layer, a continuous reduction of J-V parameters is noticed. However, the 100 nm thick *n*-layer shows higher V_{oc} (694.4 mV) than the other samples where *n*-layers have 40 nm and 60 nm respectively. This could be because of the resistive majority charge carrier collection in the front *p*-layer/ITO stack which leads toward limiting the FF.

ii.Comparison Among Distinct (*n*)nc-Si:H Layers

The main difference from the last discussed section is, here the J-V parameters of the solar cells that are fabricated with non-oxidic layers (*p*)nc-Si:H (20 nm) layer was deposited on distinct (*n*)nc-Si:H layers (20 nm, 40 nm, 60 nm, 80 nm). The reason is to compare the electrical properties

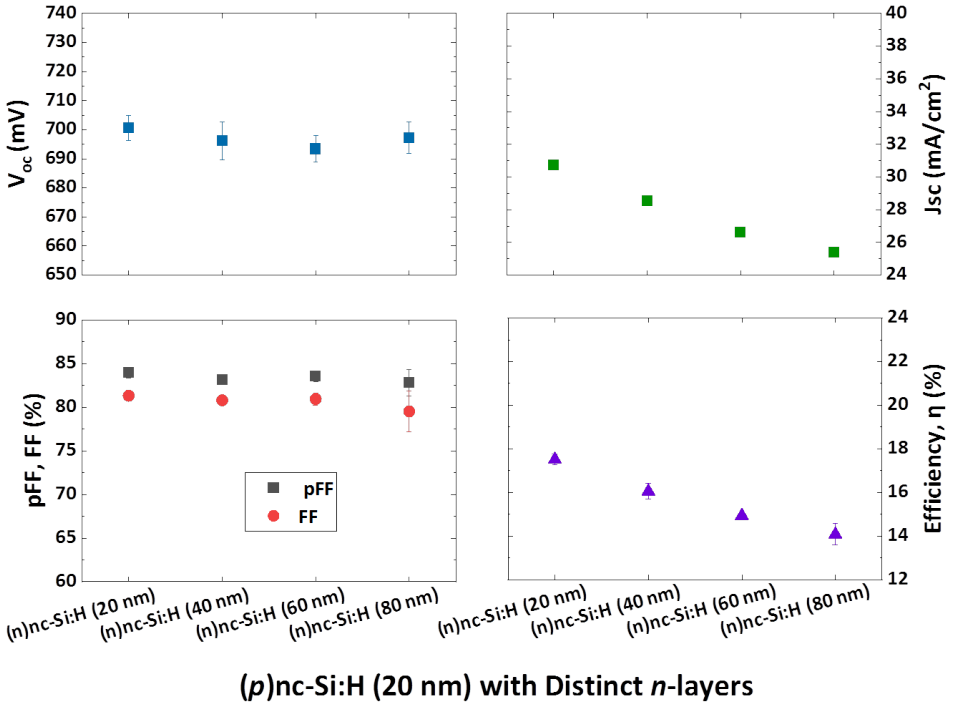

Figure 5.27: J-V Parameters of Single-side-textured SHJ solar cells fabricated by 20 nm (*p*)nc-Si:H layers with distinct (*n*)nc-Si:H layers.

discussed in the last section and (*n*)nc-Si:H layers thickness remained the same as the previous section.

Data demonstrated in Fig. 5.27 from the samples with *(p)*nc-Si:H and (*n*)nc-Si:H layers with 20 nm, the device has V_{oc} achieves 701 mV, with an average of 697 mV. The J_{sc} is 31 mA/cm^2, with the average of 28 mA/cm^2 and optically optimized as 35 mA/cm^2. FF is 81.3% with an average of 81%, pFF is 84%, with an average of 83.3% and efficiency is 18% with the average of 16%. Comparing outcomes with the previous section, where the sample with an equal thickness of the *p*-layers (20 nm) with comparatively less thick (20 nm) *n*-layers causes slight improvements of V_{oc} and J_{sc} mA/cm^2, and FF. The ΔFF = 2.67% which indicates the same thickness of these boron-doped and phosphorous-doped layers may lead to the same crystalline growth as a result of improved passivation quality in the intrinsic/c-Si interface. Moreover, the similar doping concentration may influence a higher recombination rate in the RJ, which helps the device efficient collection and recombination at the same time and leads towards the highest V_{oc} and FF of the device prepared by non-oxidic RJ layers. The best results are mentioned in table 5.8.

Table 5.8: Optimized J-V data of Single-side-textured SHJ solar cells fabricated by 10/20 nm (*p*)nc-Si:H layers with distinct (*n*)nc-Si:H layers.

Sample	V_{oc} [mV]	J_{sc} mA/cm^2	FF [%]	pFF [%]	η [%]	$Rs_{SunsVoc}$ [Ω cm^2]	$J_{se,EQE}$ mA/cm^2	J_{imp} mA/cm^2
*(p)/(n)*nc-Si:H (10/40 nm)	>698	29	>81	84	>16	0.88	31.96	35.51
*(p)/(n)*nc-Si:H (20/40 nm)	>696	29	>81	83	>16	0.85	31.51	34.38

iii.Comparison Among Distinct (*p*)nc-Si:H Layers

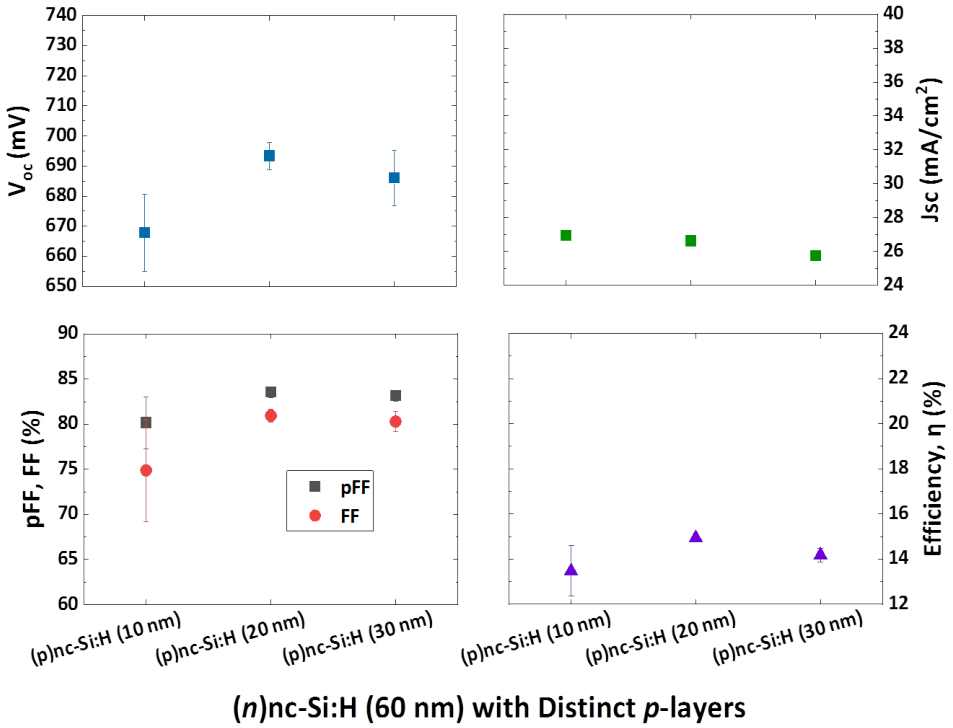

Figure 5.28: J-V Parameters of Single-side-textured SHJ solar cells fabricated by 60 nm (*n*)nc-Si:H layers with distinct (*p*)nc-Si:H layers.).

Now the J-V parameters of the solar cells that are fabricated with non-oxidic comparatively thicker (60 nm) (*n*)nc-Si:H layer, deposited in between (*i*)a-Si:H layers (5+5 nm) and distinct *(p)*nc-Si:H layers (10 nm, 20 nm, 30 nm). The electrical properties are compared with the previous two sections while a thick (*n*)nc-Si:H layers thickness remained the same for all samples, it is because we want to test if a thicker*n*-layer can perform better (which is optically optimized for tandem). Data demonstrated in Fig. 5.9 from the samples with *(p)*nc-Si:H (20 nm) and (*n*)nc-Si:H layers with (60 nm), the device has V_{oc} achieves 693.4 mV, with an average of 682.4 mV. The J_{sc} is 27 mA/cm^2, with an average of 26.4 mA/cm^2 and optically optimized as 31.1 mA/cm^2. FF is 81% with an average of 79% , pFF is 84%, with an average of 82.2% and efficiency is 15% with an average of 14.1%.

Comparing outcomes with the previous section the cell's performance was slightly dropped with a reduction of V_{oc}, J_{sc} and efficiency of 8 mV, 4 mA/cm^2 and 0.3% respectively, respectively where FF remains the same. This means a thick (*n*)nc-Si:H layer (60 nm) works better with a thin (*p*)nc-Si:H layer (20 nm). This may indicate that a thin *p*-layer can be attributed to enhancing R_s for the fact that a thicker incubation amorphous layer beneath the formation of comparatively lower crystalline volume fraction for the influence of intrinsic/c-Si interface's defect density. A poor recombination contact to the *p*-layer/ITO interface can also affect the FF while increasing the R_s, as a very highly doped *p*-layer is comparatively less compatible with highly conductive ITO [119] and depositing bi-layer *p*-layer can be a possible solution. However, the cells may also experience V_{oc} losses for the sputtering effect and metallization procedure.

Table 5.9: Optimized J-V data of Single-side-textured SHJ solar cells fabricated by 60 nm (*n*)nc-Si:H layers with distinct (*p*)nc-Si:H layers.

Sample	V_{oc} [mV]	J_{sc} mA/cm^2	FF [%]	pFF [%]	η [%]	$Rs_{SunsVoc}$ [Ω cm^2]	$J_{se,EQE}$ mA/cm^2	J_{imp} mA/cm^2
*(p)/(n)*nc-Si:H (20/60 nm)	>693	27	81	84	15	0.92	29.75	31.84

5.5.2. EQE Measurement

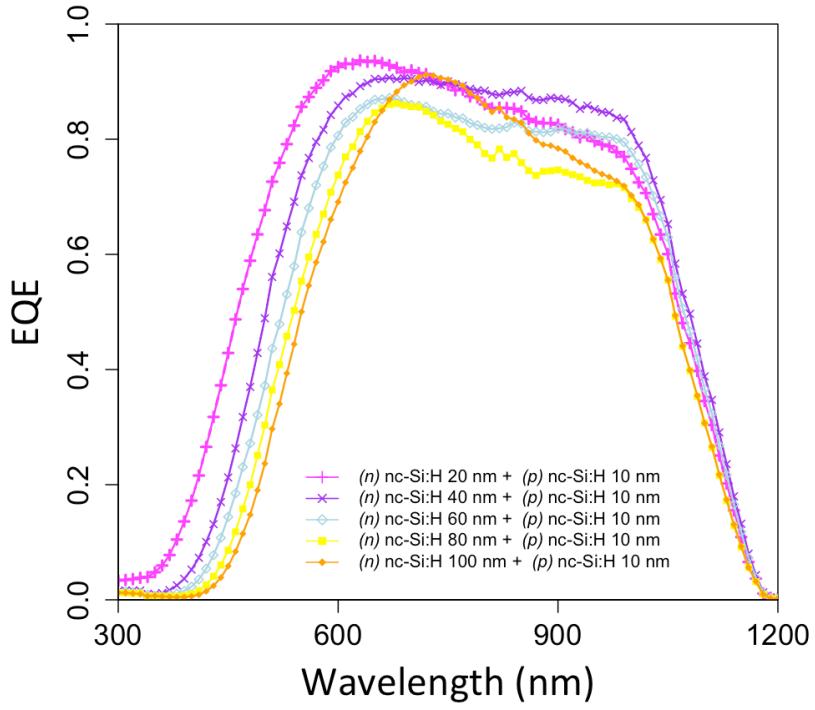

Figure 5.29: EQE curves of Single-side-textured SHJ solar cells fabricated by 10 nm (*p*)nc-Si:H layers with distinct (*n*)nc-Si:H layers.

The same pattern as mentioned in the preceding section was used to analyze electrical properties while using doped non-oxidic RJ layers in the optical thickness range. The 10 nm (*p*)nc-Si:H sample performs better than the other two samples with 20 nm for the single-junction devices. Here, the (*n*)nc-Si:H layer's 40 nm thickness exhibits a higher J_{sc} of 29 mA/cm^2, which is closely correlated with the EQE measurement. As shown in the yellow (Fig. 5.29) and dark-red color curve in (Fig. 5.30) thicker (*n*)nc-Si:H of 80 nm absorbs fewer photons, leading to the highest reflectance loss (6.5 to 6.7 mA/cm^2) and the lowest current generation (31.25 to 33.63 mA/cm^2) in optical experiments in the Fig 9 and 10. Furthermore, *i*-V_{oc} measurements for samples with 10 nm and 20 nm of a thick (*p*)nc-Si:H layer result 725 mV and 726 mV, respectively, with greater R_{sh}, whereas 40 nm thick (*n*)nc-Si:H RJ layer higher V_{oc} of 698.2 mV and 696.2 mV are indicated by the nc-Si:H RJ layer. As the effect of optical losses is also included with EQE (transmission (T) and reflection (R)), shown in Fig. 9,10 and 11, For the insufficient photon absorption near NIR with higher reflection loss may overall J_{sc} was suffered. The results of the best outcomes with optimized sample thickness are shown in 5.9.

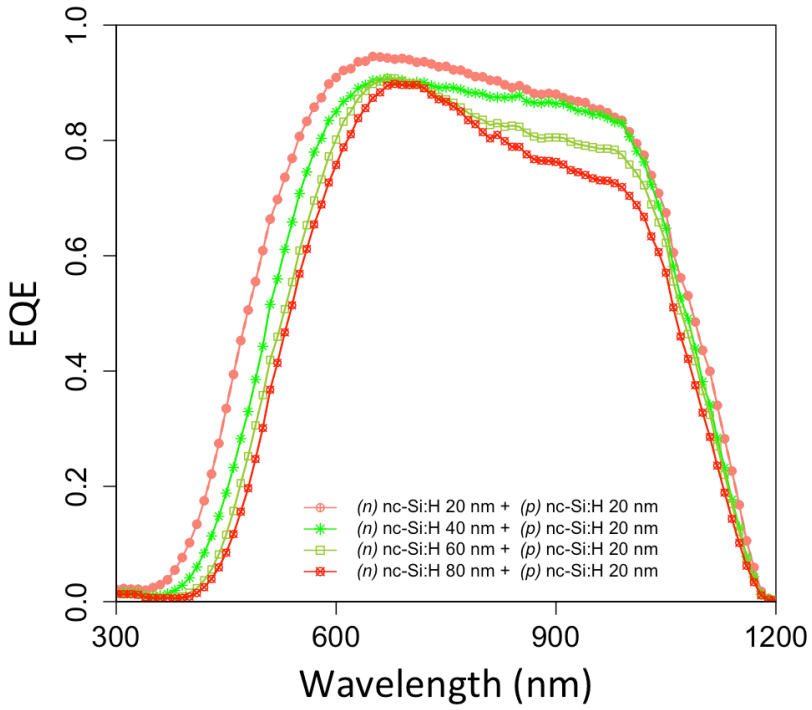

Figure 5.30: EQE curves of Single-side-textured SHJ solar cells fabricated by 20 nm (*p*)nc-Si:H layers with distinct (*n*)nc-Si:H layers.

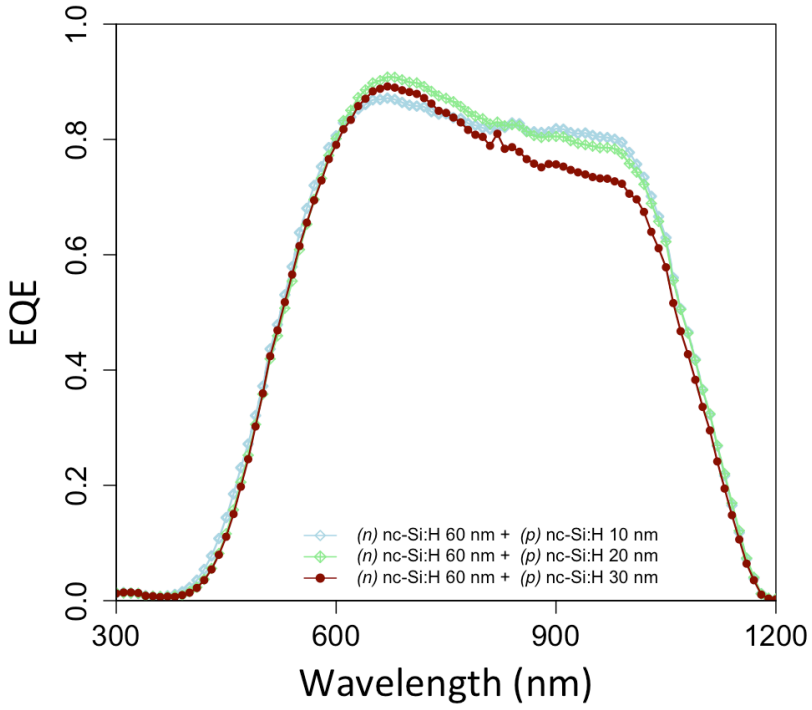

Figure 5.31: EQE curves of Single-side-textured SHJ solar cells fabricated by 60 nm (*n*)nc-Si:H layers with distinct (*p*)nc-Si:H layers.

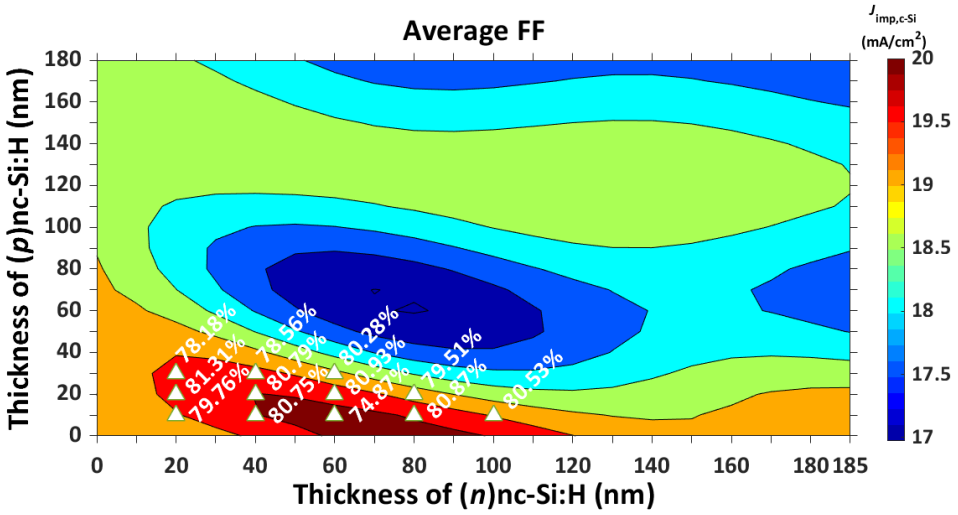

Figure 5.32: Contour plot of optically simulated Single-side-textured 2T tandem device w/ doped Non-odixic layers as RJ (average FF).

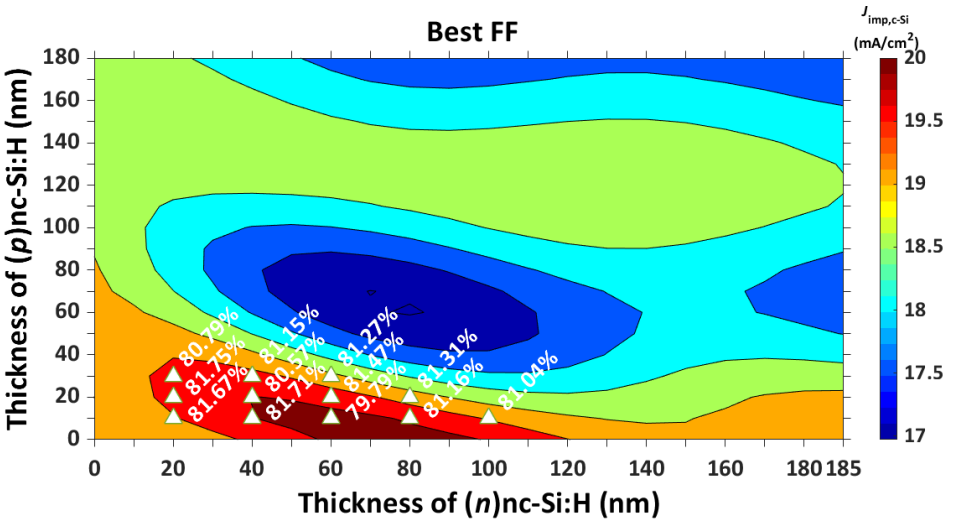

Figure 5.33: Contour plot of optically simulated Single-side-textured 2T tandem device w/ doped Non-odixic layers as RJ : (best FF in optimal thickness range).

Summary

In summary, the optically optimal thickness range for the RJ layers was used to fabricate all single-junction cells. The objective was to evaluate the cells' electrical performance with the implementation of proposed highly doped RJ layers for sufficient recombination in the junction. However, before applying the optically optimized parameters to fabricate the TCO-free tandem devices. Although the nc-Si:H layers offer higher conductivity, the devices with comparatively thin oxidic RJ layers perform in a similar range in terms of total V_{oc} and J_{sc} as well as FF. The highest optimized FF is 81.75% (5.33) while the average FF ranges from 78 to 79 percent (Fig. 5.32). Further invention with the thickness of both RJ layers in the range of (21-30 nm) may offer slightly better crystalline growth and reduce sputtering damage.

5.6. Single-junction SHJ Solar Cells with Bilayer *p*-contact/*n*-layer as RJ

A similar pattern was followed to fabricate the SHJ solar cells with bilayer *p*-layer/*n*-layer composition for the mentioned reason (in chapter 4) to investigate the electrical performance while applying it to the single-junction SHJ solar cells. The optically optimized thickness of the RJ layers for the 2T device as well as single junction solar cells, shown in Fig 5.36 and 5.37, the cells were fabricated.

5.6.1. J-V measurement

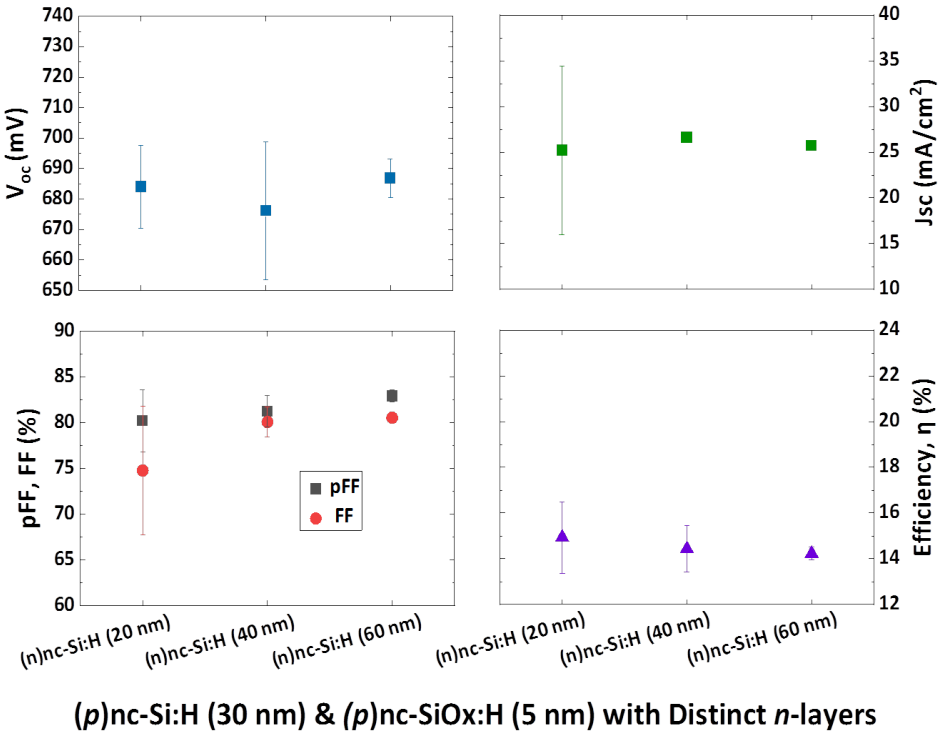

Figure 5.34: J-V Parameters of Single-side-textured SHJ solar cells fabricated by 30/5 nm (*p*)nc-Si:H /(*p*)nc-SiO_x:H layers with distinct (*n*)nc-Si:H layers.

J-V parameters are investigated of the solar cells fabricated with oxide/non-oxidic layer deposited as *(*p)nc-Si:H/(*p*)nc-SiO_x:H (30/5 nm) on the top of (*n*)nc-Si:H layers. Keeping (*p*)nc-SiO_x:H 5nm and *(p)*nc-Si:H 30 nm constant, (getting inspired by the prior research [15, 73] while three thickness variations were applied for depositing (*n*)nc-Si:H layers (20 nm, 40 nm, 60 nm). This combination was chosen to grow first (*n*)nc-Si:H layer that is highly conductive, then growing a high bandgap (*p*)nc-SiO_x:H to maximize the band bending, and then grow again a highly conductive *(*p)nc-Si:H layer to contact with perovskite's HTL to accumulate holes.

The electrical properties can be demonstrated from Fig.5.34. The optimized sample was surprisingly the sample with (*n*)nc-Si:H (60 nm) layer, the device has V_{oc} achieves 687 mV, with an average of 682 mV. The J_{sc} is 26 mA/cm^2, with the average of 26 mA/cm^2 and optically optimized as 29.4 mA/cm^2. FF is 81% with an average of 79% , pFF is 83%, with an average of 81.4% and efficiency is 14% with the average of 15%.

Table 5.10: Optimized J-V data of Single-side-textured SHJ solar cells fabricated by 30/5 nm (*p*)nc-Si:H /(*p*)nc-SiO_x:H layers with distinct (*n*)nc-Si:H layers.

Sample	V_{oc} [mV]	J_{sc} mA/cm^2	FF [%]	pFF [%]	η [%]	$Rs_{SunsVoc}$ [Ω cm^2]	$J_{se,EQE}$ [mA/cm^2]	J_{imp} mA/cm^2
*(p/n)*nc-Si:H w/ *(p)*nc-SiO_x:H	687	26	81	83	>14	1.09	32	30.2

5.6.2. EQE Measurement

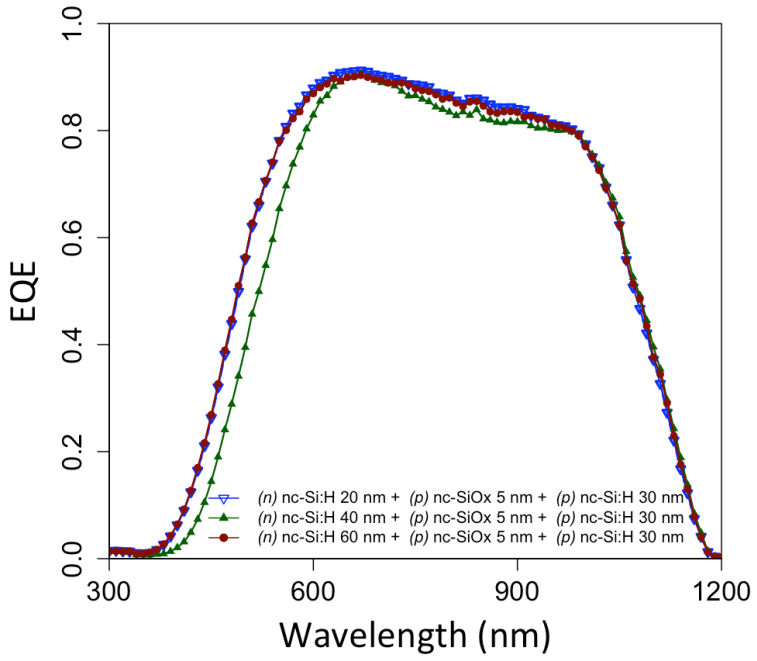

Figure 5.35: EQE curves of Single-side-textured SHJ solar cells fabricated by 30/5 nm (*p*)nc-Si:H /(*p*)nc-SiO_x:H layers with distinct (*n*)nc-Si:H layers.

A similar pattern was followed to analyze EQE while using doped oxidic/non-oxidic RJ layers while following the optically simulated thickness range. The question of whether the combined electrical performance of the oxidic and non-oxidic layers was investigated using a similar trend. Specifically, (*p*)nc-SiO_x:H/(*p*)nc-Si:H (5/30 nm) (or simply bi-layer*p*-layer) with different thickness variations (of 20, 40, and 60 nm) (*n*)nc-Si:H layers are used for single-side textured single-junction solar cells. The EQE curves of three separate samples are shown in the Fig. 5.35 where (*p*)nc-SiO_x:H/(*p*)nc-Si:H (5/30 nm) (or simply, bi-layer*p*-layer) with (*n*)nc-Si:H layer of 20 and 60 nm layers absorbs more photon while with 40 nm thick (*n*)nc-Si:H layer absorbs less. For these single-junction devices the samples with 20 nm and 60 thick (*n*)nc-Si:H layer deposited beneath 5 nm (*p*)nc-SiO_x:H and 30 nm (*p*)nc-Si:H (bi-layer *p*-layer) sample performs slightly better (blue and maroon colors in Fig. 5.35) than the other the sample (40 nm thick (*n*)nc-Si:H with bi-layer*p*-layers). Comparing with optically simulated results where the white area indicates the highest reflectance loss (7.2 and 8.6 mA/cm^2 for the samples with 30 nm and 60 nm (*n*)nc-Si:H layers respectively) in the Fig. 12, the reflection loss area is similar to the electrically measured samples. The possible reasons for less absorption could also be the parasitic loss (see Fig. 12) NIR with the parasitic loss (6.3 and 7.3 mA/cm^2 for the samples with 30 nm and 60 nm (*n*)nc-Si:H layers respectively) and the mentioned higher reflection loss may cause the reduction of J_{sc}.

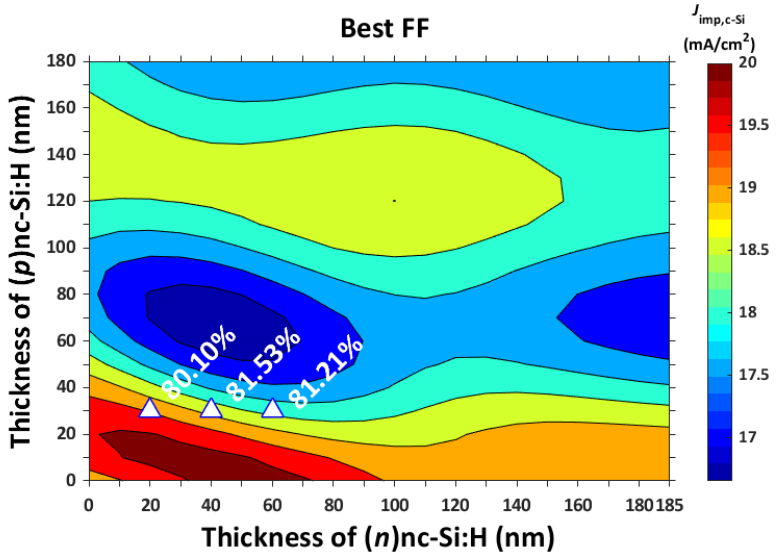

Figure 5.36: Contour plot of optically simulated Single-side-textured 2T tandem device w/ doped Oxidic/Non-oxidic layers as RJ : (best FF in optimal thickness range).

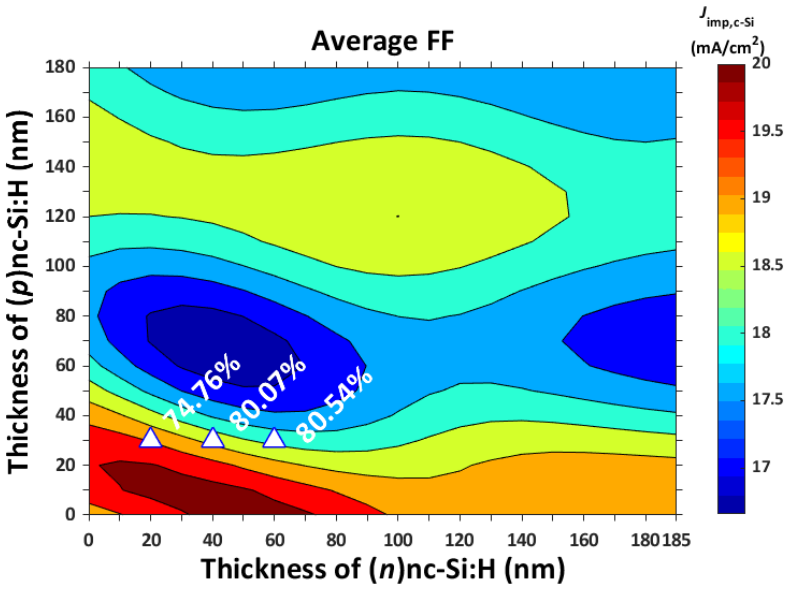

Figure 5.37: Contour plot of optically simulated Single-side-textured 2T tandem device w/ doped Oxidic/Non-oxidic layers as RJ : (average FF in optimal thickness range).

Summary

In summary, with the same objective as mentioned before, the bilayer *p*-contact with the*n*-layer, together to form *n*-contact for the bottom device was investigated for the single-junction device. Perform similarly in terms of total V_{oc},J_{sc} as well as FF. The J_{sc} 26 mA/cm^2 is quite close to compared with $J_{imp,c–Si}$ 30.2 mA/cm^2. The highest accumulated FF is 81.75% see table 5.10) while the average FF ranges from 78 to 79 percent.

5.7. Investigating Crystalline Growth of Prepared Samples

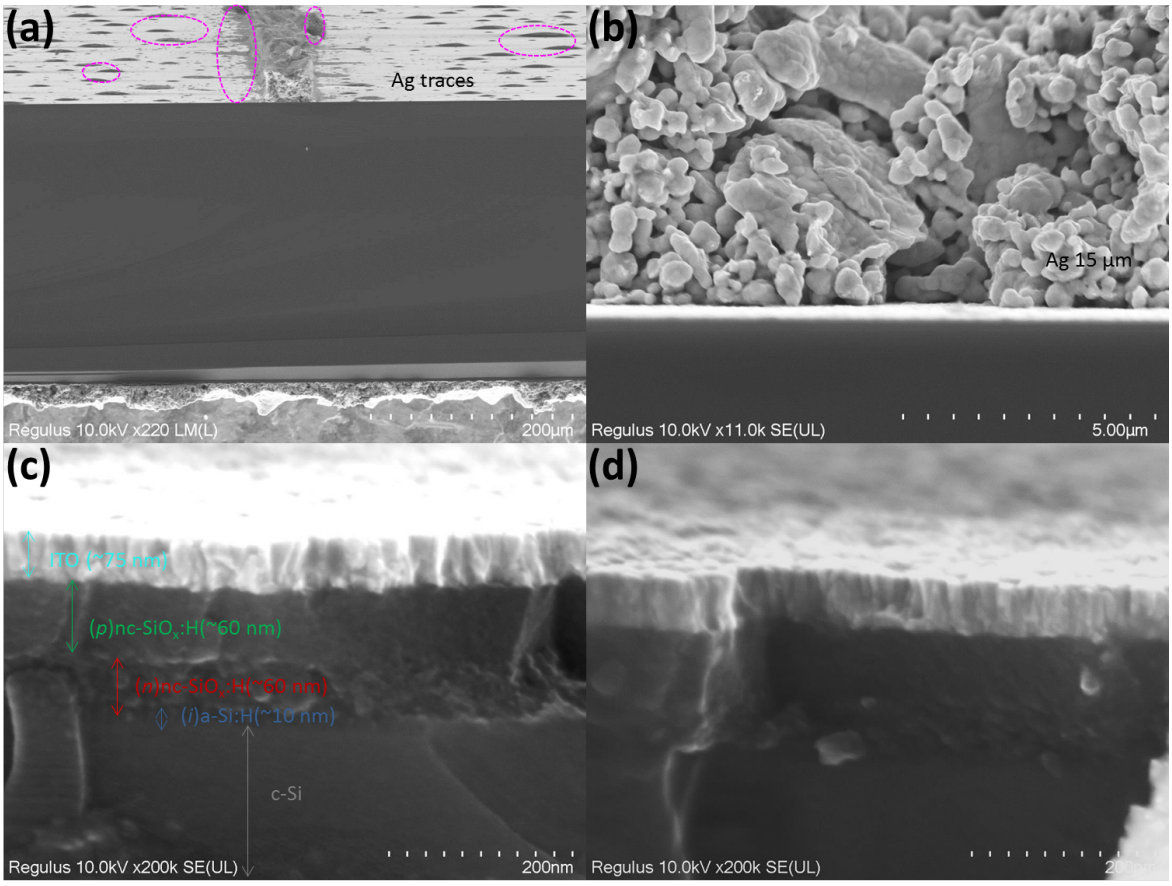

Figure 5.38: Sample M16993's cross-section as shown in with a closer view of a finger (a), while (b) shows an enlarged picture of Ag, (c) and (d) show the (*i*)a-Si:H (5 + 5 nm)/(*n*)nc-SiO_x:H (60 nm)/(*p*)nc-SiO_x:H (60 nm) layers stacks.

SEM measurements were performed to get a better view of crystalline growth within the cell, as well as any other possible defects. Even though it might be challenging to draw conclusions from the layer topologies of these tiny layers we could see possible crystal structure in that doped nc-SiO_x:H layers.

Fig.5.38 is the cross-section of sample M16993. It has the following properties: *(i)*a-Si:H (5 + 5 nm)/*(n)*nc-SiO_x:H (60 nm)/*(n)*nc-SiO_x:H (60 nm) font layers stacks can be seen. The resultant V_{oc}, J_{sc}, FF, and efficiency for this sample are 700 mV, 26 mA/cm^2, 78%, and 14%, respectively. In Fig.5.38 (a), The Ag paste may have smeared close to the finger due to its poor viscosity. It is good to know that Ag is susceptible to contaminating other materials, such as doped layers of the primary absorber c-Si, during the metalization process diffusing traces may enter the window (doped) layers and the cell's efficiency may decrease when contaminated because of a drop in shunt resistance and a surge in series resistance.

Similarly Fig.5.39 is the cross-sction of sample M17956, with *(i)*a-Si:H (5 + 5 nm)/*(n)*nc-Si:H (40 nm)/*(p)*nc-Si:H (30 nm) layers stacks was investigated to check possible crystal growth. Although it was pretty much impossible to see any clear image for comparatively thin doped layers. The uniformity of the growth may indicate the possible reason for obtaining higher V_{oc} and FF for the optimized samples, however investigating thinner layers crosssection' measurement was quite challenging.

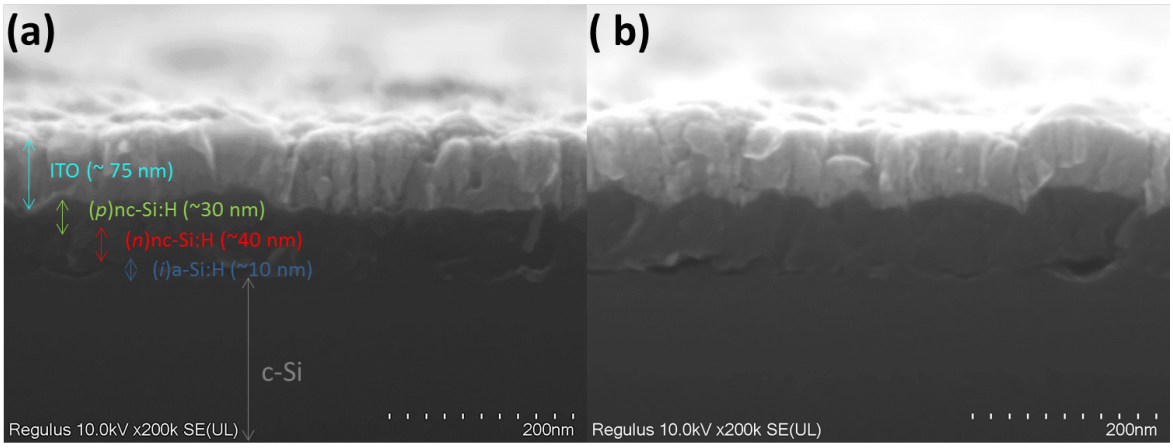

Figure 5.39: Sample M17956's cross-section as shown in with a closer view of a finger (a), while (b) shows an enlarged picture of Ag, (c) and (d) show the *(*i)a-Si:H (5 + 5 nm)/*(*n)nc-Si:H (40 nm)/*(p)*nc-Si:H (30 nm) layers stacks.

To summarise, for the proposed designs of 2T tandem devices, the experimental part plays the role of a 'proof of concept'. However, thicker RJ layers (within a certain range, mentioned in chapter 4) are preferred (for accumulating charges as well as generating higher J_sc) for SHJ bottom cells for the actual monolithic 2T tandem device. The performance of single-junction SHJ solar cells tested with thin RJ layers is not comparable to 2T tandem applications, in contrast, the single-junction devices with thicker RJ layers result in less FF for obvious reasons. Moreover, selective transport may lead to a higher FF of the device. Further investigation of E_a and E_G of the simulated optimized (*p*)-layers to accumulate hole collection, E_a and work function investigation of the proposed (*n*)-layers for electron transport, and the proper match with the work function of rear TCO (for instance IWO) can result in a better tandem. Matching work function may reduce field-effect passivation in the (*p*)-contact/TCO interface to accumulate hole collection. For further improvement, the 'refractive index grading' can be used to investigate the properties of the optically suggested thickness of RJ layers to lessen the reflection loss while improving EQE in the devices.

6

Conclusions and Outlooks

This master thesis focused on the optical simulation-assisted optimization of silicon heterojunction (SHJ) bottom cells for high-efficiency monolithic Perovskite/c-Si tandem solar cells featuring TCO-free recombination junction layers. Two main research goals have been explored within this work: (i) optically optimizing monolithic 2T tandem devices with various TCO-free recombination junctions; and (ii) fabrication of proof-of-concept single junction SHJ solar cells featuring proposed recombination junctions. In this chapter, conclusions are first drawn after summarizing the key findings of this research. Then, outlooks on future research topics for developing high-efficiency 2T Perovskite/c-Si tandem solar cells are provided.

6.1. Conclusions

6.1.1. Optical Optimization of Monolithic 2T Perovskite/c-Si Tandem Devices

In Chapter 4, optical simulations of monolithic single-side-textured and double-side-textured 2T Perovskite/c-Si tandem solar cells with various conventional TCO-based and proposed TCO-free recombination junction layers were performed and the results were analyzed. The primary focus initially centered on improving the light absorption in the bottom cell, followed by optimizing the tandem solar cell design to attain the highest possible tandem current density.

First, various TCO layers including tin-doped indium oxide (ITO), tungsten-doped indium oxide (IWO), and aluminum-doped zinc oxide (AZO) were utilized as the recombination junction, and the rear TCO of the bottom cell. The reference single-side-textured device with ITO_ITO configuration shows 18.30 mA/cm^2 implied photocurrent density whereas the bottom device was the current limiter. In order to enhance the absorption of bottom cells, the more transparent IWO was implemented as the recombination junction in the simulated tandem solar cells. Devices with IWO_IWO exhibited an improved $J_{imp,bottom}$ of 18.70 mA/cm^2 as compared to the ITO_ITO reference sample.

As compared to TCO-based recombination junctions, the use of optimized TCO-free recombination junctions consisting of doped nc-Si:H-based layers was found to further minimize reflection losses originating from the intermediate interfaces between the sub-cells, thus contributing to higher $J_{imp,bottom}$ values. For example, in single-side-textured tandem solar cells, the use of 30 nm (*p*)nc-SiO_x:H and 30 nm (*n*)nc-SiO_x:H as the recombination junction can significantly boost the $J_{imp,bottom}$ to 20.30 mA/cm^2. Similarly, by optimizing the thickness combinations of (*p*)nc-Si:H (30 nm) and (*n*)nc-Si:H (20 nm), the $J_{imp,bottom}$ can be also improved to 19.80 mA/cm^2. It is crucial to emphasize that by adjusting the thickness of the (*p*)-type and (*n*)-type nc-Si:H-based layers, optimal thickness ranges for both doped layers resulting in an improved current generation in the bottom cell were discovered. Overall, optimum $J_{imp,bottom}$ in the range of 19.60-20.30 mA/cm^2 can be obtained with nc-Si:H-based recombination junctions in the proposed configurations. This allows maximized light coupling to the bottom cell.

Eventually, with the optimized recombination junction, the whole tandem solar cells were optimized in order to achieve maximum matched tandem current density. In the case of ITO_ITO reference sample, a $J_{imp,tandem}$ of 19.40 mA/cm^2 was realized. By using the more transparent IWO instead of ITO, the $J_{imp,tandem}$ can be improved to 19.50 mA/cm^2. Furthermore, the use of (*p*)nc-SiO_x:H and (*n*)nc-SiO_x:H as the recombination junction with thicknesses of 65 nm and 45 nm, respectively, contributed to a high $J_{imp,tandem}$ of 19.79 mA/cm^2. Similarly, recombination junction using 35 nm (*p*)nc-Si:H and 44 nm (*n*)nc-Si:H also exhibited a high $J_{imp,tandem}$ of of 19.78 mA/cm^2. Overall, optimum $J_{imp,bottom}$ in the range of 19.70-19.80 mA/cm^2 can be obtained with nc-Si:H-based recombination junctions thanks to the optimized interference effect at the intermediate interfaces between sub-cells. The results demonstrated the optical advantageous implementations of the proposed TCO-free recombination junctions in single-side-textured 2T tandem solar cells.

Similar optimizations were performed for double-side-textured 2T tandem devices. In this configuration, the reference ITO_ITO exhibited 20.10 mA/cm^2 implied photocurrent density whereas the top device was the current limiter. In this configuration, due to the already minimized reflection as a result of the textured front surface, the gain by using optimized TCO-free recombination junctions is less significant as compared to their application in single-side-textured tandem devices. To enhance the absorption of the top cells as well as the bottom cell, IWO was implemented as the recombination junction and in the rear side of the simulated tandem solar cells. A similar pattern of results as the single-side-textured devices the device with IWO_IWO configuration exhibited an improved $J_{imp,bottom}$ of 20.40 mA/cm^2 as compared to the ITO_ITO reference sample.

In comparison with TCO-based recombination junctions, the use of optimized TCO-free recombination junctions consisting of doped nc-Si: H-based layers wer found to further minimize reflection losses originating from the intermediate interfaces between each sub-cells and the interfaces contribute a higher $J_{imp,bottom}$ values. For example, in double-side-textured tandem solar cells, the use of 30 nm (*p*)nc-SiO_x:H and 30 nm (*n*)nc-SiO_x:H as the recombination junction can significantly boost the $J_{imp,bottom}$ to 20.80 mA/cm^2. In a similar trend, by optimizing the thickness combinations of (*p*)nc-Si:H (30 nm) and (*n*)nc-Si:H (20 nm), the $J_{imp,bottom}$ boosted up to 20.70 mA/cm^2. It is crucial to emphasize that by adjusting the thickness of the (*p*)-type and (*n*)-type nc-Si:H-based layers, optimal thickness ranges for both doped layers resulting in an improved current generation with reduces parasitic absorption loss in the bottom cell were discovered. Overall, optimum $J_{imp,bottom}$ in the range of 20.50-20.80 mA/cm^2 can be obtained with nc-Si:H-based recombination junctions in the proposed configurations. This proves that the maximized light coupling to the bottom cell was possible for the textured configurations while diminishing the interference effect in the interfaces of these two cells and the interlayers.

Subsequently, following the same trend as single-side-textured devices, with the optimized recombination junction, the whole 2T tandem solar cells were optimized in order to achieve maximum matched tandem current density. The reference sample ITO_ITO shows a $J_{imp,tandem}$ of 20.50 mA/cm^2. By replacing ITO with IWO, the $J_{imp,tandem}$ was further improved to 20.60 mA/cm^2. Furthermore, the use of (*p*)nc-SiO_x:H and (*n*)nc-SiO_x:H as the recombination junction with thicknesses of 80 nm and 40 nm, respectively, contributed to a high $J_{imp,tandem}$ of 20.57 mA/cm^2. Following that, the recombination junction using non-oxidic layers of 40 nm (*p*)nc-Si:H and 30 nm (*n*)nc-Si:H also exhibited a similar range of implied photocurrent density $J_{imp,tandem}$ of 20.58 mA/cm^2. Overall, optimum $J_{imp,bottom}$ in the range of 20.50-20.60 mA/cm^2 can be obtained with the proposed nc-Si:H-based recombination junctions. The results demonstrated the effective light management in the interlayers-interfaces for having similar refractive index (n) value of the proposed TCO-free recombination junction layers with the main absorbers dipped reflection and parasitic loss in double-side-textured 2T tandem solar cells.

6.1.2. Optimization of Proof-of-concept Single-side-textured SHJ Solar Cells for Tandem Applications

Based on optical simulation studies conducted on 2T tandem solar cells, the electrical effectiveness of proposed TCO-free recombination junctions was examined by fabricating proof-of-concept single junction single-side-textured SHJ solar cells.

First, we focused on the passivation optimization of the flat (100) c-Si surface as it is prone to detrimental epitaxial growth. Different (*i*)a-Si:H passivation strategies were implemented, namely, (*i*)a-Si:H mono-layer (10 nm), (*i*)a-Si:H bi-layer (5 nm + 5 nm) and (*i*)a-Si:H bi-layer (5 nm + 5 nm) with an intermediate hydrogen plasma treatment (HPT). Different from mono-layer which was deposited with a pure SiH_4 plasma, the bilayer deposit first 5 nm (*i*)a-Si:H without additional H dilution and then stack on top a 5 nm (*i*)a-Si:H deposited with hydrogen-diluted SiH_4 plasma. In a symmetrical configuration, a lifetime of 0.71 ms was obtained for (*i*)a-Si:H mono-layer. This was slightly improved to 1.18 ms by using the bi-layer approach. Notably, a lifetime of 3.48 ms was achieved by adding an extra HPT to the bi-layer. The improved lifetimes by using bi-layer and bi-layer with HPT can be mainly ascribed to the beneficial H incorporation into the film reaching the c-S/(*i*)a-Si:H interface when using hydrogen-diluted or hydrogen plasma, thus providing better chemical passivation quality. Subsequent deposition of (*n*)a-Si:H allowed overall improvement of lifetime and the same lifetime trend as that of (*i*)a-Si:H passivating layer was observed. That is, the best lifetime of 14.62 ms was achieved when combining (*n*)a-Si:H with (*i*)a-Si:H bi-layer with HPT. Interestingly, the bi-layer utilizing HPT, which demonstrated superior (*i*)a-Si:H passivation quality, experienced a decline in minority carrier lifetime when combined with high hydrogen-diluted nc-Si:H layers. Conversely, the bi-layer without the HPT approach, but incorporating (*n*)nc-Si:H in a symmetrical sample, showcased an impressive minority carrier lifetime of 16.87 ms. Similarly, the best lifetime after the deposition of (*p*)nc-SiO_x:H and (*p*)nc-Si:H was seen for the (*i*)a-Si:H bi-layer.
Before fabricating SHJ solar cells, the electrical properties of doped nc-SiO_x:H layers were investigated. We observed a general thickness-dependent dark conductivity and activation energy trend for samples with glass/doped layers and glass/(*i*)a-Si:H/doped layers. Specifically, by increasing the thickness of doped layers, we obtained a higher conductivity or lower activation energy of the film. Especially, the largest increment of dark conductivity or the largest decrement of the activation energy was seen when the thickness was thinner than around 30 nm. Further increasing layer thickness tends to result in gradual saturations of dark conductivity and activation energy. Moreover, the thicker samples with glass/doped layers (3.52E-1) are comparatively less conductive than the samples with glass/(*i*)a-Si:H/doped layer (3.31E-1).
Eventually, proof-of-concept single junction single-side-textured SHJ solar cells featuring the proposed TCO-free recombination junction were fabricated. According to the optical simulations, various optimum thickness combinations of (*n*)nc-SiO_x:H and (*p*)nc-SiO_x:H or (*n*)nc-Si:H and (*p*)nc-Si:H that composes the recombination junction were tested. Overall, the optically promising TCO-free recombination junctions in monolithic 2T tandem solar cells also delivered high FF values in proof-of-concept single-junction SHJ solar cells, demonstrating their potential to be implemented to fabricate high-efficiency monolithic 2T tandem solar cells. Specifically, an average FF above 81% and a best FF of 82.2% were obtained when using (*n*)nc-SiO_x:H and (*p*)nc-SiO_x:H recombination junction, and an average FF above 81.31% and a best FF of 81.75% were obtained when using (*n*)nc-Si:H and (*p*)nc-Si:H recombination junction. All these cells featured rather good V_{oc} above 713.4 mV. The EQE responses of these single-junction SHJ solar cells were further optically stimulated, which gave more insight into the optical losses in these single-junction devices.

6.2. Outlooks

6.2.1. Optical Optimization of Perovskite/c-Si Tandem Devices

It may be possible to undertake further research using the suggested devices with a different TCO layer, for instance, IWO. This highly transparent material may help to reduce parasitic absorption, as it does in recombination junctions.
Selecting appropriate bandgap materials (wide E_G may be investigated further.
The regular configuration 'n-i-p' PVK/Front junction SHJ can be investigated with suggested TCO-free recombination junctions. Although different materials are required for developing this configuration, it might be interesting to carry out additional research while choosing wide-band materials (Perovskite) with compatible refractive indices. Then, apply such information to create 2T devices and compare them to the currently available designs in order to optimize the most

promising PVK/c-Si combinations.
The optical simulation of mechanically stacked 4T 'p-i-n' PVK/Rear junction c-Si SHJ configuration can be investigated. Optical simulations with single-side-textured and double-side-textured were in the early stages of development. However, due to time constraints, it was not possible to continue. Investigating 4T devices with similar bottom devices mentioned in this research might be interesting.
Considering the optical advantages of A reversed structure of 'n-i-p' top-cell with 'FJ' bottom cell can be investigated with the proposed TCO-free RJ layers stacks.
In a nutshell, for further investigation:

- **Optimizing interference effects while replacing any material in the 2T tandem :** By taking into account that all of the regions indicate higher parasitic/reflection losses, investigating the interference effects of the interlayers would be an excellent solution for overall tandem current improvement. More specifically the higher reflection loss (R_2) in the Perovskite/c-Si interface can be solved by working on the RJ of the tandem.
- **n and k values :** Choosing materials with more optimized n and k values may reduce the interface losses.
- **Optimizing different materials for double-side-textured devices:** Textured interface reduces reflection loss and allows more light to pass through the layers. On the contrary, as a result of higher photon absorption, parasitic losses increased. Reoptimizing the layers with more transparent materials with proper refractive index is crucial to minimize the parasitic loss in the doped layers.
- **Optimization of the Perovskite/c-Si 2T tandem solar cell layer stack :** A reversed structure of 'n-i-p' top-cell with 'FJ' bottom cell can be investigated with the proposed TCO-free RJ layers stacks.
- **Optimizing 4T Perovskite/c-Si tandem solar cell layer stack :** The mechanically stacked 4T configuration can be investigated.

6.2.2. Electrical Investigation as 'proof of concept'

To optimize better passivation quality in the c-Si/(*i*)-layer interface, several (*i*)a-Si:H passivation strategies were implemented in this research. It is possible to investigate the passivation quality of double-side-textured surfaces to fabricate double-side-textured 2T devices. However, texturing surface induces roughness on the surface, and cleaning techniques may reduce the roughness. The fabrication of single-junction SHJ solar cells using optically investigated thickness parameters may provide some suggestions for the 2T device manufacturing.

In addition to the optically optimized thickness of 2T solar cells, before fabrication, the single-junction SHJ solar cells are also optically investigated with certain thickness parameters. It comes without saying that these criteria are unrealistic in the context of actually manufacturing a 2T device since they strictly need to adhere to the recommended range of thickness for particular devices. However, the electrical functionality of single-junction cells shows that the suggested concept is reasonable and appropriate for implementation in manufacturing 2T devices.

In a nutshell, for further investigation:

- **Demonstrate the proposed TCO-free 2T structure :** While taking into account the partial 'proof-of-concept', the single-junction SHJ solar cell's performance only proves that with the suggested RJ combinations, the single-junction device can perform well. To prove it entirely, the proposed parameters can be applied to demonstrate a 2T tandem device.
- **Optimizing double-side-textured substrate in 2T tandem :** A similar pattern can be followed to investigate double-side-textured substrate with optimized *i*-layers passivation for single-junction SHJ solar cells. It seems obvious that the cells will electrically perform, however, to prove that, experimental investigations are obvious.
- **Optimizing front-junction SHJ solar cells :** To prepare 'n-i-p' PVK/Front junction SHJ combination, an initial investigation of the electrical performance of single-junction front junction SHJ solar cells needs to be fabricated and studied.

- **Optimization of the Perovskite/c-Si 4T tandem solar cell layer stack** A complete pattern needs to be investigated to fabricate 4T devices while considering possible optical outcomes.
- **Optimizing different materials for double-side-textured devices:** Reoptimizing the doped layers with suggested thickness to obtain n,k values with varied doping concentration is crucial to enhance the cell's performance.

Acknowledgements

My main objective in pursuing a Master's degree at Delft University of Technology in the Netherlands was to engage in a research-driven, high-tech project focused on solar energy technology. Consequently, I chose Solar as my primary specialization, a decision that has proven to be one of the best of my life. I was deeply passionate about honing my technical and analytical skills for my future career while actively contributing to cutting-edge research.
I am grateful to the PVMD group for creating such an exceptional program focused on photovoltaic (PV) technology and its diverse applications in promoting green energy production. Meeting and learning from some of the most talented researchers in person was truly inspiring. Their expertise in photovoltaics motivated me daily, whether I was facing challenges or striving to enhance my research. Working in state-of-the-art cleanrooms (CR100K and CR10K) fueled my curiosity for exploring new scientific directions and tackling complex challenges. My thesis experience stands as a testament to the power of scientific collaboration across multiple research groups with different specialties, uniting the PVMD group in the Department of Electrical Sustainable Energy, the Else Kooi Laboratory, and both TU Delft and TU Eindhoven.
I sincerely thank Prof. Dr. Olindo Isabella for the wonderful opportunity to contribute to this innovative Master's thesis and for his invaluable guidance, which significantly expanded my research approach from diverse perspectives.
I am deeply grateful to Ir. Yifeng Zhao, my daily supervisor, for his brilliant vision and generous expertise on the hybrid project. His accessibility, lab assistance, and openness to my ideas boosted my confidence, while his support and encouragement, especially during challenging times, kept me motivated. Despite his academic excellence, he remained an inspiring mentor, guiding me through difficulties. His leadership and belief in my abilities made the journey rewarding and meaningful.
Sincere gratitude to Dr. Rudi Santbergen for sharing his knowledge and providing exceptional support with the GenPro4 software and solar systems. His insightful guidance, paired with his expertise in MATLAB, simulation, optics, and PV technology, was crucial to my learning curve.
Thanks to Dr. Luana Mazzarella and Dr. Paul Procel Moya for their helpful assistance. A special thanks to Johannes van Wingerden for his help with SEM measurement. Tom Scholtes' unceasing attention and support are greatly appreciated. A very special thanks to Dr. Engin Özkol for his continuous unconditional support and guidance. His deep knowledge of deposition methods and atomic behaviors has been invaluable in refining my research approach and overcoming technical challenges. I sincerely thank Liqi Cao for his help and continued support, Yilong Zhao for his generosity and guidance, and Gianluca Limodio for his help.
I am sincerely grateful to all the brilliant academics and researchers I encountered at TU Delft for setting an outstanding example and inspiring me. Special thanks to Stefaan Heirman for his endless help and support in the ESP/PV lab. I also appreciate Martijn Tijssen and Tim Velzeboer for their generosity in the lab and for sharing their expertise with the instruments and equipment.
My appreciation also extends to my friends and colleagues for joining me on this journey. Lastly, I want to express my heartfelt gratitude to my parents, sister, family, and my cats for their unwavering love and support. Despite the distance, they have been and always will be my greatest source of strength.
My appreciation also extends to my friends and colleagues for joining me on this journey. Lastly, I want to express my heartfelt gratitude to my parents, sister, family, and my cats for their unwavering love and support. Despite the distance, they have been and always will be my greatest source of strength.

Appendix

Work Package 1: Optical Simulation

Optical Simulation Figures

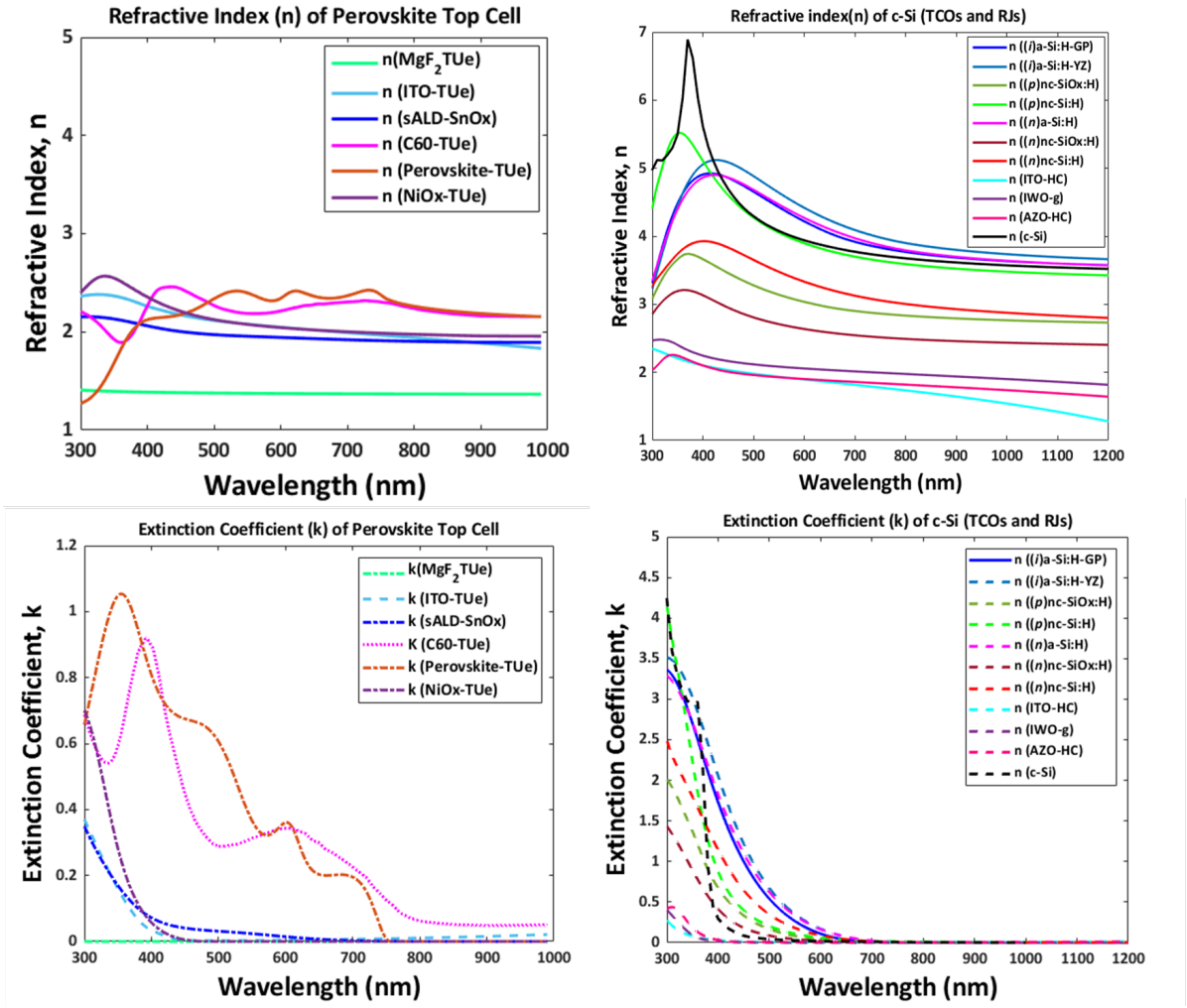

Figure 1: Wavelength-dependent refractive indexes (n) and the Extinction Coefficients(k) of Perovskite/c-Si solar cells.

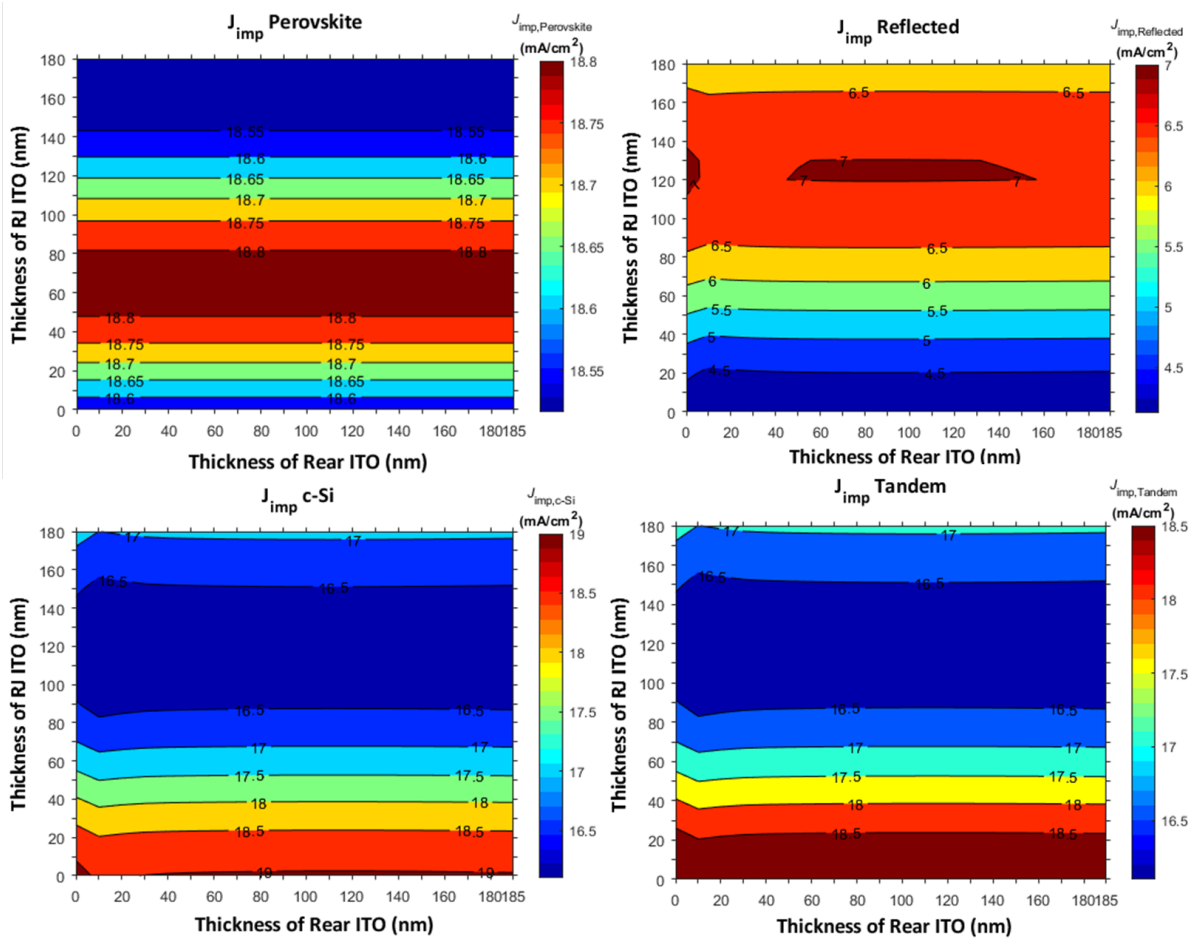

Figure 2: Contour plots of Single-side-textured ITO_ITO 2T tandem configuration.

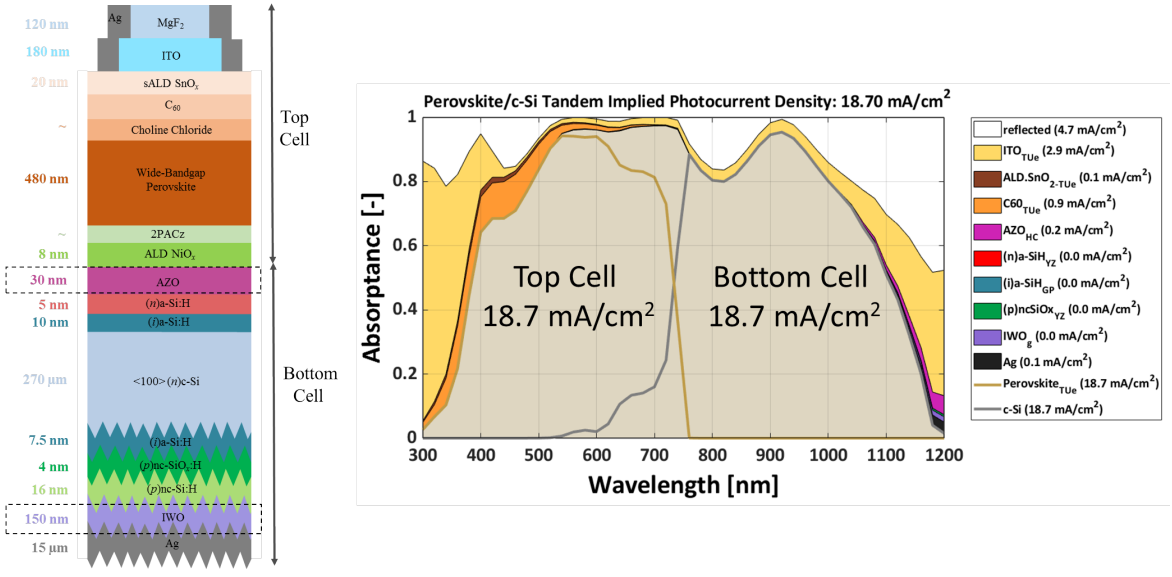

Figure 3: Device architecture of Single-side-textured AZO_IWO 2T tandem configuration.

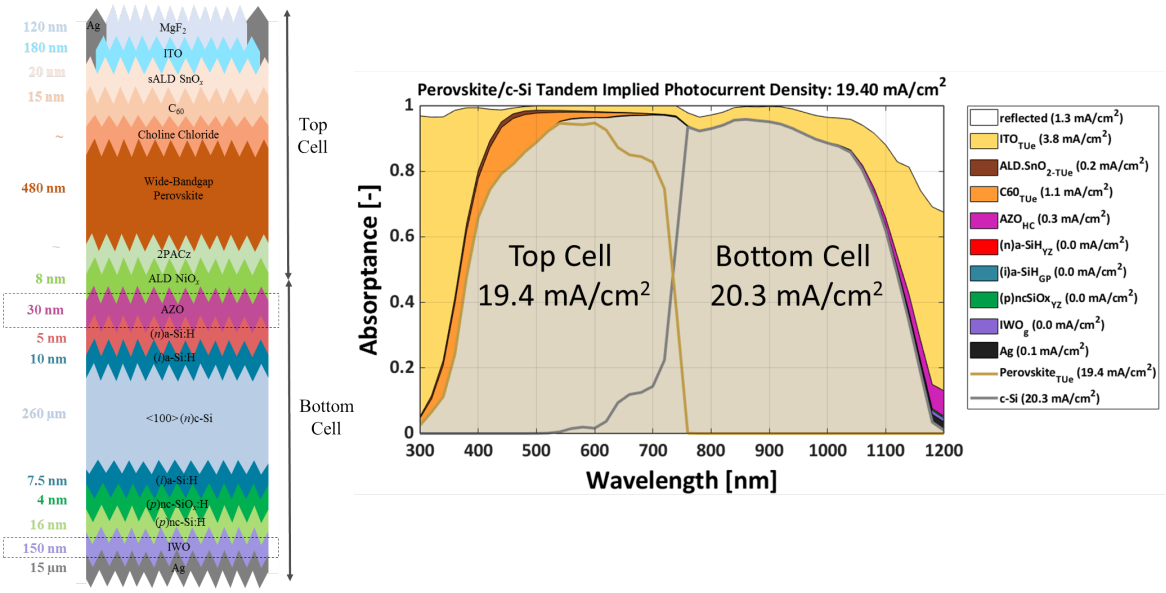

Figure 4: Device architecture of Double-side-textured AZO_IWO 2T tandem configuration.

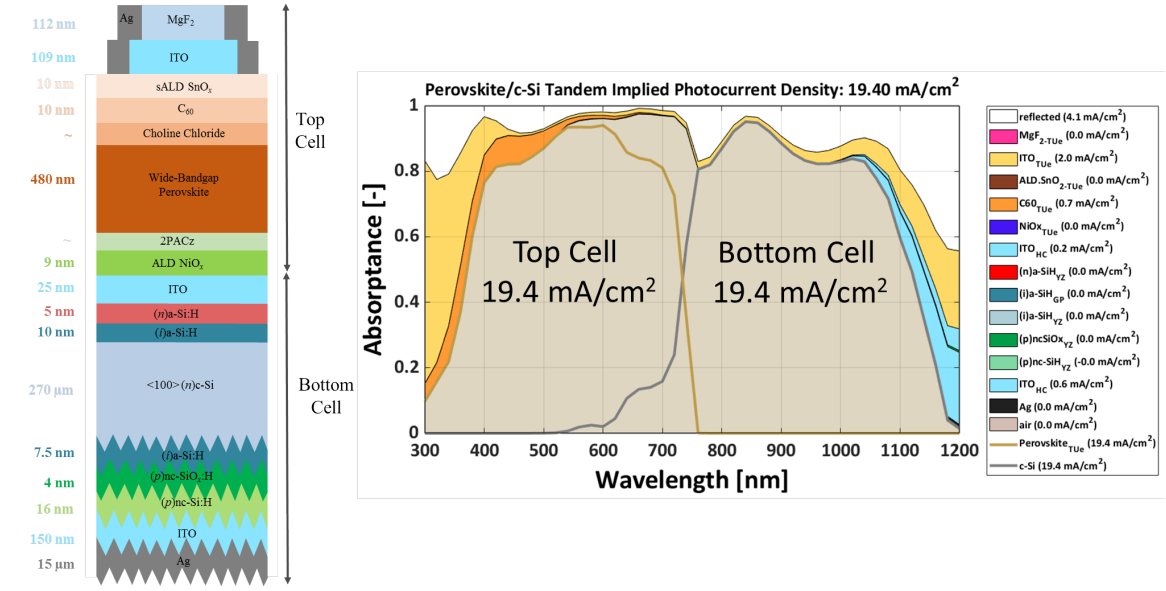

Figure 5: Optimized device architecture of Double-side-textured ITO_ITO 2T tandem configuration.

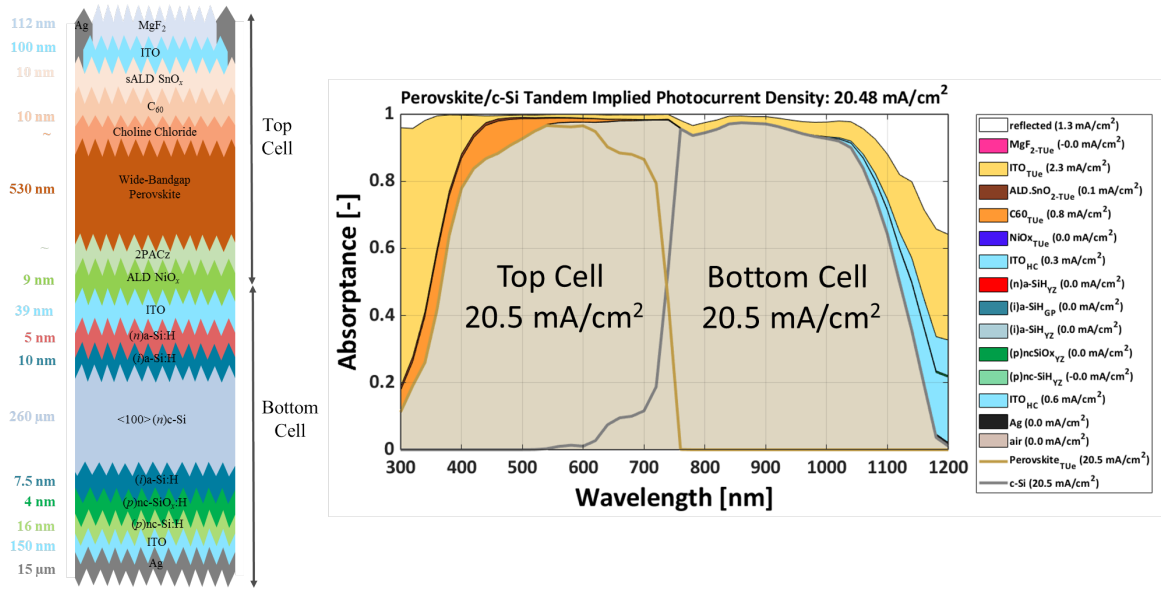

Figure 6: Optimized device architecture of Double-side-textured ITO_ITO 2T tandem configuration.

Optical Simulation Tables

Table 1: Summarizing optical outcomes of Single-side-textured 2T Perovskite/c-Si tandem (with initial RJ thickness) devices.

RJ	Thickness (nm)	Rear TCO	Thickness (nm)	Implied Photocurrent Density				
				Tandem Current J_{Tandem} (mA/cm^2)	Perov. Top cell J_{Perov} (mA/cm^2)	SHJ Bot cell J_{c-Si} (mA/cm^2)	Refl. Loss J_{Refl} (mA/cm^2)	Parasitic Loss $J_{parasitic}$ (mA/cm^2)
ITO	30	ITO	150	18.30	18.7	18.3	4.8	4.5
ITO	30	IWO	150	18.45	18.7	18.4	4.9	4.2
ITO	30	AZO	150	18.42	18.7	18.4	4.7	4.6
IWO	30	ITO	150	18.50	18.7	18.7	4.5	4.5
IWO	30	IWO	150	18.70	18.7	18.8	4.7	4.1
IWO	30	AZO	150	18.59	18.7	18.6	4.6	4.6
AZO	30	ITO	150	18.42	18.7	18.4	4.6	4.5
AZO	30	IWO	150	18.56	18.7	18.6	4.8	4.2
AZO	30	AZO	150	18.35	18.7	18.4	4.6	4.6
(*p*)/(*n*)nc-SiO$_x$:H	30/30	ITO	150	18.45	18.5	20.1	3.2	4.6
(*p*)/(*n*)nc-SiO$_x$:H	30/30	IWO	150	18.45	18.5	20.3	3.3	4.2
(*p*)/(*n*)nc-SiO$_x$:H	30/20	AZO	150	18.45	18.56	20.0	3.1	4.8
(*p*)/(*n*)nc-Si:H	30/20	ITO	150	18.50	18.5	19.7	3.5	4.7
(*p*)/(*n*)nc-Si:H	30/20	IWO	150	18.50	18.5	19.8	3.7	4.3
(*p*)/(*n*)nc-Si:H	30/20	AZO	150	18.50	18.5	19.6	3.5	4.8
(*p*)/(*n*)nc-Si:H w/ (*p*)nc-SiO$_x$:H	30/5/20	ITO	150	18.49	18.5	19.8	3.4	4.7
(*p*)/(*n*)nc-Si:H w/ (*p*)nc-SiO$_x$:H	30/5/20	IWO	150	18.49	18.5	19.9	3.5	4.4
(*p*)/(*n*)nc-Si:H w/ (*p*)nc-SiO$_x$:H	30/5/20	AZO	150	18.49	18.5	19.7	3.3	4.8
(*p*)/(*n*)nc-SiO$_x$:H w/ (*p*)nc-Si:H	30/5/30	ITO	150	18.44	18.4	20.2	3.0	4.6
(*p*)/(*n*)nc-SiO$_x$:H w/ (*p*)nc-Si:H	30/5/30	IWO	150	18.44	18.4	20.4	3.2	4.2
(*p*)/(*n*)nc-SiO$_x$:H w/ (*p*)nc-Si:H	30/5/30	AZO	150	18.44	18.4	20.0	3.0	4.8

Table 2: Summarizing optical outcomes of Single-side-textured 2T Perovskite/c-Si tandem (pre-optimized tandem current) devices.

RJ	Thickness (nm)	Rear TCO	Thickness (nm)	Implied Photocurrent Density: Tandem Current J_{Tandem} (mA/cm^2)	Perov. Top cell J_{Perov} (mA/cm^2)	SHJ Bot cell J_{c-Si} (mA/cm^2)	Refl. Loss J_{Refl} (mA/cm^2)	Parasitic Loss $J_{parasitic}$ (mA/cm^2)
ITO	15	ITO	150	18.65	18.60	18.80	4.4	4.7
ITO	22	IWO	150	18.69	18.70	18.87	4.7	4.2
ITO	15	AZO	150	18.65	18.60	18.70	4.6	4.7
IWO	20	ITO	150	18.66	18.70	18.80	4.4	4.4
IWO	35	IWO	150	18.71	18.70	18.70	4.8	4.1
IWO	20	AZO	150	18.66	18.70	18.70	4.4	4.6
AZO	25	AZO	150	18.67	18.70	18.70	4.4	4.6
AZO	25	IWO	150	18.70	18.70	18.70	4.7	4.2
AZO	15	AZO	150	18.65	18.60	18.70	4.3	4.7
(*p*)/(*n*)nc-SiO_x:H	60/70	ITO	150	18.66	18.70	18.70	4.1	4.9
(*p*)/(*n*)nc-SiO_x:H	59/78	IWO	150	18.66	18.70	18.90	4.5	4.6
(*p*)/(*n*)nc-SiO_x:H	60/70	AZO	150	18.64	18.60	19.00	3.7	5.0
(*p*)/(*n*)nc-Si:H	30/70	ITO	150	18.63	18.60	18.80	4.0	4.8
(*p*)/(*n*)nc-Si:H	30/75	IWO	150	18.63	18.60	18.80	4.4	4.5
(*p*)/(*n*)nc-Si:H	30/70	AZO	150	18.63	18.60	18.70	3.9	4.9
(*p*)/(*n*)nc-Si:H w/ (*p*)nc-SiO_x:H	30/50/20	ITO	150	18.66	18.70	18.70	4.0	5.1
(*p*)/(*n*)nc-Si:H w/ (*p*)nc-SiO_x:H	30/50/20	IWO	150	18.66	18.70	18.80	4.2	4.7
(*p*)/(*n*)nc-Si:H w/ (*p*)nc-SiO_x:H	30/40/20	AZO	150	18.62	18.60	19.00	3.7	5.1
(*p*)/(*n*)nc-SiO_x:H w/ (*p*)nc-Si:H	28/40/28	ITO	150	18.72	18.70	18.80	4.0	4.8
(*p*)/(*n*)nc-SiO_x:H w/ (*p*)nc-Si:H	30/40/30	IWO	150	18.73	18.70	18.80	4.3	4.3
(*p*)/(*n*)nc-SiO_x:H w/ (*p*)nc-Si:H	40/40/30	AZO	150	18.72	18.70	18.70	4.0	4.9

Table 3: Summarizing optical outcomes of Double-side-textured 2T Perovskite/c-Si tandem devices (pre-optimized tandem current).

RJ	Thickness (nm)	Rear TCO	Thickness (nm)	Implied Photocurrent Density: Tandem Current J_{Tandem} (mA/cm^2)	Perov. Top cell J_{Perov} (mA/cm^2)	SHJ Bot cell J_{c-Si} (mA/cm^2)	Refl. Loss J_{Refl} (mA/cm^2)	Parasitic Loss $J_{parasitic}$ (mA/cm^2)
ITO	60	ITO	150	19.53	19.50	19.50	1.5	5.9
ITO	65	IWO	150	19.55	19.50	19.60	1.7	5.7
ITO	55	AZO	150	19.51	19.50	19.60	1.5	5.8
IWO	75	ITO	150	19.47	19.50	20.00	1.4	5.6
IWO	78	IWO	150	19.47	19.50	20.10	1.5	5.4
IWO	75	AZO	150	19.46	19.50	19.90	1.4	5.7
AZO	55	ITO	150	19.53	19.50	19.60	1.4	5.9
AZO	75	IWO	150	19.55	19.60	19.60	1.6	5.8
AZO	65	AZO	150	19.53	19.50	19.50	1.4	5.9
(*p*)/(*n*)nc-SiO_x:H	70/80	ITO	150	19.39	19.40	20.00	1.2	5.6
(*p*)/(*n*)ncSiO_x:H	60/80	IWO	150	19.39	19.40	20.20	1.3	5.4
(*p*)/(*n*)nc-SiO_x:H	60/80	AZO	150	19.39	19.40	20.10	1.1	5.7
(*p*)/(*n*)nc-Si:H	40/70	ITO	150	19.41	19.40	19.90	1.2	5.7
(*p*)/(*n*)nc-Si:H	40/80	IWO	150	19.41	19.40	20.10	1.3	5.5
(*p*)/(*n*)nc-Si:H	40/80	AZO	150	19.40	19.40	19.80	1.3	5.8
(*p*)/(*n*)nc-Si:H w/ (*p*)nc-SiO_x:H	40/5/60	ITO	150	19.41	19.40	20.00	1.2	5.7
(*p*)/(*n*)nc-Si:H w/ (*p*)nc-SiO_x:H	40/5/60	IWO	150	19.41	19.40	20.20	1.3	5.4
(*p*)/(*n*)nc-Si:H w/ (*p*)nc-SiO_x:H	40/5/60	AZO	150	19.41	19.40	20.00	1.2	5.8
(*p*)/(*n*)nc-SiO_x:H w/ (*p*)nc-Si:H	30/50/30	ITO	150	19.46	19.50	19.90	1.2	5.6
(*p*)/(*n*)nc-SiO_x:H w/ (*p*)nc-Si:H	30/50/30	IWO	150	19.46	19.50	20.00	1.3	5.4
(*p*)/(*n*)nc-SiO_x:H w/ (*p*)nc-Si:H	30/50/30	AZO	150	19.46	19.50	19.80	1.2	5.7

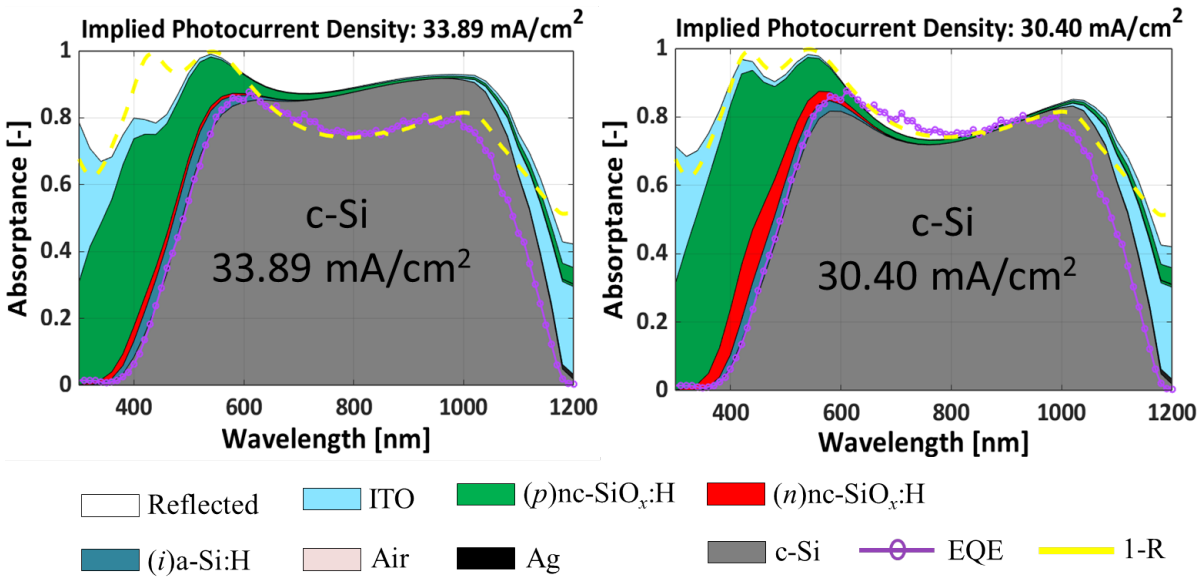

Figure 7: Single-side-textured single-junction SHJ solar cells: (*p*)nc-SiO_x:H (60 nm) samples with (*n*)nc-SiO_x:H (20 nm, 50 nm) layers.

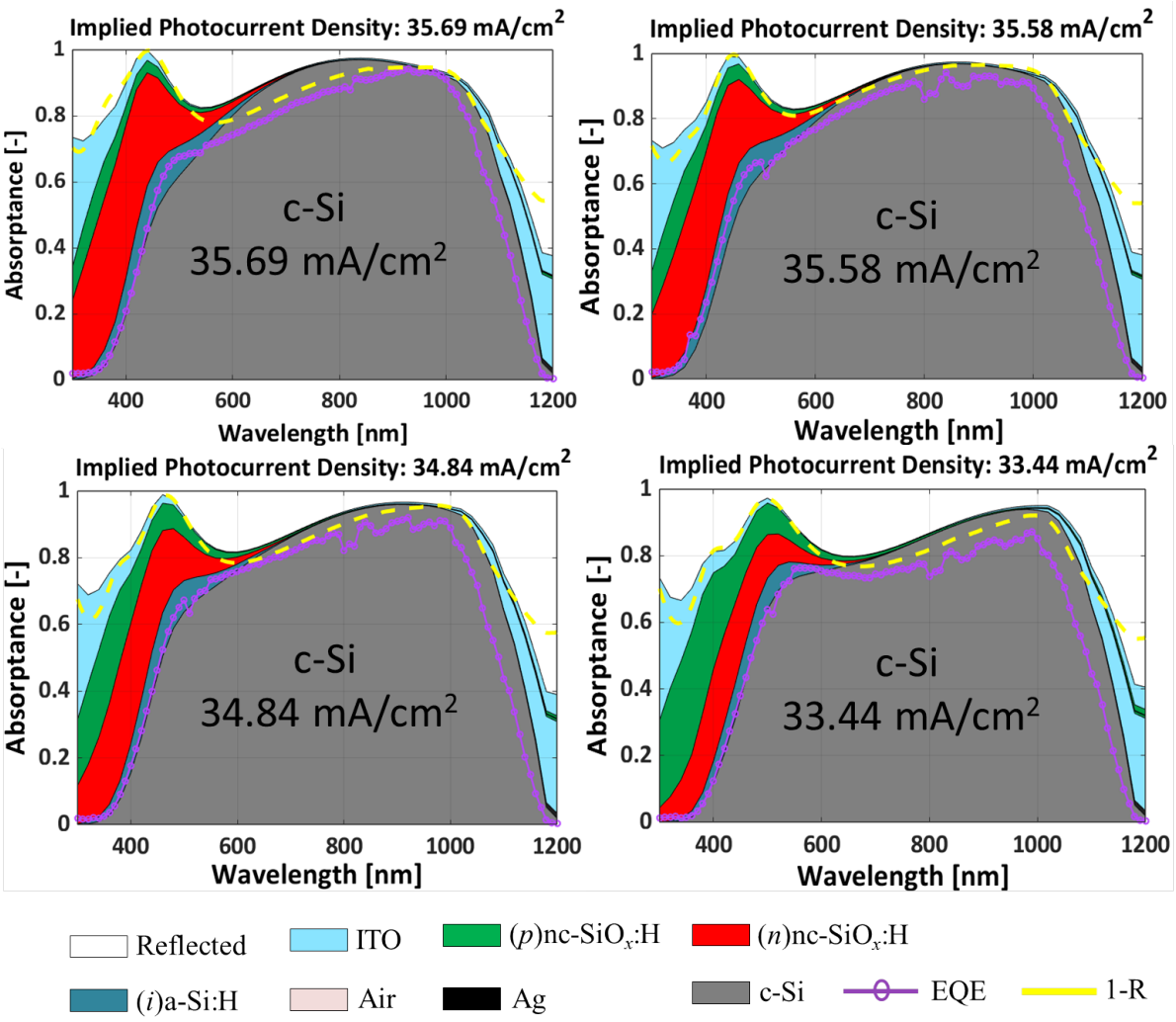

Figure 8: Single-side-textured single-junction SHJ solar cells: (*n*)nc-SiO$_x$:H (60 nm) samples with (*n*)nc-SiO$_x$:H (4 nm, 6 nm, 12 nm, 24 nm) layers.

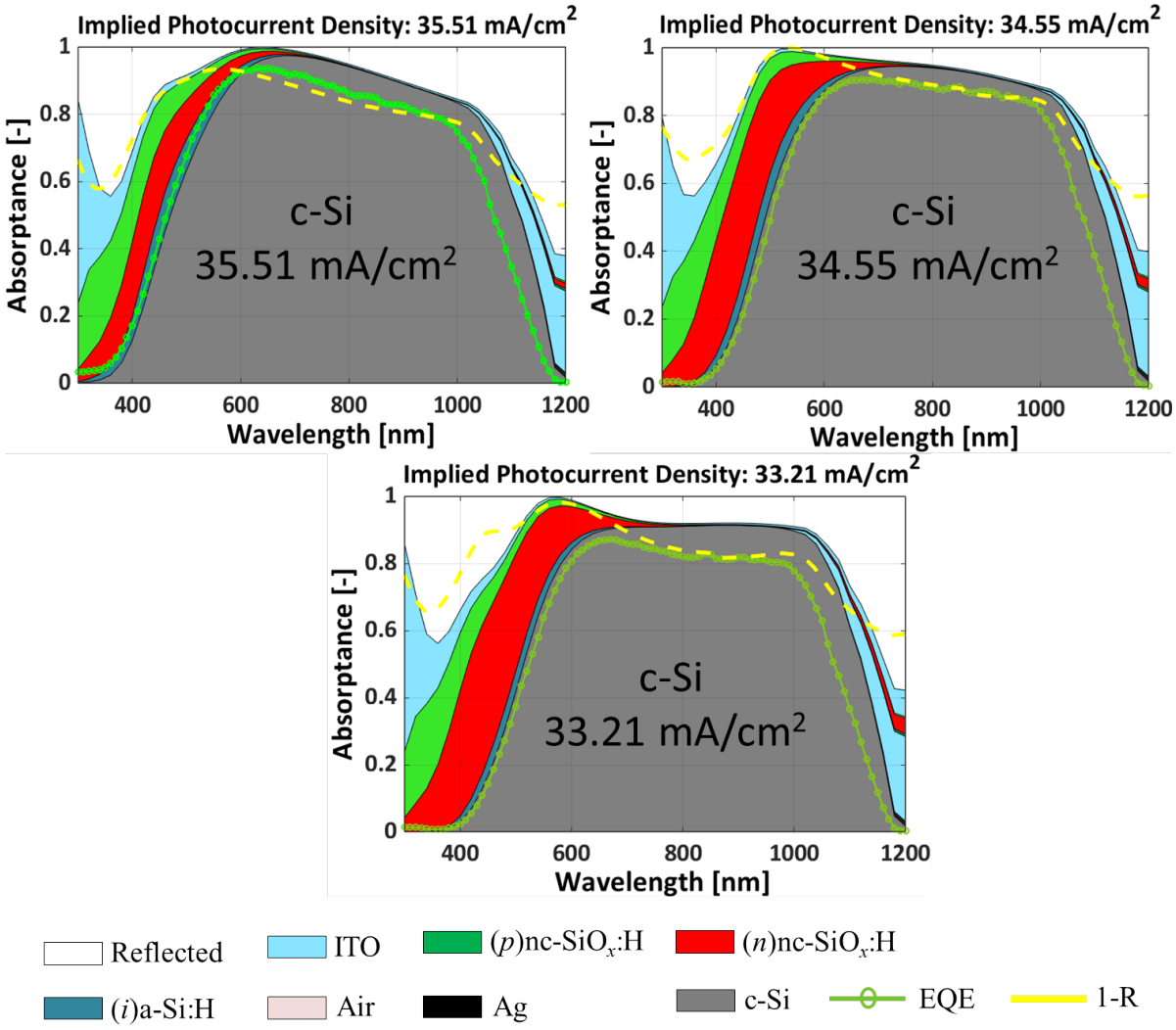

Figure 9: Single-side-textured single-junction SHJ solar cells: (p)nc-Si:H (10 nm) samples with (n)nc-Si:H (20 nm, 40 nm, 60 nm) layers.

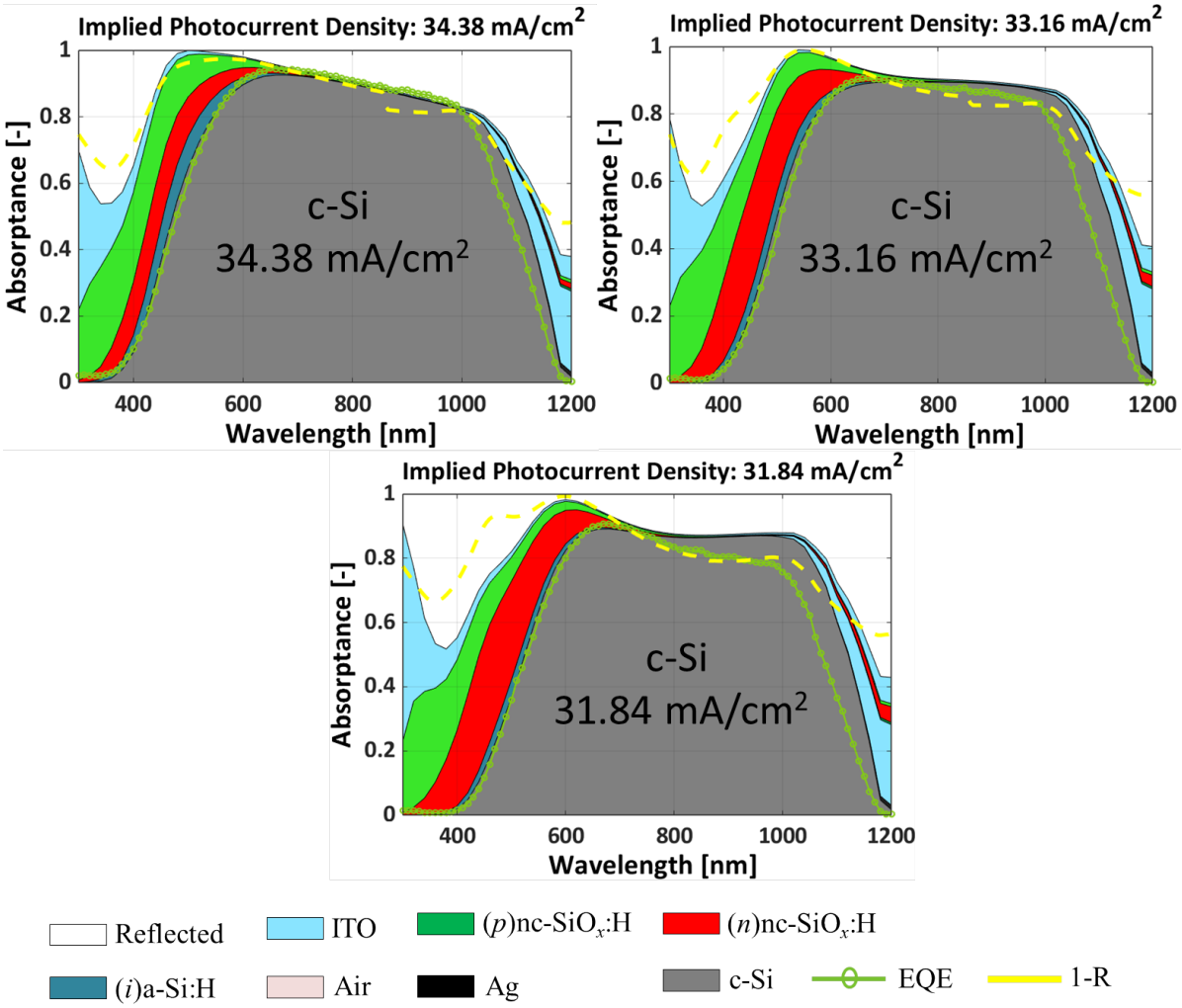

Figure 10: Single-side-textured single-junction SHJ solar cells: (p)nc-Si:H (20 nm) samples with (n)nc-Si:H (20 nm, 40 nm, 60 nm) layers.

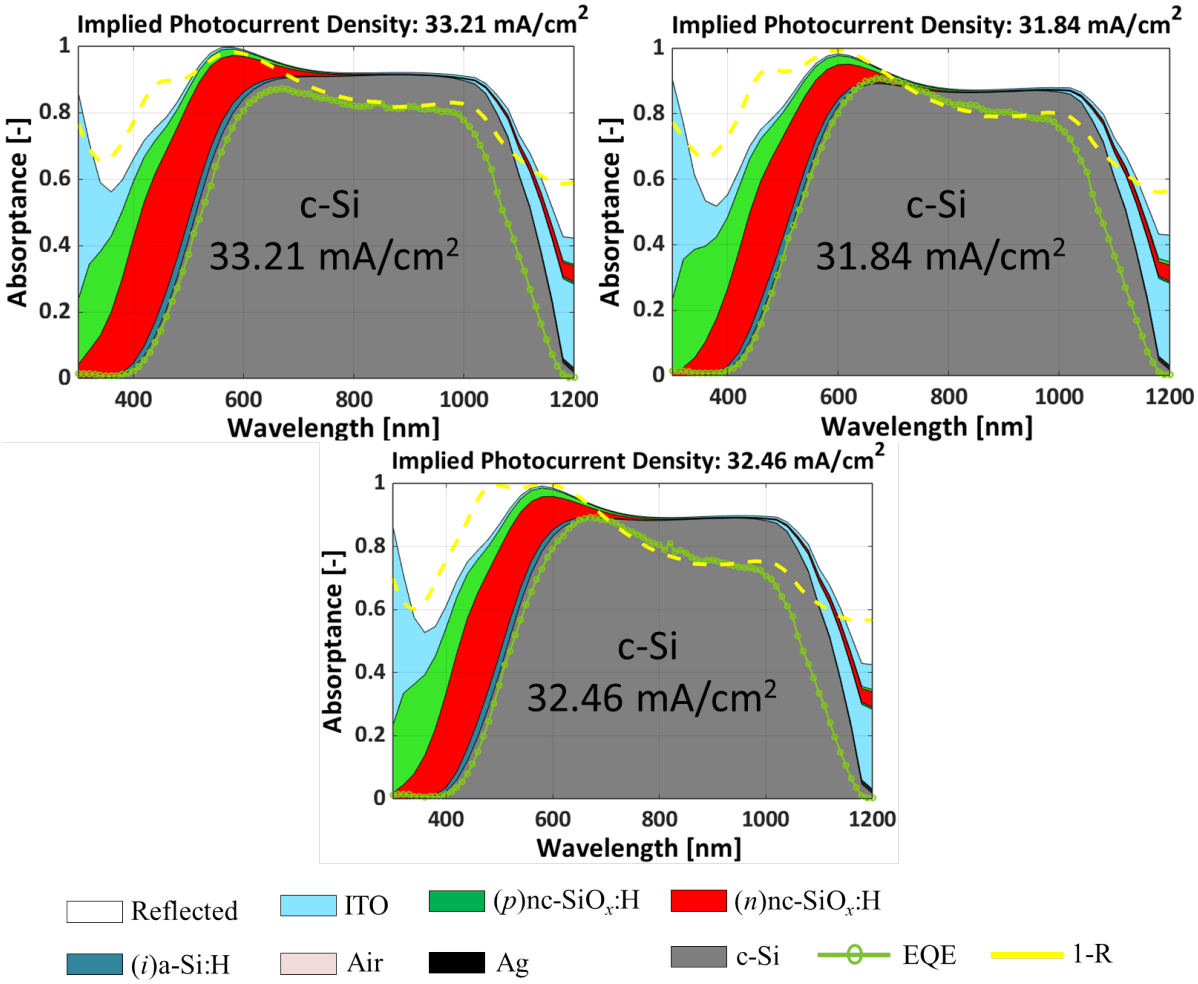

Figure 11: Single-side-textured single-junction SHJ solar cells: (n)nc-Si:H (60 nm) samples with (p)nc-Si:H (10 nm, 20 nm, 30 nm) layers.

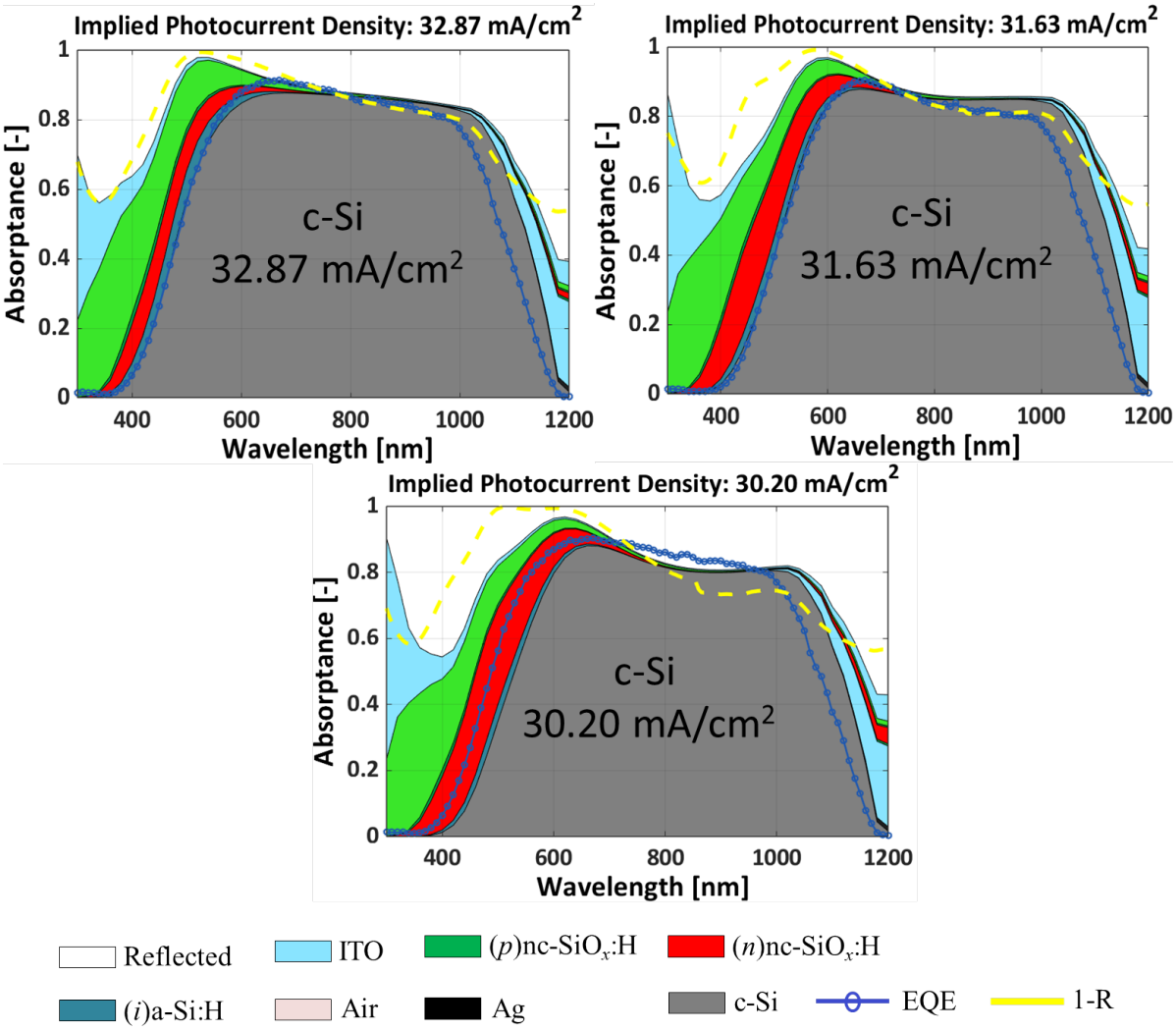

Figure 12: Single-side-textured single-junction SHJ solar cells: (p)nc-Si:H (30 nm)/(p)nc-SiO_x:H (5 nm) samples with (n)nc-Si:H (20 nm , 40 nm, 60 nm) layers.

References

[1] European Commission. *2050 long-term strategy*. URL: https://climate.ec.europa.eu/eu-action/climate-strategies-targets/2050-long-term-strategy_en.

[2] Hannah Ritchie, Max Roser, and Pablo Rosado. “Energy”. In: *Our World in Data* (2020). URL: https://ourworldindata.org/energy.

[3] International Renewable Energy Agency. *World Energy Transitions Outlook: 1.5°C Pathway*. 2022. URL: https://www.irena.org/publications/2022/mar/world-energy-transitions-outlook-2022.

[4] Stefan Ellerbeck. *These regions produce a lot of carbon emissions - here’s what they plan to do about it*. 2022. URL: https://www.weforum.org/agenda/2022/08/electricity-capacity-power-renewable-energy/.

[5] International Renewable Energy Agency. *The First Global Stocktake*. 2022.

[6] LibreTexts. *Introduction to Quantum Physics*. URL: https://phys.libretexts.org/Bookshelves/College_Physics/Book%3A_College_Physics_1e_(OpenStax)/29%3A_Introduction_to_Quantum_Physics/29.04%3A_Photon_Momentum.

[7] Marius Grundmann. *The Physics of Semiconductors*. English. Springer, 2016. ISBN: 978-3-319-23879-1.

[8] NCERT Book. *SEMICONDUCTOR ELECTRONICS: MATERIALS, DEVICES AND SIMPLE CIRCUITS*. URL: https://ncert.nic.in/textbook/pdf/leph206.pdf.

[9] Luana Mazzarella. “Nanocrystalline Silicon and Silicon Oxide Contact Layers for Silicon Heterojunction Solar Cells”. In: (2017). DOI: 10.14279/depositonce-5943. URL: https://www.proquest.com/openview/a201fa7e61a00efe2557d213b3769905/1?pq-origsite=gscholar&cbl=2026366&diss=y.

[10] A.H.M. Smets et al. *Solar energy : the physics and engineering of photovoltaic conversion technologies and systems*. English. UIT, 2016. ISBN: 978-1-906860-32-5.

[11] B. Van Zeghbroeck. *Principles of Semiconductor Devices*. English. 2002. URL: https://www.eletrica.ufpr.br/graduacao/e-books/Principles%5C%20Of%5C%20Semiconductor%5C%20Devices.pdf.

[12] *How a Solar Cell Works*. 2014. URL: https://www.acs.org/content/acs/en/education/resources/highschool/chemmatters/past-issues/archive-2013-2014/how-a-solar-cell-works.html.

[13] Solar Energy Research Institute. *Basic Photovoltaic Principles and Me1hods*. 1982. URL: https://www.nrel.gov/docs/legosti/old/1448.pdf.

[14] Electrical4U. *Solar Cell: Working Principle Construction (Diagrams Included)*. 2020. URL: https://www.electrical4u.com/solar-cell/?utm_content=cmp-true.

[15] Green Sarawak. *Photovoltaic – Harvesting the Power of the Sun*. 2017. URL: https://greensarawak.com/photovoltaic-harvesting-the-power-of-the-sun/.

[16] Miaomiao Zhang et al. “Recent progress in inorganic tin perovskite solar cells”. English. In: *Materials Today Energy* 23 (Jan. 2022). ISSN: 2468-6069. DOI: 10.1016/j.mtener.2021.100891.

[17] Hongqiao Wang et al. “Progress in Perovskite Solar Cells towards Commercialization—A Review”. In: *Materials* 14.21 (2021). ISSN: 1996-1944. DOI: 10.3390/ma14216569. URL: https://www.mdpi.com/1996-1944/14/21/6569.

[18] R. Rößler et al. “Impact of the transparent conductive oxide work function on injection-dependent a-Si:H/c-Si band bending and solar cell parameters”. In: *Journal of Applied Physics* 113.14 (Apr. 2013). 144513. ISSN: 0021-8979. DOI: 10.1063/1.4799042. URL: https://doi.org/10.1063/1.4799042.

[19] Stanislau Herasimenka, William Dauksher, and Stuart Bowden. “750 mV open circuit voltage measured on 50 µm thick silicon heterojunction solar cell”. In: *Applied Physics Letters* 103 (July 2013). DOI: 10.1063/1.4817723.

[20] Mikio Taguchi et al. “Obtaining a higher Voc in HIT cells”. In: *Progress in Photovoltaics: Research and Applications* 13 (Sept. 2005), pp. 481–488. DOI: 10.1002/pip.646.

[21] L.L. Yan et al. “A review on c-Si bottom cell for monolithic perovskite/silicon tandem solar cells”. In: *Materials Today Nano* 7 (July 2019), p. 100045. DOI: 10.1016/j.mtnano.2019.100045.

[22] Martin Bivour et al. “Improving the a-Si:H(p) rear emitter contact of n-type silicon solar cells”. In: *Solar Energy Materials and Solar Cells* 106 (Nov. 2012), pp. 11–16. DOI: 10.1016/j.solmat.2012.06.036.

[23] Kurt-Ulrich Ritzau et al. “TCO work function related transport losses at the a-Si:H/TCO-contact in SHJ solar cells”. In: *Solar Energy Materials and Solar Cells* 131 (July 2014), pp. 9–13. DOI: 10.1016/j.solmat.2014.06.026.

[24] Simon M.F. Zhang et al. “Illumination-dependent temperature coefficients of the electrical parameters of modern silicon solar cell architectures”. In: *Nano Energy* 98 (2022), p. 107221. ISSN: 2211-2855. DOI: https://doi.org/10.1016/j.nanoen.2022.107221. URL: https://www.sciencedirect.com/science/article/pii/S2211285522003020.

[25] *QD Solar Technology*. 2020. URL: https://qdsolarinc.com/technology/.

[26] A.H.M. Smets et al. *Solar energy : the physics and engineering of photovoltaic conversion technologies and systems*. English. UIT, 2016. ISBN: 978-1-906860-32-5.

[27] Wei Sha et al. “The efficiency limit of CH3NH3PbI3 perovskite solar cells”. In: *Applied Physics Letters* 106 (June 2015), p. 221104. DOI: 10.1063/1.4922150.

[28] Armin Richter, Martin Hermle, and Stefan Glunz. “Reassessment of the Limiting Efficiency for Crystalline Silicon Solar Cells”. In: *IEEE Journal of Photovoltaics* 3 (July 2013), pp. 1184–1191. DOI: 10.1109/JPHOTOV.2013.2270351.

[29] Steven Hegedus and Antonio Luque. “Status, Trends, Challenges and the Bright Future of Solar Electricity from Photovoltaics”. In: Jan. 2005, pp. 1–43. ISBN: 9780471491965. DOI: 10.1002/0470014008.ch1.

[30] Jérémie Werner, Bjoern Niesen, and Christophe Ballif. “Perovskite/Silicon Tandem Solar Cells: Marriage of Convenience or True Love Story? - An Overview”. In: *Advanced Materials Interfaces* 5 (Sept. 2017), p. 1700731. DOI: 10.1002/admi.201700731.

[31] Yuanhang Cheng and Liming Ding. “Perovskite/Si tandem solar cells: Fundamentals, advances, challenges, and novel applications”. In: *SusMat* 1 (Sept. 2021). DOI: 10.1002/sus2.25.

[32] Ehsan Raza and Zubair Ahmad. “Review on two-terminal and four-terminal crystalline-silicon/perovskite tandem solar cells; progress, challenges, and future perspectives”. In: *Energy Reports* 8 (Apr. 2022). DOI: 10.1016/j.egyr.2022.04.028.

[33] Kenji Yamamoto et al. “High-efficiency heterojunction crystalline Si solar cells”. In: *Japanese Journal of Applied Physics* 57 (Aug. 2018), 08RB20. DOI: 10.7567/JJAP.57.08RB20.

[34] Yan Li et al. “Reflective Perovskite Solar Cells for Efficient Tandem Application”. In: *J. Mater. Chem. C* 5 (Jan. 2016). DOI: 10.1039/C6TC04510C.

[35] Marko Jošt et al. “Monolithic Perovskite Tandem Solar Cells: A Review of the Present Status and Advanced Characterization Methods Toward 30% Efficiency”. In: *Advanced Energy Materials* 10 (May 2020). DOI: 10.1002/aenm.201904102.

[36] Silvia Mariotti et al. “Interface engineering for high-performance, triple-halide perovskite-silicon tandem solar cells”. In: *Science (New York, N.Y.)* 381 (July 2023), pp. 63–69. DOI: 10.1126/science.adf5872.

[37] EMILIANO BELLINI. *KAUST claims 33.2% efficiency for perovskite/silicon tandem solar cell*. 2023. URL: https://www.pv-magazine.com/2023/04/13/kaust-claims-33-2-efficiency-for-perovskite-silicon-tandem-solar-cell/.

[38] Madjda Bacha et al. “Design and numerical investigation of Perovskite/Silicon tandem solar cell”. In: *Optical Materials* 131 (July 2022). DOI: 10.1016/j.optmat.2022.112671.

[39] Philipp Tockhorn et al. “Nano-optical designs enhance monolithic perovskite/silicon tandem solar cells toward 29.8% efficiency”. In: (Mar. 2022). DOI: 10.21203/rs.3.rs-1439562/v1.

[40] Eike Köhnen et al. “27.9% Efficient Monolithic Perovskite/Silicon Tandems on Industry Compatible Bottom Cells”. In: *Solar RRL* 5 (Apr. 2021). DOI: 10.1002/solr.202100244.

[41] Amran Al-Ashouri et al. “Monolithic perovskite/silicon tandem solar cell with >29% efficiency by enhanced hole extraction”. In: *Science* 370 (Dec. 2020). DOI: 10.1126/science.abd4016.

[42] Patricia Schulze et al. “25.1% high-efficiency monolithic perovskite silicon tandem solar cell with a high bandgap perovskite absorber”. In: (Mar. 2020). DOI: 10.25932/publishup-52566.

[43] Bo Chen et al. “Blade-Coated Perovskites on Textured Silicon for 26%-Efficient Monolithic Perovskite/Silicon Tandem Solar Cells”. In: *Joule* 4 (Jan. 2020). DOI: 10.1016/j.joule.2020.01.008.

[44] Alexander Bett et al. “Two□terminal Perovskite silicon tandem solar cells with a high□Bandgap Perovskite absorber enabling voltages over 1.8 V”. In: *Progress in Photovoltaics: Research and Applications* 28 (Nov. 2019). DOI: 10.1002/pip.3208.

[45] Eike Köhnen et al. “Highly Efficient Monolithic Perovskite Silicon Tandem Solar Cells: Analyzing the Influence of Current Mismatch on Device Performance”. In: *Sustainable Energy & Fuels* 3 (May 2019). DOI: 10.1039/C9SE00120D.

[46] Luana Mazzarella et al. “Infrared Light Management Using a Nanocrystalline Silicon Oxide Interlayer in Monolithic Perovskite/Silicon Heterojunction Tandem Solar Cells with Efficiency above 25%”. In: *Advanced Energy Materials* (Feb. 2019). DOI: 10.1002/aenm.201803241.

[47] Fuhua Hou et al. “Monolithic Perovskite/Silicon-Heterojunction Tandem Solar Cells with Open-Circuit Voltage of over 1.8 V”. In: *ACS Applied Energy Materials* 2 (Jan. 2019). DOI: 10.1021/acsaem.8b00926.

[48] Bo Chen et al. “Grain Engineering for Perovskite/Silicon Monolithic Tandem Solar Cells with Efficiency of 25.4%”. In: *Joule* 3 (Oct. 2018). DOI: 10.1016/j.joule.2018.10.003.

[49] Marko Jošt et al. “Textured interfaces in monolithic perovskite/silicon tandem solar cells: Advanced light management for improved efficiency and energy yield”. In: *Energy & Environmental Science* 11 (Jan. 2019). DOI: 10.1039/C8EE02469C.

[50] Kevin A. Bush et al. “Minimizing Current and Voltage Losses to Reach 25% Efficient Monolithic Two-Terminal Perovskite-Silicon Tandem Solar Cells”. English (US). In: *ACS Energy Letters* 3.9 (Sept. 2018), pp. 2173–2180. ISSN: 2380-8195. DOI: 10.1021/acsenergylett.8b01201.

[51] Florent Sahli et al. “Fully textured monolithic perovskite/silicon tandem solar cells with 25.2% power conversion efficiency”. In: *Nature Materials* 17 (Sept. 2018). DOI: 10.1038/s41563-018-0115-4.

[52] Jianghui Zheng et al. “Large area efficient interface layer free monolithic perovskite/homojunction-silicon tandem solar cell with over 20% efficiency”. In: *Energy Environmental Science* 11 (June 2018). DOI: 10.1039/C8EE00689J.

[53] Florent Sahli et al. “Improved Optics in Monolithic Perovskite/Silicon Tandem Solar Cells with a Nanocrystalline Silicon Recombination Junction”. In: *Advanced Energy Materials* 8 (Oct. 2017), p. 1701609. DOI: 10.1002/aenm.201701609.

[54] Yiliang Wu et al. “Monolithic perovskite/silicon-homojunction tandem solar cell with over 22% efficiency”. In: *Energy Environ. Sci.* 10 (Oct. 2017). DOI: 10.1039/C7EE02288C.

[55] Kevin Bush et al. “23.6%-efficient monolithic perovskite/silicon tandem solar cells with improved stability”. In: *Nature Energy* 2 (Feb. 2017), p. 17009. DOI: 10.1038/nenergy.2017.9.

[56] Jérémie Werner et al. “Zinc tin oxide as high-temperature stable recombination layer for mesoscopic perovskite/silicon monolithic tandem solar cells”. In: *Applied Physics Letters* 109 (Dec. 2016), p. 233902. DOI: 10.1063/1.4971361.

[57] Jérémie Werner et al. “Efficient Near-Infrared-Transparent Perovskite Solar Cells Enabling Direct Comparison of 4-Terminal and Monolithic Perovskite/Silicon Tandem Cells”. In: *ACS Energy Letters* 1.2 (July 2016). DOI: 10.1021/acsenergylett.6b00254.

[58] Jérémie Werner et al. “Efficient Monolithic Perovskite/Silicon Tandem Solar Cell With Cell Area > 1 cm2”. In: (Dec. 2015).

[59] Steve Albrecht et al. “Monolithic Perovskite/Silicon-Heterojunction Tandem Solar Cells Processed at Low Temperature”. In: *Energy Environmental Science* (Nov. 2015). DOI: 10.1039/C5EE02965A.

[60] Bo Chen et al. “Grain Engineering for Perovskite/Silicon Monolithic Tandem Solar Cells with Efficiency of 25.4%”. In: *Joule* 3.1 (2019), pp. 177–190. ISSN: 2542-4351. DOI: https://doi.org/10.1016/j.joule.2018.10.003. URL: https://www.sciencedirect.com/science/article/pii/S2542435118304653.

[61] S. Altazin et al. “Design of perovskite/crystalline-silicon monolithic tandem solar cells”. In: *Optics Express* 26 (May 2018), A579. DOI: 10.1364/OE.26.00A579.

[62] Apolline Puaud et al. “Microcrystalline Silicon Tunnel Junction for Monolithic Tandem Solar Cells Using Silicon Heterojunction Technology”. In: *IEEE Journal of Photovoltaics* PP (Nov. 2020), pp. 1–7. DOI: 10.1109/JPHOTOV.2020.3038600.

[63] Jinju Park et al. “Improved Carrier Tunneling and Recombination in Tandem Solar Cell with p-type Nanocrystalline Si Intermediate Layer”. In: *Current Photovoltaic Research* 8.1 (2020), pp. 6–11. ISSN: 2288-3274. DOI: 10.21218/CPR.2020.8.1.006.

[64] Michele De Bastiani et al. “Recombination junctions for efficient monolithic perovskite-based tandem solar cells: Physical principles, properties, processing and prospects”. In: *Materials Horizons* 7 (Nov. 2020), pp. 2791–2809. DOI: 10.1039/d0mh00990c.

[65] Luana Mazzarella et al. “Versatility of Nanocrystalline Silicon Films: from Thin-Film to Perovskite/c-Si Tandem Solar Cell Applications”. In: *Coatings* 10 (Aug. 2020), p. 759. DOI: 10.3390/coatings10080759.

[66] Romain Cariou. “Low temperature plasma enhanced CVD epitaxial growth of silicon on GaAs: a new paradigm for III-V Si integration”. In: *Scientific Reports* 6 (2016). DOI: doi.org/10.1038/srep25674.

[67] Stefaan De Wolf. “Intrinsic and Doped a-Si:H/c-Si Interface Passivation”. In: Jan. 2012, pp. 223–259. ISBN: 978-3-642-22274-0. DOI: 10.1007/978-3-642-22275-7_7.

[68] Yifeng Zhao et al. “Effects of (i)a-Si: H deposition temperature on high-efficiency silicon heterojunction solar cells”. English. In: *Progress in Photovoltaics: research and applications* (2022). ISSN: 1062-7995. DOI: 10.1002/pip.3620.

[69] Dimitrios Deligiannis et al. “Passivation mechanism in silicon heterojunction solar cells with intrinsic hydrogenated amorphous silicon oxide layers”. In: 121 (Feb. 2017). DOI: 10.1063/1.4977242.

[70] Zachary Holman et al. “Record Infrared Internal Quantum Efficiency in Silicon Heterojunction Solar Cells With Dielectric/Metal Rear Reflectors”. In: *Photovoltaics, IEEE Journal of* 3 (Oct. 2013), pp. 1243–1249. DOI: 10.1109/JPHOTOV.2013.2276484.

[71] Atse Louwen et al. “A cost roadmap for silicon heterojunction solar cells”. In: *Solar Energy Materials and Solar Cells* 147 (Apr. 2016), pp. 295–314. DOI: 10.1016/j.solmat.2015.12.026.

[72] Engin Özkol et al. “Effective Passivation of Black Silicon Surfaces via Plasma□Enhanced Chemical Vapor Deposition Grown Conformal Hydrogenated Amorphous Silicon Layer”. In: *physica status solidi (RRL) - Rapid Research Letters* 14 (Oct. 2019). DOI: 10.1002/pssr.201900087.

[73] Thierry de Vrijer et al. “The fundamental operation mechanisms of nc-SiOX≥0:H based tunnel recombination junctions revealed”. In: *Solar Energy Materials and Solar Cells* 236 (2022), p. 111501. ISSN: 0927-0248. DOI: https://doi.org/10.1016/j.solmat.2021.111501. URL: https://www.sciencedirect.com/science/article/pii/S0927024821005390.

[74] Yuchao Zhang et al. “Design Considerations for Multi-terawatt Scale Manufacturing of Existing and Future Photovoltaic Technologies: Challenges and Opportunities Related to Silver, Indium and Bismuth Consumption”. In: *Energy Environmental Science* 14 (Nov. 2021). DOI: 10.1039/D1EE01814K.

[75] W.E. Spear and P.G. Le Comber. “Substitutional doping of amorphous silicon”. In: *Solid State Communications* 17.9 (1975), pp. 1193–1196. ISSN: 0038-1098. DOI: https://doi.org/10.1016/0038-1098(75)90284-7. URL: https://www.sciencedirect.com/science/article/pii/0038109875902847.

[76] S. A. Kokorowski et al. “Investigation of the Melting Temperature of Amorphous Silicon”. In: *Phys. Rev. Lett.* 48 (7 Feb. 1982), pp. 498–501. DOI: 10.1103/PhysRevLett.48.498. URL: https://link.aps.org/doi/10.1103/PhysRevLett.48.498.

[77] www.americanelements.com. *Amorphous Silicon*. URL: https://www.americanelements.com/amorphous-silicon-7440-21-3.

[78] Jimmy Melskens. “Optimisation of a protocrystalline hydrogenated amorphous silicon top solar cell for highest stabilised efficiency”. PhD thesis. Nov. 2007.

[79] M. Menichelli, L. Servoli, and N. Wyrsch. “Status and perspectives of hydrogenated amorphous silicon detectors for MIP detection and beam flux measurements”. In: *Frontiers in Physics* 10 (2022). ISSN: 2296-424X. DOI: 10.3389/fphy.2022.943306. URL: https://www.frontiersin.org/articles/10.3389/fphy.2022.943306.

[80] Jimmy Melskens. “Hydrogenated amorphous silicon: nanostructure and defects”. PhD thesis. Feb. 2015. DOI: 10.4233/uuid:13d60d5e-3d68-4ac7-b2b6-a867cc393231.

[81] J.P.M. Schmitt. “Amorphous silicon deposition: Industrial and technical challenges”. In: *Thin Solid Films* 174 (1989), pp. 193–202. ISSN: 0040-6090. DOI: https://doi.org/10.1016/0040-6090(89)90889-4. URL: https://www.sciencedirect.com/science/article/pii/0040609089908894.

[82] Sanjeev Sharma et al. “Review on Se-and S-doped hydrogenated amorphous silicon thin films”. In: *Indian Journal of Pure and Applied Physics* 52 (May 2014), pp. 293–313.

[83] Andrés Cuevas and Daniel Macdonald. “Measuring and interpreting the lifetime of silicon wafers”. In: *Solar Energy* 76 (Mar. 2004), pp. 255–262. DOI: 10.1016/j.solener.2003.07.033.

[84] Yifeng Zhao. *Contact Stack Evaluation for SHJ Solar Cells and Process Development of IBC-SHJ Solar Cells*. 2018.

[85] Ihor Kupchak et al. “Temperature dependent vibrational spectra and bond dynamics in hydrogenated amorphous silicon”. In: *Journal of Applied Physics* 103 (July 2008), pp. 123525–123525. DOI: 10.1063/1.2946454.

[86] Giulia Paggiaro. *Optimizations of high-efficiency silicon heterojunction solar cells for tandem applications*. 2021.

[87] Hosni Meddeb et al. “Structural, hydrogen bonding and in situ studies of the effect of hydrogen dilution on the passivation by amorphous silicon of n-type crystalline (1 0 0) silicon surfaces”. In: *Journal of Physics D Applied Physics* 48 (Sept. 2015), p. 415301. DOI: 10.1088/0022-3727/48/41/415301.

[88] Wilfried van Sark, Lars Korte, and Francesco Roca. *Physics and technology of amorphous-crystalline heterostructure silicon solar cells*. Jan. 2011. ISBN: 978-3-642-22274-0. DOI: 10.1007/978-3-642-22275-7.

[89] John Knights et al. “Erratum: Effects of inert gas dilution of silane on plasma-deposited aSi:H films”. In: *Applied Physics Letters* 39 (July 1981). DOI: 10.1063/1.92883.

[90] Akihisa Matsuda and Kazunobu Tanaka. “Investigation of the growth kinetics of glow□discharge hydrogenated amorphous silicon using a radical separation technique”. In: *Journal of Applied Physics* 60 (June 1986). DOI: https://doi.org/10.1063/1.337144.

[91] Alan Gallagher. “Neutral radical deposition from silane discharges”. In: *Journal of Applied Physics* 63 (1988). DOI: doi.org/10.1063/1.341034.

[92] Akihisa Matsuda et al. “Control of plasma chemistry for preparing highly stabilized amorphous silicon at high growth rate”. In: *Solar Energy Materials and Solar Cells* 78 (July 2003), pp. 3–26. DOI: 10.1016/S0927-0248(02)00431-2.

[93] W.M.M. Kessels et al. “The a-Si:H Growth Mechanism: Temperature Study of the SiH3 Surface Reactivity and the Surface Silicon Hydride Composition During Film Growth”. In: *MRS Proceedings* 762 (Jan. 2003). DOI: 10.1557/PROC-762-A9.3.

[94] Ihor Kupchak et al. “Film formation mechanisms in the plasma deposition of hydrogenated amorphous silicon”. In: *Journal of Applied Physics* 59 (June 1986). DOI: doi.org/10.1063/1.336920.

[95] Yun-Shao Cho et al. “Effect of Hydrogen Content in Intrinsic a-Si:H on Performances of Heterojunction Solar Cells”. In: *International Journal of Photoenergy* 2013 (Jan. 2013). DOI: 10.1155/2013/121875.

[96] U. Das et al. “Surface passivation and heterojunction cells on Si (100) and (111) wafers using dc and rf plasma deposited Si:H thin films”. In: *Applied Physics Letters* 92 (Mar. 2008), pp. 063504–063504. DOI: 10.1063/1.2857465.

[97] Pere Cabarrocas, R. Cariou, and Martin Labrune. “Low temperature plasma deposition of silicon thin films: From amorphous to crystalline”. In: *Journal of Non-Crystalline Solids* 358 (Sept. 2012), pp. 2000–2003. DOI: 10.1016/j.jnoncrysol.2011.12.113.

[98] Dean Levi et al. “Real Time Spectroscopic Ellipsometry Studies of the Growth of Amorphous and Epitaxial Silicon for Photovoltaic Applications”. In: *Journal of Vacuum Science Technology A - J VAC SCI TECHNOL A* 24 (July 2006). DOI: 10.1116/1.2167083.

[99] F. Jona. “STUDY OF THE EARLY STAGES OF THE EPITAXY OF SILICON ON SILICON”. In: *Applied Physics Letters* 9.6 (Nov. 2004), pp. 235–237.

[100] academic-accelerator.com. *Dangling Bond*. URL: https://academic-accelerator.com/encyclopedia/dangling-bond?Journal=hydrogen+atoms+and+adsorbed+to+the+dangling+bond%5C%2C.

[101] Armin G. Aberle. *PCrystalline Silicon Solar Cells: Advanced Surface Passivation and Analysis*. English. Centre for Photovoltaic Engineering, University of New South Wales, 1999. ISBN: 9780733406454.

[102] Jan-Willem Schüttauf et al. “Excellent crystalline silicon surface passivation by amorphous silicon irrespective of the technique used for chemical vapor deposition”. In: *Applied Physics Letters* 98 (Apr. 2011), pp. 153514–153514. DOI: 10.1063/1.3579540.

[103] Hiroyuki Fujiwara and Michio Kondo. “Effects of a-Si:H layer thicknesses on the performance of a-Si:H/c-Si heterojunction solar cells”. In: *Journal of Applied Physics* 101 (Apr. 2007), pp. 054516–054516. DOI: 10.1063/1.2559975.

[104] Fengyou Wang et al. “Role of Hydrogen Plasma Pretreatment in Improving Passivation of the Silicon Surface for Solar Cells Applications”. In: *ACS applied materials interfaces* 6 (Aug. 2014). DOI: 10.1021/am5031837.

[105] Christoph Luderer et al. “Intrinsic layer modification in silicon heterojunctions: Balancing transport and surface passivation”. In: *Solar Energy Materials and Solar Cells* 238 (May 2022), p. 111412. DOI: 10.1016/j.solmat.2021.111412.

[106] Sara Olibet, Evelyne Vallat, and Christophe Ballif. “Model for a-Si:H/C-Si interface recombination based on the amphoteric nature of silicon dangling bonds”. In: *Physical Review B* 76 (July 2007). DOI: 10.1103/PhysRevB.76.035326.

[107] T. Itoh et al. “Characterization and role of hydrogen in nc-Si:H”. In: *Journal of Non-crystalline Solids - J NON-CRYST SOLIDS* 266 (May 2000), pp. 201–205. DOI: 10.1016/S0022-3093(99)00821-2.

[108] Pavel Babál. “Doped nanocrystalline silicon oxide for use as (intermediate) reflecting layers in thin-film silicon solar cells”. PhD thesis. Delft University of Technology, 2014. ISBN: 9789462036826. DOI: https://doi.org/10.4233/uuid:448b63f4-2128-409e-bbd8-866e720116ed.

[109] Guozhen Yue et al. “Material structure and metastability of hydrogenated nanocrystalline silicon solar cells”. In: *Applied Physics Letters* 88 (June 2006), pp. 263507–263507. DOI: 10.1063/1.2216022.

[110] Arno Smets et al. *Solar Energy: The physics and engineering of photovoltaic conversion, technologies and systems*. English. UIT Cambridge Limited, 2016. ISBN: 978-1-906860-32-5.

[111] Mansi Sharma, Jagannath Panigrahi, and Vamsi Komarala. “Nanocrystalline silicon thin film growth and application for silicon heterojunction solar cells: a short review”. In: *Nanoscale Advances* 3 (May 2021). DOI: 10.1039/D0NA00791A.

[112] Wei Wensheng et al. “Preferred growth of nanocrystalline silicon in boron-doped nc-Si:H Films”. In: *Vacuum* 74.1 (2004), pp. 69–75. ISSN: 0042-207X. DOI: https://doi.org/10.1016/j.vacuum.2003.11.008. URL: https://www.sciencedirect.com/science/article/pii/S0042207X03002744.

[113] S. Saravanapriyan. “Mechanism of hydrogen-induced crystallization of amorphous silicon”. In: *Nature* 418 (Aug. 2002). DOI: 10.1038/nature00866.

[114] Roca Cabarrocas. “Substrate selectivity in the formation of microcrystalline silicon: Mechanisms and technological consequences”. In: *Applied Physics Letters* 66 (June 1998). DOI: doi.org/10.1063/1.113803.

[115] Joohyun Koh. “Real time spectroscopic ellipsometry studies of the nucleation and growth of p-type microcrystalline silicon films on amorphous silicon using B2H6, B(CH3)3 and BF3 dopant source gases”. In: *Applied Physics Letters* 85 (Jan. 1999). DOI: doi.org/10.1063/1.370323.

[116] Luana Mazzarella et al. “Nanocrystalline silicon emitter optimization for Si-HJ solar cells: Substrate selectivity and CO 2 plasma treatment effect: Nanocrystalline silicon emitter optimization for Si-HJ solar cells”. In: *physica status solidi (a)* 214 (Dec. 2016). DOI: 10.1002/pssa.201532958.

[117] Simon Kirner et al. “Silicon heterojunction solar cells with nanocrystalline Silicon Oxide emitter: Insights into charge carrier transport”. In: *2015 IEEE 42nd Photovoltaic Specialist Conference (PVSC)*. 2015, pp. 1–5. DOI: 10.1109/PVSC.2015.7356164.

[118] N. H. Nickel and W. B. Jackson. “Hydrogen-mediated creation and annihilation of strain in amorphous silicon”. In: *Phys. Rev. B* 51 (8 Feb. 1995), pp. 4872–4881. DOI: 10.1103/PhysRevB.51.4872. URL: https://link.aps.org/doi/10.1103/PhysRevB.51.4872.

[119] Luana Mazzarella et al. “P-type microcrystalline silicon oxide emitter for silicon heterojunction solar cells allowing current densities above 40 mA/cm2”. In: *Applied Physics Letters* 106 (Jan. 2015), p. 023902. DOI: 10.1063/1.4905906.

[120] Josua Stuckelberger et al. “Passivating electron contact based on highly crystalline nanostructured silicon oxide layers for silicon solar cells”. In: *Solar Energy Materials and Solar Cells* 158 (July 2016). DOI: 10.1016/j.solmat.2016.06.040.

[121] Alexei Richter et al. “Versatility of doped nanocrystalline silicon oxide for applications in silicon thin-film and heterojunction solar cells”. In: *Solar Energy Materials and Solar Cells* 174 (Jan. 2018), pp. 196–201. DOI: 10.1016/j.solmat.2017.08.035.

[122] Henriette Gatz et al. “p-type nc-SiOx:H emitter layer for silicon heterojunction solar cells grown by rf-PECVD”. In: *MRS Proceedings* 1770 (Jan. 2015). DOI: 10.1557/opl.2015.552.

[123] Luana Mazzarella et al. “Ultra-thin nanocrystalline n-type silicon oxide front contact layers for rearemitter silicon heterojunction solar cells”. In: *Solar Energy Materials and Solar Cells* 179 (Feb. 2018). DOI: 10.1016/j.solmat.2018.01.034.

[124] Ravi Vasudevan. *Characterization of n-type Silicon Oxide for Use in Thin Film Solar Cells*. 2011.

[125] Rudi Santbergen et al. “Function Analysis of the Phosphine Gas Flow for n-Type Nanocrystalline Silicon Oxide Layer in Silicon Heterojunction Solar Cells”. In: *ACS Applied Energy Materials* (Aug. 2021), pp. 7544–7551. DOI: doi.org/10.1021/acsaem.1c00654.

[126] Nguyen Thanh, N. Maclean, and Sara Mahiddine. “Mechanisms of Nucleation and Growth of Nanoparticles in Solution”. In: *Chemical Reviews* 114 (July 2014). DOI: 10.1021/cr400544s.

[127] Yuhao Yang et al. “N-type nc-SiOx:H film enables efficient and stable silicon heterojunction solar cells in sodium environment”. In: *Materials Letters* 309 (Nov. 2021), p. 131360. DOI: 10.1016/j.matlet.2021.131360.

[128] Yifeng Zhao et al. “Ultra□thin electron collectors based on nc□Si:H for high□efficiency silicon heterojunction solar cells”. In: *Progress in Photovoltaics: Research and Applications* 30 (Nov. 2021). DOI: 10.1002/pip.3502.

[129] N. Rouhi et al. “Low temperature growth of silicon dioxide using hydrogenation assisted nano-crystallization and plasma enhanced oxidation”. In: *Journal of Non-Crystalline Solids* 356 (May 2010), pp. 1027–1031. DOI: 10.1016/j.jnoncrysol.2010.01.020.

[130] Alexei Richter et al. “Versatility of doped nanocrystalline silicon oxide for applications in silicon thin-film and heterojunction solar cells”. In: *Solar Energy Materials and Solar Cells* 174 (Jan. 2018), pp. 196–201. DOI: 10.1016/j.solmat.2017.08.035.

[131] Francesco Roca Wilfried G. J. H. M. Sark Lars Korte. *Physics and Technology of Amorphous-Crystalline Heterostructure Silicon Solar Cells*. English. Springer Berlin, Heidelberg, 2012. ISBN: 978-3-642-22275-7.

[132] C. Han. “High-Mobility TCO-Based Contacting Schemes for c-Si Solar Cells”. PhD thesis. Delft University of Technology, 2022. ISBN: 978-94-6421-734-6. DOI: 10.4233/uuid:d6f35adf-486e-453a-9ae9-679a81105bed.

[133] Michel Aillerie Christelle Habis Jean Zaraket. “Transparent Conductive Oxides. Part I. General Review of Structural, Electrical and Optical Properties of TCOs Related to the Growth Techniques, Materials and Dopants.” In: *Defect and Diffusion Forum* 417 (June 2022), pp. 243–256. DOI: https://doi.org/10.4028/p-97c472.

[134] Hong Sohn. *Transparent Conducting Oxides. In Encyclopedia.* Mar. 2021. URL: https://encyclopedia.pub/entry/8381.

[135] Gregory Herman et al. “Transparent oxide semiconductors: Recent material developments and new applications”. In: (Oct. 2011). DOI: 10.1109/PHO.2011.6110668.

[136] Ramakrishna Madaka et al. “Tunnel recombination junction influence on the a-Si:H/SHJ tandem solar cell”. In: https://doi.org/10.1016/j.matpr.2020.08.451 (Sept. 2020).

[137] Klaus Jäger et al. “A scattering model for nano-textured interface and its application in optoelectrical simulations of thin film solar cells”. In: *Health and Quality of Life Outcomes - HEALTH QUAL LIFE OUTCOMES* 111 (Apr. 2012). DOI: 10.1063/1.4704372.

[138] Angus Rockett. *The Materials Science of Semiconductors*. English. Springer New York, NY, 2008. ISBN: 978-1-4419-3818-3. DOI: https://doi.org/10.1007/978-0-387-68650-9.

[139] Dong Zhang. “Surface passivation and optical design of silicon heterojunction solar cells”. PhD thesis. Delft University of Technology, 2015. ISBN: 978-94-6203-802-8. DOI: https://doi.org/10.4233/uuid:ccd8c8ea-493e-45af-b04e-a27d0d7bfc77.

[140] Antonis Mandrampazakis. *Development of Silicon-rich poly-Silicon Carbide passivating contacts for solar cells*. 2019.

[141] Dimitrios Deligiannis et al. “Surface passivation of c-Si for silicon heterojunction solar cells using high-pressure hydrogen diluted plasmas”. In: *AIP Advances* 5 (Sept. 2015), p. 097165. DOI: 10.1063/1.4931821.

[142] J. Ge et al. “Optimisation of Intrinsic a-Si:H Passivation Layers in Crystalline-amorphous Silicon Heterojunction Solar Cells”. In: *Energy Procedia* 15 (2012). International Conference on Materials for Advanced Technologies 2011, Symposium O, pp. 107–117. ISSN: 1876-6102. DOI: https://doi.org/10.1016/j.egypro.2012.02.013. URL: https://www.sciencedirect.com/science/article/pii/S1876610212003499.

[143] Mathias Mews et al. “Hydrogen plasma treatments for passivation of amorphous-crystalline silicon-heterojunctions on surfaces promoting epitaxy”. In: *Applied Physics Letters* 102 (Mar. 2013). DOI: 10.1063/1.4798292.

[144] J. Ballutaud. “Study of radio-frequency plasma deposition of amorphous silicon for the improvement of solar cell production /”. In: (Jan. 2004). DOI: 10.5075/epfl-thesis-2900.

[145] Hiroyuki Fujiwara and Michio Kondo. “Real-time control and characterization of aSi:H growth in aSi:H/cSi heterojunction solar cells by spectroscopic ellipsometry and infrared spectroscopy”. In: *Conference Record of the IEEE Photovoltaic Specialists Conference* (Jan. 2005), pp. 1285–1288. DOI: 10.1109/PVSC.2005.1488375.

[146] Benedicte Demaurex et al. “Damage at hydrogenated amorphous/crystalline silicon interfaces by indium tin oxide overlayer sputtering”. In: *Applied Physics Letters* 101 (Oct. 2012). DOI: 10.1063/1.4764529.

[147] Georgios Papakonstantinou. “Investigation and Optimization of the Front Metal Contact of Silicon Heterojunction Solar Cells”. PhD thesis. Delft University of Technology, 2014. URL: http://resolver.tudelft.nl/uuid:4f372da0-7325-424a-88ba-491c08054300.

[148] Halvard Haug. “New methods for investigation of surface passivation layers for crystalline silicon solar cells”. PhD thesis. June 2014.

[149] Ronald A. Sinton and Andrés Cuevas. “Contactless determination of current–voltage characteristics and minority□carrier lifetimes in semiconductors from quasi□steady□state photoconductance data”. In: *Applied Physics Letters* 69 (1996), pp. 2510–2512.

[150] Hiroyuki Fujiwara. *Spectroscopic Ellipsometry: Principles and Applications*. English. John Wiley & Sons, 2007. ISBN: 9780470060193.

[151] Physikalisches Institut. *Ellipsometry*. URL: https://www.pi1.uni-stuttgart.de/research/methods_overview/ellipsometry/.

[152] Emmanuel Guillot. *Procedure for diagnostic on optical-thermal properties and performance of CSP components*. Dec. 2013. DOI: 10.13140/RG.2.2.19921.74085.

[153] Damian Pysch, Ansgar Mette, and Stefan Glunz. “A review and comparison of different methods to determine the series resistance of solar cells”. In: *Solar Energy Materials and Solar Cells* 91 (Nov. 2007), pp. 1698–1706. DOI: 10.1016/j.solmat.2007.05.026.

[154] Brian Ford David Joy and Savile Bradbury. *Scanning electron microscope. Encyclopedia Britannica*. Sept. 2022. URL: https://www.britannica.com/technology/scanning-electron-microscope.

[155] Engineering Atoms. *The Scanning Electron Microscope*. 2015. URL: https://www.eng-atoms.msm.cam.ac.uk/RoyalSocDemos/SEM.

[156] Rudi Santbergen et al. “GenPro4 Optical Model for Solar Cell Simulation and Its Application to Multijunction Solar Cells”. In: *IEEE Journal of Photovoltaics* PP (Mar. 2017), pp. 1–8. DOI: 10.1109/JPHOTOV.2017.2669640.

[157] Jingjing Yan et al. “Choline Chloride-Modified SnO2 Achieving High Output Voltage in MAPbI3 Perovskite Solar Cells”. In: *ACS Applied Energy Materials* 3 (Mar. 2020). DOI: doi.org/10.1021/acsaem.0c00038.

[158] Xiaofeng Tang et al. “Local Observation of Phase Segregation in Mixed-Halide Perovskite”. In: *Nano Letters* 18.3 (2018), pp. 2172–2178. DOI: 10.1021/acs.nanolett.8b00505.

[159] Rudi Santbergen et al. “Minimizing optical losses in monolithic perovskite/c-Si tandem solar cells with a flat top cell”. In: *Optics Express* 24 (Sept. 2016), A1288. DOI: 10.1364/OE.24.0A1288.

[160] U.J. Nsofor et al. “Analysis of silicon wafer surface preparation for heterojunction solar cells using X-ray photoelectron spectroscopy and effective minority carrier lifetime”. In: *Solar Energy Materials and Solar Cells* 183 (2018), pp. 205–210. ISSN: 0927-0248. DOI: https://doi.org/10.1016/j.solmat.2018.03.006. URL: https://www.sciencedirect.com/science/article/pii/S0927024818301090.

[161] Hitoshi Sai et al. “Impact of intrinsic amorphous silicon bilayers in silicon heterojunction solar cells”. In: *Journal of Applied Physics* 124 (Sept. 2018). DOI: 10.1063/1.5045155.

[162] K.-S Lee et al. “Improved Surface Passivation Using Dual-Layered a-Si:H for Silicon Heterojunction Solar Cells”. In: *ECS Solid State Letters* 3 (Dec. 2014), P33–P36. DOI: 10.1149/2.001404ssl.

[163] Luana Mazzarella et al. “Nanocrystalline silicon emitter optimization for Si-HJ solar cells: Substrate selectivity and CO 2 plasma treatment effect: Nanocrystalline silicon emitter optimization for Si-HJ solar cells”. In: *physica status solidi (a)* 214 (Dec. 2016). DOI: 10.1002/pssa.201532958.

[164] Armin Aberle. “Surface passivation of crystalline silicon solar cells: a review”. In: *Progress in Photovoltaics: Research and Applications* 8 (Sept. 2000), pp. 473–487. DOI: 10.1002/1099-159X(200009/10)8:5<473::AID-PIP337>3.0.CO%3B2-D.

[165] Megersa Wodajo Shura et al. “Non-linear injection level dependence of the excess carrier lifetime of p-type GaSb thin films: A two-layer model”. In: *Journal of Applied Physics* 111 (June 2012). DOI: 10.1063/1.4725476.

[166] Stefaan De Wolf and Michio Kondo. “Surface Passivation Properties of Stacked Doped PECVD a-Si:H Layers for Hetero-Structure c-Si Solar Cells”. In: *2006 IEEE 4th World Conference on Photovoltaic Energy Conference*. Vol. 2. 2006, pp. 1469–1472. DOI: 10.1109/WCPEC.2006.279746.

[167] Stefaan De Wolf and Michio Kondo. “Boron-doped a-Si:H/c-Si interface passivation: Degradation mechanism”. In: *Applied Physics Letters* 91.11 (Sept. 2007). 112109. ISSN: 0003-6951. DOI: 10.1063/1.2783972. URL: https://doi.org/10.1063/1.2783972.

[168] Tim Schulze et al. “Impact of Fermi-level dependent defect equilibration on Voc of amorphous/crystalline silicon heterojunction solar cells”. In: *Energy Procedia* 8 (Dec. 2011), pp. 282–287. DOI: 10.1016/j.egypro.2011.06.137.

[169] Stefaan De Wolf and Michio Kondo. “Nature of doped a-Si:H/c-Si interface recombination”. In: *Journal of Applied Physics* 105 (June 2009), pp. 103707–103707. DOI: 10.1063/1.3129578.

[170] Paul Procel et al. “Theoretical evaluation of contact stack for high efficiency IBC-SHJ solar cells”. In: *Solar Energy Materials and Solar Cells* 186 (Nov. 2018). DOI: 10.1016/j.solmat.2018.06.021.

[171] Martin Bivour, Sebastian Schröer, and Martin Hermle. “Numerical Analysis of Electrical TCO / a-Si:H(p) Contact Properties for Silicon Heterojunction Solar Cells”. In: *Energy Procedia* 38 (Dec. 2013), pp. 658–669. DOI: 10.1016/j.egypro.2013.07.330.